BERGISCHE UNIVERSITÄT
GESAMTHOCHSCHULE WUPPERTAL
FACHBEREICH PHYSIK

The New QCD at HERA and its Impact on Extended Airshower Experiments

Norbert Magnussen

Wuppertal
August 1995

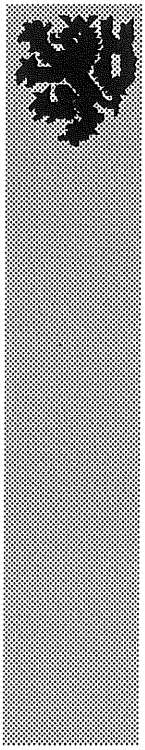

FACHBEREICH PHYSIK
BERGISCHE UNIVERSITÄT
GESAMTHOCHSCHULE WUPPERTAL

The New QCD at HERA and its Impact on Extended Airshower Experiments

Habilitationsschrift
zur Erlangung der Lehrbefugnis (Venia Legendi)
an der Bergischen Universität Gesamthochschule Wuppertal

Norbert Magnussen

Wuppertal
August 1995

Abstract

One of the current trends in physics consists of the unification of Astronomy, Astrophysics, Cosmology, Nuclear Physics and Particle Physics, into the combined field of Astroparticle Physics. A multitude of experimental and theoretical investigations are presently performed to solve some of the most puzzling questions concerning the evolution and current state of the Universe with the question of the origin of the Cosmic Rays being one of them. A subclass of experiments measuring at the highest energies are the so-called ground based γ-ray and Cosmic Ray experiments employing the Extended Airshower technique. The extraction of physics parameters from the measurements of these experiments for a great part rely on knowledge gained or verified at accelerator experiments. In particular Monte Carlo generators for simulating Extended Airshowers in the atmosphere in order to determine the acceptance functions of the experiments are based on phenomenological models and parametrizations of accelerator results. A unique accelerator yielding physics results since 1992 is the HERA *ep* collider at DESY in Hamburg. Here the two experiments H1 and ZEUS explore the structure of the proton, the photon, and the Pomeron in a very much extended kinematical range. In this report H1 physics results are discussed under the aspect of their possible impact on Astroparticle Physics questions addressed by Airshower experiments.

Contents

Chapter 1

Introduction

Over the past 30 years spectacular revolutions have taken place in several fields of experimental and theoretical physics. Contrary to the general development in most of science today, where new developments tend to be like mine shafts driven deeper into the body of the unknown and thus increasing the pathlength for information transfer between different fields, these revolutions acted like horizontal shafts meeting suddenly at great depth and giving birth to a new and combined field of physics. In this way the separate fields of Physics, Astrophysics, Cosmology, Particle Physics, Astronomy, and Nuclear Physics merged into the field of Astroparticle Physics. Schematically this is shown below, where Astronomy as the overall science of observation and explanation of the Universe is embedded into four fundamental fields of Physics.

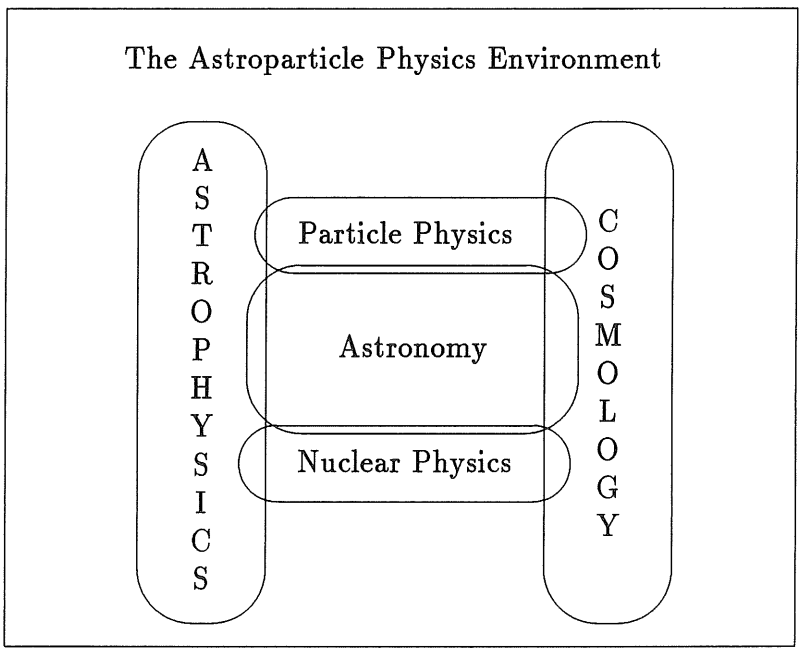

The revolution that mankinds oldest science, Astronomy, underwent during the 20th century was the extension of the observation window from the optical wavelength band to longer and shorter wavelengths. The extension of observations into the longer wavelengths started with the radio frequency band in 1945 and by now spans the whole range from the infrared to the radio. The enlargement of the experimenters horizon into shorter wavelengths gave rise to the fields of UV and X-ray Astronomy and finally γ-ray Astronomy in 1972. The first detection of γ-rays had already taken place in 1961 when the *Explorer XI* satellite recorded a few γ-rays. The year 1972, though, can be defined as the date of birth of γ-ray Astronomy because then for the first time statistically significant observations in the γ energy band from 30 to 5000 MeV were made. In addition to this electromagnetic radiation a particle component reaches the earth. This component, named Cosmic Rays (CR), was first observed during balloon flights by Hess and Kohlhörster in 1912.

The highest energetic particles observed in CR had energies in excess of 10^{20} eV. Including these in all-wavelength observations, the astronomical observation window now spans more than 28 decades in energy. The origin of CR is one of the main enigmas of 20th century physics. Much work has gone into the search for CR and into the modelling of their potential sources. For reviews on the field of CR physics see e.g. [1, 2, 3]. The measurements of the flux and composition of charged particle radiation at the very high energies ($E \geq 10^{14}$ eV) can only be performed by measuring Extended Airshowers (EAS) developing after the particle's interaction in the atmosphere. Because of galactic and intergalactic magnetic fields, in order to find the sources of this radiation, the measurement objectives in general have to be neutral particles. These are either γ-rays or neutrinos. At the highest energies ($E \geq 10^{19}$ eV) also charged nuclei and neutrons may retain directional information over long distances. For incident γ-rays, the relevant energy for the transition from only space-bound to both space and earth-bound EAS experiments is about 10^{11} eV. For incident neutrinos no transition energy defined by experimental boundary conditions can be given as direct measurements in space are nearly impossible.

In this report we will first discuss some aspects of the field of EAS physics and point out possible connections to the physics results currently obtained at the HERA *ep* collider. In the second part we will then discuss some of the outstanding physics results obtained so far at the H1 experiment. We will see that the new kinematical domain investigated at HERA provides a natural link between these accelerator results and Astroparticle Physics with EAS.

The link is established due to the physics results obtained from the EAS data critically depending on a variety of Particle and Nuclear Physics inputs such as cross sections and detailed models of interactions for the indispensable Monte Carlo generators. Some of the main inputs are the structure of the proton and nuclei as projectiles and targets, of the Pomeron as the envisaged exchange object in soft hadronic interactions, and the structure of the photon as one of the major projectiles.

Until HERA our knowledge on these particles or objects was based on hadron collider and low energy deep inelastic experiments which provided data on inclusive and exclusive cross sections, on parametrizations for the structure of the proton, and on the qualitative structure of the Pomeron. Due to the operation of the HERA *ep* collider at the DESY laboratory since 1992, the knowledge on these particles or objects has dramatically improved. The region in phase space accessible for the first time in deep inelastic scattering experiments is the region of extremely small Bjorken-x. It constitutes both, the deep structure of the proton where we expect to approach the transition from perturbative to non-perturbative QCD regime, and the Regge limit, in which we can test the high energy asymptotic behaviour of QCD governing both total inclusive hadronic cross sections and the semi-hard exclusive processes in very high energy interactions of CR with nuclei in the atmosphere.

The report is structured as follows: in chapter 2 a short discussion of the field of Astroparticle Physics with extended airshowers (EAS) within its environment as sketched above is given. In chapter 3 the EAS experimental techniques will be presented and the EAS research topics will be discussed under the aspect of their connection to the HERA results. The HERA machine, the H1 detector, and the HEGRA airshower detector array situated on the Canarian island, La Palma are presented in chapter 4. The structure of the proton and the Pomeron within QCD are discussed in chapter 5 and the relevant experimental results gathered by the H1 experiment at HERA are presented in chapter 6. The measurements concerning the hadronic structure of the photon are presented in chapter 7. After this we will present the CORSIKA EAS Monte Carlo generator [4] employed by the HEGRA collaboration and finally, in chapter 9, the influence of the H1 data on current and future airshower physics projects are discussed in the light of the research topics listed in chapter 3.

Chapter 2

Astroparticle Physics

In this chapter the field of Astroparticle Physics using the experimental technique of measuring Extended Air showers (EAS) in the atmosphere is discussed.

2.1 Astroparticle Physics with EAS

One of the goals of Astroparticle Physics is to identify and understand the sources and processes that give rise to the particles measured on earth. The grand unified spectrum of the electromagnetic radiation reaching the earth is shown in Fig. 2.1. Also shown in the same figure is the particle component, the CR, which reach the earth with energies larger than about 1 GeV and which have been found to reach out to energies of more than 10^{20} eV (10^{11} GeV). The lower energy cutoff on CR is due to the magnetic field of the earth and to the solar wind emanating from our sun that carries with it a magnetic field which sweeps particles with momenta of less than a few GeV/c out of the solar system.

Up to energies of about 10^5 GeV direct measurements of the flux and composition of this radiation, either on satellites or on high altitude balloons, have been carried out. For energies larger than about 100 GeV also indirect measurements can be performed with large detectors placed on the ground. These indirect measurements of the flux and composition can be achieved by using the earths atmosphere as absorber or calorimeter depending on the instrumentation. The signal of the Extended Airshowers (EAS) which result from the interaction of the incident particle with nuclei in the atmosphere and the subsequent cascade of radiation and particles which develops within the atmosphere is then sampled. Since for energies above 1000 GeV the incoming flux is below 10^{-5} $cm^{-2}sr^{-1}s^{-1}$ and the resulting EAS are spread over large areas, the effective detector areas have to be larger than about 10^5 m^2.

It is customary to divide the energy band investigated with EAS into two regions

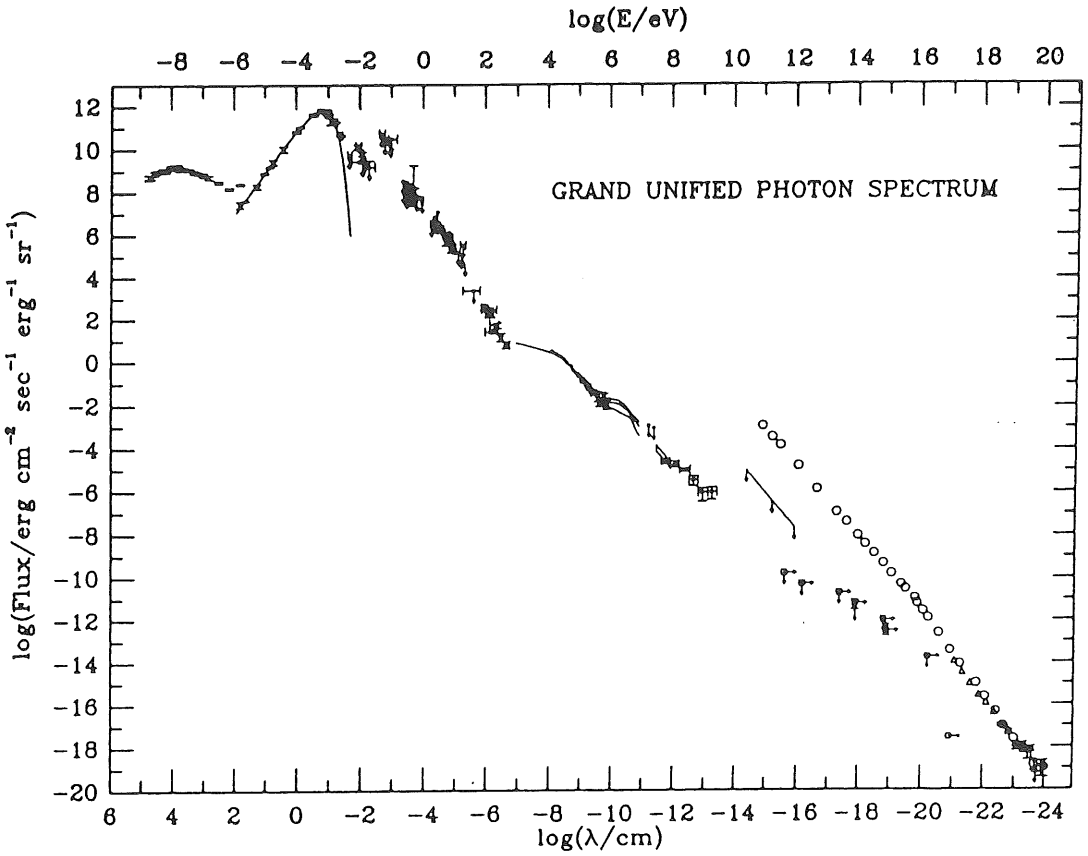

Figure 2.1: Photon spectrum for energies between 10^{-9} and 10^{10} eV and the All-particle spectrum of Cosmic Rays above 10^{11} eV/nucleon. Taken from [5].

distinguished by the detection technique. These bands are the very high energy (VHE) band from 0.1 - 10 TeV and the ultrahigh energy (UHE) band for energies larger than about 100 TeV. The reason for defining these non-overlapping bands lay in the status of the measurement technology employed in EAS physics until the advent of the HEGRA AIROBICC technique [6]. The Imaging Čerenkov Telecopes (ICT) could record Čerenkov photons emitted by relativistic particles (mainly electrons and positrons) in EAS for the VHE band and large array detectors the secondary electrons and positrons themselves for the UHE band. The AIROBICC detector operating within the HEGRA installation is an optimization of the open photomultiplier Čerenkov technique introduced in 1953 by Galbraith and Jelley [7] (see 3). With this installation (see 4.3) it is possible to bridge the gap between VHE and UHE and measure from about 10 TeV up to beyond 10,000 TeV.

In total the vertical thickness of the atmosphere above the sea level is about 27 radiation lengths (1030 g/cm^2). In contrast to sampling calorimeters employed in Particle Physics experiments, only one sensitive layer can be instrumented in the atmosphere. When recording the secondary particles produced in the cascade is the aim of the measurement, this instrumented layer ought to be as near to the

shower maximum as possible in order to record a sufficient number of secondary particles from which the energy, direction, and nature of the primary projectile can be reconstructed.

In case of the AIROBICC or the Imaging Čerenkov telecope method, the atmosphere does not act any more as a sampling calorimeter but as a full active calorimeter comparable to CsI or leadglass detectors employed in Particle Physics. Since the density of the atmosphere is much smaller than the abovementioned Particle Physics detectors, the useful signal is completely different from the ionisation signal integrated over in e.g. leadglass detectors. E.g. the AIROBICC technique [6] relies on the integration of the Čerenkov radiation that is emitted by most of the secondaries within the EAS due to the extremely high incident and secondary energies. The produced light pools extend over more than 10^5 m^2 for energies above 1 TeV. For this type of detector, the site has to have the best possible optical environment. This means a high fraction of clear nights, negligible light pollution from man-made sources, and also little pollution of the atmosphere with chemicals in order for the atmospheric conditions to be as stable as possible.

These requirements make it necessary to build detectors for these airshowers at as high as possible locations and secondly to equip an as large as possible area with detectors sensitive to the secondary radiation in order to achieve a high point-source sensitivity. The actual setup, i.e. the size of the detector, the relative coverage of the detector area with active components, the location of the detector in altitude, and the type of the individual detector elements themselves lastly determine the actual lower and upper threshold energies between which the EAS detector is sensitive to incident radiation and can determine parameters with sensible error margins.

In the following some the physics topics that can be investigated with the EAS technique are discussed.

2.2 Overview of EAS Physics Topics

The field of EAS is concerned with the upper end of the radiation band filled in todays Universe (10^{11} eV $\rightarrow$ 10^{20} eV). The goals of the measurements can be summed into the quest of the sources of this radiation. Some restrictions apply to the list of potential signal particles.

Our galaxy contains inhomogeneous magnetic fields of an average strength of 10^{-6} Gauss. Consequently, e.g. singly charged particles with momenta of 1 TeV/c have gyro radii of

$$R_{\mathrm{Gyro}} = \frac{mv}{eB} = 3 \cdot 10^{-1}\mathrm{pc}, \tag{2.1}$$

i.e. much smaller than the thickness of the galactic disk. This means that the

momenta are too small for the particles to leave our galaxy and the trajectories will be curled up already close to any galactic source. In the case of extragalactic sources, possible intergalactic magnetic fields (see [8] for a review) will also destroy directional information for charged particles over large distances. Identification of possible sources thus has to rely on the measurement of neutral or magnetically stiff charged particles. This shortens the list of potential source particles to

- γ-rays,
- neutrinos,
- ultrahigh energetic neutrons ($E_n > 10^{19}$ eV), and
- ultrahigh energetic protons ($E_p > 10^{19}$ eV) from distances ≤ 50 Mpc.

The minimum energy requirement on the neutrons is needed in order for them to live long enough to travel cosmic distances. This source particle, though, does not play a rôle in all practical considerations and will thus not be discussed any further. Of course, also other charged nuclei besides protons with energies exceeding 10^{19} eV are even less bended out of their original direction due to galactic or intergalactic magnetic fields and could reach the earth, if their source is not too far away.

From Fig. 2.1 it can be deduced that the main radiation component at EAS energies is in form of charged particles with the all-particle spectral index about -2.7 up to about $3 \cdot 10^{15}$ eV. At this energy a "knee" in the spectrum is observed with the spectral index changing to about 3.1 up to about 10^{19} eV [9, 10]. The charged particles themselves are predominantly hadrons. The lepton component (e^- and e^+) is important at the low end of the EAS energy window, i.e. around 100 GeV, which will be the typical threshold energy above which EAS detectors employing Imaging Čerenkov Telescopes will operate (see chapter 3). Since electrons initiate EAS which are indistinguishable from photon initiated ones, this background has to be studied carefully with space-bound detectors. The measured electron spectrum above about 30 GeV can be well described by a power law with a spectral index of -3.26 [11, 12]. Due to this steep spectrum this component is most probably negligible at the energies the EAS arrays are sensitive to. Classical EAS array detectors like the AKENO and Yakutsk arrays are sensitive from about 10^{15} eV up to energies of above about 10^{19} eV [13, 14]. The HEGRA hybrid detector array (see 3 and 4.3) is sensitive from about 10^{12} eV up to energies of above about 10^{17} eV and with this covers both the direct measurements and the "knee". Even though the charged particles do in general not carry directional information, they carry very important information on source parameters and on the medium they propagated through in order to reach the earth. To measure the chemical composition especially in the "knee" region is thus one of the major aims of EAS installations in addition to the search for sources.

The list of particles which allow for a clear identification of their source is in practice limited to γ-rays and neutrinos. They also carry time information which

may e.g. be compared to pulsar periods etc. in other wavelenghts. The probabilities for the three types of CR, electromagnetically interacting γ-rays, weakly interacting neutrinos, and electromagnetically and strongly interacting hadrons to interact within the source where they are accelerated (hadrons) or produced (γ-rays and neutrinos), or to interact while propagating towards the observer, are very different. E.g. neutrinos have the best chances to escape any source and they are practically undamped on propagation. This makes neutrinos the ideal source particle when looking for cosmologically distant sources. On the other hand, detecting these neutrinos is of course difficult due to the same fact: they interact only weakly. The detectors thus have to employ huge target masses and mostly huge active detector volumes.

Models for acceleration mechanisms for CR that can accelerate particles up to 10^{20} eV are being sought since their discovery and span the band of physics from standard shock-acceleration, topological deffects stemming from the Age of Cosmic symmetry-breaking [15] to the decay of Cosmic strings [15, 16]. To estimate the expected fluxes from potential sources detailed source models are needed and have been developed. Due to the very complex magnetic field structure in our galaxy and the unknown structure in intergalactic space, the expected fluxes of charged hadrons are given by the convolution of all possible sources. In this way features in the all-particle and in individual spectra still are predictable. E. g. the "knee" in the all-particle spectrum is successfully predicted by the diffusion model [17] in which the chemical composition is supposed to change to a heavier composition at the "knee" [18]. In the case of γ-rays and neutrinos, however, it is possible for most of the models to predict fluxes for individual sources. A selection of source candidates is discussed below.

Usually a distinction is made between galactic and extragalactic sources with the relative importance being a function of the energy of the hadronic CR. A few examples of possible conventional sources for CR containing galactic (G) and extragalactic (E) candidates are:

1. Supernova explosions into the interstellar medium (G),
2. Supernova explosions into a predecessor stellar wind (G),
3. X-ray binary systems (G),
4. Compact binaries with interacting wind zones (G),
5. Young supernova remnants (G)
6. The central region of Active Galactic Nuclei (AGN) (E)
7. Hot spots of giant powerful Radio Galaxies (radio-*loud* AGN) (E),

In the following some comments on the above list are given.

1. That supernova (SN) explosions might produce CR was already proposed by Baade and Zwicky in 1934 [19]. The isotopic abundances of CR not only convey information on the nucleosynthesis origin at astrophysical sites, but also keep track of the time elapsed during their acceleration and propagation. The determination of the age of CR by the measurement of the abundance of the spallation product ^{10}Be [20] in 1977 confirmed their galactic origin in the energy region around 1 GeV/nucleon. This had been speculated upon already in 1939 by Alvén [21].

   At the highest energies, though, the CR have to be of extragalactic origin due to their extreme magnetic stiffness [22]. The observation of the "knee" in the CR spectrum at about $5 \cdot 10^{15}$ eV, where the spectral index of the all-particle spectrum changes from about -2.7 to -3.1, is believed to mark the transition region from galactic to extragalactic origin of the CR.

   The fraction of galactic CR due to explosions of supernovae (SN) into the interstellar medium and the fraction due to explosions into predecessor stellar winds (2.) is still under dispute. The normal SN scenario is the explosion of the star into the interstellar medium. One possible model is that CR below about 10^{13} eV are produced by the explosion of stars into the normal interstellar medium [23]. This assumption is backed by the observation that the chemical composition of the CR at the lower energies is similar to the chemical composition of the interstellar medium but for an underabundance of Hydrogen and Helium relative to Silicon. The maximum energies that electrons can reach in SN explosions into the interstellar medium are about 100 GeV [24].

2. For energies from about 10^{13} eV up to the "knee" at $5 \cdot 10^{15}$ eV, Völk and Biermann [25] argue that CR should predominantly stem from the explosion of stars into their own former stellar wind. The important differences to the explosion into the interstellar medium are [24] i) the density gradient of the stellar wind which leads to persistent high shock velocities in contrast to the case of the interstellar medium where the shock wave acts like a snow-plough and is consequently slowed down, ii) stellar winds may carry with it much higher magnetic fields than the normal interstellar medium, and iii) that the winds of massive stars are enriched in heavy elements. The average energies obtainable in the shock acceleration process will thus be higher. Also electrons can be accelerated to much higher energies in this case. Biermann [24] finds maximum energies in the order of 3 TeV consistent with observations [11].

3. The X-ray binary system Cygnus X-3 has been reported to be a source of ultrahigh energy (UHE, $E > 10^{14}$ eV) γ-rays in 1983 [26, 27]. Even though by now only upper limits can be placed on the steady emission from this source candidate which are about an order of magnitude below the 1983 detection in the energy range above $2 \cdot 10^{15}$ eV, the X-ray binaries are still good candidates as accelerators of CR. These systems consist of a compact object, i.e. a neutron star or a black hole, and a non-compact companion star and mass flowing from the non-compact to the compact partner. This

mass will in general form an accretion disk around the compact object.

Since neutron stars are also known to have very strong magnetic fields (up to 10^{12} G), both plasma flow and strong magnetic fields are available to form strong shocks and accelerate particles. Since the neutron stars are also often spinning very rapidly as can be inferred from millisecond pulsar frequencies, magnetic dipole radiation and the accretion both may serve as the energy source for the acceleration process.

4. compact binary systems with interacting winds are discussed in [28]. Again strong shocks may develop to accelerate particles up to very high energies.

5. young supernova remnants are discussed as point sources for neutrinos in *e.g.* [29]

6. Active Galactic Nuclei (AGN) belong to a class of objects known as Quasars. These objects have for a long time been supposed to be the most powerful emitters of radiation in the universe [30] and are presumed to be powered by the gravitational energy released by enormous amounts of matter falling onto a supermassive black hole. Exactly how the conversion of gravitational into luminous energy is accomplished is not known, but two classes of models are discussed both of which contain a stage where high energy particles are produced in order to transfer the energy.

   The first is connected to the central engine of the AGN [31, 32]. The second is connected to the jets of radio-loud AGNs (see 7.). In the first model the accretion flow becomes spherical close to the black hole. A shock with a typical shock radius of 10 to 100 Schwarzschild radii of the black hole is formed when the ram pressure of the accretion flow is balanced by radiation pressure close to the black hole. One important prediction of this model is that the continuous emission is dominated by the ultraviolet and X-ray radiation emanating from the shock region. Features of this kind have been observed. The most prominent features observed for AGNs are steady dust emission in the infrared, an excess of ultraviolet emission (UV bump) variable on a timescale of days [33] and X-ray emission variable on similar or shorter timescales [34].

   The protons accelerated in the shock can produce high energy γs and neutrinos through photomeson production off the UV accretion disk photons [35, 36, 37]. As Stecker *et al.* [36] pointed out, following the photopion production ($p + \gamma \rightarrow N + \pi$), pair cascading of γs from π^0 decays off the intense quasar photon field ($\gamma\gamma \rightarrow e^+e^-$) would destroy the high energy γ-rays and produce the observed quasar X-ray emission [38]. High energy neutrinos are produced in photomeson production and in *pp* scattering reactions by the subsequent $\pi^\pm \rightarrow \mu^\pm \rightarrow e^\pm$ decay chain. In contrast to the high energy γs they will escape the source unscathed. By normalizing to the X-ray emission, Stecker *et al.* predict the AGNs to be by far the strongest sources of ultrahigh energy neutrinos in the universe. They further predict, by summing over all quasars in the universe, that a large and measurable neutrino flux should be present on earth.

In addition, other and conflicting predictions have been discussed. See [39]. The EAS possibilities to detect a cosmological neutrino background are discussed below.

7. The second class of AGN that has been proposed as the site for the production of the highest energetic CR [37, 40] are the so-called *blazars*, i.e. radio-loud active galactic nuclei. In the original model proton acceleration up to energies of the order of 10^{20} eV takes place in the hot spots found in the jets of these radio galaxies [41]. Another possibility is that not protons but electrons are accelerated within the jets [42, 43, 44].

   Both jet models would account for the high energy γ-ray fluxes that have been observed for about 40 such sources by the EGRET detector aboard the Compton Gamma Ray Observatory (C-GRO) [45] and for the ultrahigh energy γ radiation observed by the Whipple [46] and HEGRA [47] installations from the blazar Mrk421. Especially the two flares of Mrk421 in the TeV γ energy range as observed by the Whipple Collaboration [48, 49] give some confidence in the hot-spot scenario. Another interesting fact associated with these flares is that the correlated flares in the X-ray region as observed by the ASCA satellite [49, 50] served to really identify Mrk421 as the source of the TeV emission since the angular resolution of ASCA is less than 1 arcmin compared to about 0.1° of Čerenkov Telescopes.

   Whereas the accelerated protons would give rise to γ and neutrino beams, no neutrino flux would be expected within the electron scenario.

In contrast to γ-rays which may be damped on propagation via pair production processes on the Intergalactic Infrared Background Field (IIBF) (see 2.2.1), neutrinos from cosmic sources reach the earth practically undamped.

Since a high flux of high energy γ-rays as detected from the AGN Mrk 421, will in the case of proton acceleration be accompanied by a closely related high neutrino flux, the measurement of γ-rays and neutrinos complement each other.

To summarize, neutrino production is expected whenever a cosmic beam dump occurs, i.e. accelerated protons or heavy ions hit a target. Since the target has to be just thick enough to allow for the production of γ-rays, but not so thick as to absorb them, the observation of neutrinos from a source will not be accompanied by the observation of very high energetic γ-rays. The additional requirement for the production of neutrinos to occur, is that the target is not too thick as to not allow the pions and muons to decay, is fullfilled in almost every imagined cosmic source. For this reason and because many more cosmologically distant neutrino than γ-ray sources should be visible, the interest in neutrino astrophysics has been growing constantly.

In addition to the above there are other potential sources of neutrinos which will have to be investigated in the future, the main being neutralino annihilation in the sun and earth [51], supernovae [3], and neutrinos from the decay of leptons

produced in high energy CR interactions in the interstellar and intergalactic media [52].

2.2.1 Boundary Conditions imposed on the Measurements

The search for CR at the highest energies has intensified considerably lately because several EAS installations have in their many years of running recorded events with the incident particle energy above $5 \cdot 10^{19}$ eV [53, 54, 55, 56]. This energy is the threshold energy known as the Greisen-Zatsepin-Kuzmin (GZK) cutoff [52, 57] above which protons will loose energy through interactions with the 2.7K Cosmic Microwave Background (CMB) radiation via

$$p + \gamma_{\mathrm{CMB}} \rightarrow p + \pi^0. \tag{2.2}$$

Due to the very high number density of the CMB no measurable particle flux above this cutoff can stem from cosmological distances. That a non-zero flux is measured nonetheless has triggered many experimental, phenomenological, and theoretical activities (see e.g. [24, 58]). The HEGRA EAS array is not sensitive to energies above about 10^{17} eV due to its limited size.

Also in the energy region where the HEGRA array reaches its best sensitivity (above about 20 TeV) fundamental cutoffs exist. In this case they are imposed on the cosmological γ radiation. The first cutoff consists of the damping of γ radiation via the pair production process

$$\gamma + \gamma_{\mathrm{CMB}} \rightarrow e^+ + e^- \tag{2.3}$$

on the cosmic microwave background (CMB). The threshold γ-ray energies are about 100 TeV.

At energies lower than this, a second cutoff may occur due to the same pair production process, but now the γ-rays may be damped by an intergalactic infrared photon field [36]. The source of the intergalactic infrared photon field is the starlight from distant (i.e. early) galaxies red-shifted due to the expansion of the Universe.

Chapter 3

EAS Techniques and HERA Connection

In this chapter the main experimental techniques employed in EAS applications and the possible influence of HERA physics results on the extraction of EAS physics signals will be discussed. In EAS not the initial particle but only the showers developing in the atmosphere can be observed. The incoming radiation consists of γ-rays and a mixture of nuclei from protons to iron and beyond. The energy spectrum is steeply falling, the composition might change with energy, and the fluxes of γ-rays from most sources are a few orders of magnitude weaker than the charged hadronic background. We will discuss the signals emanating from an EAS in the atmosphere, the relevant experimental techniques, and the physics signals under the aspect of a possible HERA physics influence. A short introduction into the very important subject of γ/hadron separation techniques is given to highlight the importance of reliable Monte Carlo simulation programs based on High Energy and Nuclear Physics results.

3.1 The EAS Environment

From the technical point-of-view, the field of EAS Physics can be thought of as being constructed out of three building blocks. These blocks are the goals of the measurements, the problems encountered towards these goals, and the performance of the measurement devices themselves. Their relation can be sketched as shown in Fig. 3.1.

Assuming the knowledge of the physics contained in any two of these boxes, the field of Airshower Physics can contribute to the third one. This is what determines the big physics potential of this field and which on the other hand makes it necessary for the researchers active in this field to be able and willing

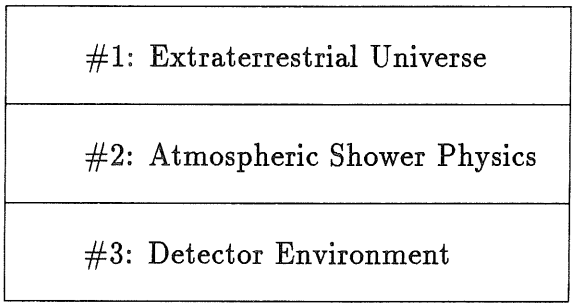

Figure 3.1: The building blocks of EAS physics.

to tackle the physics questions of all of the above areas. Of course, any big shift in the knowledge on any of the three ingredients could necessitate a revision of the deduced results obtained from the measurements so far.

Each of these three boxes contains a diversity of physical processes that are important to measure. Box #1 contains the physics that is either relevant to the Astrophysics of stars and the Milky Way, or to Astrophysics and Cosmology in the case of extragalactical sources.

The measurements performed at HERA mainly can be linked to the physical processes pertaining to box #2, the atmosphere. Below we will discuss the main physics topics that can be addressed by the EAS technique and show that the Monte Carlo simulation of EAS can easily be identified as an important common factor. The results obtained by the H1 collaboration which affect the simulations and extraction of results are discussed in the chapters 6 and 7. Basically, for the following three types of incident particles the HERA results contribute to EAS physics.

- For incoming photons due to the improved knowledge of the structure of the photon;
- for incoming hadrons, since the structure of the proton and the nature and structure of the Pomeron have been determined in an extended kinematical range;
- for incoming neutrinos also due to the deep structure of the proton now accessible experimentally.

Finally, the physics issues contained in box #3 are the influence of the atmospheric conditions like temperature, pressure, pollution, etc. on the measurements. In addition, in the case of horizontal EAS measured to detect high energy neutrino interactions, the physics of electromagnetic radiative energy losses close to EAS detector is needed to be understood in detail.

3.2 The EAS Signals

In EAS physics the atmosphere serves as a calorimeter. The expectation about the performance of this calorimeter can only be specified after taking the type of instrumentation into consideration. In short, in EAS physics the following equation holds

$$\text{Atmosphere} + \text{Instrument} = \text{EAS Calorimetertyp}$$

A calorimeter as employed in High Energy Physics may be characterized as follows [59]:

1. it is sensitive to both charged and neutral particles;
2. the 'energy degradation' through the development of the particle cascade is a statistical process, and the average number $< N >$ of secondary particles is proportional to the energy of the incident particle. In principle, the uncertainty in the energy measurement is governed by statistical fluctuations of N, and hence the relative energy resolution σ/E improves as $1/\sqrt{N} \propto E^{-1/2}$;
3. the length of the detector scales logarithmically with particle energy E;
4. with segmented detectors, information on the shower development allows precise measurements of the position and angle of the incident particle;
5. their different response to electrons, muons, and hadrons can be exploited for particle identification;
6. their fast time response allows operation at high particle rates, and the pattern of energy deposition can be used for rapid on-line event selection.

Almost all of these characteristics can be found again in EAS applications. Note, however, that the standard mode of operation of the EAS calorimeter is the mode of a badly leaking type. The relative amount of leakage scales (see 3.) with the logarithm of the energy. This fact is used in the NKG-fit to determine the age and energy of an EAS based on charged particle information well after the maximum of the shower development. The NKG-formula has been derived from cascade theory by Nishimura, Kamata and Greisen [60] and relates the measured particle density as a function of radius r from the shower core, $\rho(r)$, to the shower age, s, and the total number of electrons, N, in the EAS. The age s of the shower is defined through

$$\frac{d\ln N(t)}{dt} = \lambda(s) \tag{3.1}$$

with t the distance along the shower in radiation lengths, N the shower size, and $\lambda(s) = 0$ when $s = 1$. The NKG formula then takes the form

$$\rho(r) = \frac{N}{r_1^2} \cdot \left(\frac{r}{r_1}\right)^{s-2} \left(1 + \frac{r}{r_1}\right)^{s-4.5} \frac{\Gamma(4.5 - s)}{2\pi\Gamma(4.5 - 2s)} \tag{3.2}$$

Applied to EAS, the signals and the employed instrumentation may be characterized as follows:

- the 'old' component consisting out of $e^{\pm}$, γs, hadrons, and muons with energies larger than about 1 MeV is measured in scintillator arrays, tracking detectors, and (sometimes) calorimeters. The measurement objective is the number of particles reaching the observation level (N_e), the radial distribution thereof (dN_e/dr), and the energy density and its radial distribution (dE/dN, dE/dr).
  The resulting type of calorimeter is a sampling calorimeter with 1(!) active layer after the maximum of the shower. The active layer only covers typically a few % of the total area. Sampling fluctuations and fluctuations in the amount of leakage (note, the amount of leakage is the signal), which in this type of detector limit the obtainable energy resolution, thus influence the measurement twice. The energy resolution is expected and found to be poor.

- Components with contributions of all ages are the number of muons, N_μ, and the number of Čerenkov photons, $N_{\check{C}}$. The measurement of these components and the resulting calorimeter types are as follows:

  .. N_μ: This component is measured either by tracking detectors or detectors situated after a thick absorber. For a sufficiently large detector acceptance at low energies, or for a large enough number of muons, the resulting calorimeter is an active hadron calorimeter.

  .. $N_{\check{C}}$: Outside the core region, *e.g.* for 30 m $< r_{\text{core}} <$ 100 m, where r_{core} is the distance of the measuring device to the reconstructed position of the extrapolation of the incident particle's impact point in the detector array, the density of Čerenkov photons is very large compared to the density of charged particles:

  $$\frac{dN_{\check{C}}}{dA} \simeq 10^5 \cdot \frac{dN_{\text{Charged}}(E > MeV)}{dA}$$

  This component is currently measured by two techniques:

  ... Imaging Čerenkov telescopes measure the angular distribution of Čerenkov photons and make use of the fact that hadron images will be more fussy due to the larger transverse momenta transferred on average in hadronic interactions. In the search for γ sources this image allows for strong suppression of the hadronic background. Since also the intensity is recorded, the resulting calorimeter is of the active type, but only a small fraction of the calorimetric signal is utilized.

  ... Angle integrating Čerenkov arrays are employed to measure the full Čerenkov light pool. This is, as in the case of the scintillator arrays, done with a relatively low coverage factor of the area irradiated by the light pool. The huge number of photons compared

to energetic secondary particles, though, does not make this a limiting factor on the obtainable energy resolution. The resulting calorimeter thus constitutes a non-compensating, i.e. giving different signals for hadrons and electrons, fully active calorimeter for hadrons, electrons, and photons.

Using the CORSIKA Monte Carlo generator [4], the potential of the angle integrating Čerenkov method may be illustrated. Figs. 3.2 to 3.4 show the number densities of Čerenkov photons (light pool) on an area of $1.6 \cdot 10^5$ m^2 at an observation level of 2200 m, and the relation between the emission height of the Č photons and the distance from the core they are emitted into, for γs and protons of 1, 10, and 100 TeV energy. In Fig. 3.5 the corresponding number density for high energy particles, i.e. energies above 3 MeV, is shown for γs and protons at the same energies. From these figures it is obvious that the measurement of Čerenkov photons instead of high energy particles can be superior in quality, and, that with this method, lower energy thresholds may be reached.

To be more specific, for the above discussed array detectors the measurements of selected observables of EAS and the detector performance itself leads to the following accuracies on the measurement of EAS parameters:

1. Singlelayer detector arrays
   - the measurement of dN_e/dA and dN_e/dr are input to the NKG-Fit to determine the energy of the incident particle. This measurement is maximally sensitive to fluctuations in the longitudinal shower development. The energy resolution $\sigma(E)/E$ consequently is bad, and is typically of the order of 40%. The energy threshold for this type of detector depends strongly on the observation level, size, and area coverage. For the HEGRA installation the threshold is around 35 TeV for γ-rays and around 45 TeV protons.
   - the arrival time of the particles is converted into the direction of the incident particle. The accuracy of this measurement is determined by the size of the intrinsic fluctuations caused by multiple scattering and is typically of the order of $\sigma(\theta) \simeq 0.7°$.
2. Multilayer detector arrays
   - The number of muons (N_μ) and its directions can be utilized to measure incident direction, to suppress the hadronic background in investigations of γ sources, and to measure the chemical composition of the incident CR. These components usually work in connection with detectors of type 1 and 3.
   - The measurement of $\mathrm{d}N_e/\mathrm{d}A$ and $\mathrm{d}N_e/\mathrm{d}r$ can be used as in the scintillator case to determine the incident energy. For the planned MILAGRO [61] multilayer detector, which will use water Čerenkov detec-

tors located in pools above ground, an energy threshold of the order of 2 TeV is envisaged.

- From the arrival time, if measured in a high resolution device like the MILAGRO detector, the incident direction can be reconstructed. Multiple scattering of the observed particles limits the angular resolution to around 0.5°.
- The additional measurement of the energy densities, $dE/dN(r_{\rm core})$, can be used for hadron suppression. *

3. Angle Integrating Čerenkov Arrays (AICA) like AIROBICC [6]

   - the measurement of the rate of decline of the light pool intensity for increasing distance from the core position, called the light radius $R_{\rm L}$, allows a reconstruction of the height of the shower maximum, $X_{\rm max}$.
   - After the application of this correction, the measurement of $dN_{\check{\rm C}}/dA$ allows the reconstruction of the core position and the determination of the incident energy. The measurement of $dN_{\check{\rm C}}/dr$, $R_{\rm L}$, and the ratio of Čerenkov light intensities at different distances from the core position, $L(r_{\rm i})/{\rm L}({\rm r_j})$, can be used to suppress the hadronic background, or may be used to determine the chemical composition of CR. † Since the Čerenkov light emitted at different depths of the shower development is radiated into different distances from the core position, the determination of the depth of the maximum of the shower development can be performed using the light radius $R_{\rm L}$. Again, due to this instance, the determination of the energy of the primary is not limited by longitudinal fluctuations, and the resulting energy resolution for the AIROBICC installation was found to be $\sigma(E)/E \leq 10\%$. The much higher number density of Č photons and the much sharper Č light front due to the very much reduced influence of multiple scattering, make possible resolutions on the determination of the incident angles of the order of $\sigma(\theta) \simeq 0.2 - 0.3°$. The energy threshold for γ-rays is around 12 TeV, while for protons it is around 27 TeV. ‡

Scintillator stations are up to now the cheapest and still reliable detectors to record secondary particles. They can be operated very stable at sea level as well as at the unfriendly sites the elevated observation level requirement imposes on the physicists when a low energy threshold is needed. Airshowers which are ignited by incident particles with energies exceeding 10 TeV still consist of more than 10^4 particles spread out over the order of 10^4 m^2 after about 23 radiation lengths. This atmospheric depth corresponds to a detector location of about 2000 m above sea level (2000 m a.s.l.). Thus by equipping areas of the order of 10^4 m^2 at locations higher than about 2000 m a.s.l. one is able to detect airshowers and

*Suppression factors Q (see Eq. (3.4)) of about 3 have been reached [62].

†Values for the quality factor Q of around 5 have been reached [63].

‡With the spectral index of the integral CR flux this may be converted to a $x_{\rm t}$ value of around 3.7 (see Eq. (3.5)).

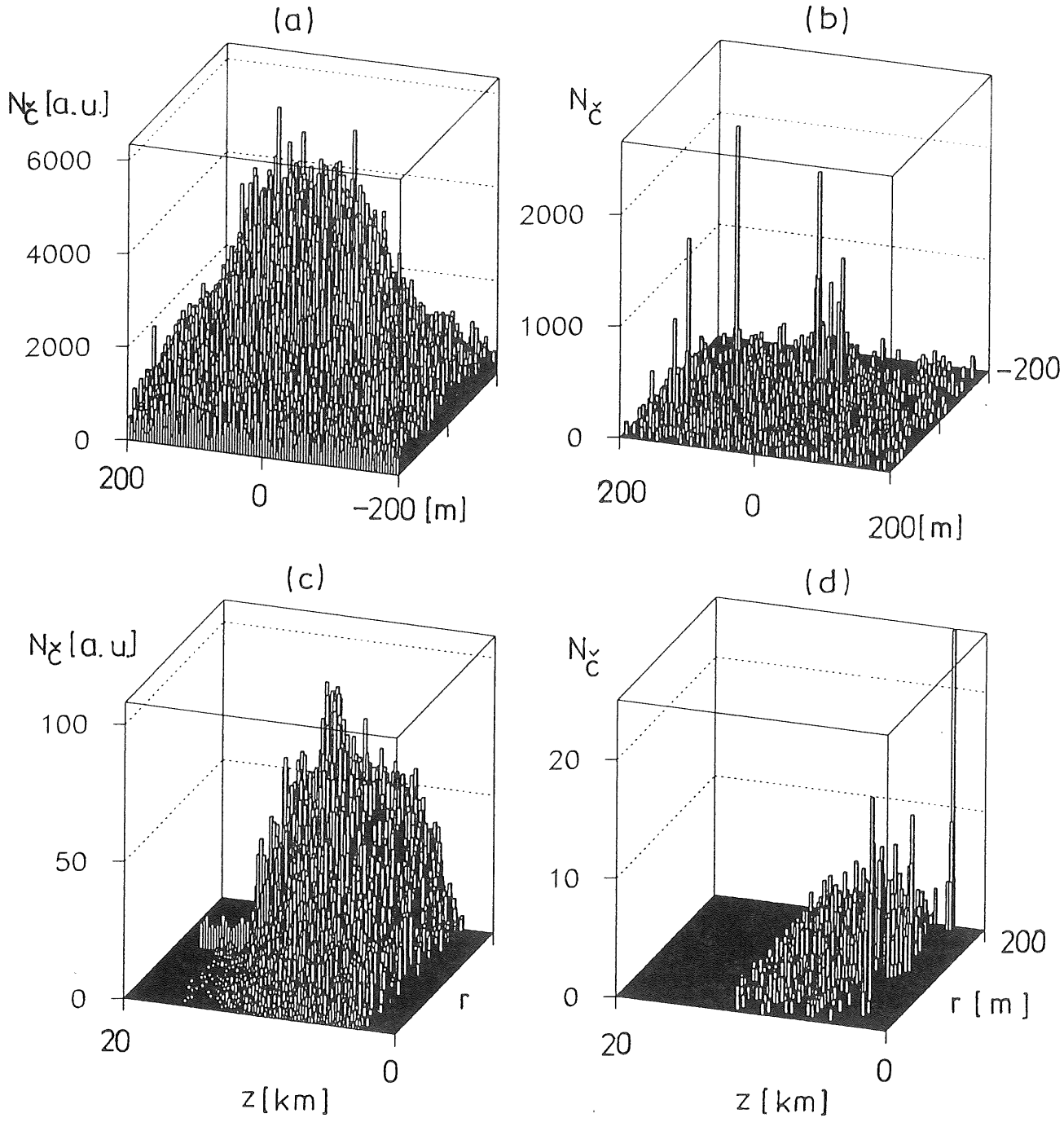

Figure 3.2: Light pools for (a) 1 TeV γ and (b) 1 TeV proton on a 400 m by 400 m array. (c) shows the correlation between the emission height z_{emis} of Čerenkov photons and their impact radial distance from the core at an observation level of 2200 m a.s.l. for an incident 1 TeV γ, (d) for a 1 TeV proton.

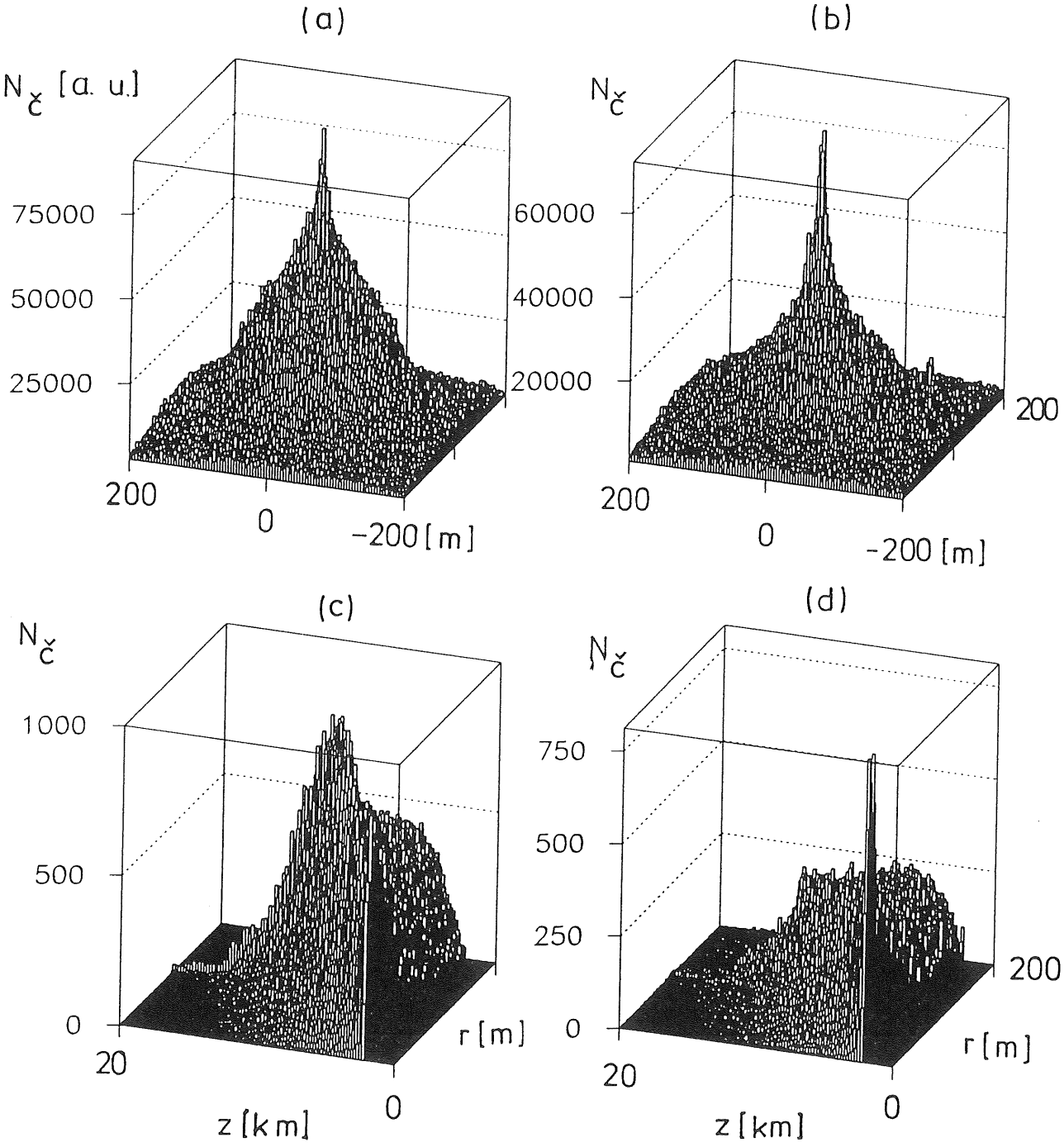

Figure 3.3: Light pools for (a) 10 TeV γ and (b) 10 TeV proton on a 400 m by 400 m array. (c) shows the correlation between the emission height z_{emi}, of Čerenkov photons and their impact radial distance from the core at an observation level of 2200 m a.s.l. for an incident 10 TeV γ, (d) for a 10 TeV proton.

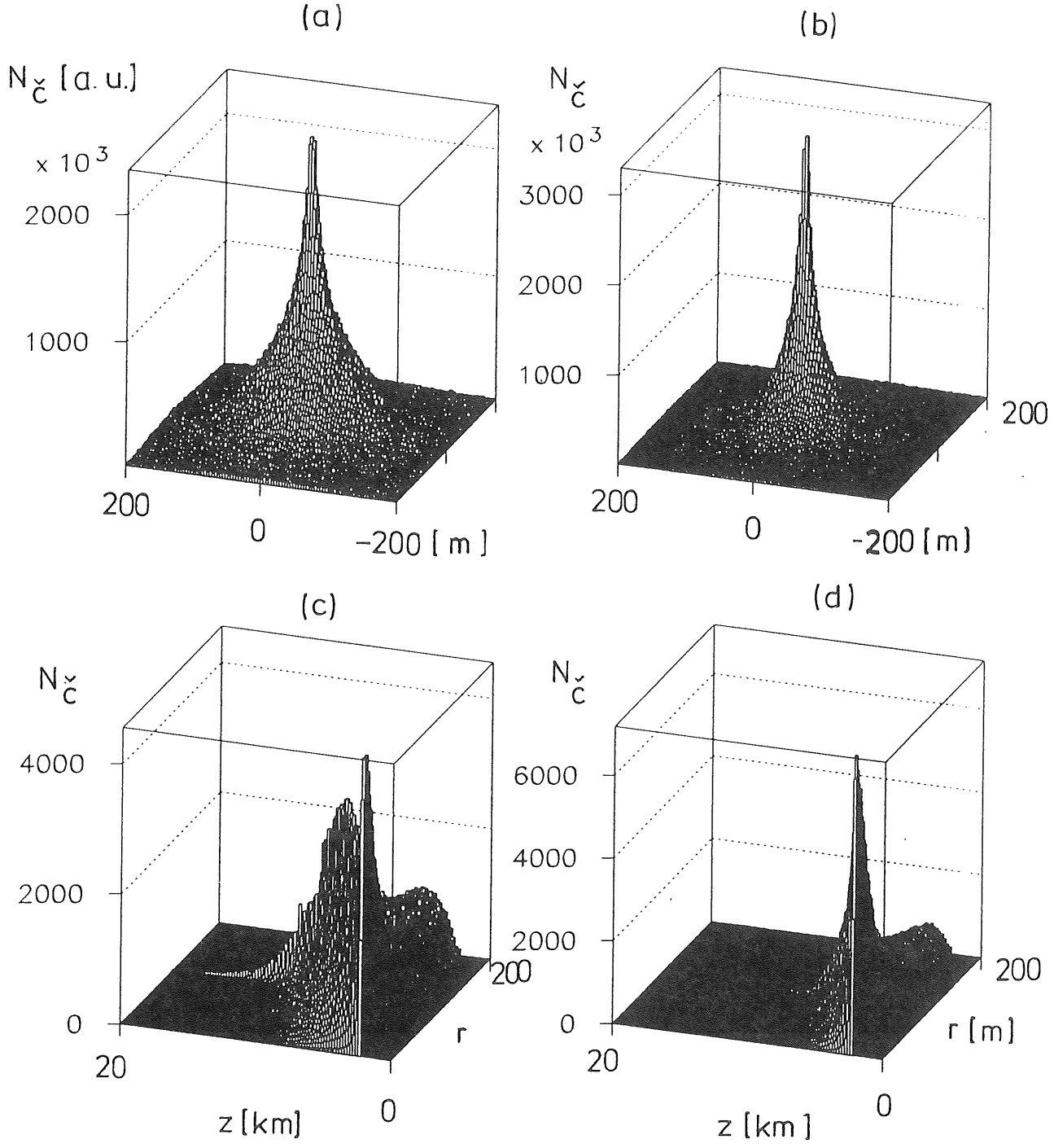

Figure 3.4: Light pools for (a) 100 TeV γ and (b) 100 TeV proton on a 400 m by 400 m array. (c) shows the correlation between the emission height z_{emis} of Čerenkov photons and their impact radial distance from the core at an observation level of 2200 m a.s.l. for an incident 100 TeV γ, (d) for a 100 TeV proton.

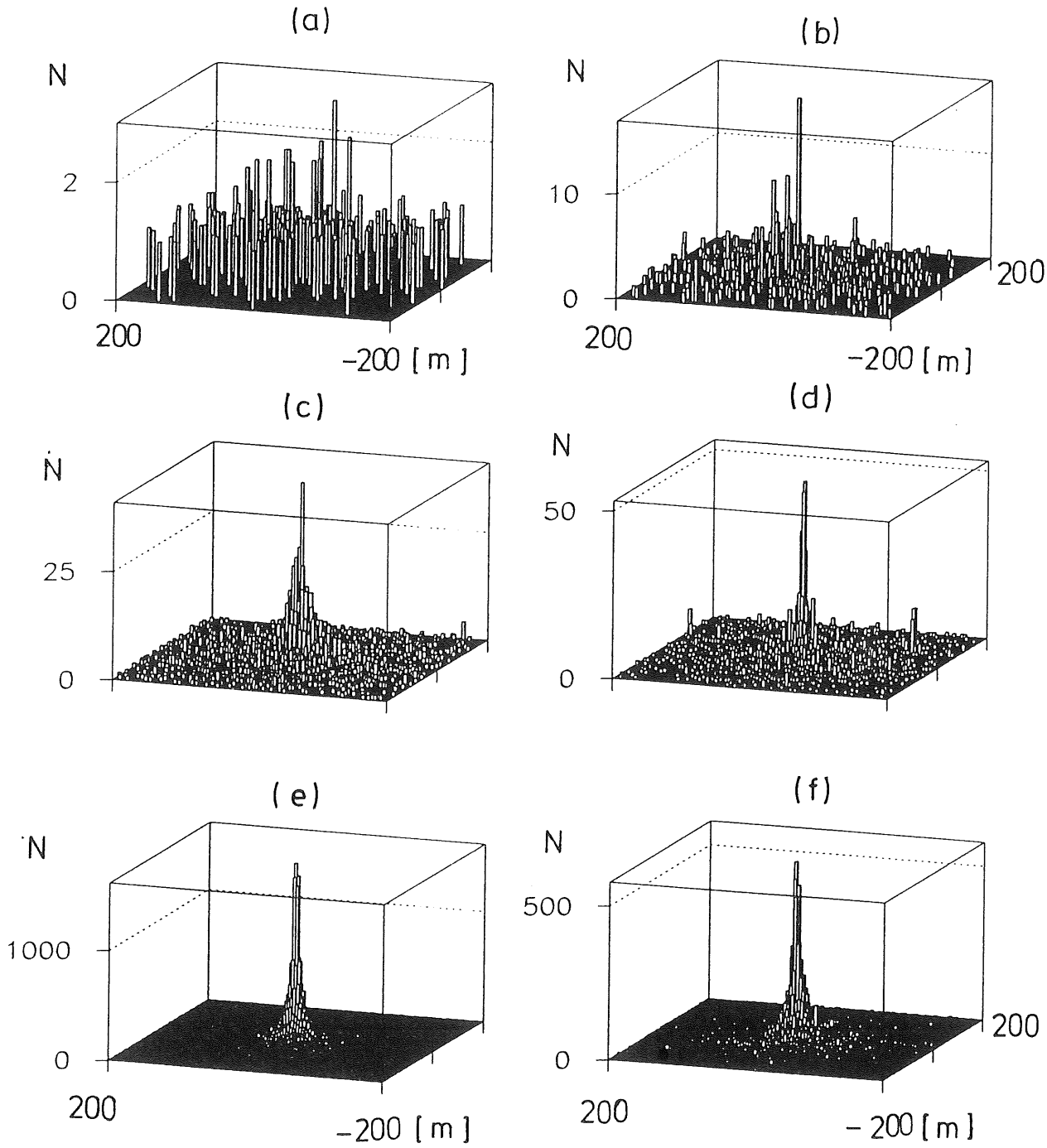

Figure 3.5: Number density of particles with energies exceeding 3 MeV at 2200 m a.s.l. for (a) 1 TeV γ, (b) 1 TeV proton, (c) 10 TeV γ, (d) 10 TeV proton, (e) 10 TeV γ, and (f) 100 TeV proton on a 400 m by 400 m array.

measure low fluxes up to energies of about 10^{16} eV. Airshower detectors of this type have been operated in many incarnations at many locations on earth (see [64] for a review on airshower arrays).

The further improvement of the AICA-type detectors not only yielded a big improvement in energy resolution and lowering of energy thresholds, but in addition one of the outstanding features of this detector array together with information from a scintillator array is the energy response which was found to be practically insensitive to the type of the incident particle [65]. Note that this is one of the requirements for the determination of the composition of the charged particle component because the all-particle energy spectrum at TeV and higher energies is very steep. Any change in the composition as a function of energy would be very hard to disentangle should the response of the detector not be independent of the particle type. In order to successfully operate this type of detector, at least as long as the covered area is much smaller than 10^6 m^2, it has to be accompanied by a second type of detector in order to determine the electron shower size N_e. This measurement taken together with the Čerenkov light intensity then allows for the separation of γs and hadrons [66]. The scintillator array should thus not be completely discarded.

For the highest energies, i.e. $E > 10^{17}$ eV, also other than the above techniques have been used. The main additional technique that has been developed to record particles in this energy regime is the Fly's Eye technique [67] based on the fluorescence light emitted by nitrogen molecules excited by the secondaries of the gigantic airshowers ignited by particles of this energies. The other standard possibility is to spread airshower detectors over many km^2 in order to measure the up to 10^{11} secondary particles. This has been done at Havarah Park [68], Akeno [13], and Yakutsk [14].

The most successful ground-based observation technique of EAS has operated in the 250 GeV to 15 TeV energy band. This is the employment of imaging Čerenkov telescopes (ICT) by the Whipple collaboration [69], the HEGRA collaboration [70], the CANGAROOH collaboration [71], and by the Themistocle collaboration [72]. These detectors up to now have reported the observation of ultra high energy γ radiation from the Crab Nebula with energies in the 500 GeV to about 5 TeV range or other galactic sources of the pulsar type. In addition to these galactic sources one extragalactic source has been positively identified [46, 47]. This is the AGN Mrk 421. The redshift z for this galaxy has been determined to be $z = 0.033$. This can be translated into a distance of about 100 Mpc using a value for the Hubble parameter of 100 km/sec/Mpc. The violent variability of this source is one of the strongest arguments to aim at installations with the highest possible sensitivity to be able to monitor the dynamics in sources of this type.

Some of the factors determining the sensitivity of an installation have been discussed above. The sensitivity for point sources is given by the signal to back-

ground ratio. Its dependence on the detector parameters is given by

$$\frac{S}{N} \propto \frac{Q}{\sigma(\theta)}\sqrt{At} \tag{3.3}$$

with A the sensitive detector area and t the time the potential source has been observed, $\sigma(\theta)$ the detector angular resolution, and Q is the quality factor for background suppression, which in the case of the search for γ-ray sources is defined as

$$\mathrm{Q} = \frac{\epsilon_\gamma}{\sqrt{\epsilon_{\mathrm{hadron}}}}, \tag{3.4}$$

with ϵ_γ the cut efficiency for the signal and $\epsilon_{\mathrm{hadron}} = \epsilon_{\mathrm{bg}}$ the efficiency for keeping background events. Of these factors A and t are limited due to cost of the installation and maintenance, whereas Q and $\sigma(\theta)$ are limited by physics. Typical numbers for A and $\sigma(\theta)$ have been discussed above for the energy region around 100 TeV. Possible improvements of the AIROBICC technique may reduce $\sigma(\theta)$ to around 0.1°. The instrumented area may by as large as 1 km^2 (the ongoing work to build an 100 km^2 array is dedicated to the measurement of the highest energetic particles, $E > 10^{18}$ eV, and will not be discussed here), which would be an enlargement of about a factor of 25 compared to the running AIROBICC detector. The measurement time, for the above discussed reasons, should be as short as possible. This leaves the need to raise the quality factor Q as much as possible.

Are there any physics limitations on the achievable Q? This question can be high-lighted by making a simple table of Q as a function of background retaining factors ϵ_{bg} and signal efficiency ϵ_γ:

		Quality factors Q ϵ_γ[%]				
		100	50	10	5	1
ϵ_{bg}[%]	100	1.0				
	10	3.2	1.6			
	1	10.0	<u>5.0</u>	1.0		
	0.1	32.0	16.0	3.2	1.6	
	0.01	100.0	<u>50.0</u>	10.0	5.0	1.0
	0.001	320.0	160.0	32.0	16.0	3.2

From this table the measurement objective can be inferred: if 50% of γ signal are to survive the cuts, the hadronic background has to be suppressed to a level of 0.01%, i.e. 10^{-4} (!) in order to improve over the current AIROBICC quality factor by a factor of 10, i.e. reach a quality factor of 50. Whether the Monte Carlo simulation programs used in EAS physics are tested to such a high degree, as to allow the identification of observables allowing a hadron reduction factor of 10^{-4} while conserving about 50% of the γ signal is questionable.

One major problem in the field of EAS applications is the difficulty in comparing different installations. Recently, Arqueros *et al.* [66] have made the suggestion to calculate a so-called *reduced quality factor* $Q_{\rm red}$ for every installation aiming at measuring γ-rays, defined as

$$Q_{\rm red} = Q \cdot \frac{0.7}{\sigma(\theta)} \cdot f_0^{\frac{1}{2}} \cdot x_t^{\frac{1}{2}}, \tag{3.5}$$

with f_0 the ontime of the detector, and $x_{\rm t}$ a threshold factor which is larger than 1 if the signal (γ-rays) has an energy threshold below the background (hadrons). This threshold factor is defined as $x_{\rm t} = f_{\rm em}^{\gamma-1}$ where $f_{\rm em}$ is the fraction of the total shower energy transformed into Čerenkov photons *relative* to a γ-ray and γ in this case the spectral index of the integral CR flux (around 1.7 at energies E around 10^{12} eV), i.e. the CR flux is given by

$$\Phi(E) = \Phi_0(E) \cdot E^{-\gamma}. \tag{3.6}$$

The threshold factor will consequently be set to 1 for detectors not sensitive to Čerenkov radiation. From this definition it is already clear that one of the big advantages of measuring Čerenkov radiation lies in its intrinsic enhancement of the γ signal.

The HEGRA experiment installed on the Canarian island, La Palma (see chapter 4) can be viewed as a prototype airshower experiment in the respect that it combines many different detector types sensitive to different aspects of the airshower. In the future, other installations will in addition use water Čerenkov detectors located in pools above ground. The advantage of water Čerenkov detectors will be the large sensitive area covered by the water pool. For a more detailed discussion of the future possibilities of experiments in this fields see [58].

The overlap of energy bands between the direct and the EAS measurements ($10^3 - 10^5$ GeV) serves the very important purpose of calibrating and testing the EAS parameters. Since in most of the current EAS installations, the relationship between measured observable and initial particle parameter is established via a Monte Carlo simulation, in this low energy EAS region the simulations can be cross checked to a limited degree.

3.3 HERA Influence on EAS Physics Signals

3.3.1 Gamma-Ray Sources

When the measurement objective is the identification or monitoring of point sources, the identification of the signal is based on a simple signal-to-noise analysis in bins defined by the resolution power of the employed detector. Since the hadronic background (the noise) is large even for the strongest anticipated

sources, procedures to reduce the background are paramount for analyses of this kind. The main analysis techniques are

- the search for single sources selected from a cataloque of potential sources.
- the application of the standard astronomical procedure in the case of weak potential sources consisting of accumulating the signals for classes of potential sources.
- to take each bin resolved by the experimental setup as a potential source.

In all cases, the background reduction quality, i.e. the γ/hadron separation power Q (Eq. (3.4)) has to be optimized. To find the best observables a detailed Monte Carlo simulation of the signal and background events is needed.

In the case of incoming electromagnetic radiation, most of the physics of the airshower that develops is supposed to be understood in detail [73]. The only major physics problem seemed to be the absolute value of the total cross section for photon-proton interactions at high energies. The centre-of-mass (CMS) energy of the interaction of an incident γ with an energy of 40 TeV impinging on a stationary atmospheric proton is about 200 GeV. Before the commissioning of the HERA *ep* collider in 1992 this was about a factor of 10 higher than all existing laboratory measurements.

In the years 1983 to 1990 several airshower experiments claimed to have observed an excess of airshowers with energies exceeding 50 TeV stemming from the direction of the point-source Cyg X-3 [26], the Crab Nebula [74], and the point-source Her X-1 [75], **and** that these excess showers were characterized by an anomalous high muon content. Anomalous here meaning much more than expected for initial photons triggering electromagnetic cascades during which the production of muons is strongly suppressed against the dominating Bethe-Heitler production of e^+e^- pairs. The expected muon content in γ initiated showers is of the order of a few per cent of the muon content found in hadronic showers. If the excess really was due to radiation emitted by the above sources it had to be initiated by neutral particles.

At about the same time it was noted by Drees and Halzen [76] that perturbative QCD *predicts* an increase of the partonic structure of the photon at high photon energies giving rise to the production of mini-jet structures in photon proton collisions. Since the obvious candidate for the excess events recorded by the experiments were γ-rays, the possibility of the total photoproduction cross section rising sharply between the energies explored in experiments up to then and the PeV energies measured in EAS experiments had to be considered.

To explain the observed muon excess by the partonic structure of the photon, the total cross section for photon proton scattering was required to rise much

faster than logarithmicly from about 100 μb at $\sqrt{s} = 20\,\text{GeV}$ to $\mathcal{O}(100)$ mb at $\sqrt{s} = \mathcal{O}(1000\,\text{GeV})$ [75]. This can only happen if the threshold of a new process is passed when going to PeV fixed target energies. The onset of strong mini-jet production could be this new threshold. The HERA data point with $\sqrt{s} \simeq 200\,\text{GeV}$ is lying in between these extremes. Already at HERA a strong increase of the total photon proton cross section should be visible and the total cross section was predicted to be between 200 and more than 800 μb in various mini-jet calculations [77]. This was in sharp contrast to Regge predictions (see 5.3) which predicted a total cross section value of about 150 μb at $\sqrt{s} = 200\,\text{GeV}$.

The HERA measurements essential to this question and the current status of this question will be presented and discussed in chapter 7.

3.3.2 Gamma-Ray Bursts

For transient phenomena, the extraction of signals has to be achieved by the application of different techniques depending on the possible sources of the bursts. The main techniques are to

- search for burst signals without imposing a source model. In this case every event recorded in the detector defines a possible burst candidate. The analysis thus looks for an enhancement of events in varying time windows around each event. The probability for the found number of events to be consistent with the background (no-signal hypothesis) is calculated. A signal would show up at extreme small probabilities (see e.g. [78]).

- search for burst signals of a specified source. Here the search for the evaporation burst of primordial black holes (PBH) is the most commonly searched for phenomenon. Since here theoretical predictions exist for the spectrum and duration of such a burst, the analysis makes use of this information and is performed in fixed time windows around every burst candidate event. Again every recorded event may serve as a candidate event.

- search for counterparts to burst events recorded by satellites, the most common one to date being the burst events recorded by the BATSE burst monitor onboard the Compton Gamma Ray Observatory [79, 80].

As in the case of γ-ray sources, also in this case the γ/hadron separation power has to be optimized by Monte Carlo studies anf the possible photon interaction channels have to be known.

3.3.3 Cosmic Gamma-Ray Background

Important information on particle densities can be gathered by measuring the amount of diffuse γ-radiation piled up in the so-called cosmological window between about 65 and 100 TeV. The reason lies in the enormous density of the cosmological microwave (CMB) photon densities leading to the GZK cutoff off at about $6 \cdot 10^{19}$ eV (see 2.2.1). The interaction products of the photonuclear reactions will initiate an electromagnetic cascade again due to electromagnetic interactions with the CMB photons. Only at γ energies below about 100 TeV the universe becomes much more transparent. The γ radiation stemming from the cascades will thus be piled up in the cosmological window.

The extraction of the signal for this diffuse radiation is based on the application of γ/hadron separation techniques optimized to this problem. Note that the thus optimized techniques may well be different from the one developed for the search for point sources.

The best upper limit on the ratio of primary γ to charged CR has recently been derived by the HEGRA Collaboration in the energy window between 65 and 200 TeV with 1.03% [63]. It relied on the simulation of EAS with the Monte Carlo generator CORSIKA [4] (see 8). The HERA influence is as in 3.3.1 and 3.3.2.

3.3.4 Chemical Composition of Cosmic Rays

EAS detectors allow to make a coarse determination of the chemical composition of CR. Separation techniques will be based on the following properties [81]:

- Light nuclei interact deeper in the atmosphere, therefore their shower maximum will occur also deeper in the atmosphere than for showers from heavy particles of the same energy.
- The height $X_{\max}$ of the shower maximum for showers induced by light nuclei fluctuates stronger than for showers from heavy primaries.
- Showers from heavy particles decrease faster after the shower maximum than showers from light nuclei.
- Showers from heavier particles will be wider, therefore their Čerenkov light disk will extend to larger radii on the ground.

The separation power of the experimental setup in question has to be optimized by extensive Monte Carlo studies. The Monte Carlo generators written to describe heavy-ion collisions and which also are employed in EAS physics have been

developed within the *framework* of QCD but cannot be based on strict QCD calculations, since the interactions themselves involve only small momentum transfers and are thus "soft". Based on a multitude of data successful phenomenological models for these type of interactions like the Dual Parton Model (DPM) [82], the Quark Gluon String Model [83], and VENUS [84] have been developed on the basis of Gribov-Regge theory [85] (see 5.3). In these models, the production of the hadronic high multiplicity final state is achieved through the conversion of kinetic energy into colour field energy.

In Gribov-Regge theory Pomeron exchange is the basic process in high energy hadron-hadron scattering. At HERA, Pomeron exchange in high energy lepton-nucleon scattering could for the first time be investigated. The measurement of the diffractive structure function, F_2^D, in deep inelastic scattering allowed for a determination of the Pomeron structure.

One of the major HERA results concerns the measurement of the proton structure function, F_2, and especially the gluon density $xg(x, Q^2)$ at low x. All these results constitute important input to EAS generators and will be presented in 6. The quark densities derived from the measurement of F_2 have a strong influence on the simulation of high energy nucleus-nucleus interactions for energies beyond about 10^{15} eV and are very important in the determination of signals and backgrounds of neutrino processes which can also be measured with the EAS technique (see 3.3.5). The gluon density at low x will determine the cross section for semi-hard processes which dominate CR interactions in the atmosphere at the highest EAS energies. Taken together, the HERA measurements allow to infer important characteristics of the Pomeron and it's energy behaviour. This will be discussed in 9.

3.3.5 Cosmic Neutrino Background

To measure fluxes of cosmological neutrinos reaching the earth two promising experimental possibility exist which are distinguished by a large amount of shielding between source and detector. These can either be detectors shielded by a large amount of condensed matter or shielded by a large amount of air in form of the atmosphere at large zenith angles. The first group of detectors are placed either deep underground or underwater and either record the interaction of the neutrinos in the detectors (contained events), or they record muons produced in interactions of neutrinos with the material surrounding these detectors (stopping and uncontained events). These type of detectors will not be discussed any further.

The other class of detectors are huge detectors for EAS which record so-called horizontal showers originating from muons produced in very high energetic neutrino interactions in the atmosphere at large zenith-angles. The slant depth of the atmosphere increases from about 1030 g/cm^2 at zero zenith angle to about 36000 g/cm^2 at 90° corresponding to an amount of matter of about 360 m water

equivalent (360 m w. e.) serving as neutrino target. The hadronic and electromagnetic background from showers originating from the interaction of the primary CR within the atmosphere is negligible after almost 1000 radiation lengths of absorber near the horizon.

Very high energy neutrinos interact in the atmosphere or the medium surrounding underground installations via the following reactions

$$\nu_\mu(\bar{\nu}_\mu) + N \rightarrow \mu^-(\mu^+) + X \tag{3.7}$$
$$\nu_e(\bar{\nu}_e) + N \rightarrow e^-(e^+) + X \tag{3.8}$$
$$\nu_\mu(\bar{\nu}_\mu) + N \rightarrow \nu_\mu(\bar{\nu}_\mu) + X \tag{3.9}$$
$$\nu_e(\bar{\nu}_e) + N \rightarrow \nu_e(\bar{\nu}_e) + X \tag{3.10}$$
$$\nu_e(\bar{\nu}_e) + e \rightarrow X \tag{3.11}$$

At very high energies, the reaction involving electrons in the initial state also can proceed through the formation of a W resonance in

$$\bar{\nu}_e + e^- \rightarrow W^- \rightarrow X. \tag{3.12}$$

This resonance is formed for incident neutrino energies larger than

$$E_0 = \frac{m_W^2}{2m_e} = 6.4 \cdot 10^{15}\text{eV}. \tag{3.13}$$

Since also EAS initiated by hadrons do not penetrate deeply into the atmosphere from their origin, this signal will only be detected if the neutrino interaction occurred close to EAS detector. Basically two kind of signals are expected depending on the nature of the neutrino interaction.

For neutral current interactions only the recoil shower can be detected if the reaction takes place close to EAS detector. For charged current interactions involving electron neutrinos an electromagnetic shower will develop which also can only be recorded provided it did not start too far away from the detector.

For charged current interactions involving muon neutrinos the outgoing muon can be detected through its energy losses when propagating through the atmosphere close to the detector. The muon path length in air at muon energies above about 100 GeV is larger than the depth of the atmosphere at the horizon. The neutrino interaction may thus take place anywhere along the path towards the EAS detector. The detection of the high energy final state muon as the signal particle can be performed by detecting electromagnetic showers from catastrophic bremsstrahlung reactions close to the EAS detector. This signal is thus dependent on the ν_μ flux, the charged current cross section, and the knowledge of catastrophic energy losses due to bremsstrahlung at very high energies. The cross section can be calculated and the measurement performed provided the background is under control.

The HERA connection is made when calculating the cross sections for the neutrino interaction processes at very high energies. These calculations need the

knowledge of the quark distributions inside the nucleons at very small values of Bjorken-x. This knowledge has improved considerably due to the operation of HERA.

The background to this muon signal, however, is overwhelming, but, fortunately, very interesting in itself. It stems from the so-called prompt muons originating from primary CR interactions in the atmosphere where charm or bottom quarks are produced and which subsequently decay semi-leptonically. An estimate on this background rate compared to the expected cosmological neutrino induced one shows the background to dominate the signal by about 10 orders of magnitude at the threshold neutrino energies which result in muons with energies high enough to traverse the absorber (in the EAS case the atmosphere). To measure a signal of low energy neutrinos ($E \simeq$ GeV) thus is hopeless unless the EAS detector is shielded by a large amount of matter in form of a mountain. At very high neutrino energies, however, the situation might change due to steeply falling spectrum of the CR background. To detect muons from these very energetic neutrinos though, the EAS installations have to be very large.

Nevertheless, the background from CR interactions itself can serve to make important particle physics measurements with EAS installations. The CMS energies present in these interactions may exceed current and future accelerator energies by about 2 orders of magnitude (*e.g.* a 10^{17} eV proton incident on a stationary nitrogen nucleus corresponds to a CMS energy of about 50 TeV).

In addition to the above-mentioned potential increase in available CMS energy, there is a long-standing Particle Physics interest in the production of charm quarks. The reasons for this are

- the intermediate mass of the charm quark between the almost massless light quarks and the very heavy bottom and top quarks, which is not yet large enough to warrant approximations like the infinite mass approximations but leads to the fact that the calculation of charm production is beyond the scope of perturbative QCD,
- the semi-leptonic decays of heavy quarks will constitute the major background to New Physics hoped for at future collider experiments,
- the production of charm quarks mainly proceeds through the boson-gluon fusion channel, which is proportional to the gluon density at small values of Bjorken-x (see also chapter 5).

The neutrino signal thus depends on the quark distributions at low x, the background on the gluon distributions in about the same regions of x. Another influencing factor at very energies is the W propagator. At HERA it was possible for the first time to measure the charged current cross section for the reaction in Eq. (3.8) in an energy range corresponding to an equivalent incoming neutrino

energy of 50 TeV. The HERA results on the structure function and on the charged current cross section will be presented in chapter 6 and the influence on neutrino cross sections discussed in (see 9.3.2).

3.3.6 Formation of Quark-Gluon Plasma

A class of accelerator experiments planning to study the properties of nuclear matter under extreme conditions are the heavy-ion colliders. These accelerators are the dedicated RHIC installation [86] at Brookhaven and the LHC at CERN with its option to store, accelerate, and collide heavy ions in addition to the standard proton mode [87].

One of the questions that these experiments will address is concerned with the expectation that at very high energies the constituents relevant in nuclear interactions are not any more nuclei or nucleons, but instead the elementary particles of strong interaction physics, i.e. quarks and gluons. This state, called Quark-Gluon Plasma (QGP), is believed to be obtained by compressing nucleons until they start to overlap and the concept of individual nucleons is no longer valid. In going to higher and higher CMS energies a transition phase from hadronic matter to a matter of *deconfined* quarks is anticipated. The implications of the physics of the Quark-Gluon plasma reaches from quark interactions to the astrophysics of neutron stars and the cosmology of the early universe.

As always the case when searching for signals of "new physics", the detection of this new state of matter depends on the ability to either very well describe the background processes or predict an undisputable signal. In the case of the well understood background, the signal could then be extracted due to the data not being described by the expectations in every detail. On the other hand, if a tell-tale signal exists, the observation of the "new physics" can be based on cuts optimized accordingly.

In interactions of incident heavy nuclei with nuclei in the atmosphere CMS energies per nucleon exceeding 1 TeV are reached for incident iron nuclei above about 10^{17} eV. The flux of CR at these energies, however, is very small. Another possibility would be the collision of a 500 TeV iron nucleus with an argon nucleus in the atmosphere. The CMS energy of this type of collision is about 60 GeV/nucleon. This already may result in collision energy densities in excess of $\epsilon_0 \simeq 1$ GeV/fm^3 which commonly is regarded as the threshold density for the onset of the QGP.

Even though the reactions that will take place at the heavy ion-colliders and those taking place at the beginning of EAS are similar, the phase space region deployed by instruments is quite different. In the case of accelerator experiments the instrumentation usually is most sensitive in the high-p_T region of phase space (the central rapidity region), whereas the EAS development is governed by the forward region, i.e. small transverse momenta (large rapidities). The rapidity is

given by

$$y = \frac{1}{2}\ln\frac{(E + p_l)}{(E - p_l)}, \tag{3.14}$$

where E is the energy and p_l the longitudinal momentum of the produced particle. The two fields may thus yield complementary information.

Two of the Monte Carlo models developed to treat nucleon-nucleon, nucleon-nucleus, and nucleus-nucleus scattering at ultrarelativistic energies, the Dual Parton Model and the VENUS model are also at the heart of the Monte Carlo generator CORSIKA [4] employed to simulate EAS (see 8). The search for events which differ significantly from the predictions of the Monte Carlo and which may signal the onset of the QGP can thus also be performed at EAS installations provided the Monte Carlo generator contains the correct physics. See *e.g.* [88].

In an event where a QGP was formed a higher multiplicity of secondaries is expected in the first interaction and large isospin fluctuations may occur. These isospin fluctuations are speculated to occur in ultrahigh-energy hadronic collisions [89] giving rise to the Centauro events observed in EAS experiments [90]. These events are characterized by a anomalously high ratio of charged to neutral pions in an event. The signals for QGP which might be expected in Hybrid EAS installations like HEGRA where the height of the shower maximum, the radial distribution of the Čerenkov light pool, and the number of muons and electrons are recorded are i) very high shower maximum corresponding to very flat radial light pool accompanied by a large total amount of light but a small number of electrons and positrons due to the early shower development, and ii) Centauro or anti-Centauro type of events due to large fluctuations in the neutral to charged pion ratio.

For these very high energies the influence of the HERA physics results on the EAS generators is considerable. Not only the new knowledge about the low x structure functions but also the nature of the Pomeron, it's parton structure and the energy and p_T dependences of the effective intercepts and the soft and hard contributions to the scattering amplitude usually in the form of soft and hard eikonals have to be known. To all these parameters HERA supplied new information. In the following two chapters we introduce the experimental environment and supply the theoretical and phenomenological background necessary for the discussion of the H1 measurements in the light of EAS applications.

Chapter 4

The Experimental Environment

In this chapter some of the main features and parameters of the HERA *ep* collider, the H1 experiment, and the HEGRA EAS experiment as an example of a state-of-the-art experiment currently taking data are presented.

4.1 The HERA machine

The electron hadron colliding beam facility HERA began its operation in 1992. It is the first electron proton collider ever built and it consists of two independent accelerators designed to store 820 GeV protons and 30 GeV electrons, respectively, and to collide the two beams in four interaction points distributed evenly spaced around its 6.3 km circumference. Two general purpose detectors, H1 and ZEUS, have been installed in two opposite interaction regions. A layout of the accelerator site is shown in Fig. 4.1. The design luminosity of $1.5 \cdot 10^{31}$ $cm^{-2}s^{-1}$ at the nominal CMS energy of 314 GeV is to be reached with 210 bunches.

Table 4.1 compares some of the HERA operation parameters for the running periods from 1992 to 1994. The integrated luminosity produced by HERA and used for physics analyses is shown in Fig. 4.2. During the two running periods in 1992 and 1993 each of the experiments collected integrated luminosities of about 500 nb^{-1}. On these data the results presented in chapters 6 and 7 will be based.

The comparison of the design values for the number of bunches and the currents in the machine with the values reached up to 1994 shows the potential still dormant in the HERA machine. Some of the conclusions which we would have liked to draw from the H1 data are thus not as firm as they will be once the full HERA potential is available.

parameter	1992	1993	1994	design value
E_p	820 GeV	820 GeV	820 GeV	820 GeV
E_e	26.7 GeV	26.7 GeV	27.5 GeV	30 GeV
nr of bunches	9	84	153	210
p current	2.0 mA	14 mA	54 mA	163 mA
e current	2.5 mA	16 mA	32 mA	58 mA
$\int_{year}$ lumi	50 nb^{-1}	1 pb^{-1}	6 pb^{-1}	50 pb^{-1}

Table 4.1: Comparison of some HERA parameters reached over the last 3 years of running in collider mode, with their design values. The number of bunches only counts the ep colliding bunches, the integrated luminosity is the one delivered by HERA.

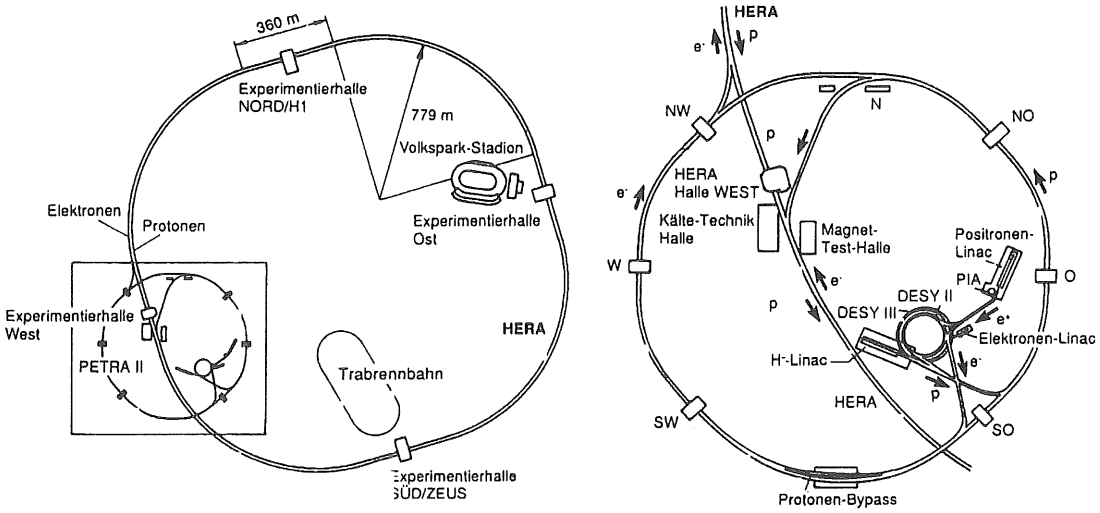

Figure 4.1: A schematic view of the HERA accelerator complex. The figure on the left shows the HERA ring and location of experimental halls. The figure on the right shows the pre-accelerators for protons and electrons, before injection into HERA.

4.2 The H1 detector

The multipurpose detector H1 is schematically shown in Fig. 4.3. Technical details on the different components can be found in [91]. Its main components to which we will refer to in the presentation of the analyses are

- the Central Tracker

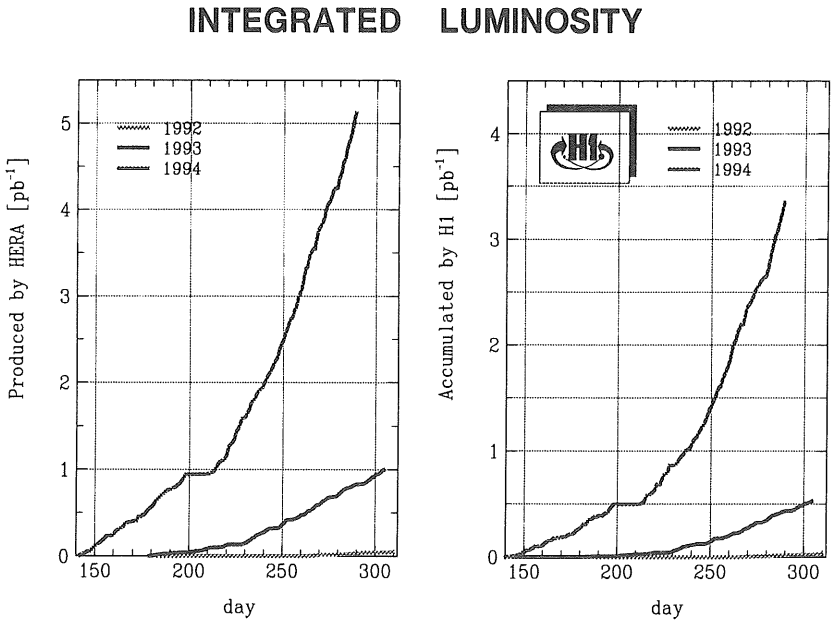

Figure 4.2: The integrated luminosity produced by HERA (left) and used by the experiments for physics (right) for the years 1992, 1993 and 1994. This result is for the H1 experiment; the ZEUS result is very similar.

- the Backward Calorimeter
- the Liquid Argon (LAr) calorimeter
- the PLUG Calorimeter
- the Forward Muon System

4.3 The HEGRA detector array

The HEGRA experiment is located at the Canarian island La Palma at an altitude of 2200 m a.s.l. and covers an area of about $180 \cdot 180\,\mathrm{m}^2$. The detector array which is instrumented with four different types of detectors is shown schematically in Fig. 4.4. It consists of

- an array covering the full 35000 m^2 consisting out of 219, $1\,\mathrm{m}^2$ scintillator huts with 15 m grid spacing and a more dense part with 10 m spacing near the centre. The area coverage or sampling density is about 0.75%. Each hut is covered by 5 mm of lead to convert photons.

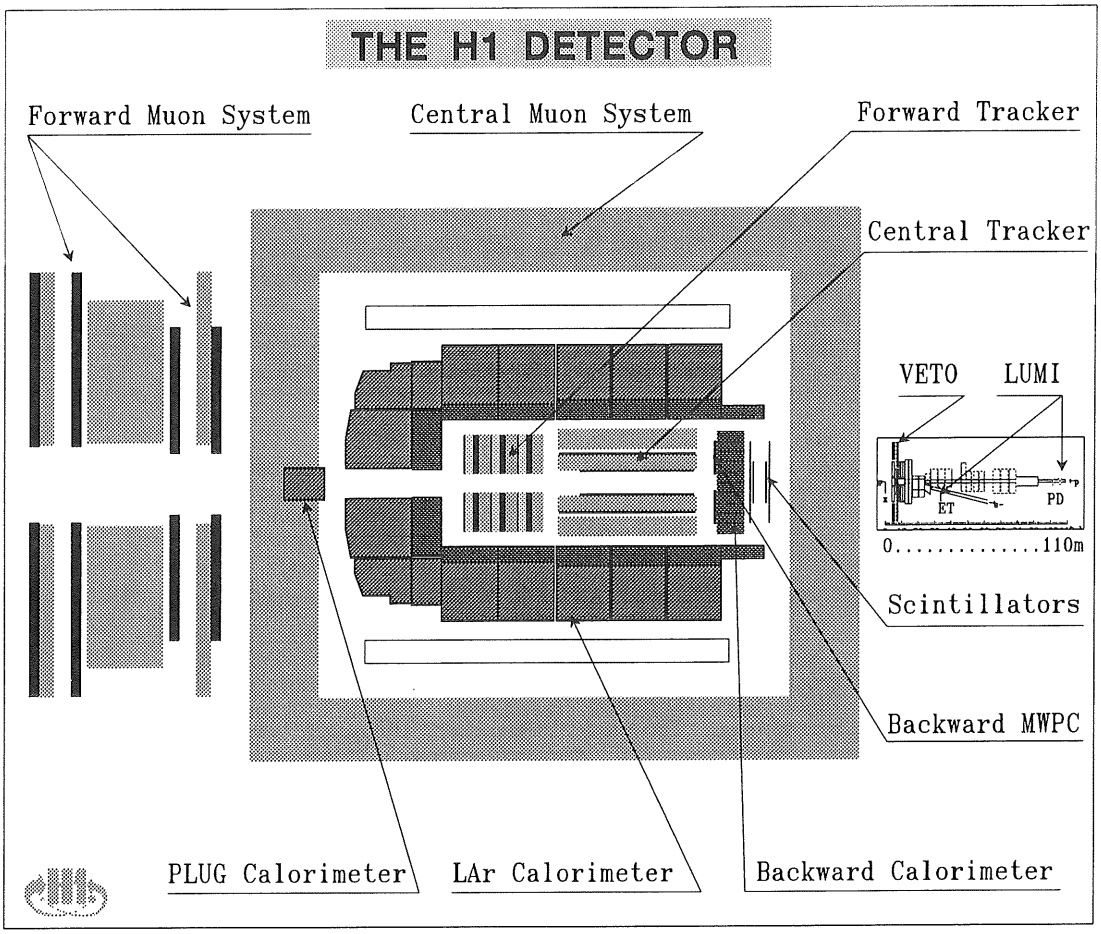

Figure 4.3: Side view of the H1 detector.

- A 7 x 7 matrix of open air Čerenkov counters (AIROBICC) [6] with a solid angle acceptance of about 1 sr and covering the same area as the scintillator array with a sampling density of 0.15%.

- 17 geiger 'towers' covering 10000 m^2 with a sampling density of 2.7%, where each counter consists out of 6 layers of 160 geiger tubes with the three upper layers separated by 2 lead sheets of 4.5 radiation length thickness each. The geiger 'towers' allow to measure the distribution of muons and they provide a modest local energy measurement in the shower tail.

- 2 different Imaging Čerenkov telescopes (ICT) [70]. The first telescope is the HEGRA prototype telescope. It has a 5 m^2 reflector and a 37 pixel fast imaging camera in the focal plane. The second ICT is the first of a total of five full-scale telescopes with a 61 pixel camera and an effective mirror size of 8 m^2.

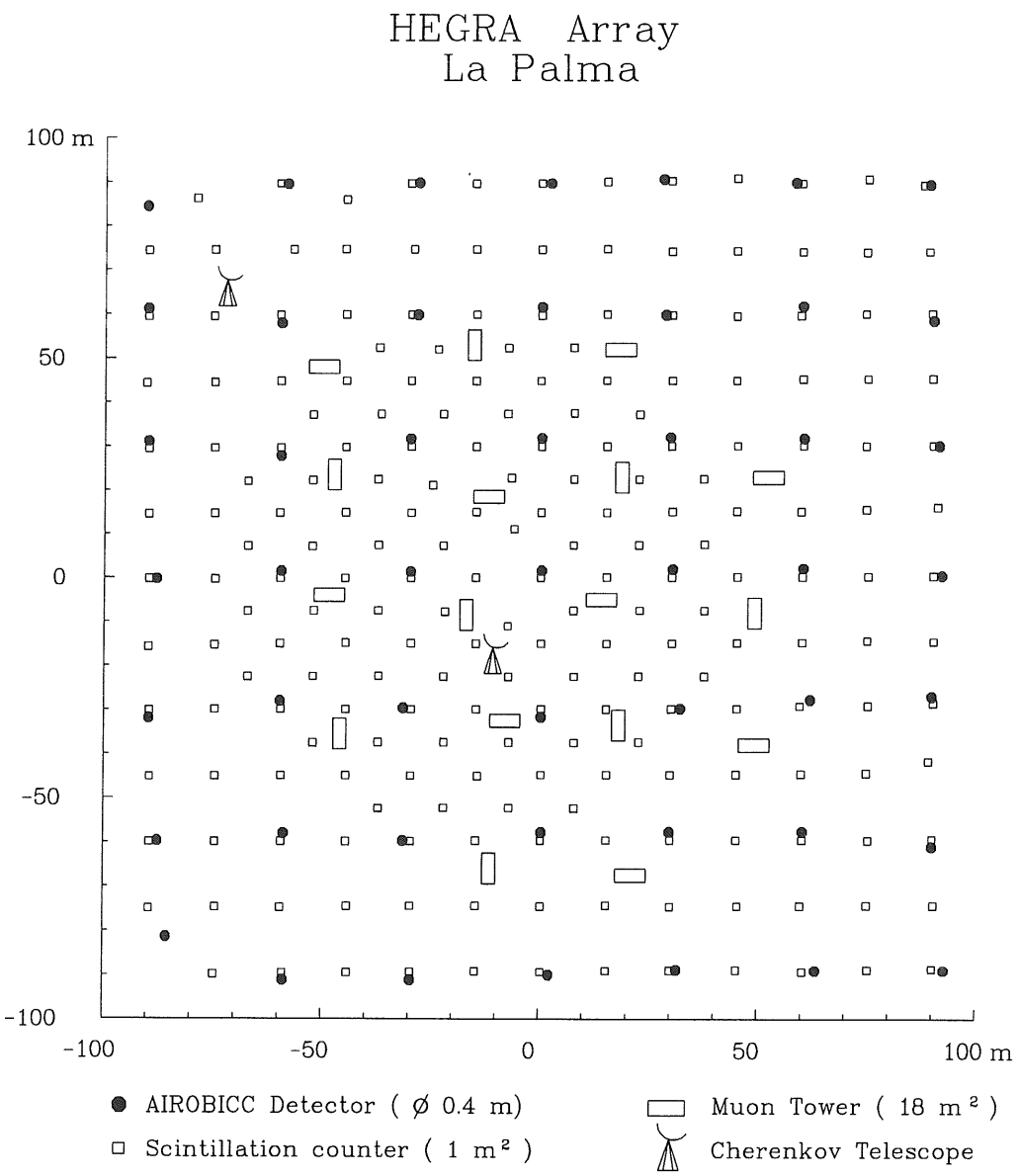

Figure 4.4: Layout of the HEGRA detector array at La Palma.

In addition to this setup, seven AIROBICC huts are equipped with FADCs to record the pulse spread of the Čerenkov light signal [92].

The individual detector stations are connected via cables to a central data aquisition system situated in the centre of the array. The Čerenkov telescopes either seperately trigger on typically two pixels of the cameras recording more than a certain number of photoelectrons or the two telescopes are operated in coincidence. In addition, the telescope triggers also start the readout of all other active detector components. From these other components the scintillator and AIROBICC arrays also generate trigger signals which start the read-out of all the array information but the telescopes. The trigger conditions are in both cases the verification of coincident signals of a predefined number of stations.

The energy thresholds of the installed trigger conditions are between 1 and 2 TeV for the Čerenkov telescopes, 13 TeV for γ showers for the AIROBICC array when requiring at least 6 stations as a trigger and 35 TeV for γ showers for the scintillator array when requiring at least 14 stations in the trigger. For the AIROBICC and scintillator arrays the threshold energies for proton showers are about 10 TeV higher due to the lower Čerenkov light yield and larger fluctuations in the proton showers, respectively. The upper limit on the energy sensitivity of the detectors determined mainly by the dynamic range of the ADC channels is around 25 TeV for the telescopes for small zenith angles and of the order of 10 PeV for the array detectors.

Chapter 5

The Structure of Proton and Pomeron

The study of the structure of hadrons began in 1956 when McAllister and Hofstadter discovered the proton not to be a pointlike object. They determined its root-mean-square charge radius in an elastic electron-proton scattering experiment [93] to be

$$< r^2 >^{1/2} = 0.74 \pm 0.24 \quad \text{fm.} \tag{5.1}$$

Until the late 1960s when the Stanford Linear Accelerator was commissioned many experiments were performed in the elastic and quasi-elastic scattering regions gathering a multitude of results on form factors and resonances which led to the formulation of the constituent quark model in 1964 [94]. With the completion of the SLAC accelerator, the investigations of the proton were carried into a new kinematical domain. At the very high momentum-transfers Q^2 (up to $10\,\text{GeV}^2$) then available a large part of the scattering progressed through inelastic channels. Since then the experiments on high-energy inelastic (or deeply inelastic) scattering of electrons on protons have played a crucial role in painting todays scientists picture of matter. The first and most important brush strokes were applied in the experiment of the SLAC-MIT collaboration [95] who found that the cross section for electron proton scattering at large inelastically produced hadronic masses W and large momentum transfers Q^2 did not fall off rapidly as a function of Q^2, but showed an almost Q^2-independent behaviour as anticipated by Bjorken in his work [96].

Bjorken's conjecture was that the structure functions needed to describe the behaviour of the differential cross section and which a priori could depend on two variables Q^2 and x, should scale with the dimensionless variable x. This scaling behaviour, originally deduced from current algebra, was borne out by the data and was expected if deeply inelastic scattering of electrons and protons could be viewed as elastic scattering of the probing virtual photons on point-like free constituents of the protons, the partons. This was the picture that Feynman had advocated in his parton model [97]. In the parton model, the partons are viewed

in the infinite momentum frame and carry fractions x of the (longitudinal) momentum of the hadron. The momentum distribution functions are functions of x only.

The violation of scaling was one of the most striking predictions of the theory of the strong interactions which emerged from the foundations of the parton model strengthened by the observation of scaling. This theory of the strong interaction is Quantum Chromodynamics (QCD) formulated in 1973 [98]. Based on these theoretical and experimental results, the so-called QCD improved parton model evolved as the current picture of the hadron structure. In this model the partons are identified with the quarks and gluons of QCD and are treated as the elementary objects with appropriate interactions. QCD being a field theory mainly modified the parton model by creation and annihilation processes which occur during the interaction of the hadron with an external boson. As a consequence of this, the parton momentum distribution functions were found to depend weakly (logarithmically) on Q^2, the virtuality of the probing boson. But the parton model was saved in the respect that even in the QCD improved picture the physical cross section is still the convolution of an elementary cross section that can be calculated perturbatively and a term that describes the momentum distribution of the hadron constituents and has to be taken from experimental measurements.

Not only are a multitude of experimental results available on deeply inelastic scattering, but this process also theoretically is the most studied QCD process. In order to take the structure of the nucleons from one experiment and make predictions for another one, the precise definition of the structure functions has to be given.

The asymptotic behaviour of strong interactions was also investigated long before the formulation of QCD. Out of the measurements of hadron-hadron cross sections in the 1950's and beginning of the 1960's grew the Regge model which was able to explain the energy dependences seen in the data by postulating an exchange object carrying the quantum numbers of the vacuum. This 'object' was named Pomeron. The Pomeron is now with us for more than 30 years but its structure within QCD, the microscopic theory of the strong interactions, has not been resolved experimentally. Theoretically there have been promising investigations and phenomenological models have been developed that describe a vast amount of measured data.

With the new HERA data as the final step in mind (see 6), in this chapter we will follow some of the steps that led to the current proton picture as seen in deeply inelastic electron(positron) proton scattering in more detail. Along the way we will naturally meet again the Pomeron. Its structure could for the first time be investigated in deeply inelastic scattering in the HERA data. To elucidate this new knowledge, the data measured by the H1 collaboration on the proton and Pomeron structure will be discussed.

5.1 Definition of Structure Functions

The structure functions parametrize our knowledge about the structure of hadrons and can only be determined through measurements. The cleanest experimental environment to do so is provided by lepton-hadron scattering. This process proceeds through the t-channel, where $t = (p - q)^2$ (see Fig. 5.1), and the exchanged current couples to one purely leptonic and one hadronic vertex. When restricting the calculations to single boson exchange, the electroweak leptonic vertex structure can be calculated perturbatively up to any desired accuracy and the process thus provides the possibility of measuring the structure of the hadronic vertex. Higher order electroweak corrections will already need the knowledge on the hadronic vertex as input to the calculations.

The deeply inelastic scattering (DIS) of an unpolarized lepton with four-momentum k on a hadron with four-momentum p proceeds via the reaction

$$l(k) + h(p) \rightarrow l'(k') + X. \tag{5.2}$$

At HERA, where the lepton will be either an electron or a positron, and the hadron a proton, the process will be as illustrated in Fig. 5.1. A set of invariants

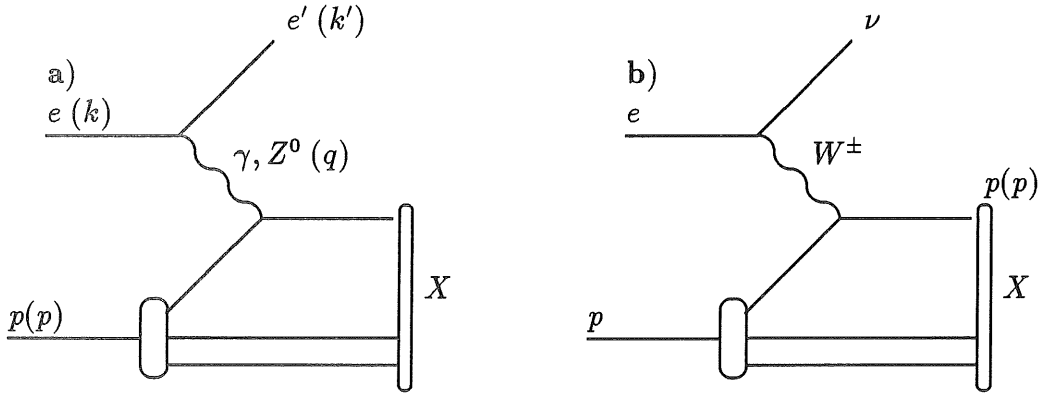

Figure 5.1: Deep inelastic scattering at HERA for (**a**) a neutral current process, (**b**) a charged current process.

to describe the process is usually defined as

$$\begin{aligned} q = k - k', \qquad Q^2 &= -q^2 > 0 \\ s &= (p + k)^2 \\ \nu &= \frac{p \cdot q}{m_p} \end{aligned} \tag{5.3}$$

where q denotes the momentum of the virtual vector boson exchanged between the electron and the proton, s the CMS energy and ν the energy of the virtual

boson in the lab frame. In DIS in general, the incoming lepton can be an electron, a muon, or a neutrino (or its antiparticles), and the exchanged vector boson a photon or Z^0 constituting the neutral current or a $W^{\pm}$, i.e. a charged current.

In the past, DIS experiments mostly have been totally inclusive in the hadronic final state and the kinematics of the process was determined by the initial and scattered lepton's four-momenta. The Bjorken scaling variable x and the ratio of the energy transferred from the lepton to the hadron to the total leptonic energy available in the target rest frame y can be defined as

$$x = \frac{Q^2}{2p \cdot q} \quad (0 < x < 1), \qquad y = \frac{p \cdot q}{p \cdot k} \quad (0 < y < 1). \tag{5.4}$$

In lowest order in the electroweak interaction, the cross section for DIS can be calculated by the convolution of the leptonic and hadronic parts describing the interactions at the respective vertices:

$$d\sigma = \frac{d^3k'}{2s|\vec{k'}|} \cdot \frac{e^4}{4\pi^2(q^2 - m_V^2)^2} \cdot L_{lV}^{\mu\nu}(k,q) W_{\mu\nu}^{Vh}(p,q) \tag{5.5}$$

with l, V, h the labels for the participating particles. The leptonic tensor $L_{lV}^{\mu\nu}(k,q)$ can be calculated analytically

$$L_{lV}^{\mu\nu}(k,q) = \frac{1}{2} Tr[\not{k} \gamma_{Vl}^{\mu} (\not{k} - \not{q}) \gamma_{Vl}^{\nu}], \tag{5.6}$$

where γ_{Vl} is the perturbative vertex coupling lepton l, vector boson V, and outgoing lepton l' with the factor c_V^2 removed. The factor $1/2$ for the spin average in the case of unpolarized leptons has to be removed for incoming neutrinos.

The hadronic tensor on the other hand is defined by

$$\begin{aligned} W_{\mu\nu}^{Vh}(p,q) &= \frac{1}{8\pi} \sum_{\sigma} \sum_{X} \langle h(p,\sigma) | j_{\mu}^{V\dagger}(0) | X \rangle \langle X | j_{\nu}^{V}(0) | h(p,\sigma) \rangle \\ &\quad \times (2\pi)^4 \delta^4(p + q - p_X), \end{aligned} \tag{5.7}$$

and can be expanded in terms of scalar structure functions W_i^{Vh}

$$\begin{aligned} W_{\mu\nu}^{Vh} &= -\left(g_{\mu\nu} - \frac{q_\mu q_\nu}{q^2} \right) W_1^{Vh}(x, Q^2) \\ &\quad + \left(p_\mu - q_\mu \frac{p \cdot q}{q^2} \right) \left(p_\nu - q_\nu \frac{p \cdot q}{q^2} \right) \frac{1}{m_h^2} W_2^{Vh}(x, Q^2) \\ &\quad - i\epsilon_{\mu\nu\lambda\sigma} p^\lambda q^\sigma \frac{1}{m_h^2} W_3^{Vh}(x, Q^2) \end{aligned} \tag{5.8}$$

which usually are expressed in terms of x and Q^2. As defined here, there is no relation between the W_i^{Vh} for different vector bosons. Parity invariance of the strong interaction, however, implies that for photon exchange

$$W_3^{Vh}(x, Q^2) = 0. \tag{5.9}$$

The structure functions W_i^{Vh} are usually replaced by the (equivalent) structure functions F_i:

$$\begin{aligned} F_1(x,Q^2) &= W_1(x,Q^2) \\ F_2(x,Q^2) &= \frac{\nu}{m_h} W_2(x,Q^2) \\ F_3(x,Q^2) &= \frac{\nu}{m_h} W_3(x,Q^2). \end{aligned} \tag{5.10}$$

Depending on the polarization of the vector boson in the target rest frame another basis for the structure functions can be defined. The helicity of the boson can be either +1 (r) or -1 (l) or it can be longitudinally polarized (L; sometimes called "scalar"). Up to corrections of the order m_h^2/Q^2, $W_{\mu\nu}^{Vh}$ has the expansion

$$W_{\mu\nu}^{Vh} = \sum_\lambda \epsilon_\lambda^*(q)_\mu \epsilon_\lambda(q)_\nu F_\lambda^{(Vh)}(x,Q^2), \tag{5.11}$$

where $\lambda = l, r, L$ labels the helicities given by

$$\begin{aligned} \epsilon_l(q) &= \frac{1}{\sqrt{2}}(0;1,-i,0) \\ \epsilon_r(q) &= \frac{1}{\sqrt{2}}(0;1,i,0) \\ \epsilon_L(q) &= \frac{1}{\sqrt{Q^2}}(\sqrt{Q^2+\nu^2};0,0,\nu). \end{aligned} \tag{5.12}$$

These so defined structure functions are related to the structure functions defined in Eq. (5.11) by

$$F_{l,r} = F_1 \pm F_3, \qquad F_L = F_2 - 2xF_1. \tag{5.13}$$

Another relationship between the structure functions that is often used, is the ratio R of the absorption cross section of the longitudinally to transversely polarized virtual boson, $R(x) = \sigma_L/\sigma_T$, given by

$$R = \frac{\sigma_L}{\sigma_T} = \frac{F_2 - 2xF_1}{2xF_1} \equiv \frac{F_L}{2xF_1}. \tag{5.14}$$

5.2 Parton Distribution Functions

The structure functions take on a particularly illustrative form in the parton model. The foundation of the parton model is the impulse approximation for hadronic cross sections involving large momentum transfers. Its basic assumption is that a physically observed hadron with the momentum p^μ is made out of constituent particles, the 'partons', which can be identified with the quarks and gluons of the quark model. At sufficiently high energies the masses of the hadron and the partons can be neglected compared to the scale Q of the hard scattering process. Under the additional assumption that every parton participating in the

hard interaction carries a momentum xp^μ, with $0 \leq x \leq 1$, parton model cross sections are calculated as the convolution of elastic partonic scattering cross sections with probability densities for finding the relevant partons in the participating hadrons.

A typical parton model DIS cross section is therefore given by

$$\sigma^{(lh)}(p,q) = \sum_i \int_0^1 dx \sigma^{(li)}_{Born}(xp,q) f_i(x), \tag{5.15}$$

where the sum runs over all possible flavours i. The distributions $f_i(x)$ are the probability densities for finding partons of flavour i in the hadron h carrying the momentum fraction xp and are called the distributions of partons i in the hadron h.

As indicated by the subscript *Born*, the parton cross sections are calculated from the tree graphs for partonic scattering only. That this is justified can be seen from the following parton model argument [99]: at any given time the hadron consists of a set of partons in some virtual state of definite fractional momenta $x_i p$. This virtual state is characterized by a lifetime τ in the hadron restframe. In going to the CMS system the hadron suffers a Lorentz contraction and a time dilation, and in the limit of infinite CMS energy, the lifetime of the virtual state will be large compared to the time it takes the electron to cross the hadron, i.e. the collision time. The parton configuration the electron 'sees' during the collision is thus effectively 'frozen'. This is the impulse approximation and is one of the main assumptions of the parton model.

Moreover, at large momentum transfers Q, the transverse dimension of the hadron probed by the electron is of the order $(1/Q)$. The probability of finding an additional parton to the one the electron scatters off can be estimated in the 'frozen' scenario by the purely geometrical factor $(1/Q^2)/(\pi R_0^2)$, with R_0 the radius of the hadron. Loop corrections to the scattering cross section can thus be neglected and the cross section calculated as the probability of finding the parton with a given momentum fraction times the tree-level electroweak elastic interaction cross section as given in Eq. (5.15). In the parton model picture the deep inelastic scattering can be depicted as shown in Fig. 5.2.

To summarize, in the parton model deep inelastic scattering reduces to the incoherent elastic scattering of the virtual bosons off the partons i which are characterized by the probability density distributions $f_i(x)$. From the Eqs. (5.5), (5.8), and (5.11) the following relations for the structure functions in the parton model can be derived:

$$F_k^{(Vh)}(x) = \sum_i \int_0^1 \frac{dy}{y} F_i^{(Vi)}(x/y) f_i(y) \qquad (k = 1, 3) \tag{5.16}$$

$$F_2^{(Vh)}(x) = \sum_i \int_0^1 dy F_2^{(Vi)}(x/y) f_i(y). \tag{5.17}$$

Thus at parton level the structure of the hadrons, i.e. the structure functions

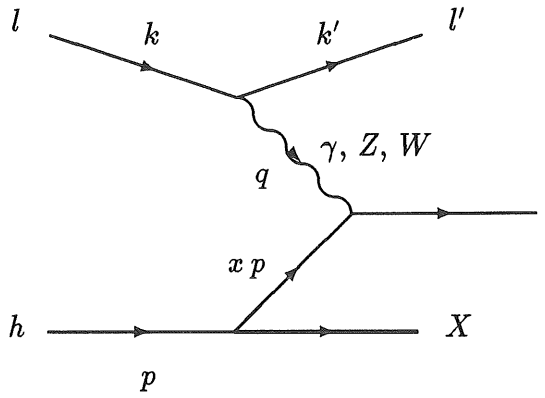

Figure 5.2: Lowest order lepton-hadron scattering in the parton model

$F_k^{(Vi)}$, can be calculated from the Born diagram in Fig. 5.2. For electromagnetic scattering the calculation yields [99, 100]:

$$2F_1^{(Vi)}(x) = F_2^{(Vi)}(x) = e_i^2\delta(1-x). \tag{5.18}$$

From Eqs. (5.17) and (5.17) it now follows that [100]

$$2xF_1^{(Vh)}(x) = F_2^{(Vh)}(x) = \sum_i e_i^2 x f_i(x). \tag{5.19}$$

This equation shows two of the important consequences of the impulse approximation:

- the structure functions only depend on the Bjorken scaling variable x;
- the structure functions satisfy the Callan-Gross relation $2xF_1 = F_2$ which, from Eq. (5.14), implies that $R(x) = \sigma_L/\sigma_T = 0$.

Note that the Callan-Gross relation is a direct consequence of the spin-1/2 nature of the quarks as taken into account in the calculation of the electromagnetic Born cross section in Eq. (5.18).

As the final step of illustrating the physical content of the structure functions in the parton model one now can take the parton content of the hadron in question from the constituent Quark Model and insert this in Eq. (5.19). This constitutes the Quark Parton Model (QPM). The possible virtual quark-antiquark pairs of every flavour taken into account it follows for electromagnetic electron-proton scattering

$$\begin{aligned} F_2^{ep}(x) &= \frac{4}{9}[xu(x) + x\bar{u}(x) + xc(x) + x\bar{c}(x)] \\ &+ \frac{1}{9}[xd(x) + x\bar{d}(x) + xs(x) + x\bar{s}(x)]. \end{aligned} \tag{5.20}$$

for four flavours u, d, s, and c and the generic parton distribution functions $f_i(x)$ denoted by the distribution functions according to the individual flavours.

At HERA two additional facts have to be taken into account. For one, the electron or positron beams in the machine (see 4.1) will be polarized to a degree λ, and at high momentum transfers the weak part of the neutral current has to be considered as well. This changes $F_2(x)$ in terms of generic quark and antiquark distributions into

$$F_2(x) = 2xF_1(x) = \sum_i^{N_f} A_i(\lambda, Q^2)[xq_i(x) + x\bar{q}_i(x)] \tag{5.21}$$

and $xF_3(x)$ will be given by

$$xF_3(x) = \sum_i^{N_F} B_i(\lambda, Q^2)[xq_i(x) - x\bar{q}_i(x)] \tag{5.22}$$

with $A^{L,R}$ and $B^{L,R}$ given by

$$(A, B)_i(\lambda, Q^2) = \frac{1-\lambda}{2}(A, B)_i^L(Q^2) + \frac{1+\lambda}{2}(A, B)_i^R(Q^2). \tag{5.23}$$

For electron-proton scattering

$$\begin{aligned} A_i^{L,R}(Q^2) &= e_i^2 - 2e_i(v_e \pm a_e)v_i P_Z + (v_e \pm a_e)^2(v_i^2 + a_i^2)P_Z^2 \\ B_i^{L,R}(Q^2) &= -2e_i(v_e \pm a_e)a_i P_Z \pm 2(v_e \pm a_e)^2 v_f a_i P_Z^2 \end{aligned} \tag{5.24}$$

with

$$P_Z = \frac{Q^2}{Q^2 + M_Z^2} \qquad v_i = \frac{T_{3i} - 2e_i sin^2\Theta_W}{sin2\Theta_W} \qquad a_i = \frac{T_{3i}}{sin2\Theta_W} \tag{5.25}$$

where e_i, v_i, and a_i are the charge, the weak vector and axial-vector couplings of a quark of type i, v_e and a_e the corresponding couplings for the electron, T_{3i} the third component of the weak isospin and Θ_W the Weinberg angle.

A commonly used distinction between F_2 and F_3 is that F_2 for an isoscalar target is the **flavour singlet** structure function, i.e. given by the sum of the quark and antiquark distributions, whereas F_3 is the **non-singlet** structure function determined by the valence distribution given by the difference between the quark and antiquark distributions. At small values of x this means that the behaviour of F_2 is driven by the virtual quark-antiquark pairs, i.e. the sea of partons in the hadron.

For the also measurable charged current scattering process at HERA, the structure functions can be expressed in terms of parton distributions [100] as

$$\begin{aligned} F_2^{e^-p\to\nu X}(x) &= x[u(x) + c(x) + \bar{d}(x) + \bar{s}(x)] \\ xF_3^{e^-p\to\nu X}(x) &= x[u(x) + c(x) - \bar{d}(x) - \bar{s}(x)]. \end{aligned} \tag{5.26}$$

One of the main subjects of interest at HERA is the behaviour of the structure functions at small x. The predictions of the QPM in the limit $x \to 0$ correspond to the high energy limit of the virtual photon proton cross section. This limit can be derived within the Regge picture of the high energy asymptotic behaviour of strong interactions which will first be shortly discussed below.

5.3 The High Energy Limit - Regge Theory

One of the most important feature of any dynamic theory is its asymptotic behaviour. The basis for the description of the high energy behaviour of strong interaction cross sections was laid in the Reggeon approach formulated in the decade before the introduction of QCD as the microscopic theory of these interactions.

When studying strong interactions, a problem was observed in that the exchange of particles in the t-channel with spin values j larger than 1 led to scattering amplitudes proportional to s^j, with s the CMS energy. The total cross section would thus rise like $\sigma_{\text{tot}} \sim s^{2(j-1)}$ in contradiction to the observed almost constant or slightly falling behaviour and which would lead to a violation of unitarity at large energies. The solution of this problem was found in Regge theory.

The foundation of the Reggeon approach are first of all the general features of the S-matrix, unitarity and analyticity, which have to hold for every field theory. In addition, due to the conservation of angular momentum, the scattering amplitude can be expanded into partial waves, i.e.

$$T(t,s) = \sum_{l=0}^{\infty}(2l+1)\mathcal{T}(s,l)P_l(cos\Theta), \tag{5.27}$$

and finally, the angular momentum may be continued analytically. These are the ingredients of Regge theory. The S-matrix characteristics can be expressed in three theorems which should hold for any microscopic theory. These are

- the optical theorem, which, with the normalization

$$\frac{d\sigma}{dt} = \pi|T(s,t)|^2$$

with $t = (p-q)^2$ (see Fig. 5.1), states

$$\sigma_{\text{tot}} = 4\pi \text{Im } T(s,o)$$

and thus relates the behaviour of the imaginary part of the scattering amplitude at zero scattering angle to the measurable total cross section;

- the Froissart boundary [101]

$$\sigma_{\text{tot}} \leq \text{C} \cdot \ln^2 s$$

with s the CMS energy of the elastic reaction $a + b \rightarrow a + b$ and C = 60 mb;

- the crossing symmetry as expressed in the Pomeranchuk theorem which states that the cross sections for the reactions $a + b \rightarrow a + b$ at $s > 0$ and $t < 0$, and $\bar{a} + b \rightarrow \bar{a} + b$ at $s < 0$ and $t < 0$ should be equal at high energies.

In Regge theory, the scattering amplitudes are analytically continued into the complex angular-momentum (l) plane [102]. Regge showed that for a partial wave expansion of potential scattering amplitudes, the only singularities of the scattering amplitude $\mathcal{T}(s, l)$ in the complex l-plane were poles dependent on s. For changing CMS energy s one thus obtains running poles and the scattering amplitude is found to be described by the exchange of a so-called Regge trajectory with non-integer spin and not any more by the exchange of single particles. These trajectories are called Reggeons (see Fig. 5.3). At the t values where the angular momentum takes on half-integer of integer values, the Regge poles are found to be known particles or resonances. Interesting enough it turned out that the exchange of many particles with high spins gave rise to power-like asymptotic behaviour of the cross sections with the power of the CMS energy smaller than 1.

It is thus found in Regge theory, that the high energy behaviour of the scattering amplitude is determined by the exchange of Regge poles taking into account the exchange of all particles or resonances lying on its trajectory. A prediction of Regge theory thus was that particles should appear in families, with the members of the families differing by two units in their angular momentum; they should lie on trajectories with the pole with the lowest mass, known as the leading pole, dominating the cross section dependence. Trajectories for different scattering processes would be populated by different particles or resonances. The trajectories $l = \alpha(t)$ are given as

$$\alpha_i(t) = \alpha_i(0) + \alpha_i' \cdot t \tag{5.28}$$

and are distinguished by the intercept $\alpha_i(0)$ and the slope α_i'.

Regge trajectories could be verified experimentally. It was observed that the resonances when plotted in a diagram of spin j versus the mass squared m^2 of the resonance, populate on only a few lines with a universal slope α_i'. This slope is $\alpha_i' \simeq 0.9\,\text{GeV}^{-2}$ for hadrons built out of light quarks. The intercepts $\alpha_i(0)$ of some trajectories (Reggeons) and some well established Regge poles are

- $\rho, \omega, f, a_2, \cdots$ with $\alpha_i(0) \simeq 0.4 - 0.5$
- K^*, K^{**} with $\alpha_i(0) \simeq 0.25 - 0.3$
- ϕ, f' with $\alpha_i(0) \simeq 0 - 0.1$.

The Regge trajectory corresponding to $\rho, \omega, \cdots$ exchange is shown in figure 5.3.

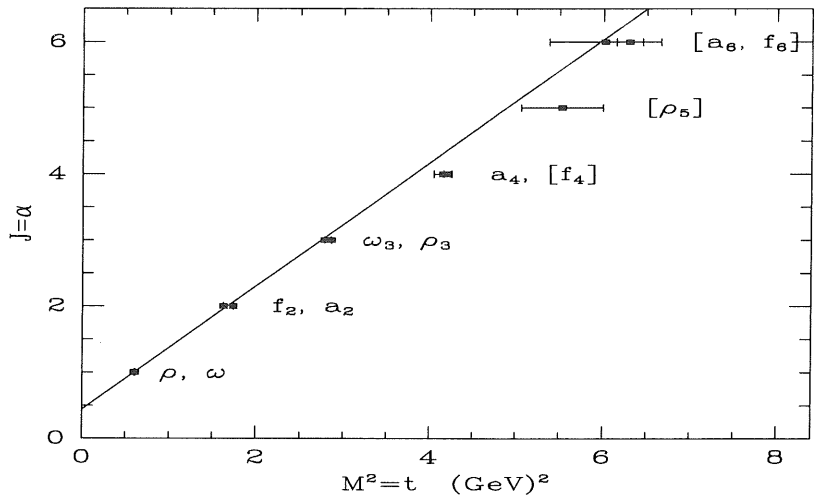

Figure 5.3: Meson Regge trajectory.

The high energy behaviour of the total cross section with CMS energy s for the exchange of Reggeons was found to be $s^{\alpha_i(0)-1}$, i.e. only dependent on the Reggeon intercept. For the exchange of ρ, ω, f, etc. mesons the total cross section thus behaves like $\sigma_{\text{tot}} \sim s^{0.5-1} = s^{-\frac{1}{2}}$, and the Froissart boundary is safe. In addition, the Reggeon scattering amplitude was found to factorize into vertex functions for the two colliding hadrons times the energy dependence given by the exchanged Reggeon. In DIS this means that if we describe DIS through the exchange of the Reggeon, the vertex function only depends on the momentum transfer Q^2 while the energy dependence is contained in a factor $x^{\alpha(Q^2)}$.

Besides the discovery of Regge trajectories, the other measurement result in the 1960's was that the total cross section for hadron-hadron scattering was approximately constant at high energies. In the Reggeon approach this means the existence of a Reggeon with the intercept close to 1 which had not been observed experimentally. The measured cross section behaviour thus led to the introduction of the Pomeranchuk trajectory, with the leading Regge pole giving rise to it called the Pomeron $\mathbb{P}$. The Pomeranchuk trajectory is defined as the Regge trajectory with $\alpha(0)$ - 1 = 0. This was later called the "critical" Pomeron, after it was observed that, when going to higher CMS energies, the total cross sections for hadron-hadron scattering not became constant, but instead continued to grow with a rate describable by a power law of the form $s^{\sim 0.07-0.085}$. To describe this energy dependence, the existence of the "supercritical" Pomeron with an intercept $\alpha(0) = 1 + \Delta$ with $\Delta > 0$ was postulated. In addition to the exchange of single Pomerons, also more than one Pomeron or Reggeon may be exchanged. These processes give rise to the so-called Regge cuts. See *e.g.* [108] for details.

The intercept of the supercritical Pomeron being larger than 1.0 of course again opened the problem of violation of the Froissart boundary at very high energies. The effective Pomeron intercept thus had to decrease with rising energy. Exactly how this can be done was found to be very much dependent on the value for Δ and more than one solution was found to this problem resulting in many different approaches of how to treat high energy soft interactions. Today values of Δ varying between 0.07 and 0.24, depending on the model of the Pomeron, are discussed. In the analysis of the H1 data we will refer to the single Pomeron exchange model favoured by Donnachie and Landshoff, where Δ is taken to be 0.085 and $\alpha'(0) \simeq 0.25\,\mathrm{GeV}^{-2}$ independent of s and which will thus lead to a violation of unitarity at asymptotic energies.

A review of all models is beyond the scope of this work. In principle, though, in order to achieve an energy dependent effective intercept, the Pomeron is treated like a field and the exchange of more than 1 Pomeron and interactions between Pomerons is considered in other models. The interference effects associated with taking higher order exchanges into account then reduce the effective intercept from the bare supercritical intercept to an observed 1.0808. This unitarization procedure leads to the total cross section at asymptotic energies behaving like

$$\sigma_{\mathrm{tot}} \propto \ln^2 s \tag{5.29}$$

and thus saturates the Froissart limit. The basic difference between different models lies in the type of Pomeron interactions considered to contribute. The "effective" Pomeron intercept at currently measured energies is thus 1.0808. This "effective" Pomeron is known as the "soft" Pomeron. All high energy cross sections are found to be describable as a superposition of postulated Pomeron and observed Reggeon exchange. The energy dependence of the "effective" Pomeron is however not yet derivable from the models and has to rely on measurements up to now.

Note, that the Pomeron is lying on the trajectory with the largest intercept $\alpha_i(0)$ discovered in the data so far, and that it has vacuum quantum numbers, i.e. I = 0, C = +, G = +, and P = +. Note also, that the Pomeron is not an observed particle but a Regge pole lying on the trajectory deduced from the asymptotic behaviour of the total cross section. We do not yet know which particles or resonances belong to its trajectory! It seems reasonable, though, to assume that these states are made out of gluons instead of valence quarks as in the case of the meson trajectories. In the Quark Parton Model the picture of the Pomeron being two gluons in a colour singlet state immediately comes to mind, and in the scattering process thus two (or more) gluons are exchanged between the hadrons. Since higher order corrections to the exchange of a single particle result in ladder type diagrams, the simplest picture of a Pomeron is thus one of a gluon ladder exchanged between the interacting hadrons.

A very interesting measurement in this direction has recently been published by the WA91 collaboration [104]. If one extrapolates the Pomeron trajectory the $\alpha(m^2) = 2$ state is reached for $m \simeq 1900\,\mathrm{MeV}$. At $m = 1900\,\mathrm{MeV}$ is where the

WA91 collaboration found a 2^{++} broad single ($370 \pm 70\,\mathrm{MeV}$) or a double state which could be a glueball candidate because it is produced isolated in rapidity and decays to four pions. This could be the first hint that Pomeron exchange indeed is the effect of the exchange of glueballs.

On the sound mathematical basis of the theory of complex angular momenta subsequently the phenomenological field of Reggeon Calculus was developed to calculate Pomeron exchange and Pomeron interactions in many reactions. As the calculations within Regge theory also involve the calculation of Pomeron interactions contained in the triple Pomeron interaction depicted in Fig.6.22 and the exchange of more than one Pomeron an effective Regge Lagrangian could be constructed and the Regge model turned into Regge field theory. In the case of multi-Pomeron interactions, the AGK cutting rules [105] were derived which relate Pomeron interactions to specific inelastic contributions to the total cross section. The basic relation which allows to derive these important rules is that for elastic scattering $a + b \rightarrow a + b$ the equality

$$\mathrm{Im} < a|T|a >= \frac{1}{2i}\mathrm{Disc} < a|T|a >= s\sigma_{\mathrm{tot}} \tag{5.30}$$

relating the imaginary part of the elastic scattering amplitude to its discontinuities holds. The discontinuities can be identified with cuts in Pomeron exchange graphs (see also 5.8 and 8.1.2). In this way, the relationship between the contributions of multi-Pomeron exchange and different exclusive and inclusive processes in the Reggeon approach is established. The resulting field theory is known as Gribov-Regge theory [85]. It assumes *multiple* Pomeron/Reggeon exchange as the dominating process at high energies and one of its main successes is the cure of the violation of unitarity which occurs if single Pomeron exchange with an intercept larger than 1.0 is assumed to mediate the interactions.

Regge theory turned out to be a successful phenomenological approach that passed numerous experimental tests. Let it suffice at this point to only mention the successful parametrizations of the total cross sections for pp, $p\overline{p}$ and πp scattering. The s-dependence of these cross sections can be fitted by the sum of two terms proportional to $s^{0.0808}$ and $s^{-0.4525}$. These fits performed by Donnachie and Landshoff [106] are shown in figure 5.4.

The first term is just the "effective" Pomeron intercept, whereas the second is the ρ etc. meson trajectory. The energy dependence of the effective intercept, however, has to be kept in mind in EAS physics when tackling the energy range beyond $10^{18}\,\mathrm{eV}$ with Monte Carlos developed around an effective lower energy Pomeron.

The behaviour of measured hadronic cross sections is well described by the exchange of mesons and "soft" Pomerons. Additional experimental verification of the Regge model is *e.g.* that the pp and $p\overline{p}$ cross sections only differ in the meson exchange term. This is expected, since the Pomeron carrying the quantum numbers of the vacuum should couple equally to p and $\overline{p}$. The same qualitative

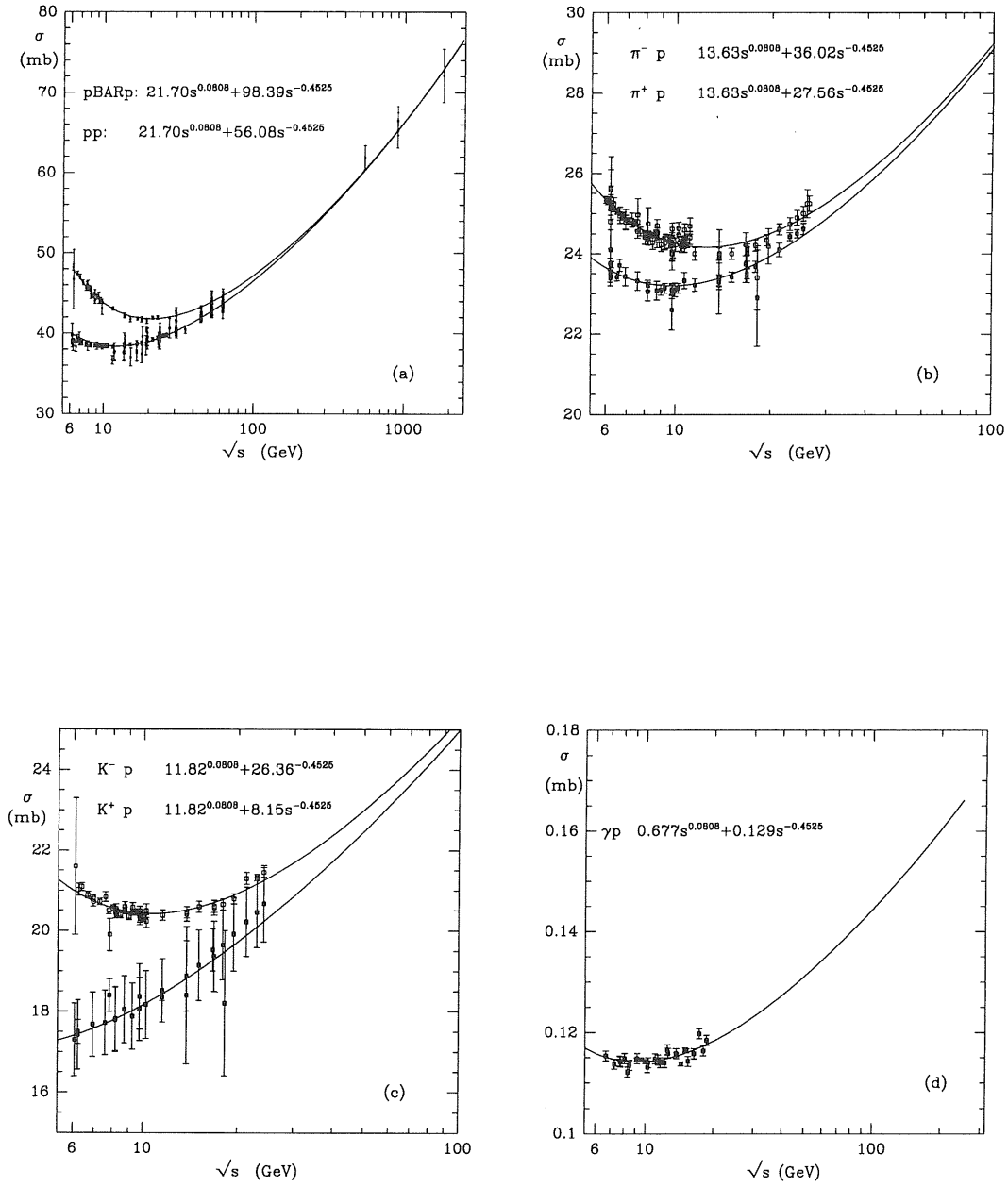

Figure 5.4: Fit of the measurements of the total cross sections for $p\bar{p}$, pp, $\pi^{\pm}p$, $K^{\pm}p$, and γp scattering by a two term function derived from the intercepts of the "soft" Pomeron and the ρ meson trajectory. Taken from [106].

behaviour is found in the $\pi^+ p$ and $\pi^- p$ cross sections. Again, only the meson exchange sensitive to the flavour composition of the scattering partners is different. When comparing the absolute magnitude of the $s^{0.0808}$ terms found in pp and πp cross sections one finds that the ratio of these terms is equal to 2/3, i.e. equal to the ratio of the number of valence quarks of p and π. The third type of total cross section that can be fitted by the two component ansatz is the total cross section for photoproduction. The H1 result concerning this measurement will be shown in 7.

Without quoting all the experimental facts that backs them up, the characteristics of the "soft" Pomeron can be summarized as

- it couples to quarks
- it results in simple power behaviour of cross sections
- it behaves like a $C = +1$ isoscalar photon

This last property has been tested in elastic pp scattering where the "soft" Pomeron coupling exhibits a Dirac form factor just like the photon coupling to a proton.

The multitude of experimental verification of Regge theory was taken by phenomenologists as the building ground for the dual string-theories [82, 83] where the constant string tension is responsible for the formation of Regge trajectories as a function of the spin value, i.e. the length of the string ($\propto \alpha(t)$) versus $\alpha' M^2$, with $\alpha' = 1/(2\pi a)$ and a the string tension, lies on straight lines.

Among the phenomenological models developed to describe this kind of soft interactions are the Dual Parton Model (DPM) [82] and the Quark Gluon String Model (QGSM) [83]. Since these are among the basics ingredients of the Monte Carlo generator (see 8) employed by EAS experiments, the close relationship between the HERA data and EAS investigations will become clear when we discuss the H1 results.

The Regge analysis of the structure functions in the limit $x \to 0$ yields the following prediction for the asymptotic behaviour. The total photon-hadron and hadron-hadron cross sections depend on the CMS energy like

$$\sigma_{\mathrm{tot}}^{\gamma(h)}(s) \sim s^{(\alpha(0)-1)}.$$

This behaviour is also valid for the virtual photon for $x = Q^2/2m\nu \ll 1$. With F_2 the total $\gamma^* p$ cross section, i.e.

$$\sigma_{\mathrm{tot}}^{\gamma p} = \lim_{Q^2 \to 0} \left[\frac{4\pi^2 \alpha}{Q^2} F_2(x, Q^2) \right], \tag{5.31}$$

the prediction of Regge theory for the structure function to be measured at HERA in the Regge limit (i.e. $x \to 0$) is

$$F_2(x, Q^2) \sim x^{-0.08} \quad \text{for} \quad x \to 0. \tag{5.32}$$

The limiting behaviour of the sea quark distributions is thus expected to be

$$x q_{sea} \sim x^0, \tag{5.33}$$

whereas the valence distribution should die out as

$$x q_{valence} \sim x^{0.5}. \tag{5.34}$$

Despite all the successes of Regge theory, the hope to build an effective theory for strong interactions on the basis of the effective Lagrangian derived from triple Pomeron interactions and the AGK cutting rules turned out to be in vain. The calculations of interacting ladder diagrams as the simplest picture of Pomeron structure led to a series of theoretical problems and finally to the exodus of theoreticians from the field of Regge theory as the fundamental ansatz for the strong interaction theory. Theorists at that time thought that a more detailed description of the *Pomeron structure* in terms of a microscopic theory was necessary. Around that time QCD was proposed as the theory for strong interactions but it was not developed enough to solve the problem of high energy asymptotics. Regge theory as an effective for soft hadronic interactions which still cannot be calculated with perturbative QCD is, however, very much alive and even received considerable backing by the HERA results discussed below.

In the next section we will summarize some of the crucial aspects of the field theory of the strong interactions, Quantum Chromodynamics (QCD). On this basis we will then discuss what QCD has added to the above picture of structure functions, and whether the predictions of the QPM for the limiting behaviour of the structure functions will be changed or will survive. Note, that the prediction for the x-dependence of F_2 is derived from a phenomenological theory that has passed numerous experimental tests. Any deviation from this prediction would be very exciting and signal the presence of physics not previously measurable.

The terminology and phenomenology developed in the Regge Calculus were revived due to the developments in the description of QCD in the limit when the density of partons becomes very large. Since these developments were achieved especially with the intention of understanding QCD within the new region of phase accessible at HERA, the discussion of the structure functions at small x (see 5.7) will naturally lead back to the high energy behaviour of QCD.

5.4 Some basic properties of QCD

The field theory describing the interactions of quarks, QCD, reproduces the QPM in the asymptotic energy regime. Here quarks can be considered to be free particles within the hadrons because of the 'asymptotic freedom' property of QCD

[98]. This makes it possible at high energies to calculate many processes in the framework of perturbation theory.

Another aspect of QCD which is responsible for a big part of the difficulties encountered by experimenters in their endeavour to falsify the theory, is the confinement of quarks and gluons within the hadrons. The confinement property of QCD follows from the fact that the force between quarks does not decrease with distance, and it thus would require an infinite amount of energy to separate a quark and antiquark up to macroscopic distances. Since the QCD vacuum on the other hand is filled with quark-antiquark pairs, when a quark and antiquark are provided with enough energy to fly apart, the energy stored in the confining potential is transformed into a cascade of quark-antiquark pairs until the energy is below the $2m_q$ threshold. At that energy the quarks and antiquarks group themselves in a nonperturbative stage into the observed hadrons.

Whereas the QPM gives a static picture of the hadrons, QCD adds the dynamics through the introduction of the binding vector bosons, the gluons. The Lagrangian is given by [98]

$$L = -\frac{1}{2}G^a_{\mu\nu}G^{\mu\nu}_a + \sum_k^{N_f} \bar{q}_k(i\gamma^\mu D_\mu - m_k)q_k \tag{5.35}$$

where q_k is the quark field of flavour k (k = 1,...,N_f), a the colour index (a = 1,...,8), and m_k the mass of quarks of flavour k. Here

$$G^a_{\mu\nu} = \partial_\mu A^a_\nu - \partial_\nu A^a_\mu + g f_{abc} A^b_\mu A^c_\nu, \tag{5.36}$$

$$D_\mu \equiv \partial_\mu - igT^a A^a_\mu, \tag{5.37}$$

where A^a_μ is the μth component of the ath gluon vector field, and

$$[T_a, T_b] = i f_{abc} T^c \tag{5.38}$$

are the $SU(3)$ colour matrices and f_{abc} the antisymmetric structure constants of $SU(3)$.

Below we will discuss the dynamical influence of the gluons on the parton distribution functions when changing the scale of the external momenta. For HERA physics the discussion will center on the low x domain. But already at low energies and correspondingly large values of x (note that $W^2 \simeq Q^2/x$) the gluons play an important role as a constituent of the proton carrying a fraction of the protons momentum, as was found in the analysis of the SLAC-MIT data [107].

Denoting the distribution of gluons in the proton by $g(x)$ one can define

$$U \equiv \int_0^1 x u(x) dx, \tag{5.39}$$

$$D \equiv \int_0^1 x d(x) dx, \tag{5.40}$$

etc., as the total fractions of the protons momentum carried by the partons of flavour u, d, etc., and

$$G \equiv \int_0^1 xg(x)dx, \tag{5.41}$$

as the total fraction of the protons momentum carried by gluons. Within QCD we presume that

$$Q + \bar{Q} + G = 1 \tag{5.42}$$

with Q and $\bar{Q}$ denoting the sum of quark and antiquark momenta fractions, respectively.

From the data [107] it was found that

$$\begin{aligned} Q &= U + D + S \simeq 0.44 \\ \bar{Q} &= \bar{U} + \bar{D} + \bar{S} \simeq 0.07. \end{aligned} \tag{5.43}$$

The rest, i.e. about 50% of the proton momentum is carried by the gluons. Since the gluons are not an ingredient in the naive QPM, we expect the Quark Model not to be able to describe all the features of the scattering process at large Q^2 or at low x.

In experiments where strongly interacting particles are present in the initial or final state and in which the observables are not fully inclusive the confinement of the quarks and gluons leads to the fact that the observables have to be described as a convolution of two types of physics:

$$\text{Observable} = \text{Perturbative Part} \otimes \text{Non-Perturbative Part}.$$

Of these, the perturbative part is calculable as a power series in α_s.

On the size of the non-perturbative contribution to any observable a strong constraint is provided by the factorization theorems of QCD [108] (see Eq. (5.60) and discussion thereof) which limit these contributions to inverse powers of Q. Further than that, the non-perturbative parts cannot be calculated yet and have to be modelled. A lot of work has gone into this modelling which usually is done within Monte Carlo simulation programs containing a perturbative result which then is modified by non-perturbative effects modelled after a multitude of experimental results. In the case of DIS during the workshop on HERA physics held in 1991 the subject of these phenomenological programs warranted its own working group [109].

The perturbative calculation of observables also is not without its problems and 'theoretical uncertainties'. A common problem arising in these calculations stems from the fact that observables have only been calculated up to at most the order α_s^3 which leaves uncertainties due to missing higher orders and due to the uncertainty of the renormalization scale μ^2. This scale enters as a residue of the quantum nature of the fields.

The quantum fields of massless quarks and gluons which are the basic fields of QCD, can fluctuate very strongly on short distances. These fluctuations appear in the form of loop diagrams at higher orders in which the particle momenta can go to infinity. This leads to the bare parameters of the theory as appearing in the Lagrangian to being infinite. This type of divergence is denoted ultraviolet divergence. In a highly non-trivial manner it is now possible in QCD through the introduction of counterterms in the Lagrangian to cancel these divergences by only redefining (renormalizing) the fields and parameters of the theory in each order of the perturbative expansion [110]. This redefinition is performed at a fixed scale μ^2, the renormalization scale. All parameters of the theory now depend on this scale.

Before the counterterms that have to be added to the Lagrangian can be determined, the theory has to be regulated in order to make the ultraviolet divergent loop integrals calculable. The regularization procedure replaces the theory by a slightly shifted model using a cut-off. In this model the observed parameters are finite and in the renormalization procedure the contributions to the fields and parameters are then divided into a finite part, which should be chosen such that the perturbation series for the physical observable will converge best, and an infinite part which is cancelled by the counterterms. The rule of how to choose the counterterms is called the renormalization prescription. In order to believe that the renormalized theory still describes the same physics as the original Lagrangian one had to show that even though the relation between the bare and the observed parameters tend to become divergent, the effects of the cut-off become negligible at large distance scales. QCD is such a theory in which the counterterms can be rigorously defined in the limit of a vanishing cut-off.

The regularization is performed within a defined **regularization scheme** which has no influence on the result of the calculations other than making the calculations possible. Especially popular is the dimensional regularization scheme which, as it turns out, not only regulates the ultraviolet divergencies, but at the same time the infrared divergencies which again appear because the fields are massless. This type of divergency always turns up in the calculation of observables which are sensitive to the following effects:

- the presence of a soft massless particle or
- two massless particles being emitted in a parallel configuration.

Note, that in this regularization scheme the scale μ appears naturally in order to keep the coupling dimensionless in the $d = 4 - 2\epsilon$ dimensions in which the regularization is performed. Defining the counterterms such that exactly the singular piece is canceled defines the minimal subtraction (MS) **renormalization scheme**. Removing an additional piece involving the Euler constant γ_E and $\ln 4\pi$ constitutes the modified minimal subtraction scheme ($\overline{MS}$). In this fashion more renormalization schemes can be defined.

The above described completely mathematical procedure of renormalization is of no consequence for observables calculated up to infinite order, which in practice would mean up to the order where the asymptotic perturbation series for the observable has converged. This has not yet been achieved for any observable. For any calculation up to finite order in α_s it renders the calculated observables renormalization scheme and renormalization scale dependent. The renormalization scale can be chosen freely and should in fact be chosen such that it corresponds to the typical scale of the process in question, and thus produces the fastest convergence of the perturbation series.

QCD as a self-consistent theory fixes the way the parameters of the theory have to be changed if the arbitrary renormalization scale is changed. This is the content of the renormalization-group equation [111, 112, 113]. The necessary ingredients for this equation are the QCD β-function defined via

$$\mu \frac{dg(\mu)}{d\mu} = \beta(g) \tag{5.44}$$

which determines the scaling properties of the coupling g. The second ingredient is the anomalous dimension function γ_ϕ of the specific processes Green's function (or amplitude) Γ defined by

$$Z_\phi^{-1} \mu \frac{d}{d\mu} Z_\phi = \gamma_\phi, \tag{5.45}$$

with Z_ϕ the renormalization constants which are the scale factors that relate the bare (ϕ_0) and renormalized fields (ϕ) via

$$\phi_0 = Z_\phi(g_0, \frac{\Lambda}{\mu})\phi \tag{5.46}$$

and thus

$$\Gamma^{(n)}(p, g, \mu) = Z_\phi^{(n)}(g_0, \frac{\Lambda}{\mu})\Gamma^{(n)}(p, g_0, \Lambda) \tag{5.47}$$

for the Green's function with n external fields and the external momentum p. Using these definitions, one can now write the renormalization group equation (RGE) which determines how the fields and the coupling have to be varied to compensate for a change in the scale μ

$$(\mu \frac{\partial}{\partial \mu} + \beta(g) \frac{\partial}{\partial g} - n\gamma_\phi)\Gamma^{(n)}(p, g, \mu) = 0. \tag{5.48}$$

The powerful property of the RGE that will be discussed in more detail in section 5.5 is that the RGE derived from independence of the physics from the **internal subtraction scale** also establishes the mathematical procedure of how changes in the **external momenta** influence the parameters of the theory. This is called the renormalization group evolution and it determines the scaling properties of observables such as the coupling constant and e.g. the structure functions.

For the coupling constant, the RGE yields the solution that the external momentum scale can be absorbed by a description in terms of an effective coupling $\bar{g}$

which 'runs' with the value of the scale change [114]. This redefinition of the coupling is contained in the so-called running coupling constant obtained from

$$\mu^2 \frac{\partial \alpha_s}{\partial \mu^2} = -(\beta_0 \alpha_s^2 + \beta_1 \alpha_s^3 + \beta_2 \alpha_s^4 \cdots). \tag{5.49}$$

At the one-loop level, i.e. in **leading order** this equation reduces to

$$\mu^2 \frac{\partial \alpha_s}{\partial \mu^2} \equiv \frac{\partial \alpha_s}{\partial \ln \mu^2} = -\beta_0 \alpha_s^2. \tag{5.50}$$

The solution for integrating from $\alpha_s(\mu_0^2)$ to the coupling at the external scale $\alpha_s(Q^2)$

$$\alpha_s(Q^2) = \frac{\alpha_s(\mu_0^2)}{1 + \beta_0 \alpha_s(\mu_0^2) \ln(Q^2/\mu_0^2)} \tag{5.51}$$

can be rewritten with the definition

$$\Lambda_{\rm QCD} = \mu_0 e^{\frac{1}{2}\beta_0 \alpha_s(\mu_0^2)} \tag{5.52}$$

to yield

$$\alpha_s(Q^2) = \frac{4\pi}{\beta_0 \ln(Q^2/\Lambda_{\rm QCD}^2)}. \tag{5.53}$$

The first three coefficients of the β-function are [115, 116, 117]

$$\begin{aligned} \beta_0 &= 11 - \frac{2}{3} N_f, \quad \beta_1 = 102 - \frac{38}{3} N_f, \\ \beta_2 &= \frac{2857}{2} - \frac{5033}{18} N_F + \frac{325}{54} N_f^2 \end{aligned} \tag{5.54}$$

with N_f the number of active flavours. To leading order, the QCD constant $\Lambda_{\rm QCD}$ is not well defined as can easily be seen by changing $\Lambda_{\rm QCD}$ in Eq. (5.53) and realizing that this introduces a change of $\alpha_s(Q^2)$ in $\mathcal{O}(\alpha_s^2)$ and thus no change in the value of $\alpha_s(Q^2)$ to the studied order. In just the same way also the exact definition of Q^2 itself is arbitrary in leading order, since also a change in Q^2 only introduces changes in order α_s^2. Any measurement of QCD parameters needs thus to be done to at least **next-to-leading order** in order to prevent these ambiguities. At the two-loop level the solution of Eq. (5.49) is given by

$$\alpha_s(Q^2) = \frac{4\pi}{\beta_0 \ln(Q^2/\Lambda_{\rm QCD}^2)} \left[1 - \frac{2\beta_1}{\beta_0^2} \frac{\ln\ln(Q^2/\Lambda_{\rm QCD}^2)}{\ln(Q^2/\Lambda_{\rm QCD}^2)} \right]. \tag{5.55}$$

To this and to higher orders the scale parameter Λ has a definite meaning. Whereas α_s and consequently observables calculated to $\mathcal{O}(\alpha_s)$ do not change when the value of Λ is changed according to $\Lambda \to \Lambda' = \Lambda/\kappa$, in next-to-leading order this changes α_s like

$$\alpha_s \to \alpha_s' = \alpha_s - \left[\frac{\beta_0}{4\pi} \ln\kappa \right] \alpha_s^2 + O(\alpha_s^3), \tag{5.56}$$

i.e. a change in $\mathcal{O}(\alpha_s^2)$ is encountered. Similarly, a change in the renormalization scheme effects only $\mathcal{O}(\alpha_s^2)$ and beyond and is equivalent to a change in the

magnitude of $\Lambda_{\rm QCD}$. This scale is thus conventionally denoted by Λ_{MS} or $\Lambda_{\overline{MS}}$ etc..

If the calculation of the observable does not involve infrared divergencies, a change in the external momenta is completely compensated by the redefinition of the reference scale of the 'running coupling constant'. This is in general only the case for completely inclusive observables. If, on the other hand, in the calculation of the observable infrared divergencies are encountered, applying the renormalization-group equation when the external momenta are changed, results in two effects:

- a redefinition of the scale of the coupling constant and
- a multiplicative factor which depends on the anomalous and engineering dimension of the amplitude (see Eq. (5.48).

A distinctive signature of the appearance of divergencies is the appearance of two types of logarithmic terms in the calculations. With Q^2 the external scale of the specific process, μ^2 the chosen renormalization scale, and $\Lambda = \Lambda_{\rm QCD}$, logarithms of the type

$$\ln\frac{\rm Q^2}{\mu^2} \tag{5.57}$$

signal the fact that a renormalization because of the presence of ultraviolet and (or) collinear divergencies has been performed, and

$$\ln\frac{\rm Q^2}{\Lambda^2} \tag{5.58}$$

that a regularization has been performed due to the occurence of Feynman diagrams with a bad behaviour if one or more external momenta vanish. Finally, the third type of logarithms appearing in the calculations involves the masses of the participating particles, m, is of the form

$$\ln\frac{\rm Q^2}{\rm m^2}. \tag{5.59}$$

Regarding the two types of infrared divergencies, the calculations of physical observables are ensured to be finite by the validity of two theorems. The Bloch-Nordsiek theorem [118] states that in inclusive cross sections the infrared divergencies stemming from massless particles cancel, and the Kinoshita-Lee-Nauenberg theorem [119], that again for inclusive cross sections also the mass singularities cancel.

5.5 Structure Functions and QCD

The strong interaction effects in deep inelastic scattering are contained in the hadronic tensor $W^{\mu\nu}(p,q)$. The key to applying QCD to this process are the

factorization properties of QCD [108]. As summarized in the Eqs. (5.57) - (5.59), there are three classes of variables with the dimensions of mass that enter the calculations of cross sections. These are the momentum transfer scale Q, the mass m, and the renormalization scale μ. In general, the cross sections are dependent on a combination of short- and long-distance behaviour as can be visualized e.g. by Eq. (5.59), since terms of this form will play an important role at large distances where the propagators are close to their mass shells, which in case of gluons is zero. A cross section of this type is of course not directly calculable within perturbative QCD.

This is where the factorization theorem of QCD enters, which states that scattering amplitudes with incoming high energy hadrons can be written as a product of a hard scattering piece which contains only high energy and high momentum components, and a remainder factor which contains the physics of low energies and momenta. $W^{\mu\nu}(p,q)$ can thus be expressed as

$$W^{\mu\nu}(p^\mu,q^\mu)=\sum_f\int_x^1\frac{dx}{x}H_i^{\mu\nu}(xp^\mu,q^\mu,\mu,\alpha_s(\mu))f_i(x,\mu)+\text{remainder} \qquad (5.60)$$

where the factor $f_i(x,\mu)$ contains the *process independent* low energy physics and is called the parton distribution function. It gives the probability of finding a parton of type i in a hadron of type h carrying a momentum fraction x to $x+dx$ of the hadron's momentum. This equation can be proven in perturbation theory with the remainder down by powers of Q^2 [120, 121, 122, 123, 124]. The explicit form of the remainder depends of the process in question and has not always been determined, yet.

The additional function $H_i^{\mu\nu}$ appearing in Eq. (5.60) has two important properties. It only depends on the parton i and not any more on the hadron h and it is ultraviolet dominated, which means that the result of the calculation of $H_i^{\mu\nu}$ will be a power-series in $\alpha_s(Q^2)$ with finite coefficients. Under the *one assumption* that the non-perturbative long-distance effects in the complete theory factorize in the same way as the perturbative ones, one can interpret the perturbative calculation of $H_i^{\mu\nu}$ as the prediction of the theory. In order to perform the factorization, the scale μ^2 had to be introduced to separate the long- and short-distance physics.

Projecting $W^{\mu\nu}$ of Eq. (5.60) onto the individual structure functions as defined in Eq. (5.8), a measurement of $F_2(x,Q^2)$ will determine the process independent f_i, which then can be used in the predictions of other processes. This can be done because the parton distribution functions derived from the factorization theorem are universal. Note the similarity between Eqs. (5.15) and (5.60). The deep reason behind this is the fact that the basic factorization theorems of QCD may be thought of as a field theoretic realization of the parton model. The so-called QCD improved parton model is thus well suited to get an intuitive picture of the processes involving hadrons.

Note, that in the QCD improved parton model, just as discussed in the descrip-

tion of the QPM, the factorization into a convolution of parton densities times a parton-current cross section is also true. But, since QCD is a field theory, the parton cross section receive contributions from all orders of the perturbative expansion. The divergencies appearing in the loop and phase space integrals have to be removed as discussed above. The ultraviolet divergencies can be removed by a coupling constant renormalization, leading to a running coupling. The infrared ones will cancel between real and virtual contributions. This leaves the collinear (or mass) singularities which can be removed by renormalizing the parton densities, i.e. changing the bare parton densities $f_i^{\rm ibare}(x)$ to $f_i^{\rm ren}(x,Q^2)$. This procedure is called mass factorization and absorbs terms of the form $\log M^2/\mu^2$, where M is the factorization scale into the renormalized parton densities. The mass factorization scale at which the short distance (partonic) effects are separated from the not calculable long distance (hadronic) effects is mostly, but not necessarily, chosen to be equal to Q. The remaining partonic observable is thus infrared safe and finite and it does not anymore depend on the hadron involved in the process.

This process renders the parton densities scale-dependent. The appearance of the mass singularity may be pictured in the QCD improved parton model as follows: in the QPM the partons scatter incoherently when their transverse momenta are larger than Q_0^2 which is of the order of $1\,\mathrm{GeV}^2$. If Q^2 is much larger than this inherent parton model scale, the large transverse momentum gap ($Q_0^2 \ll k_{\rm T} \ll Q^2$) can be filled with QCD radiation of massless partons in the QCD improved model. The relevant Feynman diagram in the appropriate (axial) gauge is shown in Fig. 5.5.

The logarithmic spectrum in transverse momentum leads to corrections of the type

$$\alpha_s \int_{\mu^2}^{Q^2} \frac{dk_{\rm T}^2}{k_{\rm T}^2} = \alpha_s \ln \frac{\mathrm{Q}^2}{\mu^2}. \tag{5.61}$$

For $Q^2 \gg Q_0^2$ and $x = O(1)$ this correction receives the main contribution for a emission chain strongly ordered in transverse momenta $k_{\rm T,i}$ along the chain (i.e. along the ladder which appears once the amplitude is squared) ($Q^2 \ll k_{\rm T,n} \ll k_{\rm T,n-1} \cdots$), and the incoherent sum over all possible chains connecting the 'valence' quarks (Q_0^2) and the 'struck' quarks (Q^2) therefore leads to a power series in $\alpha_s \log(\mathrm{Q}^2)$, i.e. diagrams of this type at each order n of the perturbative expansion have a leading term with the maximum power of $\log(Q^2)$ called the leading logarithms $\alpha_s^n \log^{\rm n}(\mathrm{Q}^2)$. The incoherent sum of these leading logarithms constitutes a **leading logarithm approximation (LLA)**, in this case a leading $\log Q^2$ approximation.

In general the full perturbative expansion for any observable (*e.g.* the parton density xf_i) can be written as

$$xf_i = \sum_{n=0} c_n(\alpha_s)^n \cdot (L^n + a_{n-1}L^{n-1} + \cdots + a_0), \tag{5.62}$$

with L logarithms to be calculated from the diagrams. In a leading logarithm

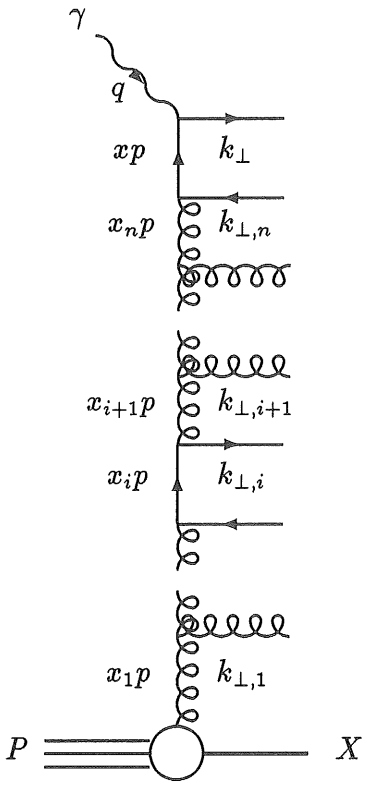

Figure 5.5: QCD improved parton model picture of the Q^2dependence of parton density distributions

approximation this series is then approximated by

$$xf_i = \sum_{n=0} c_n(\alpha_s \cdot L)^n, \tag{5.63}$$

with L now the leading logarithm.

For the parton densities this effectively means that depending on the external scale Q^2 the observed parton densities change due to the $\log(Q^2/\mu^2)$ dependent amount of initial radiation before the hard scattering. This type of radiation correction can be absorbed into the definition of the parton densities rendering them thus Q^2-dependent [125], i.e.

$$xf_i(x,Q^2)_{LLA} = \sum_{n=0} c_n(\alpha_s \cdot \log Q^2)^n. \tag{5.64}$$

Since this mass factorization is a purely mathematical procedure, the ambiguity of the freedom of choice as to how much of the infinities is to be absorbed into the redefinition of the parton densities and how much is retained in the calculable part, constitutes a **mass factorization scheme** ambiguity. This scheme thus has to be defined and used consistently when taking parton densities from one process and appling them to another one. Most commonly two factorization schemes are used. One is the $\overline{MS}$ (see 5.4) and the other the DIS scheme in which all the QCD corrections to the *particular* structure function F_2 are absorbed into the

definition of the parton densities and the F_2 structure function is given to all orders as

$$\frac{F_2(x,Q^2)}{x} = \sum_i e_i^2 f_i(x,Q^2).$$

In this scheme, the QCD corrections for the other structure functions and processes, however, become more complicated.

The prediction of QCD on the dependence of results on the mass factorization scale, i.e. the **Q^2-dependence** of the QCD initial state radiation governing the Q^2-dependence of the structure functions can either be derived applying renormalization group techniques or by using the parton picture by Kogut and Susskind [126], where higher momenta correspond to a higher resolution power, which can be expressed in the language of parton splitting functions as developed by Altarelli and Parisi [127]. In the region of the applicability of the LLQ^2 approximation (large x and large Q^2 ($\gg Q_0^2$)) this will lead to the Altarelli-Parisi Q^2 evolution of the parton densities.

5.5.1 The Renormalization Group Approach To QCD Evolution

The QCD evolution of the structure functions with Q^2 can be derived by starting from Eq. (5.7) using the Operator Product Expansion (OPE) [128].

The hadronic tensor can be written as

$$\begin{aligned}\sum_X \langle h(p,\sigma)|j_\mu^{V\dagger}(0)|X\rangle\langle X|j_\nu^V(0)|h(p,\sigma)\rangle &= \\ \int d^4z e^{iqz}\langle h(p,\sigma)|j_\mu(z)j_\nu(0)|h(p,\sigma)\rangle &= \mathrm{Im}\Pi_{\mu\nu}(\mathrm{q}).\end{aligned} \tag{5.65}$$

Regarding the Q^2 behaviour of the structure functions we see, that in the case of $-q^2 \to \infty$, the integral is dominated by the $z^2 \to 0$ behaviour, i.e. the short distance behaviour of the product of the currents. This behaviour can be derived by the OPE. The product of the composite operators is decomposed into a series of local i.e. *short-distance*, symmetric and traceless operators $O^i_{\mu_1\cdots\mu_n}(0)$:

$$j_\mu(z)j_\nu(0) \simeq \sum_{i,n} C_n^i(z^2) z^{\mu_1}\cdots z^{\mu_n} O^i_{\mu_1\cdots\mu_n}(0), \tag{5.66}$$

where the sum runs over the spin n and over the possible types of operators i. The functions $C_n^i(z^2)$ are the Wilson coefficients. They are *independent* of the target states and can be calculated within perturbative QCD. Their behaviour as $z^2 \to 0$ is

$$C_n^i(z^2) \sim (z^2)^{-d_0+\frac{1}{2}(d_0^i(n)-n)+2} \tag{5.67}$$

where d_0 is the dimension of the current $j(\mu)$ and d_0^i the one of $O^i_{\mu_1\cdots\mu_n}$. The combination $d_0^i(n) - n$ is called *the twist of the operator.*

The most singular behaviour is given by the leading twist operators and the contribution from higher twist is down by inverse powers of Q^2 just as maximally allowed by the factorization theorem. When using the expansions of Eq. (5.66) in a Green function, the *local* operators have to be renormalized and consequently the Wilson coefficients are changed and found to depend logarithmically on (Q^2/μ^2). This is the source of the logarithmic scaling violations as discussed in the introduction of the QCD improved parton model in the language of the OPE.

The derivation can be sketched as follows: The amplitude decomposed in Eq. (5.66) is related to the $n-th$ moments of the structure functions via

$$M^n(Q^2) \equiv \int_0^1 dx x^{n-2} F(x,Q^2) = \sum_i A_n^i(\mu^2) C_n^i(Q^2,\mu^2), \tag{5.68}$$

with $F = F_1, xF_2, xF_L$, or xF_3 and where the A^i are the non-perturbative matrix elements for the local operators defined through the expectation values of these operators. The A^i are not calculable within the theory and have to be taken from the experiment.

Since the products $A_n^i(\mu^2)C_n^i(Q^2,\mu^2)$ are integrals over structure functions, they constitute physical observables, and thus should be renormalization scale independent. To satisfy this requirement, the $C_n^i(Q^2,\mu^2)$ satisfy a renormalization-group type equation, which in the non-singlet case reads as

$$(\mu\frac{\partial}{\partial\mu} + \alpha_s\beta\frac{\partial}{\partial\alpha_s} - \gamma_n^{NS})C_n^{NS}(\frac{Q^2}{\mu^2}, g^2) = 0, \tag{5.69}$$

where γ_n^{NS} is the anomalous dimension of the non-singlet operator related to the number n of external quark and gluon fields. Due to the possible mixing between gluon and singlet-quark contributions, the evolution of the singlet moments is more complicated. Here and in the following the singlet case will not be discussed in detail. For details on the singlet structure functions please refer to the literature, *e.g.* [129]. The last equation can be solved and yields

$$C_n^{NS}(\frac{Q^2}{\mu^2}, g^2) = C_n^{NS}(1,\bar{g}^2) exp\left[-\int_{\bar{g}(\mu^2)}^{\bar{g}(Q^2)} dg' \frac{\gamma^{n,NS}(g')}{\beta(g')}\right]. \tag{5.70}$$

with

$$\gamma_n^{NS} = \gamma_n^{0,NS}\left(\frac{\alpha_s}{2\pi}\right) + \gamma_n^{1,NS}{}_{NLO}\left(\frac{\alpha_s}{2\pi}\right)^2 + \cdots \tag{5.71}$$

and

$$C_{f,n}^{NS}(1,\bar{g}^2) = 1 + \frac{\alpha_s}{2\pi}B_{f,n}^{NS} + \cdots \tag{5.72}$$

for the fermionic, and

$$C_{g,n}^{NS}(1,\bar{g}^2) = \frac{\alpha_s}{2\pi}B_{g,n}^{NS} + \cdots \tag{5.73}$$

for the gluonic Wilson coefficients. The NLO corrections have been calculated within different renormalization schemes. The dependence of the third ingredient, β, that determines the scale dependence of the Wilson coefficients on the scale

and the order of the expansion, will be automatically incorporated by using the running coupling constant.

In leading order ($\gamma^n \propto O(\alpha_s)$) $C_f = 1$ and $C_g = 0$, and the equations (5.69) and (5.70) yield

$$M_i^n(Q^2) = A_n^i C_n^i(1, \bar{g}^2) exp\left[-\int_{\bar{g}(\mu^2)}^{\bar{g}(Q^2)} dg' \frac{\gamma^{n,NS}(g')}{\beta(g')}\right]. \tag{5.74}$$

It is customary to express the unknown Q^2-*independent* matrix elements A^i by the structure function *measured* at an arbitrary Q_0^2, i.e.:

$$M_i^n(Q_0^2) = A_n^i C_n^i(1, \bar{g}^2) exp\left[-\int_{\bar{g}(\mu^2)}^{\bar{g}(Q^2)} dg' \frac{\gamma^{n,NS}(g')}{\beta(g')}\right]_{Q^2=Q_0^2}. \tag{5.75}$$

This can now be inserted into Eq. (5.68) to yield the final result:

$$M_i^n(Q^2) = M_i^n(Q_0^2)\left(\frac{\alpha_s(Q_0^2)}{\alpha_s(Q^2)}\right)^{-\frac{\gamma_n^O}{2\beta_0}}. \tag{5.76}$$

Here O in γ_n^O stands for the observable O. This equation is also often expressed in terms of the variable $t \equiv \ln(Q^2/Q_0^2)$ as

$$M_i^n(t) = M_i^n(0)\left(\frac{\alpha_s(t)}{\alpha_s(0)}\right)^{-\frac{\gamma_n^O}{2\beta_0}}. \tag{5.77}$$

From this equation, in the case of the non-singlet structure function, it follows that in leading order

$$\frac{d}{dt}M^n(t) = -\frac{\alpha_s(Q^2)}{4\pi} \cdot [\frac{1}{2}\gamma_n^{0,NS} + O(\alpha_s)] \tag{5.78}$$

with $\gamma_n^O = \gamma_n^{0,NS}$. Please note, that because of the *complete* factorization of the Q^2-dependence into the Wilson coefficient, the full Q^2-dependence is predicted by QCD and thus constitutes an ideal observable to test this theory. From Eq. (5.70) we see that the Wilson coefficients $C_n^{NS}(\frac{Q^2}{\mu^2}, g^2)$ contain the full QCD prediction for the Q^2 evolution through all three ingredients determining the scale dependence of QCD depending on the order of the expansion. These are the QCD β function governing the running of the coupling, the anomalous dimensions, and the Wilson coefficients $C_n(1, \bar{g}^2)$. As discussed above, the dependence on the β-function is trivially incorporated by applying the running coupling constant at the respective order.

Eq. (5.77) states the prediction of perturbative QCD for the *evolution* of the moments of the structure functions. The *size* of the moments is not fixed by the theory because the A^i cannot be calculated. In the leading twist scenario all soft non-perturbative effects like bound-state effects are contained in $M_i^n(Q_0^2)$. This is called the infrared (IR) factorization property of the structure functions which

holds to all orders and which is an important result of the RG improved QCD. As mentioned in section 5.4, we have described how by applying Renormalization group techniques a change in the *external* momenta, e.g. Q^2, is logarithmically compensated by a change in the moments of the structure functions.

From this discussion we also see clearly why a large lever arm in energy or momentum transfer Q^2 as provided by HERA is so very important in detailed tests of QCD, since over a small finite range of scale, the $1/Q^2$ contributions from higher twists might obscure the logarithmic changes with scale that are predicted in leading twist.

5.5.2 The DGLAP Approach To QCD Evolution

In the light of the discussion of the parton model visualization of structure functions in leading order QCD, it turns out to be also more intuitive to discuss the evolution of the parton distributions which underly the structure functions than to discuss the evolution of the structure functions themselves.

Since the moment of a convolution of two functions is the product of the moments of the functions, one can invert Eq. (5.78) once the function is found whose moments are γ_n^O. This is accomplished by the application of the Mellin transform of the anomalous dimension to *define* the parton splitting function $P(z)$. For the non-singlet structure function this gives

$$-\frac{1}{4}\gamma_n^{NS} = \int_0^1 dz z^{n-1} P_{NS}(z) \tag{5.79}$$

where γ_n^{NS} is the anomalous dimension of the studied process at the given order and e.g. for the parton splitting $q \to qg$ in leading order

$$-\frac{1}{4}\gamma_n^{0,NS} = \int_0^1 dz z^{n-1} P_{q\to qg}(z) \Rightarrow P_{q\to qg}(z) = \frac{-1}{8\pi i}\int_{b-i\infty}^{b+i\infty} dz z^{n-1}\gamma_n^{0,NS}. \tag{5.80}$$

Using the QCD improved parton model decomposition of the structure functions into parton distribution functions (see Eqs. (5.60), (5.21), and (5.22)), the inverse of Eq. (5.78) yields the evolution of the non-singlet structure function and is one of the **Dokshitzer-Gribov-Lipatov-Altarelli-Parisi (DGLAP) equations**, sometimes named GLAP equations, or more commonly just Altarelli-Parisi equations (AP) [127]:

$$\frac{\partial q^{NS}(x,t)}{\partial t} = \frac{\alpha_s(t)}{2\pi}\int_x^1 \frac{dz}{z} q^{NS}(\frac{x}{z},t) P_{q\to qg}(z) \equiv \frac{\alpha_s(t)}{2\pi} q_f \otimes P_{q\to qg} \tag{5.81}$$

with $t = \ln Q^2/Q_0^2$. $P_{q\to qg}$ is the variation of the probability density of finding a quark in a quark with the fraction $z = x/y$ of its momentum.

In **leading order QCD**, in addition to the splitting $q \to qg$, the parton splittings $q \to gq$, $g \to q\bar{q}$, and $g \to gg$ occur and determine parton splitting functions.

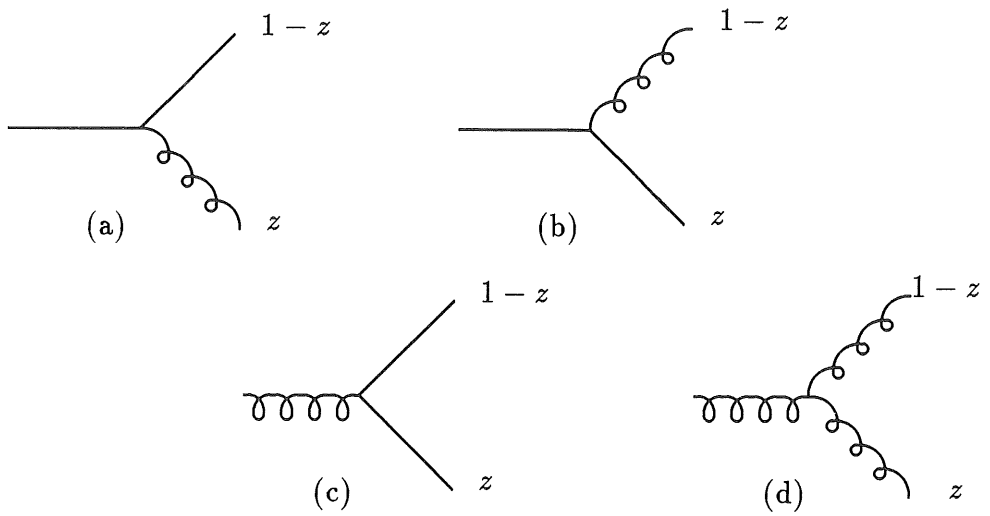

Figure 5.6: Vertices determining parton splitting functions: a) $q \to qg$, b) $q \to gq$, c) $g \to q\bar{q}$, d) $g \to gg$.

These vertices are collected in Fig. 5.5.2. The splitting functions give the probabilities for a quark radiating a gluon (Fig. 5.5.2(a)) such that the quark's momentum is reduced by a fraction z, $P_{q\to qg}$, and equivalently for the other processes. These probabilities can either be calculated from the above Feynman diagrams or through the Mellin transform of the anomalous dimensions and are

$$P^{LO}_{q\to qg}(z) = C_F \frac{(1+z^2)}{(1-z)_+} + 2\delta(1-z) \tag{5.82}$$

$$P^{LO}_{q\to gq}(z) = C_F \frac{1+(1-z)^2}{z} \tag{5.83}$$

$$P^{LO}_{g\to q\bar{q}}(z) = T_R[z^2+(1-z)^2] \tag{5.84}$$

$$P^{LO}_{g\to gg}(z) = 2C_A\left[\frac{z}{(1-z)_+} + \frac{1-z}{z} + z(1-z)\right] + \frac{1}{2}\beta_0\delta(1-z), \tag{5.85}$$

with the group constants of QCD being $C_F = 4/3, C_A = 3$, and $T_R = 1/2$. The regularized function $(1-z)^{-1}_+$ is defined by the so-called *plus prescription*

$$\int_0^1 dz \frac{f(z)}{(1-z)_+} \equiv \int_0^1 \frac{f(z)-f(1)}{(1-z)}. \tag{5.86}$$

'Plus functions' are distributions that are well behaved only when convoluted with a smooth function f that does not diverge as $x \to 1$.

Any structure function can be written as the sum of non-singlet terms of the form $(q_i - q_j)$, where i, j are from $1, \cdots, N_f$, and the singlet distribution $\Sigma = u + \bar{u} + d + \bar{d} + \cdots$. In contrast to the non-singlet distribution where gluon contributions cancel, the evolution of any quark distribution q_i is driven by the $P_{q_i\to q_j g}$ *and* the $P_{g\to q_i\bar{q}_i}$ splitting functions. Since in the $q_i \to q_j g$ splitting the gluon carries no flavour quantum number, i.e.

$$P_{q_i\to q_j}(z) = P_{q\to qg}(z)\delta_{ij}, \tag{5.87}$$

no flavour index appears in the evolution of the general quark distribution. In addition, for massless quarks the $g \to q_i\bar{q}_i$ splitting will also be flavour-independent, and the evolution equation reads

$$\frac{dq_i(x,t)}{dt} = \frac{\alpha_s(t)}{2\pi}\int_x^1 \frac{dz}{z}\left[q_i(\frac{x}{z},t)P_{q\to qg}(z) + g(\frac{x}{z},t)P_{g\to q\bar{q}}(z)\right]. \tag{5.88}$$

With the definition of the singlet function

$$\Sigma(x,Q^2) = \sum_{i=1}^{N_f}(q_i(x,Q^2) + (\bar{q}_i(x,Q^2)) \tag{5.89}$$

we now can also write down the *coupled* A-P equations for the quark singlet (q^S) distribution in the form

$$\frac{d\Sigma(x,t)}{dt} = \frac{\alpha_s(t)}{2\pi}\int_x^1 \frac{dz}{z}\left[\Sigma(\frac{x}{z},t)P_{q\to qg}(z) + 2N_f g(\frac{x}{z},t)P_{g\to q\bar{q}}(z)\right]. \tag{5.90}$$

Of course, also the gluon distribution evolves. Since the gluon is a flavour singlet, it depends on the $q \to gq$ and $g \to gg$ splittings driving the quark singlet and the gluon distribution according to

$$\frac{dg(x,t)}{dt} = \frac{\alpha_s(t)}{2\pi}\int_x^1 \frac{dz}{z}\left[\Sigma(\frac{x}{z},t)P_{q\to gq}(z) + g(\frac{x}{z},t)P_{g\to gg}(z)\right]. \tag{5.91}$$

The herein determined magnitude and x-dependence of the scaling violations of the structure functions F_2 and xF_3 are some of the most solid predictions of QCD and thus allow for a tough test of the theory. Applying the QCD improved parton model, the structure functions at some value of $Q^2 > Q_0^2$ themselves are in leading order the *same as in the parton model* (Eqs. (5.21) and (5.22)) if the evolution from Q_0^2 up to Q^2 is contained in the parton densities. All that is changed in going from the parton model to leading order QCD is that the structure functions and thus the parton distribution functions are now dependent on x *and* Q^2 in the way determined by QCD. *E.g.* F_2 is thus given by

$$F_2(x,Q^2) = \sum_i^{N_f} A_i(\lambda,Q^2)[xq_i(x,Q^2) + x\bar{q}_i(x,Q^2)]. \tag{5.92}$$

Using these equations for $dF^{NS}/d\ln Q^2$ and $dF_2/d\ln Q^2$, with $F^{NS} = xq^{NS}$ the non-singlet, and F_2 the flavour singlet structure function, the test of the QCD prediction can be performed.

For the non-singlet structure function the A-P equations yield *e.g.* the following result: from the definition of the 'plus function' $(1-z)_+^{-1}$ appearing in $P_{q\to qg}$ we get

$$\begin{aligned}\int_x^1 dz f(\frac{x}{z})(1-z)_+^{-1} &= \int_0^1 dz f(\frac{x}{z})(1-z)_+^{-1} \\ &\quad - \int_0^x dz f(\frac{x}{z})(1-z)_+^{-1} \\ &= \int_x^1 dz\left[f(\frac{x}{z}) - f(x)\right](1-z)^{-1} \\ &\quad - f(x)\int_0^x dz(1-z)^{-1}\end{aligned}$$

and thus from Eq. (5.81)

$$\frac{dF^{NS}(x,Q^2)}{d\ln Q^2} = \frac{\alpha_s(Q^2)}{2\pi} C_F \left(\left[\frac{3}{2} + 2\ln(1-x)\right] F^{NS}(x,Q^2) + \int_x^1 \frac{dz}{(1-z)} \cdot \left[(1+z)^2 F^{NS}(\frac{x}{z},Q^2) - 2F^{NS}(x,Q^2)\right] \right). \quad (5.93)$$

This can be compared to measured data if a set of parameters is available which describes the x-dependence found in the data at some starting value $Q^2 = Q_0^2$. In principle, also a value of $\Lambda_{\rm QCD}$ can be determined as e.g. done by the EMC collaboration [130] although $\Lambda_{\rm QCD}$ is not well defined in leading order. We note, however, that in order to use the structure function F_2 in QCD tests, the parametrization of the gluon distribution at some starting value Q_0^2 is needed It is hard to fix the shape of the gluon distribution from the F_2 data because a 'harder' input gluon distribution can be compensated by increasing the value for $\Lambda_{\rm QCD}$. This holds in every order of the expansion. Since this value is still not very well known, it is customary to fix the shape of the gluon distribution through other measurements. The H1 measurements concerning the gluon structure function are discussed in 6.4.

Before discussing some issues on next-to-leading order corrections to the scaling violations derived in the DGLAP picture, we should note that the two approaches to QCD evolution, the renormalization group techniques and the DGLAP approach, of course are equivalent. Knowing the moments of the structure functions and their behaviour under change of scale we can also transform to the structure functions themselves by defining

$$\int dy y^{n-2} f_i(y,Q_0^2) = A_n^i(Q_0^2)$$
$$\int dz z^{n-2} \hat{F}_{ji}(z,Q^2,Q_0^2) = C_n^j(Q^2,Q_0^2). \quad (5.94)$$

With these definitions, Eq. (5.68) becomes a convolution integral

$$F_j(x,Q^2) = a_j(x) \sum_i q_i^2 \int_x^1 \frac{dz}{z} f_i(\frac{x}{z},\mu^2) \hat{F}_{ji}(z,Q^2,\mu^2) + O(\frac{1}{Q^2}) \quad (5.95)$$

with

$$a_2(x) = a_3(x) = a_L(x) = x, \qquad a_1(x) = \frac{1}{2}$$

and $f_i(z,\mu^2)$ the partons densities which **only** in the parton model can be interpreted as the probability of finding a parton i with momentum fraction z in the proton at the initial scale μ^2. $\hat{F}_{ji}(z,Q^2,\mu^2)$ is the cross section for that parton scattering elastically off a virtual photon with four-momentum squared Q^2 which includes the QCD evolution from the scale μ^2 to the larger scale Q^2. The ingredients necessary to determine the calculable part, $\hat{F}$, are the coefficient functions and the parton splitting functions. The $\mathcal{O}(1/Q^2)$ term represents the higher-twist contributions.

It is important to note at this point that the Q^2-dependence is completely factorized in Eq. (5.95) and is *completely* determined by the term calculable within

QCD. On the other hand, the x-dependence *does not* factorize, i.e. the x-dependence of e.g. the structure function $F_2(x, Q^2)$ is determined by both the input parton distribution and the perturbative QCD evolution. This fact prohibits the determination of the QCD-scale $\Lambda_{\rm QCD}$ through the measurement of the evolution of the structure functions alone.

Since gluons radiated from quark lines as depicted in Fig. 5.5 carry away part of the quark momentum the relation $x \leq y$ holds. In Fig. 5.5 also the meaning of Q_0^2 as the factorization scale which defines the point on the ladder where the ladder is cut into the two pieces $f_i(y, Q_0^2)$ and $\hat{F}(\frac{x}{y}, Q^2, Q_0^2)$. Since this point is arbitrary, the measured differential cross section , i.e. the physical structure function will be independent of this scale, *provided* care is taken to define both pieces within the same factorization scheme. This is especially important when using the tabulated parton densities as available from fits to a multitude of data [131, 132, 133] (see 5.6), since different parametrizations for the parton densities have been extracted using different factorization schemes.

Higher Order Corrections

To determine the QCD prediction for the scaling properties in next-to-leading order, first the structure functions have to be evolved using the **leading** order ($\mathcal{O}(\alpha_s)$) coefficient functions, before the next-to-leading order ($\mathcal{O}(\alpha_s^2)$) AP splitting functions can be applied. As briefly discussed in 5.4 only in at least $\mathcal{O}(\alpha_s^2)$ a determination of QCD parameters like $\Lambda_{\rm QCD}$ from the measurement of the scaling violations (Eq. (5.81) and (5.94)) *and* the determination of the structure functions can be performed simultaneously. For a **full** $\mathcal{O}(\alpha_s^2)$ analysis of structure function data, however, the anomalous dimensions, i.e. the AP splitting functions have to be known to $\mathcal{O}(\alpha_s^3)$, and the Wilson coefficients to $\mathcal{O}(\alpha_s^2)$. Whereas for the $\mathcal{O}(\alpha_s^2)$ corrections to the AP kernels were already performed around 1980, the $\mathcal{O}(\alpha_s^3)$ ones are not yet available. The $\mathcal{O}(\alpha_s^2)$ contributions to the coefficient functions have only been calculated recently (see [134] and references therein).

The discussion on higher order corrections thus has to be limited to the next-to-leading order case. For the AP Kernels the $\mathcal{O}(\alpha_s^2)$ corrections have been calculated within several renormalization schemes. As will be anticipated from the above discussion, the mathematical description will get more intricate in this order, but the physical picture, especially regarding the scales pertinent to the problem, gets clearer. In next-to-leading order both the anomalous dimensions and the coefficient functions only pick up an additional $\mathcal{O}(\alpha_s)$ term. The leading order anomalous dimension for the operator is changed according to Eq. (5.71). In the AP picture this corresponds to additional radiation and loop corrections. As an example, the quark splitting function $P_{q\to qg}(z)$ (Eq. (5.79) and (5.82)) changes into [135]

$$P_{q\to qg}(z) = P^{LO}_{q\to qg}(z) + \frac{\alpha_s(Q^2)}{2\pi} P^{NLO}_{q\to qg}(z) \tag{5.96}$$

with $P^{LO}_{q\to qg}(z)$ defined in Eq. (5.82). In addition, the parton distributions have to be evolved according to the leading order AP equation in order to define the

input structure functions . Only then the next-to-leading AP kernels may be applied. This iterative procedure renders the expressions appearing in DIS a little cumbersome.

Applying this procedure, also the quark singlet and gluon distributions can be determined. The A-P equation for the quark distributions of flavour i take on the form

$$\frac{dq_i(x,Q^2)}{d\ln Q^2} = \frac{\alpha_s(Q^2)}{2\pi}\int_x^1 \frac{dz}{z}\Big\{\sum_j\Big[P_{q_i\to q_j g}(z)q_j(\frac{x}{z},Q^2) + P_{q_i\to\bar{q}_j g}(z)\bar{q}_j(\frac{x}{z},Q^2)\Big] + P_{g\to q_i\bar{q}_i}(z)g(\frac{x}{z},Q^2)\Big\} \tag{5.97}$$

with analogous equations for the antiquark and gluon distributions.

For the example of the non-singlet structure function this then yields the structure function itself as

$$\frac{1}{x}F^{NS}(x,Q^2) = q^{NS}(x,Q^2) + \int_x^1 \frac{dz}{z}B^{NS}(z)q^{NS}(\frac{x}{z},Q^2). \tag{5.98}$$

The two steps, the evolution of the parton densities and the above convolution to define the structure function may also be concatinated into a single step. The next-to-leading order evolution of F^{NS} is thus given by

$$\frac{dF^{NS}(x,Q^2)}{d\ln Q^2} = \frac{\alpha_s(Q^2)}{2\pi}\int_x^1 \frac{dz}{z}\Big\{P^{LO}_{q\to qg}(z) + \frac{\alpha_s(Q^2)}{2\pi}\Big[P^{NLO}_{q\to qg}(z) - \frac{\beta_0}{4}B^{NS}(z)\Big]\Big\}F^{NS}(\frac{x}{z},Q^2)$$

with B^{NS} the $\mathcal{O}(\alpha_s)$ term of the NS coefficient function. The F_2 structure function in next-to-leading order takes on the form

$$\frac{F_2}{x} = \int_x^1 \frac{dz}{z}\{\sum_i^{N_f}\Big[(1+\frac{\alpha_s(Q^2)}{2\pi}B^2_{f,2})A_i(\lambda,Q^2)(q_i(\frac{x}{z},Q^2)+\bar{q}_i(\frac{x}{z},Q^2))\Big] + 2N_f\frac{\alpha_s}{2\pi}B^2_{g,2}A_i(\lambda,Q^2)g(\frac{x}{z},Q^2)\}. \tag{5.99}$$

The next-to-leading order correction to the coefficient function, $B^2_{f,2}(x)$, (see Eq. (5.72)), has been determined in the $\overline{MS}$ scheme to be

$$B^2_{f,2}(x) = C_F\left[\frac{1+x^2}{(1-x)}\left(\ln\frac{1-\mathrm{x}}{\mathrm{x}}-\frac{3}{4}\right)+\frac{9+5x}{4}\right]_+ \tag{5.100}$$

and the gluon coefficient function $C^2_{g,2}$ in next-to-leading order becomes

$$C^2_g(x,\bar{g}^2) = \frac{\alpha_s(Q^2)}{2\pi}B^2_{g,2}(x) \tag{5.101}$$

with $B^2_{g,2}(x)$ calculated in the $\overline{MS}$ scheme to be

$$B^2_{g,2}(x) = T_R\left\{(1-2x+2x^2)\ln\frac{1-\mathrm{x}}{\mathrm{x}}+8\mathrm{x}(1-\mathrm{x})-1\right\}. \tag{5.102}$$

Since at HERA and at future accelerators, higher order effects are expected to be visible, future analyses have to be performed to higher than next-to-leading order. In this case, the AP kernels have to be known to $\mathcal{O}(\alpha_s^3)$ and applied to the structure functions evolved with the $\mathcal{O}(\alpha_s^2)$ coefficient functions. For the full $\mathcal{O}(\alpha_s^2)$ expressions of the coefficient functions see [134]. To make full use of the ongoing and future precision experiments the calculation of the $\mathcal{O}(\alpha_s^3)$ AP kernels should be performed.

5.6 Determination of Parton Distributions

According to Eqs. (5.21), (5.22), and (5.26), in the QPM definite *combinations* of parton distribution functions determine the measurable structure functions. Even though in the QCD improved parton model the renormalized parton densities cannot any longer be viewed as the distributions of fractional momenta carried by partons within the proton, the decomposition of the structure functions into **universal** parton 'distribution' functions is still valid.

The procedure to determine these parton densities from experimental data starts out from a parametrization of the x *dependence* of $f_i(x, Q_0^2)$ at some low Q_0^2. The value of Q_0^2 has to be sufficiently large for perturbative QCD to be applicable. These input distributions are then evolved up in Q^2 using the next-to-leading order DGLAP evolution equations. In this way the $f_i(x, Q^2)$ are determined for all values of x and Q^2 for which data are available. Since different data depend on different combinations of the $f_i(x, Q^2)$, a global fit to determine the distributions for the individual flavour distributions and to determine the gluon distribution is performed. Procedures of this type have a long history in DIS. The analyses by Martin et al. (MRS) and Glück et al. (GRV) still based on pre-HERA data may serve as examples [132, 136].

In the MRS analysis, data from NMC and BCDMS on the measurement of $F_2^{\mu p}$ and $xF_3^{\mu n}$ [137, 138], from CCFR on $F_2^{\nu N}$ and $xF_3^{\nu N}$ [139], from WA70 collaboration on prompt photon production [140], on the Drell-Yan process, and from UA2 and CDF on W and Z^0 parameters were used (See [136] for complete references). Based on these data the input parametrizations at $Q_0^2 = 4\,\mathrm{GeV}^2$ of the gluon (g), valence (u_v, d_v), and sea ($\bar{u} = \bar{d} \simeq 2\bar{s}$) are assumed to have the form

$$x f_i(x, Q^2) = A_i x^{-\lambda_i}(1-x)^{\beta_i}(1 + \gamma_i x^{\frac{1}{2}} + \delta_i x) \tag{5.103}$$

where $u \equiv f_u = u_v + u_{sea}, \bar{u} = u_{sea}$ etc., and where the parameters $A_i, \lambda_i, \beta_i, \gamma_i, \delta_i$ are determined by the fit to the data. Not all of these parameters are free in the fit and other constraints are imposed due to sum rules etc.. For details see [136]. Especially the parameter λ_i which is governing the behaviour of the densities as $x \to 0$ for the sea and gluon densities is strongly dependent on the assumed high energy asymptotic behaviour (see 5.3). The two extreme cases are for one the "soft" Pomeron behaviour (valid for $Q^2 \to 0$) which would give $xg, x\bar{q} \sim x^{-\lambda}$

with $\lambda \simeq 0$ (see Eqs. (5.33)), and the other the "hard" or "QCD" or "Lipatov" Pomeron (at $Q^2 > Q_0^2$) (see 5.7) which gives

$$xg, x\bar{q} \sim x^{-\frac{1}{2}}. \tag{5.104}$$

The MRS-D0' and MRS-D-' parametrizations were thus obtained by fixing λ for the gluon and sea distributions to either 0 (D0') or -1/2 (D$^-$'). Fig. 5.7 shows the as an example the u_{sea} distribution of the MRS-D0' and MRS-D-' parton densities at $Q^2 = 20\,\mathrm{GeV}^2$ in the region of x between 10^{-4} and 1. The data which were the basis of these parametrizations only covered the x domain down to about 10^{-2}. The big differences obvious below $x \simeq 10^{-2}$ demonstrate the problem of extrapolating parton distributions into unmeasured kinematical regions (see also Fig. 9.3).

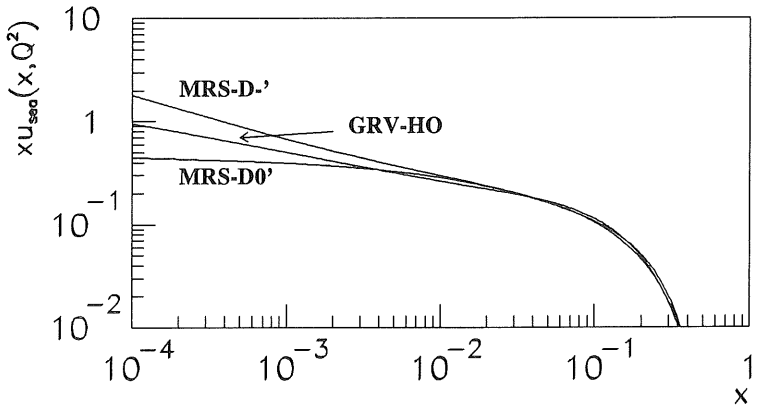

Figure 5.7: The u_{sea} distributions of the MRS-D0', MRS-D$^-$', and GRV-HO parametrizations at $Q^2 = 20\,\mathrm{GeV}^2$.

Although the parametrizations were the results of fits to the same data, significant differences in the magnitude of individual parton densities also already occurr in the region of x were data were available. This is due to the complex composition of the measured data in terms of the parton densities and the different sensitivity of the individual flavours to the data. This will have important consequences for the nucleus-nucleus cross sections relevant for EAS (see 9).

The basis for the determination of parton distributions in the GRV approach is completely different from the MRS (and other) one. In contrast to MRS where the x dependence of the parton densities at large Q^2 are heuristic distributions to be determined from experiment, the GRV determination of the densities is based on a "dynamical model" of these distributions. In this model the parton densities are *generated radiatively* starting from the densities for valence-like distributions and applying standard DGLAP evolution. The input distributions are defined at $Q_0^2 \simeq 0.3\,\mathrm{GeV}^2$. Although this starting scale Q_0^2 could be considered to be well below the applicability of perturbative QCD, starting out with parton distributions having a valence type of behaviour, i.e. vanishing for $x \to 0$, the long evolution path in

Q^2 even up to only Q^2 of about $5\,\mathrm{GeV}^2$ leads to parton distributions showing a singular behaviour as $x \to 0$. With the input distribution of the functional form $x^\alpha(1-x)^\beta$ with $\alpha > 0$ fitted to existing fixed target data, in the GRV ansatz there is very little freedom of choice. The u_{sea} distribution generated thus generated at $Q^2 = 20\,\mathrm{GeV}^2$ is also shown in Fig. 5.7.

5.7 Low x Behaviour of Structure Functions

The parton distributions thus derived from the measurements of structure functions enter into the cross sections of all hard processes with participating hadrons. At the high energies that will be accessible at future colliders like LHC, and that are available in the high energy cosmic neutrino interactions, the low x region of parton distributions give the dominant contribution to the cross sections.

At HERA, of course, one of the most intensively studied subjects is the low x behaviour of the structure functions. The kinematical limit on x only depends on the lowest value of Q^2 measurable in the detectors. At the moment this value is around $5\,\mathrm{GeV}^2$ and thus

$$x_{min} \simeq \frac{s}{Q^2_{min}} \simeq \frac{10^5}{5} = 2 \cdot 10^{-4}.$$

This region is not only new from the experimental point-of-view but it also constitutes a new field for QCD phenomenology that had already been intensively studied before the startup of HERA. This field is again concerned with the high density (high energy) asymptotics of QCD (see 5.3). The main reason behind these renewed activities is that new QCD effects are expected to become experimentally visible at very small values of x.

To discuss these effects we shall start out with investigating the limiting behaviour of the parton densities when $x \to 0$. We shall see that depending on Q^2 different limits are approached. This, of course, cannot be achieved by only the DGLAP evolution equations discussed for large x above. The additional evolution equations which might be already important in the HERA regime are shortly reviewed before the HERA data relevant for this discussion will be shown in the next chapter.

To work out QCD predictions for the small x region is especially difficult because of two reasons. For one, the parton distributions have not been determined in this region but are needed as input for any perturbative prediction. The HERA data on its own are not sufficient to pinpoint all the parton distributions separately (see 5.6). The other reason is that the perturbative expansions for this region of phase space tend to converge very slowly. At large Q^2, the limiting behaviour can be investigated in the **double leading log approximation (DLL)** on the

basis of GLAP evolution. This approximation is given by

$$\alpha_s \log\frac{1}{x} \simeq 1 \qquad \text{and} \qquad \alpha_s \log\frac{Q^2}{Q_0^2} \simeq 1, \tag{5.105}$$

and $\alpha_s \ll 1$, i.e. **both** Q^2 and $1/x$ large.

The leading order splitting functions (Eqs. (5.82) - (5.85)) for $x \to 0$, i.e. $x/y \to 0$ show the limiting behaviour

$$P_{q\to qg}(z) \to C_F \qquad P_{q\to gq}(z) \to C_F \frac{1}{z} \tag{5.106}$$

$$P_{g\to q\bar{q}}(z) \to T_R \qquad P_{g\to gg}(z) \to 2C_A \frac{1}{z}. \tag{5.107}$$

Higher order corrections will be down by powers of α_s/π and not change this limiting behaviour. When inserting these limits into the evolution equations for the quark (Eq. (5.88)) and gluon densities (Eq. (5.91)), we see that at very small x the QCD-evolution of all parton densities will be driven by the $1/z$ singularity of the gluon distribution. The contribution of the singlet distribution to the gluon can thus also be neglected at very small x and the limiting behaviour of the gluon distribution can be determined starting from (see Eq. (5.91))

$$\frac{dg(x,Q^2)}{d\ln Q^2} = \frac{\alpha_s}{2\pi}\int_x^1 \frac{dy}{y} g(y,Q^2) P_{g\to gg}(\frac{x}{y}) g(y,Q^2). \tag{5.108}$$

In the limit $x \to 0$ this becomes

$$\frac{dg(x,Q^2)}{d\ln Q^2} = \frac{3\alpha_s}{\pi}\int_x^1 \frac{dy}{y} y g(y,Q^2). \tag{5.109}$$

Assuming that the input gluon density is non-singular, i.e. $g(x,Q_0^2) \to$ constant for $x \to 0$ it follows that at small x and large Q^2

$$x g(x,Q^2) \sim \exp\left(2\left[\frac{3\alpha_s}{\pi}\ln\frac{Q^2}{Q_0^2}\ln(\frac{1}{x})\right]^{\frac{1}{2}}\right). \tag{5.110}$$

This can also be written as

$$x g(x,Q^2) \sim \exp\left(2\left[\xi(Q_0^2,Q^2)\ln(\frac{1}{x})\right]^{\frac{1}{2}}\right) \tag{5.111}$$

with ξ the "evolution length" in Q^2 space, i.e.

$$\xi(Q_0^2,Q^2) = \int_{Q_0^2}^{Q^2} \frac{dq^2}{q^2}\frac{3\alpha_s(q^2)}{\pi} \tag{5.112}$$

only slowly varying with Q^2. The gluon distribution is thus rapidly rising at small x. This growth is faster than any power of $\ln(1/x)$ but slower than any power of x. This DLL behaviour, i.e. the gluon splitting dominating the evolution, can be pictured as a gluon ladder (when squaring the amplitude) as shown in Fig. 5.7.

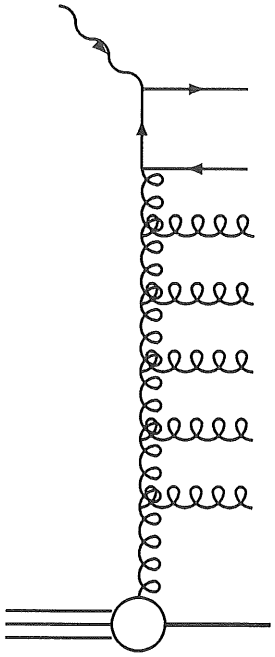

Figure 5.8: Double leading log (DLA) diagram dominating the low x behaviour of the parton density distributions

The result given in Eq. (5.110) corresponds to the asymptotic behaviour that has been calculated in QCD by summing the dominating $\alpha_s \log(1/x)$ and $\alpha_s \log Q^2$ terms in the region of validity of the DLL where both $\log Q^2/Q_0^2$ **and** $\log(1/x) \gg 1$ [141]. If one lifts the restriction of large Q^2, i.e. requires $\alpha_s \log(1/x) \sim 1$ and $\alpha_s \log(Q^2/Q_0^2) \ll 1$, the calculation of the limiting behaviour of the $g \to gg$ splitting function through the calculation of the corresponding anomalous dimension [142, 143] and the subsequent inverse Mellin transform yields for the gluon distribution

$$xg(x, Q^2) \sim x^{-\lambda} \tag{5.113}$$

with $\lambda \simeq 0.5$. This is even more strongly rising for $x \to 0$ than the one of Eq. (5.110). This behaviour of parton distribution is called the "hard" or "QCD" or, after Lipatov who first derived this limit, "Lipatov" Pomeron type of behaviour.

It is interesting and important to note at this point that in a limited (x, Q^2) region about some point $(\bar{x}, \bar{Q}^2)$, the DLL limit in Eq. (5.110) mimics a power law behaviour of the form

$$xg(x, Q^2) \sim x^{-\lambda} \tag{5.114}$$

with

$$\lambda = \left(\frac{36}{b_0} \frac{\ln[\ln(\bar{Q}^2/\Lambda^2)/\ln(Q_0^2/\Lambda^2)]}{\ln(1/\bar{x})} \right)^{\frac{1}{2}} \tag{5.115}$$

where, for $N_f = 5$, $b_0 = 23$ and $\Lambda \simeq 150\,\mathrm{MeV}$ Martin [144] finds for the GRV scale, $Q_0^2 = 0.3\,\mathrm{GeV}^2$, in the lowest x HERA regime ($\bar{x} \simeq 2 \cdot 10^{-4}, \bar{Q}^2 \simeq 10\,\mathrm{GeV}^2$) a value of $\lambda \simeq 0.4$, which increases to $\lambda \simeq 0.48$ for $\bar{x} \simeq 10^{-3}, \bar{Q}^2 \simeq 30\,\mathrm{GeV}^2$. As a

higher input scale Q_0^2 would yield smaller numbers for λ, a value of $Q_0^2 = 2\,\mathrm{GeV}^2$ results in $\lambda = 0.24$ and 0.32 respectively.

How does the evolution equation in the low x region look like? Equivalently to the LLQ^2 resummation of the leading terms with maximal powers of $\alpha_s \log(\mathrm{Q}^2)$ in the large x domain (DGLAP evolution), in the low x region terms with a maximum power of $\alpha_s \log(1/\mathrm{x})$ at each order of the perturbative expansion are not any more subleading due to the $1/x$ singularity and can be accounted for by the resummation technique. The evolution equation was first derived by Balitskij, Fadin, Kuraev, and Lipatov (BFKL) [141, 142, 143, 145, 146] and it resums these terms in the evolution of the gluon density in the **leading log$(1/x)$ (LL$1/x$) approximation**. The transverse momenta along the emission chains are not strongly ordered anymore but instead undergo a random walk type of diffusion, i.e. $k_{\mathrm{T,n}}$ will be close to $k_{\mathrm{T,n-1}}$ but it may be smaller or larger. The reason for this behaviour is, as discussed above, the singularity of the gluon splitting functions. At small x this singularity leads to an enhancement of soft gluon radiation and a breakdown of the strong ordering of the transverse momenta along the initial state radiation ladder discussed in the QCD improved parton model (Eq. (5.61)).

In contrast to the DGLAP equation at large Q^2 and x which gives the evolution of the parton densities integrated over the internal momenta k^2 (with $k^2 = k_{\mathrm{T}}^2$), the BFKL equation, because of the breakdown of the strong k^2 ordering, is based on the unintegrated gluon distribution $f(x, k^2)$ which is related to the conventional (scale dependent) gluon distribution $g(x, Q^2)$ by:

$$x g(x, Q^2) = \int_0^{Q^2} \frac{dk^2}{k^2} f(x, k^2). \tag{5.116}$$

In the LL$1/x$ approximation the unintegrated gluon distribution satisfies the BFKL (or Lipatov) equation [141, 147, 148, 149]

$$\begin{aligned} -x\frac{\partial f(x,k^2)}{\partial x} &= \frac{3\alpha_s(k^2)}{\pi} k^2 \int_{k_0^2}^{\infty} \frac{dk'}{k'^2} \left[\frac{f(x,k'^2) - f(x,k^2)}{|k'^2 - k^2|} + \frac{f(x,k^2)}{\sqrt{4k'^2 + k^4}} \right] \\ &\equiv K_{\mathrm{L}} \otimes f. \end{aligned} \tag{5.117}$$

Here k^2 stands for the transverse momentum squared of the gluons along the ladders. This equation again describes the sum of ladder diagrams like the one depicted in Fig. 6.8 but in contrast to the LLQ^2 approximation leading to DGLAP evolution, the transverse momenta of the gluons along the chain are not ordered anymore.

As discussed above, the $x \to 0$ limit at small or moderate Q^2 corresponds to the high energy ($W^2 \sim Q^2/x$) region for the virtual photon proton cross section which is expected to be dominated by the exchange of the leading Regge pole in the t-channel of the elastic amplitude, the Pomeron. The hypothesis has thus been voiced that the Pomeron reappears in the microscopic theory of strong interactions as a gluon ladder and the BFKL equation can be equated to the **structure of the Pomeron in the LL$(1/x)$ approximation** as depicted in

Fig. 5.7. This Pomeron is accordingly named the BFKL (or Lipatov) Pomeron. The reappearance of the Pomeron in QCD of course has to be expected, since the phenomenology developed in the Regge model did describe the data. The question, whether this perturbative Pomeron is the one observed in the data as a non-perturbative object still has to be answered. More than one Pomeron may exist and the structure of them in terms of partons is not *a priori* fixed. See 5.8 for more discussion on this point.

The above discussion thus forces us to divide the $(Q^2, 1/x)$ phase space into three regions defined through the respective leading logarithmic contributions (L, see Eq. (5.64)) in each order of the perturbation series:

- small $(1/x)$ and $Q^2 \gg Q_0^2$: $L = \log Q^2$, i.e. leading $\log Q^2$ approximation giving rise to DGLAP evolution. This region of phase space is dominated by emission chains with strong ordering in transverse momenta, i.e. $k_{\mathrm{T,n}} \gg k_{\mathrm{T,n-1}} \gg k_{\mathrm{T,n-2}} \gg \cdots \gg k_{\mathrm{T,1}}$ and only kinematical ordering in x, i.e. $x < x_{\mathrm{n}} < x_{\mathrm{in-1}} < x_{\mathrm{n-2}} < \cdots < x_1$ (see Fig. 5.5);

- both $(1/x)$ *and* Q^2 sufficiently large: $L = \log Q^2 \cdot \log(1/x)$, i.e. double leading log approximation leading to the DLL limiting behaviour. An evolution equation has been proposed by Marchesini [148]. In this kinematical region the dominant contributions are from gluon ladders (see Fig. 5.7) where now in addition to the transverse momenta also the fractional momenta x_i are strongly ordered: $x \ll x_{\mathrm{n}} \ll x_{\mathrm{n-1}} \ll x_{\mathrm{n-2}} \ll \cdots \ll x_1$,

- large values of $(1/x)$ and moderate values of $Q^2 (\geq Q_0^2)$: $L = \log(1/x)$, i.e. leading log(1/x) approximation giving rise to BFKL evolution. Here the dominating cascade (a gluon ladder like in Fig. 5.7 follows only a strong ordering in the fractional momenta x_i, i.e. $x_{\mathrm{n}} \ll x_{\mathrm{n-1}} \ll x_{\mathrm{n-2}} \ll \cdots \ll x_1$, whereas the transverse momenta undergo a random walk type of diffusion.

Note, that in the limit $\log(Q^2/Q_0^2) \gg \log(1/x) \gg 1$ the BFKL equation has the same solution as the DGLAP equation for $x \to 0$, i.e. Eq. (5.111). The directions of the respective evolution equations are sketched in Fig. 5.9. The corresponding parton configurations can be visualized as shown in Fig. 5.10. The GLAP and BFKL evolution directions are orthogonal in (x, Q^2) and need very different inputs to the evolution procedure. For illustration consider two points of interest in the kinematical (x, Q^2) plane which are to be reached through QCD evolution. The directions in phase space along which the respective evolution equations evolve the input parton distributions are shown. Shown is also the zone non perturbative physics where non of the evolution equations is applicable. Its border is given by the scale Q_0^2. In the case of the BFKL evolution, the necessary input parton distributions have to be known for a range of Q^2 values at some starting point x_1 and the resulting parton density at the indicated point depends on the input along the indicated line parallel to x_1. In contrast, for the GLAP evolution, the input parton distributions have to be known as a function of x at some starting

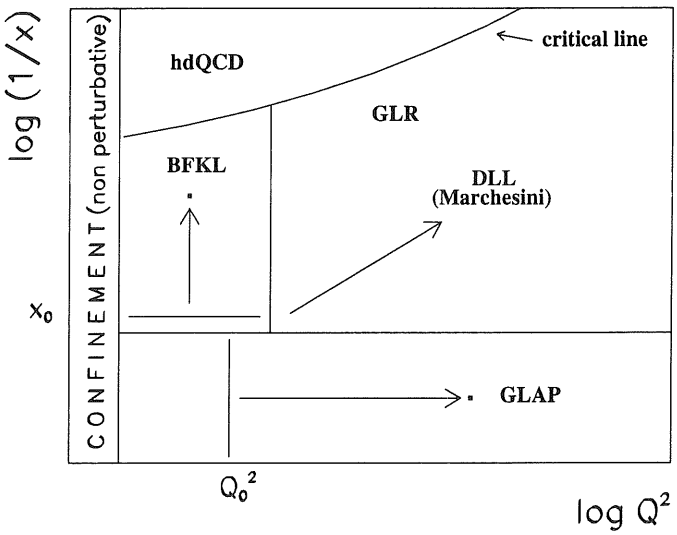

Figure 5.9: Schematics of QCD evolutions

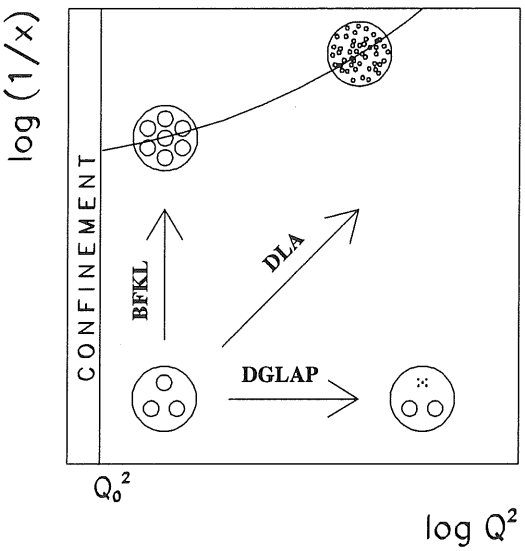

Figure 5.10: Parton configurations in phase space

value $Q_1^2 \geq Q_0^2$ and the evolution progresses along (x, Q^2) trajectories almost perpendicular to the BFKL case, until the point of interest is reached. The evolution into the direction of both large Q^2 and large $1/x$ might be expressible by an evolution equation proposed by Marchesini [148] which treats both large logarithms, $\log(1/x)$ and $\log(Q^2/Q_0^2)$ on equal footing. The discussion on this is still active in the theoretical community. The limiting behaviour of the parton densities in this region, however, can be derived in the DLL approximation.

Also indicated above the "critical line" in this picture is the region of very large $1/x$ and $Q^2 \geq Q_0^2$, above which the density of partons will be too high for the methods of perturbation theory developed for free particles at low densities to be still valid although the coupling constant is still small. None of known evolution equations will apply to this region. This high density QCD (hdQCD) region constitutes a new perturbative QCD-phase. Any knowledge gathered in this region may help us to understand the non-perturbative limit of standard perturbation theory. The knowledge to be gathered in this region is

- to find the region in phase space where we can trust perturbative QCD;
- to find new collective phenomena in QCD;
- to find analytic solutions in the hdQCD region which are non perturbative but are of a simpler form;
- to develop methods for an effective theory of hdQCD.

This region of QCD phase space will naturally be probed in heavy ion collisions and is thus also very interesting for the EAS applications. The signature in DIS on the other hand is also very clear. The presence of the hdQCD phase at low x would be signified by events with a very high multiplicity in the final state.

Before this region in phase space is approached, a phase is envisaged in which the parton density will grow so large that the partons will start to overlap. Let $N(x,Q^2)dx$ denote the number of gluons in a small x-interval around the central value x at the scale Q^2. This number of gluons is related to the gluon density via

$$xg(x,Q^2) = \left| \frac{dN(x,Q^2)}{d\ln\frac{1}{x}} \right|,$$

i.e. it tells us the number of gluons at a definite value of $\ln(1/x)$. By introducing the transverse area occupied by gluons as

$$A(x,Q^2) = \text{const} \cdot xg(x,Q^2)\frac{\alpha_s(Q^2)}{Q^2}$$

we find that the transverse density of gluons

$$\rho(x,Q^2) = \frac{A(x,Q^2)}{\pi R_p^2}$$

with R_p the radius of the proton, at fixed Q^2 will approach and would even get larger than 1 when $x \to 0$.

Long before this happens, individual gluons will start to overlap and cannot any longer be treated as free particles. The effect of overlapping partons is called

shadowing (or screening) and it will limit the pathological growth of parton densities as $x \to 0$. The limit approached for small values of x and/or Q^2 is called the saturation limit $g_{\rm sat}(x,Q^2)$ given by

$$xg_{\rm sat}(x,Q^2) = \frac{\rm const}{\alpha_{\rm s}(Q^2)} R_p^2 Q^2 \tag{5.118}$$

and shows a linear(!) scaling violation ($\sim Q^2$). If the gluons were not uniformly distributed within the proton but would be concentrated around "hot-spots", the limit would be governed by the radius of the hot-spots $R_{\rm h.s.}$ and screening effects would consequently be stronger.

The BFKL equation (5.117) modified by the screening term is called the Gribov, Levin, Ryskin (GLR) equation [149]:

$$-x\frac{\partial f(x,k^2)}{\partial x} = K_{\rm L} \otimes f - \frac{81\alpha_s^2(k^2)}{16R^2k^2} xg(x,k^2)^2 \tag{5.119}$$

with R the size of the gluon concentration region. This equation can also be written in terms of the gluon distribution at x and Q^2 as

$$\frac{\partial^2 xg(x,Q^2)}{\partial \frac{1}{x}\partial Q^2} = \frac{\alpha_s(Q^2)N_c}{\pi} xg(x,Q^2) - \frac{81\alpha_s^2(Q^2)}{16R^2Q^2} xg(x,Q^2)^2. \tag{5.120}$$

The screening term proportional to the square of the gluon density corresponds to ladder diagrams with two merging ladders. The validity of this equation, though, has been questioned [150] and the equation probably has to be modified. The chances at HERA to see the onset of shadowing, even in a hot-spot scenario seem to be small (see e.g. [151]).

In Regge theory, however, the measurement of the cross section of diffraction dissociation is a direct measurement of the screening corrections. This will be discussed in 6.7.

5.8 Soft and Hard Interactions in QCD

In this section we discuss some aspects of the relationship of the Pomeron, describing soft processes, to QCD, describing hard processes, and where HERA can contribute to improve our understanding. Since the Pomeron mostly eluded direct experimental scrutiny in the last 30 years, many different Pomeron scenarios are discussed up to now. Important for EAS generators will be phenomenological representations of the soft Pomeron, i.e. **non-perturbative QCD** determining the elastic, diffractive, and, through the optical theorem, the total cross section. In order to simulate the events dominating the EAS cascades, the minimum-bias events, Pomeron exchange has then to be connected to observable multiparticle final states. Using the AGK cutting rules (see 5.3) this can be realized by using

so-called topological expansions of QCD together with partonic ideas. For some details on how this is realized in the case of the CORSIKA EAS Monte Carlo generator see Chapter 8 where the VENUS model will be reviewed.

At HERA the Pomeron will become visible experimentally in diffractive processes and in the slope of the structure function at low x. In the following we will review some ideas behind some of the Pomeron pictures and prepare for the discussion of the H1 data on diffractive scattering and of the CORSIKA EAS Monte Carlo generator. In the discussion of the H1 results on the diffractive structure function in 6.7 we will come back to the Regge picture of diffraction based on the Pomeron.

Before HERA began its operation, it was anticipated that this unique facility would offer outstanding possibilities to study the process of diffraction and/or diffractive dissociation of the proton and photon and get some understanding of the Pomeron in terms of QCD. The qualitative new aspect of the HERA data compared to the much studied hadronic interactions is the possibility to study diffraction by highly virtual photons.

The quite spectacular diffractive processes observed in very high energy hadron hadron collisions revealed one of the hadrons to survive the interaction almost unscathed with only a small loss in longitudinal momentum, while the rest of the final state looked more or less like a normal inelastic reaction product. The process is thus, *e.g.* in proton-antiproton collisions

$$p + \overline{p} \rightarrow p + X. \tag{5.121}$$

Since the outgoing target proton retains a momentum fraction $x_p > 0.9$ of the initial momentum, the incoming beam antiproton interacts with the residual soft $(1 - x_p)$ component of the incident proton and produces the system X, which has the squared invariant mass $s_X = s(1-x_p)$. This $(1-x_p)$ object that mediates these inelastic (and elastic) diffraction reactions has to have vacuum quantum numbers and has been identified as the Pomeron Regge trajectory. The description of diffractive processes in Regge theory will be discussed in 6.7.

As a first quick overview let us have a look at the list of Pomerons that are around. The main dividing characteristics are perturbative or non-perturbative, "soft" or "hard", and "bare" or "effective" or "physical". Here "soft" labels intercepts smaller than about 1.25, and "hard", intercepts larger than about 1.25. In this way we find

- the "soft" Pomeron which is non-perturbative in origin and is found as the "physical" Pomeron governing the high energy asymptotics,
- the "effective" Pomeron being the result of including higher order screening corrections. This Pomeron has to be contrasted to the "bare" Pomeron which is the basic field of the Regge Lagrangian and is a leading (soft) Pomeron. The "soft" Pomeron thus is an "effective" one.

- the perturbative or "QCD" or BFKL Pomeron discovered in perturbative QCD which is a "hard" (bare) Pomeron, i.e. the leading "hard" Pomeron.

In order to develop an effective theory of diffractive, or more generally, of high energy "soft" processes within the language of QCD, the structure of the Pomeron has to be understood. Independent of a derivation of the Pomeron in QCD, Donnachie and Landshoff and Ingelman and Schlein have proposed physical pictures of the Pomeron that can be applied to data to extract information about the Pomeron structure. Since this picture is the basis for the data analysis on the diffractive structure function presented in Chapter 6, we will start with a short discussion thereof.

5.8.1 The Ingelman/Schlein Pomeron Picture

Ingelman and Schlein [152] proposed to view the Pomeron as a quasi-real particle with a partonic structure. In this case hard scattering phenomena, i.e. jet production should occur in diffractive reactions. To calculate predictions, they assumed factorization such that the cross section would be the product of two independent probabilities. One is the probability to find a Pomeron in the proton in a given state, i.e. the effective structure function of the Pomeron in the proton, the other is the probability for the Pomeron-proton (in proton-proton collisions) reaction, i.e. the cross section for Pomeron-proton hard scattering. To calculate this last cross section an assumption about the internal structure of the Pomeron in terms of parton distributions has to be made. This meant assuming the Pomeron to be a quasi-real object inside the proton with a partonic sub-structure.

With $\sigma_{\mathbb{P}\mathrm{p}}$ denoting the hard scattering cross section for the scattering between a parton in the Pomeron and a parton in the beam proton or anti-proton (or virtual photon in ep scattering) and $\mathrm{x}_{\mathbb{P}} = 1 - \mathrm{x}_{\mathrm{p}}$ the momentum fraction of the proton carried by the Pomeron, the observable cross section can be written as

$$\frac{d^2\sigma}{dx_{\mathbb{P}}\,dt} = F_{\mathbb{P}/\mathrm{p}}(t, x_{\mathbb{P}})\sigma_{\mathbb{P}\mathrm{p}} \tag{5.122}$$

where $F_{\mathbb{P}/\mathrm{p}}(t, x_{\mathbb{P}})$ is the flux factor (or structure function) of the Pomeron, $\mathbb{P}$, in the proton, and t the momentum transferred to the exchanged Pomeron.

Data taken by the UA8 experiment, where jets were observed in the final state of reaction (5.121), showed approximately the expected cross section and were compatible with a hard Pomeron structure [153], i.e. a parton distribution inside the Pomeron of the form $(1-z)$, with z the fraction of the Pomeron's momentum carried by the interacting parton of the Pomeron. This lend some credibility to viewing the Pomeron as a particle within the proton. The partonic structure in terms of quarks or gluons or which mixture thereof could not be resolved.

5.8.2 The Donnachie-Landshoff Pomeron Picture

The Donnachie and Landshoff picture of the Pomeron [154] is one of the basic ingredients of the Ingelman and Schlein model, namely it provides the model for the Pomeron structure function $F_{\mathbb{P}/\mathrm{p}}(t, x_{\mathbb{P}})$. The basis is the observed $s^{0.08}$ rise of the total hadron-hadron cross section being produced by the exchange of single "soft" Pomerons, i.e. the one with the intercept 1.08. Donnachie and Landshoff also observe that the total cross section for photon-proton scattering (see chapter 7) can be well described by the sum of a term proportional to $s^{0.08}$ and a term proportional to $s^{-0.45}$ corresponding to the intercept from (ρ, ω, f_2, a_2) exchange (see 5.3).

In their derivation of the Pomeron structure function, they find that the hadron collider data on elastic scattering and diffractive dissociation can be well described by supposing the soft Pomeron to be similar to photon exchange with the charge replaced by a constant Pomeron coupling $\beta_0 \simeq 2\,\mathrm{GeV}^{-1}$ and the photon propagator by a term $(\alpha' s)^{\alpha(t)-1} \cdot \xi_{\alpha(t)}$, where $\alpha(t) = \alpha(0) + \alpha' t$ is the Pomeron trajectory with $\alpha(0) = 1.08$, $\alpha' = 0.25\,\mathrm{GeV}^{-2}$, and $\xi_{\alpha(t)}$ a phase factor. By considering the diffractive structure function of the proton $F_2^D(x, Q^2)$ to be the part of F_2^p where the proton retains a large part of its initial momentum $1-\xi$ in a scattering with momentum transfer t, one can simply define $F_2^D = F_2^{D(4)}(x, Q^2, \xi, t)$ without introducing the Pomeron.

With now interpreting this expression in terms of Pomeron exchange with momentum fraction $x_{\mathbb{P}} = \xi$, this expression is of leading twist nature, i.e. only varying slowly with Q^2, and thus factorizes into a Pomeron flux factor and a Pomeron structure function

$$\frac{d^2}{dt dx_{\mathbb{P}}} F_2^D(x, Q^2, x_{\mathbb{P}}, t) = F_{\mathbb{P}/\mathrm{p}}(t, x_{\mathbb{P}}) F_2^{\mathbb{P}}(\beta, Q^2, t) \tag{5.123}$$

with

$$\beta = \frac{x}{x_{\mathbb{P}}}$$

and

$$F_{\mathbb{P}/\mathrm{p}}(t, x_{\mathbb{P}}) = \frac{9\beta_0^2}{4\pi^2} [F_1(t)]^2 x_{\mathbb{P}}^{1-2\alpha(t)} \tag{5.124}$$

with F_1 the Dirac elastic form factor of the proton.

With the Pomeron resembling the photon, Donnachie and Landshoff assume a quark structure function for the Pomeron of the form

$$\beta q_{\mathbb{P}}(\beta) = C\beta(1-\beta) \tag{5.125}$$

and predicted that about 10% of the HERA DIS events should be of diffractive nature [155].

Although the Pomeron is not a particle, with the factorization performed such that the Pomeron structure function is of leading twist nature, scaling violations

just like discussed for the parton densities in the proton should be observable for the parton densities in the Pomeron if the HERA experiments can extract the Pomeron structure function from the data. This will be discussed in 6.6.

5.8.3 The BFKL Pomeron

The basis for the hope of understanding the Pomeron within QCD was developed by discovering a perturbative equation which when solved might describe the perturbative QCD Pomeron. With the BFKL equation determining the amplitude for n-gluon production in the so called multireggeon kinematical region, i.e. low x and high parton densities, this Pomeron turns out to be a perturbative gluon ladder exchange with the ladder diagrams an effective representation of a huge set of Feynman diagrams. In this respect it is already similar to the topological expansions of QCD which so far have been at the heart of phenomenological models of the Pomeron.

Due to the high gluon density and the random walk distribution of the transverse momenta along the ladders touching upon the non-perturbatively small k_T region, the solution of the perturbative BFKL equation is basically non-perturbative. Hopes are therefore high that by studying this equation in deep theoretical depth something can be learned about the transition from perturbative to non-perturbative QCD and consequently about the non-perturbative soft Pomeron.

In the language of Regge theory, the QCD Pomeron appears in the leading logarithmic approximation as a composite object made up out of two reggeized gluons. The solution of the BFKL equation (5.117) by integrating over all k_T values was found to behave as $x^{\sim -0.5}$. With the dependence of F_2 on the Pomeron intercept to be of the form $x^{1-\alpha(0)}$ [156], this means the BFKL Pomeron exhibits an intercept of ~ 1.5 and is thus a "hard" Pomeron compared to the "soft" Pomeron with an intercept of 1.08. The very singular behaviour of the QCD Pomeron is valid for asymptotic energies. We thus expect to observe this behaviour only after a long QCD evolution. The slope of the hard Pomeron's trajectory is found to be approximately zero in the leading logarithm approximation.

What is the relationship of the QCD Pomeron to the non-perturbative one? Will the solution of the BFKL equation yield smaller values for the intercept if the k_T^2 integration region is restricted to a more physical range, i.e. not arbitrarily small values? Is there more than one Pomeron? Do they add or will one find a smooth transition from one to the other at increasing Q^2? These and other questions are at the moment very actively pursued by the theoretical community.

There have been various theoretical attempts to understand the physical content of the BFKL equation. In addition, other investigations have succeeded in deriving BFKL type equations based on other ansätze. We just mention the ones by

Mueller [157] and by Nikolaev, Zakharov and Zoller [158] which are based on a colour dipol picture of high energy hard processes.

The Mueller Approach to the BFKL Equation

Mueller's approach [157] to investigate the content of the BFKL equation was to calculate the small x infinite momentum partonic wavefunction of a hadron in QCD. He finds that if the number of colours, N_c, in the hadron is big enough, each gluon can be regarded as a $q\overline{q}$ pair, i.e. a system of colour dipols. As a consequence, since at high energy a hadron contains a large number of soft gluons, i.e. colour dipols, the scattering cross section can be understood in terms of the product of the number of dipols in target and beam times the cross section for dipol-dipol scattering due to two gluon exchange. The Pomeron is thus found to be a two gluon exchange.

This cross section grows rapidly with energy because the number of dipols N_c grows approximately as $x^{-1/2}$. When N_c becomes large multiple scatterings have to considered as well, i.e. multiple Pomeron exchange. The physical meaning of the predicted growth of F_2 at $x \rightarrow 0$ is thus due to an increasing number of "wee" partons that can interact.

When comparing this large number of "wee" gluons to the number of gluons giving rise to jet production in hadron-hadron collisions, one finds that the number of "wee" partons is much larger than the number of incoherently acting ones. The number of incoherently acting gluons can e.g. be estimated by calculating the ratio of the jet production cross section to the total cross section at small x. This behaves as $\alpha_s \ln(1/x)$ and rises much slower than $x^{-0.5}$. A conclusion that one can draw from this observation is that in a typical inelastic event the partons thus are in a very coherent state.

The NZZ BFKL Pomeron

Nikolaev, Zakharov and Zoller (NZZ) [158] derived an generalized BFKL equation for the scattering cross section of a colour dipole. In their model the process of diffractive dissociation is described as a fluctuation of the virtual photon into a $q\overline{q}$ or $q\overline{q}g$ Fock state and the interaction proceeds via the exchange of dipol radiation off of this coloured system taking on the form of the BFKL type Pomeron. The derived BFKL type equation is not identical to the original one and in this picture, the Pomeron can be thought of as the coherent emission of gluons from the virtual $q\overline{q}$ dipol, and the BFKL emission in DIS as the incoherent part. This model effectively already mixes soft and hard "Pomeron" behaviour and as an important consequence it is non-factorizable.

5.8.4 Connecting Soft and Hard Interactions

The total cross section for hadron-hadron collisions is composed of several components. The dominating one is the soft contribution not calculable within perturbative QCD. The soft component consists of an elastic contribution, a single (beam) and double (target and beam) diffractive one, and an inelastic contribution with typical momentum scales below the applicability of perturbative QCD. The other contribution to the total cross section, the hard scattering contribution, can be calculated within QCD above typical momentum scales of $\mathcal{O}$(GeV). At large CMS energies it is customary to devide the hard contribution into a dominating semi-hard and a hard component. The distinction is made based on the ratio of momentum transfer to CMS energy. If $Q^2/s \to 0$ we call the contribution semi-hard; if $Q^2/s \to 1$ it is a hard contribution.

The semi-hard contribution can experimentally be observed as mini-jet production in hadron-hadron collisions [159]. Mini-jets are characterized by relatively large transverse momenta, i.e. $p_T > 3-4\,\mathrm{GeV}$, but only a very small longitudinal momentum fraction x in accordance with the above characterization of semi-hard events. The QCD picture of mini-jet production is the hard scattering of two soft partons within the colliding hadrons. The inclusive cross section for jetproduction can be calculated within perturbative QCD as

$$\sigma_{\mathrm{incl}}^{\mathrm{QCD}} = \sum_{\mathrm{i,j}} \int_0^1 dx_1 \int_0^1 dx_2 \int_{p_{\mathrm{T,min}}^2}^{p_{\mathrm{T,max}}^2} d\hat{t} \frac{1}{1+\delta_{\mathrm{ij}}} \frac{d\sigma_{\mathrm{QCD,ij}}}{d\hat{t}} f_{\mathrm{i}}(x_1, Q^2) f_{\mathrm{j}}(x_2, Q^2) \quad (5.126)$$

where $f_{\mathrm{i}}(x, Q^2)$ are the parton density functions for flavour i and scale Q^2. The important cutoff parameter is $p_{\mathrm{T,min}}^2$ determining the border of validity of perturbative QCD. The main contributing partonic processes are a function of CMS energy. At low energies all processes, i.e. qq, qg, and gg contribute more or less equally, whereas at high CMS energies the gg process dominates due to the soft gluons playing the dominant rôle in the low x region of phase space. The mini-jet multiplicity is a steeply rising function of CMS energy due to strong increase of the number of gluons at low x as expected in perturbative QCD and as corroborated by the H1 measurement which we will discuss in 6.4.

The increase of the mini-jet cross section can thus be accounted for by hard gluon-gluon scattering at low x with the assumption that the gluon density grows for $x \to 0$ as given in Eq. (5.110). The region of x probed in EAS reactions at $\sqrt{s} \approx 1\,\mathrm{TeV}$ can be estimated as

$$x \approx \frac{p_{\mathrm{T,min}}}{\sqrt{s}} \approx 10^{-3}$$

with $p_{\mathrm{T,min}}$ taken as $1\,\mathrm{GeV/c}$. This is where HERA data will probe the gluon density in the proton. Since at very high energies the average interaction will be mini-jet production, these are thus very important measurements for EAS applications and will be presented below.

There have been speculations, that all of the observed continuous rise of total cross sections may in fact be due to mini-jet production. But since the total cross section did not change its energy dependence at the CMS energies where mini-jet production was observed, this was heavyly disputed. One group is arguing that the onset of mini-jet production, however, may occur long before they become experimentally visible and it may well drive the total cross section starting at very low energies. Others argued that the mini-jet cross section did not contribute to the total cross section, i.e. even without the production of mini-jets in the final state there was an interaction, either soft or by other jets or mini-jets and must thus be exclusively a multiple scattering reaction.

The adequate procedure to ensure unitarity and to unite the different contributions to the scattering amplitude if the possibility of multiple interactions exist, as in the case of colliding complex objects, is given by the eikonal method in the impact parameter representation. In eikonalized scattering models soft, semi-hard, and hard components may be easily incorporated through different contributions to the eikonal. The EAS Monte Carlo generators are based on this scattering model (see chapter 8). In this model, the elastic cross section can be calculated and the total cross section derived from the optical theorem. In the eikonal approach the elastic amplitude can be expressed as

$$T = \frac{2is}{C} \int d^2b \quad e^{i\mathbf{k}\cdot\mathbf{b}}[1 - e^{-C\chi(b,s)}] \tag{5.127}$$

with the eikonal $\chi(b,s) = \mathrm{Re}(\chi(b,s))$ for the impact parameter b and CMS energy s and a constant C to be determined from the data. The elastic cross section then is given by

$$\sigma_{\mathrm{el}} = \int d^2b[1 - e^{\chi(b,s)}]^2,$$

the total cross section by

$$\sigma_{\mathrm{tot}} = \int d^2b \cdot 2[1 - e^{-\chi(b,s)}],$$

and the inelastic cross section turns out to be

$$\sigma_{\mathrm{in}} = \int d^2b[1 - e^{-2\chi(b,s)}].$$

The construction of the eikonal determines the size and energy dependence of the respective contributions to the scattering cross section. It may be constructed as

$$\chi(b,s) = \chi_{\mathrm{soft}}(b,s) + \chi_{\mathrm{hard}}(b,s) \tag{5.128}$$

where the soft eikonal is determined by Pomeron exchange and the hard eikonal by QCD.

In most EAS generators the ansatz for the soft eikonal is

$$\chi_{\mathrm{soft}}(b,s) = \frac{1}{2}A(b) \cdot \sigma_0(s) \tag{5.129}$$

with the function $A(b)$ the overlap function of partons in the two hadrons

$$A(b) = \int d^2b' \rho_i(b') \rho_j(|\vec{b} - \vec{b'}|) \quad \text{with} \quad \int_0^\infty d^2b A(b) = 1. \tag{5.130}$$

and with $\rho(b)$ the overlap density taken to be energy independent and $\sigma_0(s)$ calculated from Regge theory as

$$\sigma_0(s) = g^2 s^{\alpha(0)-1} \tag{5.131}$$

with g the effective Pomeron-proton coupling and the intercept $\alpha(0)$ also taken to be energy independent. The hard eikonal is dominated by the semi-hard component and constructed as

$$\chi_{\text{hard}}(b, s) = \frac{1}{2} A(b) \cdot \sigma_{\text{incl}}^{\text{QCD}}(s) \tag{5.132}$$

with $A(b)$ as above and $\sigma_{\text{incl}}^{\text{QCD}}(s)$ taken from Eq. (5.126).

When using the inclusive mini-jet cross section as formulated above, the hard eikonal at high energies where gluon-gluon interactions dominate, is determined by one gluon-ladder exchange and the energy dependence of the cross section thus

$$\sigma_{gg}(\hat{s}, Q_0^2) \sim s^{\Delta_{\text{hard}}}$$

with Δ_{hard} the intercept of the hard QCD Pomeron. In reality we will have to consider also multi-ladder exchange processes, i.e. an effective hard intercept smaller than 0.5. The same applies to the soft Pomeron. Its energy dependence due to screening corrections and potential changes of $A(b)$ with energy have to be incorporated into the models. The relative importance of the two eikonals will thus be a function of energy with the hard eikonal taking on the dominant rôle at very high energies. The functional form, which is all-important for extrapolations from accelerator energies to the highest EAS energies, however, needs input from measurements. Note, that the influence of the uncertainties of the hard contribution on the total cross section are reduced in the eikonalisation procedure whereas the weight of individual final state channels is influenced strongly.

In the case of EAS generators, this is where the HERA data gave and will continue to give their main contribution to the field of EAS experiments through the measurements of the importance of the QCD Pomeron relative to the soft one. These measurements will *e.g.* determine the effective power Δ_{hard} in an energy region important for EAS applications. In addition the nature of the hard Pomeron has to be resolved. The knowledge gained at HERA is going to be incorporated into the VENUS generator reviewed in chapter 8. We will come back to the HERA influence on the EAS generators in chapter 9 after the presentation of some relevant H1 physics results in the next two chapters.

5.8.5 The Total Proton-Air Cross Section

One of the most important measurements for EAS Monte Carlos is the total cross section for the interaction of CR with air. Here HERA will contribute indirectly

through the measurement of parton densities and effective Pomeron intercepts as discussed below. The cross section for proton-air scattering can be directly inferred from the measurement of the total pp cross section at *e.g.* the Tevatron. This argument can also be turned around, and the total pp cross section might in principle be derived from a measurement of the $p - air$ cross section in an EAS experiment. This has been done based on measurements by the AKENO EAS [160, 162] and the Flye's Eye experiment [165]. In these derivations of $\sigma_{\mathrm{p-air}}$, the measured attenuation length, $\Lambda(E_0)$, of showers of energy E_0 in the atmosphere, is related to the nucleon interaction length, $\lambda_N(E_0)$, and the absorptive $p - air$ cross section is extracted via

$$\lambda_N(E_0) \propto \frac{1}{\sigma_{\mathrm{abs}}^{p-air}}, \tag{5.133}$$

where the proportionality is fixed by modelling the hadronic interactions and the incident particle spectrum is either assumed to be dominated by protons or in the event selection a proton dominated sample is prepared. In the AKENO analysis [162] the energy E_0 is obtained from the number of observed muons, the absorption length $\lambda_N(E_0)$ from the number of recorded muons and electrons, and the observed cross section is then extracted according to the modelled relation between $\lambda_N(E_0)$ and $\sigma_{\mathrm{p-air}}$.

From the thus determined value for $\sigma_{\mathrm{p-air}}$ the total pp cross section may be derived. The basis for this is the Glauber model [166] in which the inelastic pp cross section can be related to the absorptive cross section σ_{abs} measured in EAS experiments. See *e.g.* [64]. Here

$$\sigma_{\mathrm{abs}} = \sigma_{\mathrm{tot}} - \sigma_{\mathrm{el}} - \sigma_{\mathrm{Qel}} - \sigma_{\mathrm{diff}} - \Delta\sigma \tag{5.134}$$

where σ_{el} is the elastic, σ_{Qel} the quasielastic cross section where an elastic scattering is followed by an excitation of the target nucleus without meson production which leaves the incident proton in the primary flux, σ_{diff} the diffractive cross section, and $\Delta\sigma$ a screening correction [161].

In the latest AKENO analysis [162], the measured relation

$$\sigma_{\mathrm{abs}}^{p-air} = 290(E/1\,\mathrm{TeV})^{0.052} \quad \mathrm{mb} \tag{5.135}$$

in the energy interval $10^{16.2} - 10^{17.6}\,\mathrm{eV}$ is transformed into the cross section for pp scattering using Glauber theory under the assumption of geometrical scaling [163]. The result is

$$\sigma_{\mathrm{tot}}^{pp} = 38.5(E/1\,\mathrm{TeV})^{0.091} \quad \mathrm{mb}. \tag{5.136}$$

or

$$\sigma_{\mathrm{tot}}^{pp} = 38.5 + 1.37 \cdot \ln^2(\sqrt{s}/10\,\mathrm{GeV}). \tag{5.137}$$

When using this expression for calculating the pp cross section at $\sqrt{s} = 10^4\,\mathrm{GeV}$ we get $\sigma_{pp}^{\mathrm{tot}} = 104\,\mathrm{mb}$. This can be compared to the fit by Donnachie and Landshoff using the "soft" Pomeron intercept of 1.0808 (see 5.4) which results in $\sigma_{pp}^{\mathrm{tot}} =$

96 mb. The AKENO result is thus compatible with a continued constant "soft" Pomeron intercept driving the total cross section.

Regarding the form of the applied Glauber formula strong doubts about the validity of the AKENO ansatz have been raised by Nikolaev [164] who applies a different ansatz and arrives at significantly larger pp cross sections more compatible with a "hard" effective intercept between 1.2 and 1.3. Another grain of salt has to be added, since also the Monte Carlo program used at these high energies to extract the *p-air* cross section might have significant problems as will be obvious when we discuss the HERA data and their influence on EAS simulation in chapter 9.

This influence on EAS results however could well be a common problem of the field. The use of more than Monte Carlo generator when performing acceptance corrections or when extracting physics parameters as is common practice in high energy accelerator experiments should be considered by all EAS experiments. The EAS data might thus in principle extract very valuable physics parameters from which the very high energy cross sections might be inferred. The systematic problems are however not all solved, yet.

5.8.6 Remarks

At the end of this discussion of the Pomeron picture we here just want to summarize again some of the main ideas.

Not necessarily there has to be only one Pomeron with an intercept close to 1 as derived from the σ_{tot} measurements. Also discussed are cases where the bare single Pomeron intercept is larger than 1 and due to Pomeron cuts, i.e. multiple Pomeron exchanges, the "effective" intercept measured in the data is generated [187]. We also should mention the possibility that the QCD Pomeron could be the only bare Pomeron and all that is needed in the future is to understand higher order corrections to it. In another scenario there are two Pomerons, the "hard" one with an intercept around 1.5 and the "soft" one with an intercept around 1.0 which mix to yield the observed cross section dependence [167].

The Pomeron picture apparently is not a very easily digestable one. Let us now turn to the H1 data on the structure of the proton and the Pomeron and see what we have learned at HERA.

Chapter 6

Selection of DIS Measurements

In this chapter we will discuss a selection of measurements performed with the H1 detector at HERA. We will discuss the measurement of the F_2 structure function of the proton at low x, the extraction of the gluon density, the measurement of the charged current cross section, the measurement of topological variables with the aim to distinguish between BFKL and DGLAP phase space, and the measurements concerning the structure of the Pomeron.

6.1 Discriminating Observables at low x

What are the observables available to discriminate between the QCD phase space regions discussed in 5.7? What are the predictions for the HERA kinematical regime?

6.1.1 Inclusive Cross Section

To determine these predictions, the respective evolution equations have to be solved.

For the DGLAP equation this is easily achieved. As discussed in 5.6 and 5.7 one needs to define a phenomenological input distribution at some starting value Q_0^2 and then apply the DGLAP evolution equations. A singular behaviour of the gluon and sea densities can then be obtained by either starting out with a singular distribution (*e.g.* MRSH starts out with $x^{-0.3}$), or by having a long evolution path when starting the evolution at very small Q_0^2 (GRV starts out with valence-like distribution at $Q_0^2 \simeq 0.3\,\mathrm{GeV}^2$ and ends with a $x^{-0.4}$ to $x^{-0.45}$ in the HERA regime).

In case of the BFKL equation, the work on its solutions and interpretations thereof are still very much in progress. A standard technique to obtain a solution of the BFKL equation (Eq. (5.117)) is by step-by-step integration down in x from an input distribution $f(x_0, k_T^2)$ at some moderate $x_0 \simeq 10^{-2}$ determined from a gluon distribution of a standard set of parton densities. Without shadowing effects the characteristic BFKL behaviour $f(x, k_T^2) \sim x^{-\lambda}$ is found to set in soon when going down in x.

The prediction for F_2 following from the BFKL equation is

$$F_2(x, Q^2) = \int_x^1 \frac{dx'}{x'} \int \frac{dk_T^2}{k_T^4} f(\frac{x}{x'}, k_T^2) F_2^0(X', k_T^2, Q^2) + F_2^{bg}(x, Q^2) \qquad (6.1)$$

where x/x' is the fraction of the longitudinal momentum carried by the gluon coupling to the $q\bar{q}$ pair (see Fig. 5.7) and F_2^0 giving the contribution of the quark box to the photon-gluon fusion subprocess (for details see [168]). A slowly varying, non-BFKL "background" contribution F_2^{bg} has to be added in the region of not too small x. Only for $x \sim 10^{-4}$ is the BFKL evolution expected to describe the data without this term.

The predicted x dependence of F_2 at low Q^2 is $F_2 \sim x^{-\lambda}$ with $\lambda \simeq 0.5$. This value for λ was found to only weakly depend on the infra-red cutoff k_0^2 (see Eq. (5.117)) and to be independent of Q^2. Incorporating higher order corrections like shadowing or sub-leading contributions will tend to decrease λ.

In addition, the dependence on Q^2 can be derived from the k_T^2 dependence of $f(x, k_T^2)$ in Eq. (6.1). A $(Q^2)^{\frac{1}{2}}$ dependence was derived from the BFKL equation without shadowing [168]. This is valid at low x and moderate Q^2 and has to be compared to the $\log Q^2$ behaviour of DGLAP evolution. Shadowing effects and higher order effects will tend to slow the stronger BFKL Q^2 evolution. These calculations, where the authors calculated the x dependence of F_2 and its Q^2 behaviour once without shadowing (AKMS1) and once with a hot-spot shadowing scenario (AKMS2), can be compared to HERA measurements (see 6.2).

6.1.2 Exclusive Measurements

The evolution equations need *non-perturbative* input distributions. DGLAP evolution may thus be made to predict the same behaviour of F_2 at low x as the BFKL equation by choosing a singular input. At the same time, DGLAP evolution started at very low Q_0^2 with valence-like inputs does also predict a singular behaviour of the parton densities. To discriminate between DGLAP and BFKL phase space thus less inclusive observables have to be studied. This is attempted although both DGLAP and BFKL are only valid for inclusive processes, since it is hoped that entering a region in QCD phase space where a new evolution equation is valid will leave some footprint in exclusive final states.

Possibly discriminating observables can make use of the other outstanding characteristics of QCD in the BFKL phase space. The transverse momenta of the gluons making up the ladder rungs are not strongly ordered in contrast to DGLAP phase space. This leads to cross section growing as $(x/x')^{-\lambda}$ with (x/x') the longitudinal momentum fraction of the gluon dissociating into a $q\overline{q}$ pair at the upper end of the gluon ladder. This can be exploited in studies of

- Transverse energy flow in DIS events,
- DIS events with characteristic jets,
- Pairwise mini-jet production.

Transverse Energy Flow

The breakdown of strong k_{T} ordering will lead to an enhancement of gluon radiation into the region between the current jet and the proton remnant compared to DGLAP evolution. This can be detected by measuring the transverse energy flow (E_{T} flow) as a function of rapidity. Analytic calculations at the parton level have been performed [169] and can at least qualitatively be compared to the data.

Events with Measured Jets

This observable was proposed by Mueller [170] to directly probe the breakdown of the strong k_{T} ordering and to directly identify λ! These events contain a measured jet which satisfies (i) the transverse momentum of the jet is $k^2_{\mathrm{Tj}} \simeq Q^2$, (ii) the longitudinal momentum of the jet x_{j} is as large as experimentally possible, and (iii) $z = x/x_{\mathrm{j}}$ is small. The first requirement suppresses QCD radiation in the DGLAP evolution regime by closing the evolution window while the third requirement will in the BFKL regime lead to an enhancement of gluon radiation cross section and hence an enhancement of jet production.

Pairwise Minijets

Mueller and Navelet [171] proposed to search for an enhancement in the pairwise production of mini-jets at low x. According to their calculation the cross section should grow as $\exp(\lambda\Delta y)$ with $\Delta y = \log(\mathrm{x}/\mathrm{x}')$ the rapidity difference between the two jets. Since this effect has to be folded with the parton densities to determine experimental cross sections, it might be tough to disentangle it from the x dependence of the parton densities. Another proposal is to study the correlation of the azimuthal angles of the jets. The BFKL prediction is a weakening of the back-to-back correlation expected in DGLAP phase space.

6.1.3 The Diffractive Structure Function

An important observable at HERA turns out to be the diffractive structure function F_2^D. This is the differential cross section for DIS with no colour connection observed between the struck hadronic system and the remnant of the proton which continues down the beam pipe in the incoming proton's direction. The importance of this measurement for the investigation of the Pomeron structure within QCD has been mentioned in 5.8 and will be discussed in 6.6.3 and 6.7.

We will in the following first discuss the measurements of F_2 in the low x region and the investigation of the topological variables to discriminate DGLAP and BFKL evolution. After that we will turn to the measurement of F_2^D and the determination of the Pomeron structure from the data.

6.2 Measurement of F_2 at HERA

Taking the electroweak and QCD corrections into account, the F_2 structure function can be determined in the HERA experiments on DIS. At fixed CMS energy the inclusive scattering cross section is determined by any two variables selected from x, Q^2 and y. For the majority of the events recorded in the HERA experiments Q^2 is less than $1000\,\mathrm{GeV}^2$. The exchange of the Z^0 in the neutral current reaction and the charged current reaction may thus be neglected at low and moderate Q^2.

The double differential cross section in terms of x and y for neutral current photon exchange can be related to the measurable structure functions by [172, 173]:

$$\frac{d^2\sigma(\gamma)}{dxdy} = \frac{4\pi\alpha^2}{sx^2y^2}[(1-y+\frac{y^2}{2})F_2(x,Q^2) - \frac{y^2}{2}F_\mathrm{L}(x,Q^2)] \tag{6.2}$$

or in terms of x and Q^2 by

$$\frac{d^2\sigma(\gamma)}{dxdQ^2} = \frac{4\pi\alpha^2}{xQ^4}[(xy^2F_1(x,Q^2) + (1-y)F_2(x,Q^2)] \tag{6.3}$$

where the upper (lower) signs corresponds to $e^-(e^+)p$ scattering. The HERA accelerator and the H1 detector are described in 4. The large imbalance of the electron(positron) and proton momenta (27 and 820 GeV/c, respectively) and the electroweak radiative corrections strongly varying over the phase space lead to specific experimental difficulties in reconstructing the event kinematics in certain regions of the phase space. The radiative corrections affect the electron and proton variables to differing degrees. Each of the two variables needed to determine the kinematics may thus be taken from either the scattered electron or from the struck hadronic system depending on the event kinematics itself. Fig. 6.1 shows one neutral current DIS event as recorded in the H1 detector. The measured quantities are the four-momentum of the scattered electron

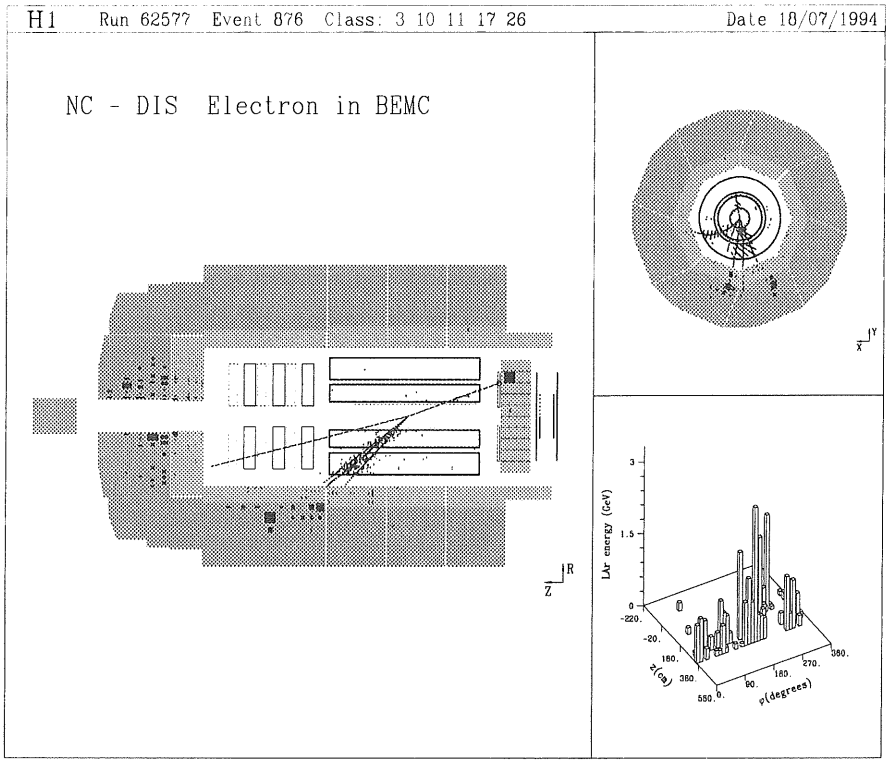

Figure 6.1: Example of a neutral current deep inelastic scattering event in the H1 detector. The electron is detected in the BEMC calorimeter, the hadronic final state in the main liquid argon calorimeter and central tracker.

$e' = (E'_e \sin\Theta_e, 0, E'_e \cos\Theta_e, E'_e)$ and the energy E_h and average angle Θ_h of the hadron flow, i.e. the hadronic final state excluding the proton remnant. The kinematical variables in terms of the measured electron quantities are

$$y = 1 - \frac{E'_e}{E_e}\sin^2(\frac{\Theta_e}{2})$$
$$Q^2 = 4E_e E'_e \cos^2(\frac{\Theta_e}{2}). \qquad (6.4)$$

and x determined by $x = Q^2/(sy)$. Correspondingly for the hadronic system

$$y = \frac{E_h}{2E_e}(1 - \cos\Theta_h)$$
$$Q^2 = E_h^2 \frac{\sin^2\Theta_h}{(1-y)}. \qquad (6.5)$$

The colour connections between the struck quark and the proton remnant render it almost impossible to isolate and measure the hadronic final state jet h. Therefore, in addition to the leptonic variables in Eq. (6.4) usually the Jaquet-Blondel

set of variables [174] or a mixed leptonic-hadronic set called the double-angle variables [175] are used instead of the pure hadronic variables.

In the Jaquet-Blondel case, the hadronic variables are determined approximately by summing the energies (E_h) and transverse (p_{Th}) and longitudinal momenta (p_{zh}) of the hadronic final state X. This method assumes that the particles escaping detection through the beam holes on both sides of a detector can be neglected. The variables are thus defined by

$$y_{JB} = \frac{\sum_h (E - p_z)_h}{2E_e}$$
$$Q^2_{JB} = \frac{(\sum_h p_{x,h})^2 + (\sum_h p_{y,h})^2}{(1 - y_{JB})}. \tag{6.6}$$

and $x_{JB} = Q^2_{JB}/(y_{JB}s)$. The H1 collaboration introduced a modified Jaquet-Blondel type set of variables called the $\sum$-set [176, 177] which is derived from the Jaquet-Blondel set by substituting $2E_e$ by $\sum_{e,h}(E - p_z)$ in the calculation of y_Σ, i.e.

$$y_\Sigma = \frac{\sum_h (E - p_z)_h}{(E - p_z)_e + \sum_h (E - p_z)_h} \tag{6.7}$$

and

$$Q^2_\Sigma = \frac{E'^2_e \sin^2\Theta_e}{1 - y_\Sigma}. \tag{6.8}$$

The motivation for this substitution is twofold. The first has to do with the fact that for genuine DIS events

$$E - p_z \equiv \sum_{e,h}(E - p_z) \simeq 2E_e, \tag{6.9}$$

whereas for the events stemming from photoproduction background

$$E - p_z \ll 2E_e. \tag{6.10}$$

The second motivation is that with this definition of y_Σ an 'internal correction' for QED radiation is applied. This works in the sense that for events where the incoming electron has radiated a substantial fraction of its energy before interacting with the proton, the expression $\sum_{e,h}(E - p_z)$ will take this fact into account through the observed reduced energy flow.

The double-angle variables are based on one leptonic and one hadronic measurement. In addition to the lepton scattering angle, the angle γ is determined from the hadronic energy flow. This angle is the polar angle of the 'struck quark' defined as

$$\tan\frac{\gamma}{2} = \frac{\sum_h (E - p_z)_h}{p^2_{T,h}}. \tag{6.11}$$

The kinematic variables are in this case

$$y_{DA} = \frac{\sin\Theta_e(1 - \cos\gamma)}{\sin\gamma + \sin\Theta_e - \sin(\gamma + \Theta_e)}$$
$$Q^2_{DA} = 4E^2_e \frac{\sin\gamma(1 + \cos\Theta_e)}{\sin\gamma + \sin\Theta_e - \sin(\gamma + \Theta_e)}. \tag{6.12}$$

As this set of variables is based on ratios of energies rather than absolute measurements, a possible scale uncertainty in the measurements of the energies will be compensated.

With these partially redundant sets of variables, the available phase space can be divided into regions where each of these sets will give the best experimental resolution. In addition, in part of the phase space, the redundancy serves to cross-check the results. The respective regions in phase space for the above variables are:

- In the case of the electron method Q_e^2 is always well measured. Limitations on the angular measurements restrict the measurement to high y ($y > 0.15$), i.e. the low x region.
- For the Σ set the resolutions are good at low y ($y < 0.15$) down to $y = 0.01$, i.e. large x. Even at low x values the resolutions are still fair.
- The double-angle method is mostly used for cross-checks and yields resolutions comparable to the Σ set.

For the extraction of F_2 the double differential cross section is cast into the form

$$\frac{d^2\sigma}{dxdQ^2} = \frac{2\pi\alpha^2}{Q^4}[2 - 2y + \frac{y^2}{1+R}]F_2(x, Q^2) \tag{6.13}$$

where $\frac{d^2\sigma}{dxdQ^2}$ denotes the Born cross section, i.e. corrected for electroweak radiative effects. R is the ratio of the absorption cross section of longitudinally to transversely polarized photons (see Eq. (5.14)) relating the structure functions F_1 and F_2 via $R = F_2/xF_1 - 1$. This ratio has not yet been measured at HERA but has to be taken from a calculation.

This relationship is well suited for the extraction of F_2 from experimental data because R and especially its dependence on x and Q^2 can be calculated within perturbative QCD to be

$$R(x, Q^2) = \frac{\alpha_s(Q^2)}{2\pi}\frac{x^2}{2xF_1(x, Q^2)}\int_x^1 \frac{dz}{z^3}\left[\frac{8}{3}F_2(z, Q^2) + 4f(1 - \frac{x}{z})zg(z, Q^2)\right], \tag{6.14}$$

where f is the number of flavors if the incident lepton is a neutrino, and the sum of the squares of quark charges if the incident lepton is charged. Using the MRSH parton distribution functions (see below) a 5-10% effect on this measurement of F_2 is obtained from this correction.

The backgrounds that have to be taken into consideration stem from two main sources. One is from photoproduction background and the other from non-beam interactions. Non-beam interactions can be reactions of electrons or protons with the rest gas in the beam pipe (beam-gas events), reactions of off track protons

with with material in or around the beam pipe, halo muons travelling parallel to the beam line, or cosmic muons. To estimate these backgrounds, in addition to the colliding bunches, the HERA ring is also filled with a few non colliding electron and proton bunches which give rise to this type of background but not to genuine events. From studying the events recorded for these bunches these processes were found to add negligible background to the measurement of F_2.

The photoproduction background on the other hand due to a much larger cross section than the one for DIS is not negligible. Photoproduction reactions at HERA are those interactions initiated by quasi real photons where the scattered electron is emitted under a very small scattering angle (i.e. $Q^2 < 4\,\mathrm{GeV}^2$). These scattering angles are too small for the electron to be detected in the backward calorimeter. The boundary between photoproduction and DIS events is thus a mere instrumental one. The majority of photoproduction events are at $Q^2 \simeq 10^{-2}\,\mathrm{GeV}^2$ with a tail up to the instrumental cutoff around 4 GeV^2. For some physics results obtained from these event sample see 7. Into the DIS event sample photoproduction background can enter if an energetic hadron emitted into the backward direction is misidentified as an "electron". About 10% of the photoproduction events are identified in H1 by detecting the scattered electron in the electron tagger (the tagged event sample). This sample has been used to calibrate the Monte Carlo simulation of photoproduction processes. These Monte Carlo generators are then employed to determine the untagged photoproduction background in the DIS event sample.

As discussed above also momentum conservation helps to suppress this background if one sums the quantity $E - p_z$ (Eq. 6.9) over all particles in the main detector. Whereas for DIS this sum is equal to $2E_e$, in photoproduction events

$$S = \sum_{e,h}(E - p_z) = 2(E_e - E'_e).$$

Applying a cut at $S > 30\,\mathrm{GeV}$ significantly reduces the background. Additional cuts on tracker hits and shower profiles of the electron candidates further reduces the background. Finally, the background was found to be negligible for large energies of the scattered electrons, and below 10% for low Q^2 and $y \leq 0.7$.

The luminosity delivered by HERA to the experiments H1 and ZEUS increased considerably from the the first running period in 1992 to the one in 1993, and again in 1994. The data discussed in the following were taken in 1993, corresponding to an integrated luminosity of about 500 nb^{-1}, i.e. a factor of 20 higher than in 1992.

The extraction of $F_2(x, Q^2)$ is based on the electron method at high y (roughly $y > 0.15$) and the Σ method at low y. The analysis of the data collected in 1992 had shown F_2 to rise strongly at low x [178, 179]. This result was not expected by the whole community but hoped for by optimists looking forward to the new QCD window discussed in 5.7. The much higher statistics of the 1993 running enabled us to extend the analysis to higher values of Q^2 (up to about $2000\,\mathrm{GeV}^2$)

and to reduce the errors on the measurement for small Q^2. At the low end of the Q^2 range (4 - 8 GeV^2) a further data point was achieved by running the HERA machine in a shifted vertex mode to enlarge the detector acceptance in the backward region. In these runs the interaction vertex was shifted by about 80 cm in the proton direction in order to enable and improve the measurement of electrons scattered backwards under very small angles Θ_e.

Fig. 6.2 summarizes the H1 measurements on F_2 [176] for different values of x and Q^2. Also shown in the same plot are the data from ZEUS [180]. The strong rise

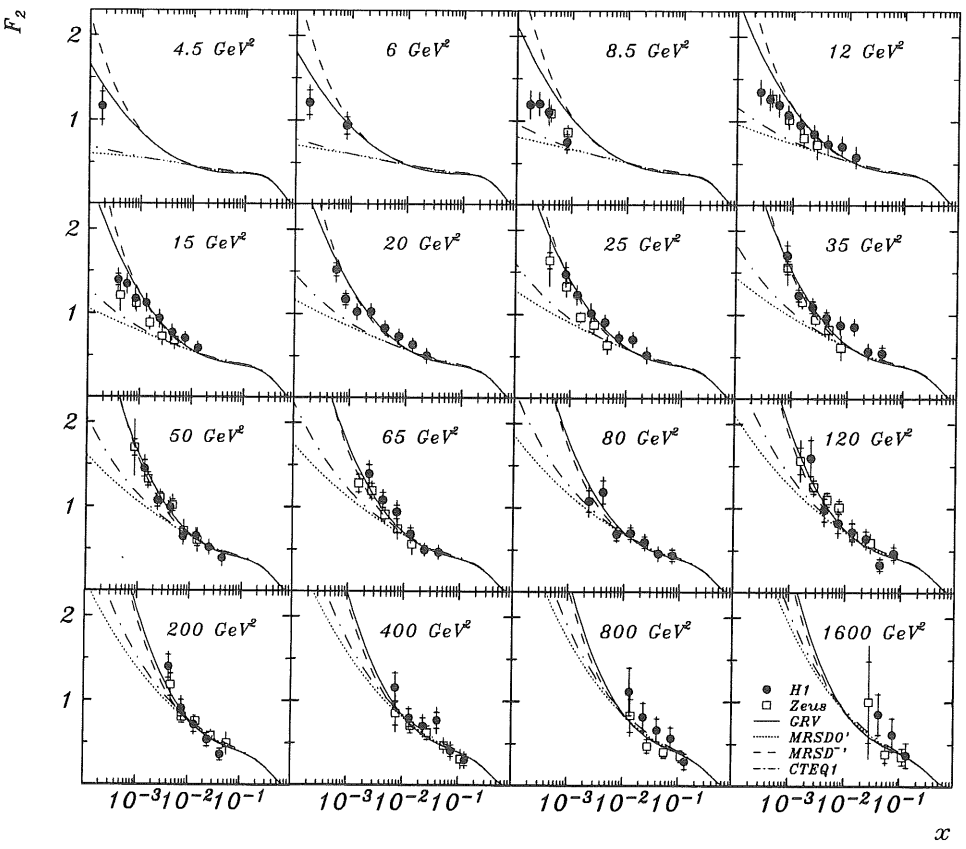

Figure 6.2: The proton structure function from H1 (full points[176]) and ZEUS (open points [180]) as a function of x for different values of Q^2. The inner error bars show the statistical error, the outer error bars include the systematical error added in quadrature. An overall normalization uncertainty of 4.5% for H1 and 3.5% for ZEUS is not shown. The curves represent pre-HERA fits to previous data.

towards low x is consistent with the one observed in the 1992 data and could thus be confirmed with a high statistical significance. The x and Q^2 dependence can be parametrized as $\ln(Q^2) \cdot x^{-0.19}$. The data from H1 and ZEUS are found to agree very well. The comparison of the measured F_2 and the predictions derived from parton distributions derived from pre-HERA data (see 5.6) especially at low Q^2

shows that only the GRV and MRSD$^{-\prime}$ parametrizations yield a fair description of the data. The fact that both GRV, based on valence-type input distributions at $Q_0^2 \simeq 0.3\,\mathrm{GeV}^2$ and then evolved with the DGLAP evolution equation over a long Q^2 lever arm, and MRSD$^{-\prime}$, assuming a BFKL-type input distribution at $Q_0^2 = 4\,\mathrm{GeV}^2$ and also evolved with DGLAP evolution, describe the data has caused a lot of excitement and discussion. Not only can the DGLAP evolution starting at Q_0^2 values commonly accepted to be large enough for QCD evolution to hold, describe the data, but DGLAP evolution evolved over evolution paths large enough will produce BFKL-type distributions at moderate Q^2 out of valence type input distributions and describe the data practically free of assumptions. The consequences for the validity and applicability of perturbative QCD are not yet understood in detail.

In Fig. 6.3 a summary plot is shown with the new data from HERA and the new data from E665[181] as function of Q^2 at fixed x, compared to published fixed target data. The HERA data agree with a smooth extrapolation from SLAC[182], BCDMS[183], NMC[137] and E665 data. Positive scaling violations are clearly visible at low x and are more and more pronounced as x decreases.

The HERA data thus provided qualitatively new input to the determination of parton distribution functions. As discussed in 5.6, fits to data in the new x regime will most probably also effect the parametrizations of the individual parton densities at large and medium x, the values governing the cross sections in nucleus-nucleus collisions in EAS. The HERA data were used in new fits by the CTEQ [184] and MRS [185] groups to yield the CTEQ2 and MRSH parametrizations. The resulting predictions for F_2 at HERA are summarized in Fig. 6.3. As expected, after fitting to the data, the new CTEQ and MRS distributions agree much better with the data. Even the new, lower Q^2 region not used in the fits is adequately described.

The GRV distributions, on the other hand, were not changed due to the HERA F_2 data. They were slightly updated, but only w.r.t. to the treatment of the charm quark threshold in the evolution. This mainly affects the lower Q^2 region [186] where now the agreement between data and prediction is very good. This good agreement with the data is less trivial than in the case of MRSH and CTEQ2, since these do not rely on the HERA measurements in the determination of the distributions. To summarize, parametrizations using the DGLAP equations are able to describe the low x data, provided a suitable non-perturbative input is chosen (*e.g.* $\sim x^{-0.3}$ for MRSH[185]), or a large lever arm is taken for the DGLAP evolution (GRV). The measured F_2 is thus well described in the whole QCD phase region observable at HERA so far by the application of DGLAP evolution.

What about the BFKL evolution then? Can it at HERA already be excluded on the basis of the inclusive structure function? To answer this question the predictions based on BFKL evolution have to be compared to the data in the region of validity of BFKL evolution. These have been worked out [168] for the x dependence of F_2 at low Q^2. Since the BFKL phase space is confined to small Q^2,

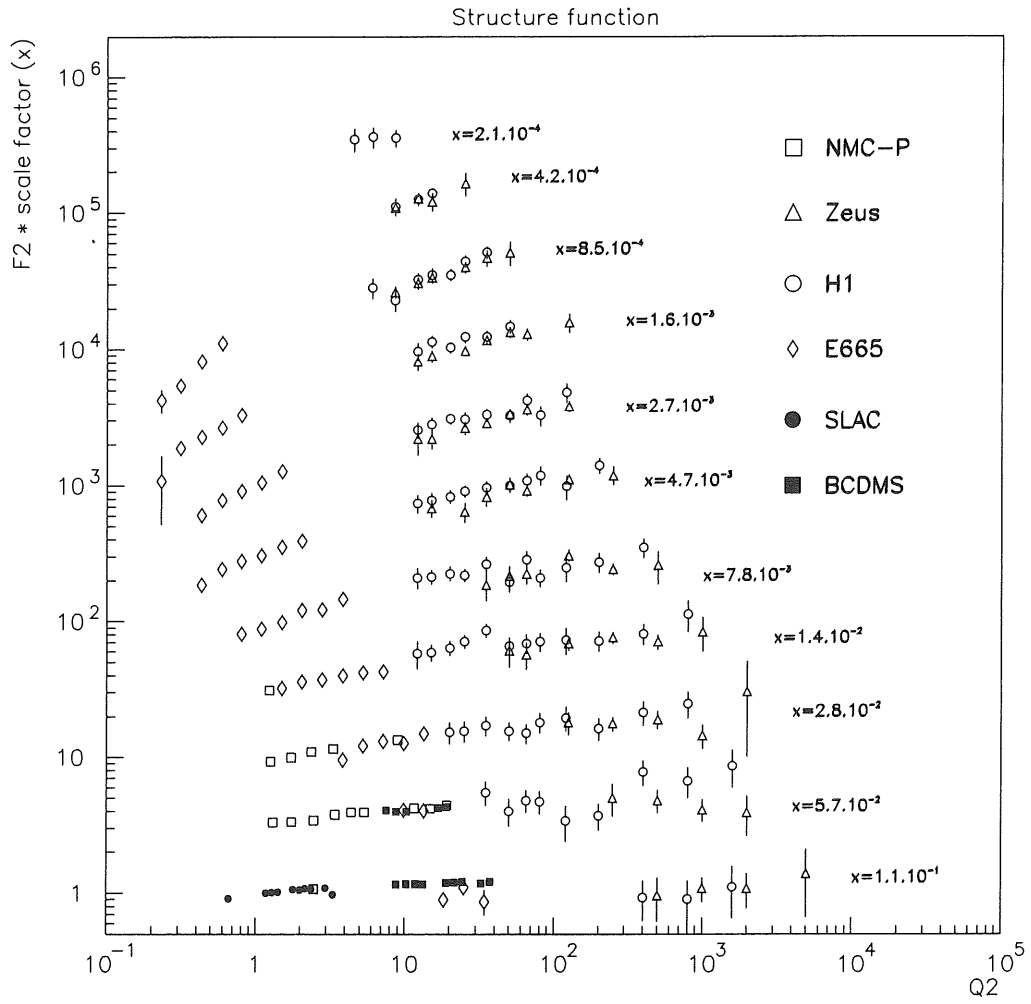

Figure 6.3: $F_2(x, Q^2)$ at fixed x values as a function of Q^2 from H1 and ZEUS together with data points from E665, SLAC, NMC and BCDMS in the same x bins as the HERA experiments. The data points of fixed target experiments have been slightly rebinned in x to match the HERA values. The error bars show the total errors. For clarity of the picture, common scale factors which are different for the different x values have been applied to all data sets.

we only take the low Q^2 data and compare them to the predictions AKMS1 and AKMS2. The difference between these two sets is the effect of gluon shadowing at very small x. AKMS1 does not include shadowing, while AKMS2 represents the "hot spot" scenario, i.e. it assumes that there are small regions in the proton where shadowing has set in.

In addition, as discussed above, the low Q^2 and low x region corresponds to the Regge limit. There exist predictions based on Regge theory. The new CKMT [187] parametrization uses the "bare" instead of the "effective" Pomeron intercept in the calculations. This parametrization finds a stronger increase of F_2

with x compared to the older Regge inspired calculation (DOLA) [188] based on the "effective" Pomeron measured in the total cross section . The DOLA calculations were already found to be significantly below our '92 data. The CKMT curves shown in Fig. 6.4 were calculated using a Pomeron intercept $1 - \Delta$, with $\Delta = 0.25$ and without the QCD evolution term accounting for the Q^2 evolution of the effective intercept. They are therefore compared to the data in the lowest Q^2 bins only. The measured values of F_2 at small Q^2 values, down to 4.5 GeV^2 open a new region for testing this Regge assumption. Fig. 6.4 shows that the parametrization undershoots the data at low Q^2. Probably this already constitutes a severe problem of conventional Regge theory and is thus very important information for EAS applications.

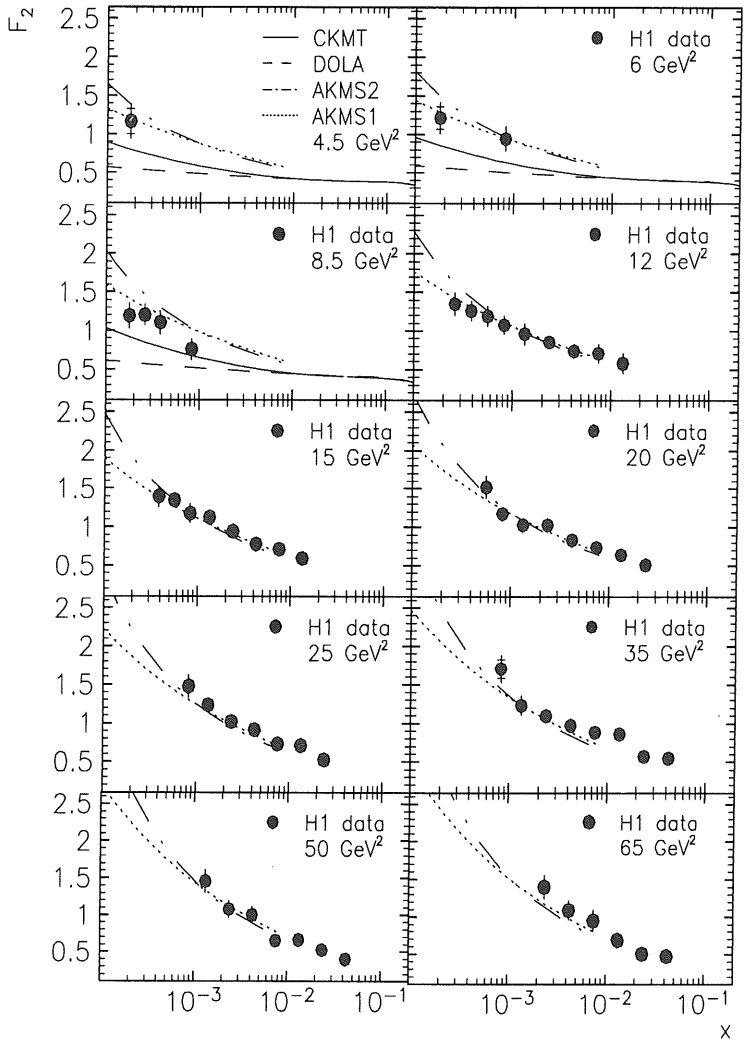

Figure 6.4: The proton structure function from H1 as a function of x for low Q^2 values, compared with model predictions described in the text: DOLA (dashed lines), CKMT (solid line), AKMS without shadowing (dash-dotted line), AKMS with shadowing (dotted line).

The parametrization based on BFKL evolution, however, describe the low Q^2 data with a quality comparable to the one shown in Fig. 6.2, based on the DGLAP evolution equations.

Shadowing was recently studied [189] using the GLR equation, and it was found that it will be necessary to detect electrons at smaller scattering angles at HERA to have a chance to identify these effects. Furthermore, restoring the momentum sum rule in the GLR equation introduces additional "anti-shadowing" terms [190], which will reduce the shadowing effect.

In summary one must say that standard DGLAP evolution is sufficient to describe the present F_2 data. At low Q^2 though, the BFKL motivated parametrizations do give a satisfactory description of the data, too. Present data thus can be described by both approaches. Regge inspired models do not describe the data in great detail and are somewhat disfavoured. It is discussed at the moment whether perhaps by lowering the Q_0^2 value of the initial non-perturbative part and allowing for more QCD evolution these models might be saved.

The experience thus gathered will have to be closely followed by the builders of EAS Monte Carlo generators. At the moment an ansatz to improve the VENUS generator is developed as a result of these data [191]. Here thus an important direct consequence of HERA measurements on the simulation of EAS becomes visible. As discussed in 5.8, the energy dependence the soft and hard eikonals is one of the determining factors in the simulation of high energy hadron-hadron interactions. The transition from soft to hard interactions has to be done at the scale Q_0^2. HERA thus will provide some insight into where this scale should be once more data at very low Q^2 are available.

In the currently covered x, Q^2 range the effect of shadowing is not yet directly visible (see however 6.7 and 9). Data at lower values of x, other observables, or observables less inclusive than F_2 have thus to used to determine which region of QCD we are in.

6.3 Measurement of Topological Variables

Of less inclusive observables H1 has studied the transverse energy flow and jet production in the configuration proposed by Mueller (see 6.1.2).

Transverse Energy Flow

Fig. 6.5 shows the mean transverse energy flow E_T measured by H1 as a function of pseudorapidity $\eta = -\ln\tan(\Theta/2)$ in the laboratory system for a low mean $< x > \simeq 5.7 \cdot 10^{-4}$ and moderate $Q^2 \simeq 15\,\mathrm{GeV}^2$.

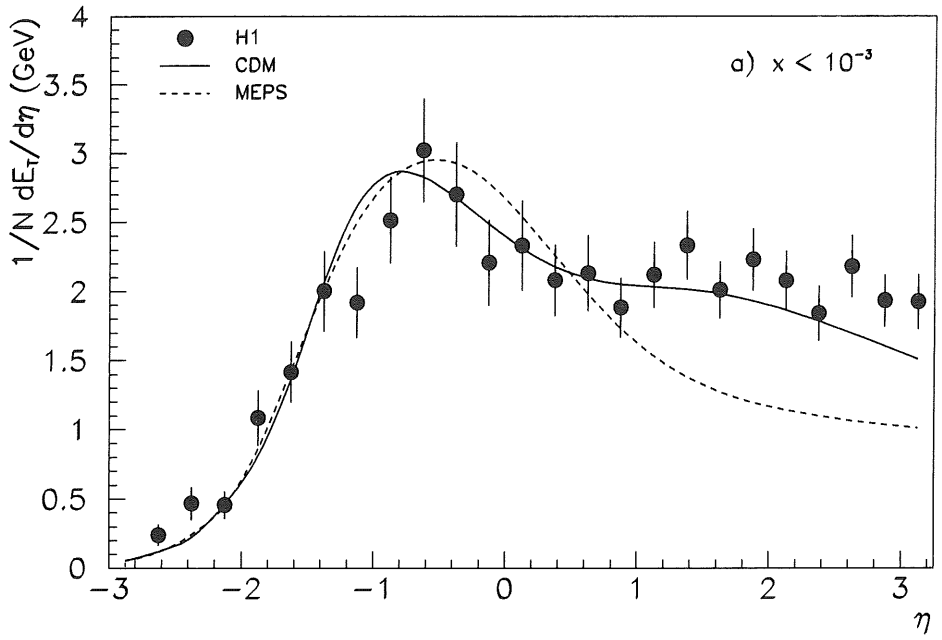

Figure 6.5: Transverse energy flow E_T in the laboratory system as a function of the pseudo-rapidity η with $x < 10^{-3}$, measured by H1. The proton direction is to the right. The error bars contain the statistical and systematic errors added in quadrature, except for an overall 6% energy scale uncertainty.

The measured data are compared to simulations performed with the LEPTO 6.1 (MEPS) and the ARIADNE (CDM) Monte Carlo generators. For details and references see [109]. In the LEPTO 6.1 generator QCD corrections are taken into consideration by DGLAP evolution on the basis of a first order QCD matrix element followed by a parton shower stage (MEPS). The fragmentation of the coloured parton systems is performed with LUND string model coded in the JETSET 7.3 program. In the ARIADNE model, QCD corrections are performed by gluon radiation from colour dipoles. In this respect this model mimics the BFKL equation (see 5.8) which can also be derived with a colour dipol ansatz.

It is apparent from the data that energy flow is indeed shifted from the current jet at small η into the remnant vicinity at large η if the MEPS prediction is taken to be the standard expectation. The CDM prediction agrees quite well with the data.

In Fig. 6.6 a parton level calculation performed in the BFKL scheme [169] is compared to the data and to the MEPS prediction without detector effects. Qualitatively the BFKL based prediction agrees much better with the data than the DGLAP based one. The influence of fragmentation corrections, however, may be large. Whether this effect survives a full simulation thus has to be studied before drawing any conclusions.

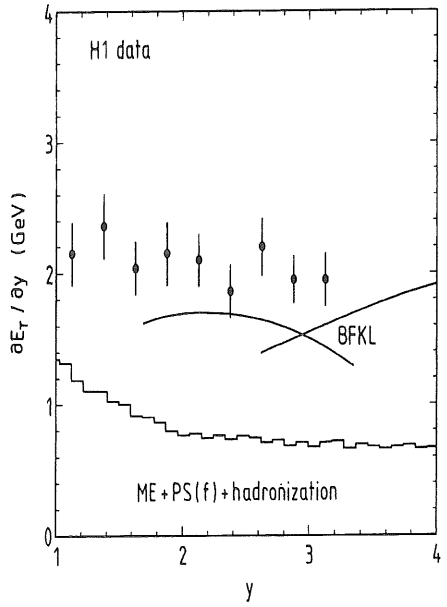

Figure 6.6: The same data as Fig. 6.5 (η is termed y here). The continuous curve shows the BFKL predictions at the parton level of $x = 5.7 \cdot 10^{-4}$ and $Q^2 = 15$ GeV^2, which correspond to the average values of the data sample. The histogram is the MEPS Monte Carlo estimate, including hadronization.

DIS Events with Measured Jets

The process giving rise to this signature of BFKL dynamics is shown in Fig. 6.7. In a sample of DIS events with $Q^2 \approx 20$ GeV^2 and $2 \cdot 10^{-4} < x < 2 \cdot 10^{-3}$ we have counted the number of events with jets reconstructed with $x_j < 0.05$ and $0.5 < k_{Tj}^2/Q^2 < 6$. The resulting number of events, corrected for background contribution, is given in Table 7.1 and compared to expectations of the MEPS and CDM models including detector simulation. The predictions were found not to

x range	data	MEPS MRSD0(–)'	CDM
$2 \cdot 10^{-4} - 2 \cdot 10^{-3}$	$128 \pm 12 \pm 26$	69 (53)	32
$2 \cdot 10^{-4} - 1 \cdot 10^{-3}$	$85 \pm 9 \pm 17$	37 (27)	21
$1 \cdot 10^{-3} - 2 \cdot 10^{-3}$	$43 \pm 7 \pm 9$	32 (26)	11

Table 6.1: The number of reconstructed and predicted events with jets of BFKL signature for different ranges of x.

depend significantly on the parametrization of the parton densities and generally lie below the measured numbers.

The size of the errors do not allow yet a firm conclusion. We notice, however, that the rate of jets rises with decreasing x. This is the expected trend from BFKL

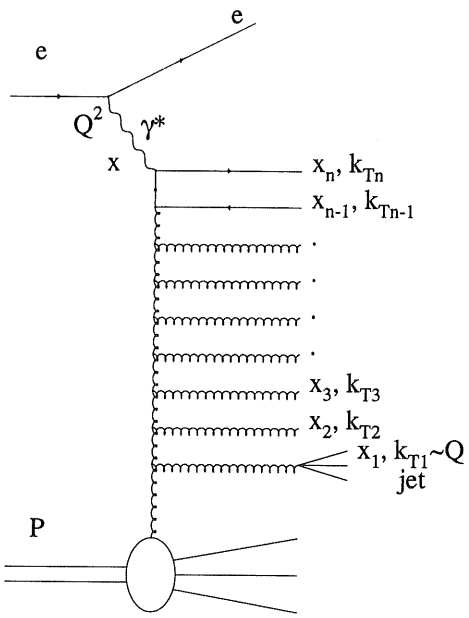

Figure 6.7: Parton evolution in the ladder approximation. The selection of forward jets in DIS events is illustrated.

dynamics as a numerical calculation[192] has shown. At the parton level, with the same cuts as for this analysis, the BFKL evolution yields 75 and 36 events for the low and high x bin respectively. Without BFKL evolution, i.e. only taking into account the box diagram, the calculation expects 25 and 20 events respectively. The data thus tend to follow the BFKL evolution expectation, but a correction from the measured jet rates to the parton level and more statistics will be needed to make quantitative comparisons with the calculations.

6.4 Determination of the Gluon Structure Function

Especially important for the calculations of expected mini-jet rates at future colliders is the determination of the gluon distribution in the proton at small x. There exist several possibilities to extract the gluon density from the HERA data. One possibility is through the isolation of the photon-gluon fusion channel giving rise to two jets as depicted in Fig. 7.2. The clearest signature would be obtained in the measurement of heavy quark production. The data statistics is however not yet sufficient to utilize this channel. At the moment we thus rely on the production of light quarks resulting in at least two jets. Another possibilities is based on the measurement of scaling violations $dF_2/d\ln Q^2$ of the F_2 structure function.

6.4.1 Extraction of $xg(x, Q^2)$ from F_2

An analysis of the F_2 structure function in the framework of perturbative QCD as discussed in 5.4 allows to extract the gluon density in the proton. In this type of analysis the gluon density is extracted from the degree of scaling violations observed in F_2. Several methods have been proposed for the deconvolution of $xg(x, Q^2)$. The QCD analysis of the H1 data is based on leading $\log Q^2$, next-to-leading $\log Q^2$, and a mixed leading $\log Q^2$ and leading $\log(1/x)$ evolution equations. The details can be found in [193].

As an example for a deconvolution procedure which reduces the coupled integro-differntial DGLAP equations to differntial equations, in the method proposed by Prytz [194] quark contributions to the scaling violations are neglected, a Taylor expansion around $x = 1/2$ is performed, and in leading order the gluon density is found to be

$$xg(x, Q^2) \simeq \frac{27\pi}{10\alpha_s(Q^2)} \frac{\partial F_2(\frac{x}{2}, Q^2)}{\partial \log Q^2}. \tag{6.15}$$

This approximation is expected to hold to about 20% at $x = 10^{-3}$ for a steeply rising gluon [195].

The data points in Fig. 6.8 shows the gluon density $xg(x, Q^2)$ as a function of x for $Q^2 = 20\,\mathrm{GeV}^2$ derived from the H1 data on F_2 by this method. Although the errors are still large, a strong increase in the gluon density as expected from the F_2 data is found. This result agrees with the gluon density obtained from the leading order DGLAP fits and also with a mixed DGALP and BFKL fit, where BFKL evolution is assumed below some parameter x_0. The leading order result is shown as shaded regions, the mixed fit as full line termed BFKL. Also in this analysis we cannot discriminate DGLAP and BFKL evolution on the basis of the current data.

6.4.2 Extraction of $xg(x, Q^2)$ from Jet Cross Sections

In the Quark Parton Model, the quark struck by the virtual photon is ejected from the proton, balancing the momentum of the scattered electron. In QCD, the balance of momenta between the scattered electron and the hadronic system is maintained, but corrections to this picture have to be applied. Due to the confinement property of QCD not the struck parton, but a spray of colourless hadrons (jet) is expected. In addition, QCD radiative corrections may give rise to more than 1 jet in the final state. In $\mathcal{O}(\alpha_s)$ processes like gluon radiation in the initial or final state (the QCD-Compton process), or photon-gluon fusion will occur. As QCD is a field theory, in order for the calculations to yield finite results, the number of jets making up the hadronic final state can only be *defined* by stating an exclusive resolution power.

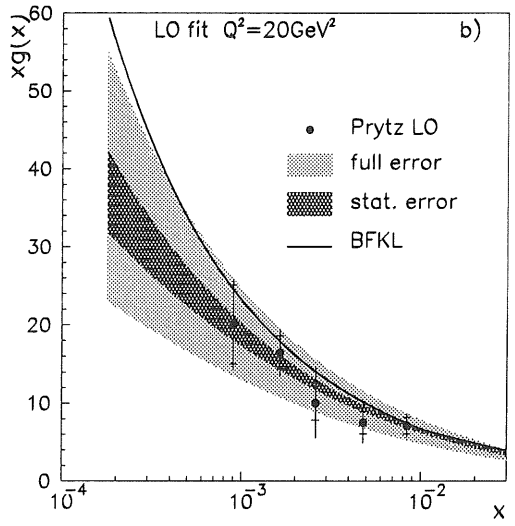

Figure 6.8: The H1 measurement of the gluon density $xg(x, Q^2)$ as a function of x at $Q^2 = 20$ GeV^2 as obtained from a leading logQ^2 QCD fit (shaded), a mixed DGLAP-BFKL fit (full line), and from an analysis according to the LO Prytz prescription.

In the analysis to extract the gluon density, the H1 collaboration uses the cone algorithm [196] to define the number of jets in an event. See [197] for the details of the analysis. In the cone algorithm an energy deposition $E_T > E_T^{min}$ exceeding some prescribed value E_T^{min} is searched for within a cone of a given radius, defined in the metric of azimuthal angle ϕ and pseudo-rapidity η. The cone radius is chosen to be

$$R = \sqrt{\Delta\phi^2 + \Delta\eta^2} = 1.$$

Fig. 6.9 shows an example of a (2+1)-jet event observed in the H1 detector. The notation (i+1)-jet stands for i jets stemming from the struck parton and the +1 jet signifies the proton remnant jet which continues mostly undeflected down the beam-pipe in the initial proton direction. In general, the compensation of colour in hadronic system will lead to a colour connection between the struck partonic system and the proton remnant. If, on the other hand, the system the virtual photon scatters on is colourless, there will be no colour connection between the two systems. Events of this kind have also been observed at HERA and have led to the measurement of the Pomeron structure (see 6.6).

As shown in Fig. 7.2, the gluon density in the proton determines the rate of the leading order ($\mathcal{O}(\alpha_s)$) photon-gluon fusion process. This process could be tagged by the observation of heavy flavours in the final state. The present statistics, however, is not large enough to do so. The other possibility rest on the observation that the QCD matrix elements for the processes giving rise to (2+1)-jets in the final state predict that regions in phase space exist where the photon-gluon fusion process dominates the event rate. The selected range is given by jets with $E_T >$ 3.5 GeV and $10° < \Theta_{jet} < 150°$. The remaining QCD-Compton background was estimated with the help of several Monte Carlo programs. As the final step the

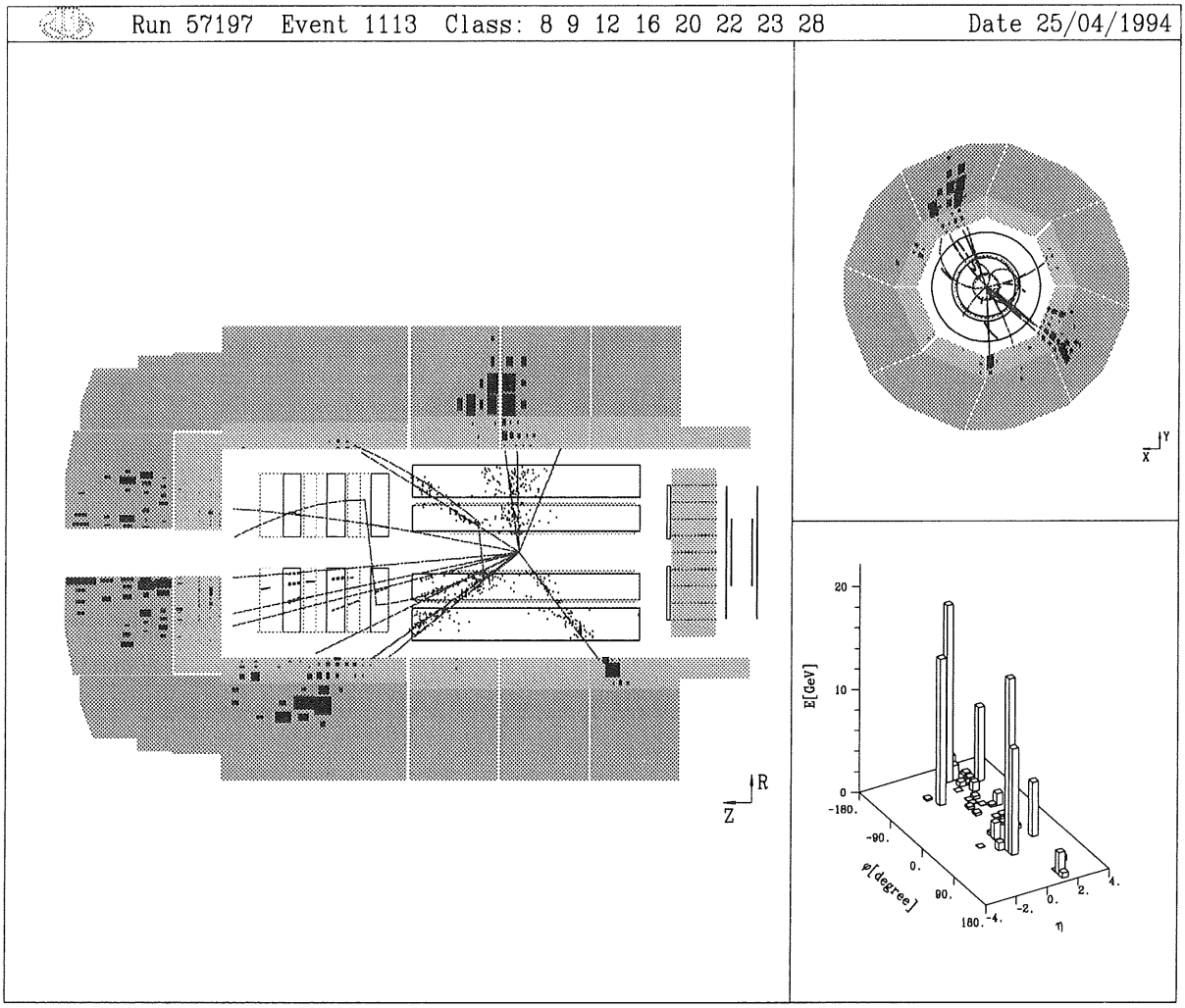

Figure 6.9: Example of a (2+1) jet deep inelastic scattering event in the H1 detector.

(2+1)-jet event rates were transformed into cross sections.

The gluon density was determined at an average Q^2 of $30\,\mathrm{GeV}^2$. The resulting gluon distribution is shown in Fig. 6.10. Although this analysis does not reach as low values in x as the indirect ones discussed above, again a strong rise of the gluon density towards small values of x can be seen. The measured distribution shows consistency with the indirect determination by QCD fits or by the method of Prytz for the H1 and ZEUS data [201], with the extraction of the gluon density by NMC based on inelastic J/ψ production [200], and with the GRV and CTEQ3L parametrizations as also shown in the figure.

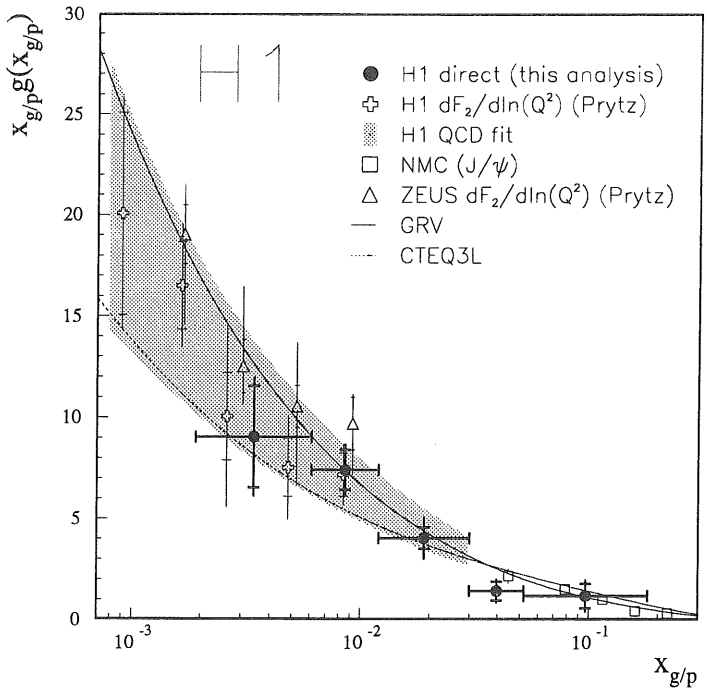

Figure 6.10: The measured gluon distribution extracted from the H1 2-jet data, as a function of x at $Q^2 = 30\,\mathrm{GeV}^2$. The error bars reflect the statistical errors and the total errors respectively. Not included is a global normalisation uncertainty of 11%. These data are compared to the indirect measurement, to the ZEUS measurement at $20\,\mathrm{GeV}^2$, and with a determination from J/ψ production by NMC evolved to $Q^2 = 30\,\mathrm{GeV}^2$.

6.5 The Charged Current Cross Section

In addition to the neutral current event samples discussed above, also charged current events have been recorded in the H1 detector. From these the charged current cross section could be determined. For the details see [198]. An example of such an event is shown in Fig. 6.11.

The charged current trigger required the vector sum, V, of the transverse momenta to exceed a threshold set just above the detector noise and well below the later imposed physics requirement. In addition it had to be sufficiently fast in order to restrict the vertex coordinate along the beam direction to about $\pm 40\,\mathrm{cm}$.

In the analysis candidate events with $V > 25\,\mathrm{GeV}$ for which an event vertex could be reconstructed were passed through halo and cosmic muon filters to reduce the background. The data sample corresponded to an integrated luminosity of $\mathcal{L}$ = 348 $\pm$ 17 nb^{-1}. After efficiency and acceptance corrections the 14 remaining events correspond to

$$\sigma(p_{\mathrm{T}} > 25\,GeV) = 55 \pm 15 \pm 6\ \mathrm{pb}, \tag{6.16}$$

where the first error is statistical, the second error systematic with all known

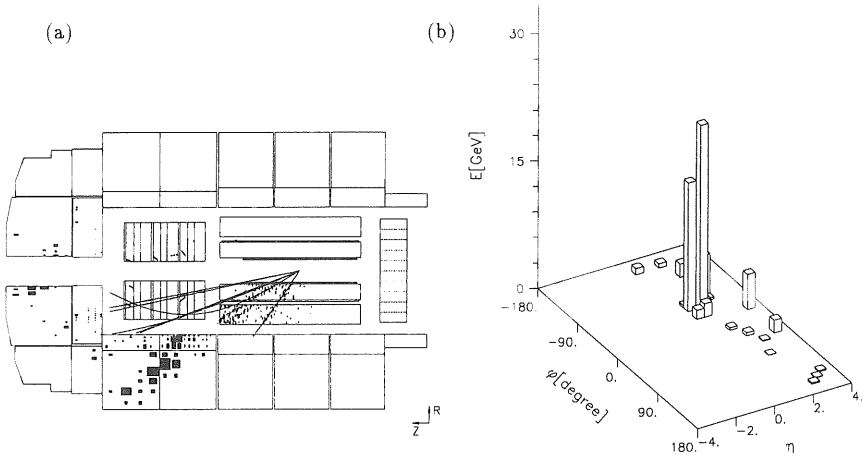

Figure 6.11: A charged current event candidate as registered in the H1 detector.

systematic effects added in quadrature.

Taking electroweak and QCD corrections into consideration the theoretical expectation for $p_T > 25\,GeV$ is 40.9 pb in satisfactory agreement with the measurement. The observed reaction $e^- p \rightarrow \nu_e + hadrons$ is the inverse of the neutrino-nucleon scattering reactions observed at fixed target experiments. This measurement of the charged current cross section thus corresponds to a measurement of the neutrino-nucleon cross section at a fixed traget energy of about 50 TeV. This measurement together with low energy νN cross section measurements is shown in Fig. 6.12.

The W propagator effect at high energies here for the first time becomes visible experimentally.

6.6 Diffraction in DIS

In this section we will review some of the measurements performed on diffractive scattering events identified in the DIS event sample.

6.6.1 Rapidity Gap Events in DIS

When studying the energy flow in DIS events, first the ZEUS collaboration [202] and later also H1 [203] found a rather large fraction of events characterized by a large rapidity interval around the proton beam direction devoid of any particles. This class of events are called rapidity gap events. The observable characterizing these events is the maximum pseudorapidity $\eta_{\max}$ of a significant energy deposition ($E > 400\,\mathrm{MeV}$) in the calorimeters. In this way a gap in pseudorapidity

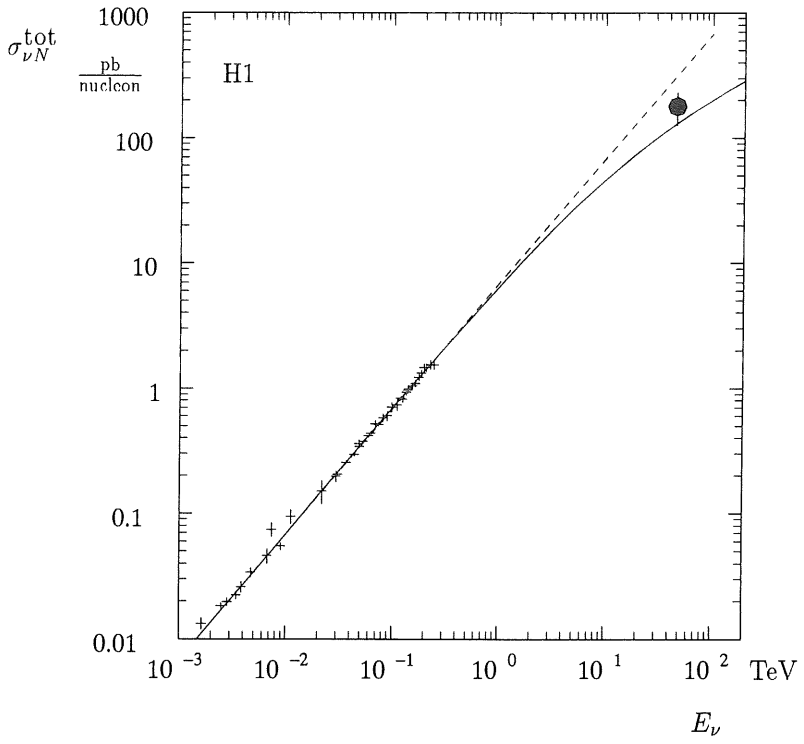

Figure 6.12: The energy dependence of the νN cross section. The crosses represent low energy data [199] while the full circle refers to the H1 measurement converted into a νN cross section at an equivalent fixed target energy of 50 TeV. The full line represents the predicted cross section including the W propagator. The dashed line the linear extrapolation from low energies.

extending from $\eta_{\max}$ up to the geometric acceptance of the H1 liquid argon detector at $\eta \sim 3.65$ can be established. Fig. 6.13 shows the distribution of $\eta_{\max}$ as measured by H1 in the standard DIS events. Superimposed on the plot is the expectation derived from the LEPTO Monte Carlo generator for standard DIS events.

Most of the events are indeed described by the LEPTO prediction but a significant number of events show rapidity gaps larger than expected in the DIS simulation. These numbers are not any more consistent with fluctuations in the exponential suppression of these gaps due to the colour connection between the struck parton and proton remnant system. By requiring the selection criterion

$$\eta_{\max} \leq 1.8$$

about 5% of the total DIS sample remains. They have to be explained by a process where no colour connection between the proton remnant and the struck hadronic system is established. A natural candidate process is diffractive scattering as depicted in Fig. 6.14.

What other observables can be found that distinguish these events? The second selective observable for rapidity gap events was found to be the invariant mass M_X of the hadronic final state as seen in the main detector. A plot of M_X shows

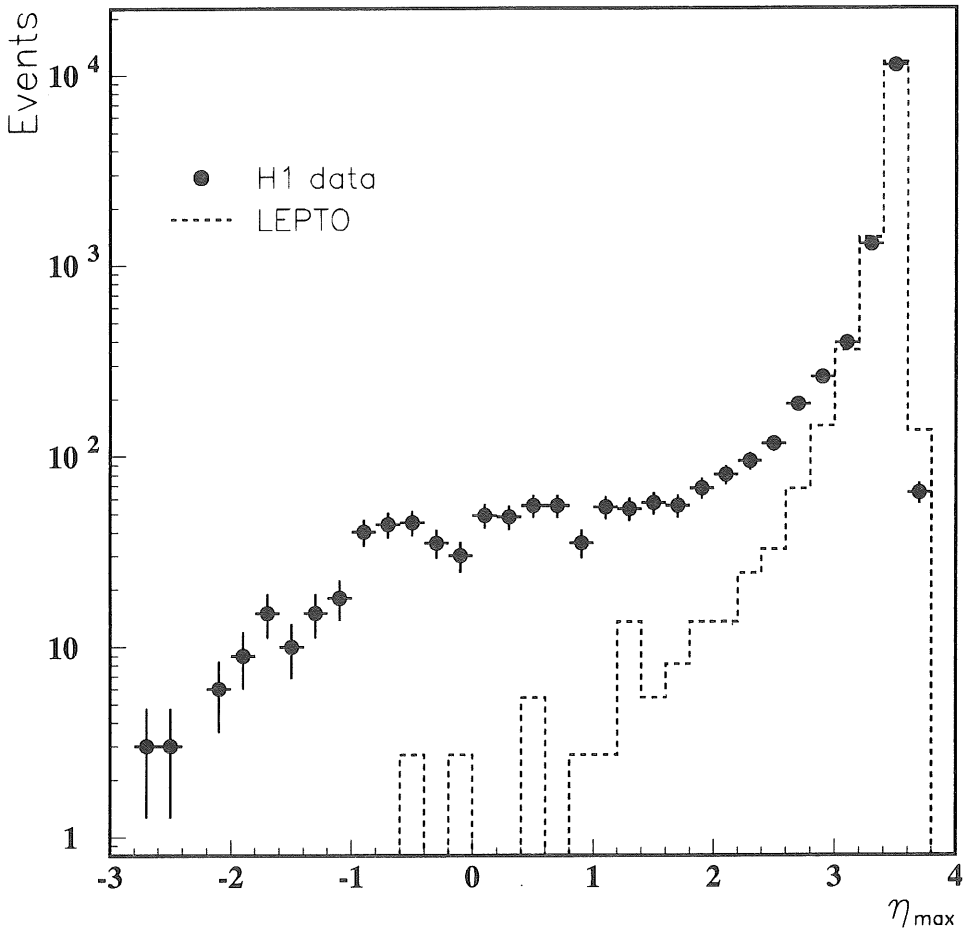

Figure 6.13: Distribution of measured η_{max} for all DIS events. The histogram corresponds to the expectation from the "standard DIS" model as contained in the LEPTO Monte Carlo generator.

that rapidity gap events form a distinctive class at low values of M_X. This is in contrast to DIS events which show a much broader M_X distribution. This is shown in Fig. 6.15 where the M_X distribution of the rapidity gap events peaks at 3.5 GeV which is considerably lower than for all DIS events. This can in part be contributed to the phase space restriction implicit in the rapidity gap selection. The largest part though is due to these events forming a separate event class as is also shown in Fig. 6.15 by omitting the energy depositions in the rapidity gap region also for the events without rapidity gap. The resulting M_X distribution is still not consistent with the one from the rapidity gap events.

A diffractive model that allows to describe the data is the Vector Meson Dominance model (VMD) which assumes the exchange of the colourless Regge pole, the Pomeron, in the t-channel. In this model the virtual photon fluctuates into vector meson states ρ, ω, ϕ which by the interaction with the Pomeron are pulled onto

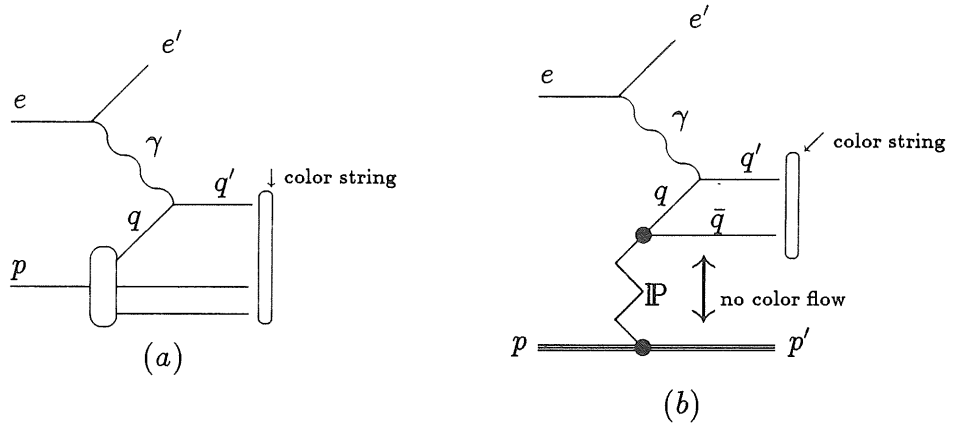

Figure 6.14: Model for the hadronic final state in usual deep inelastic scattering (**a**) and diffractive deep inelastic scattering (**b**).

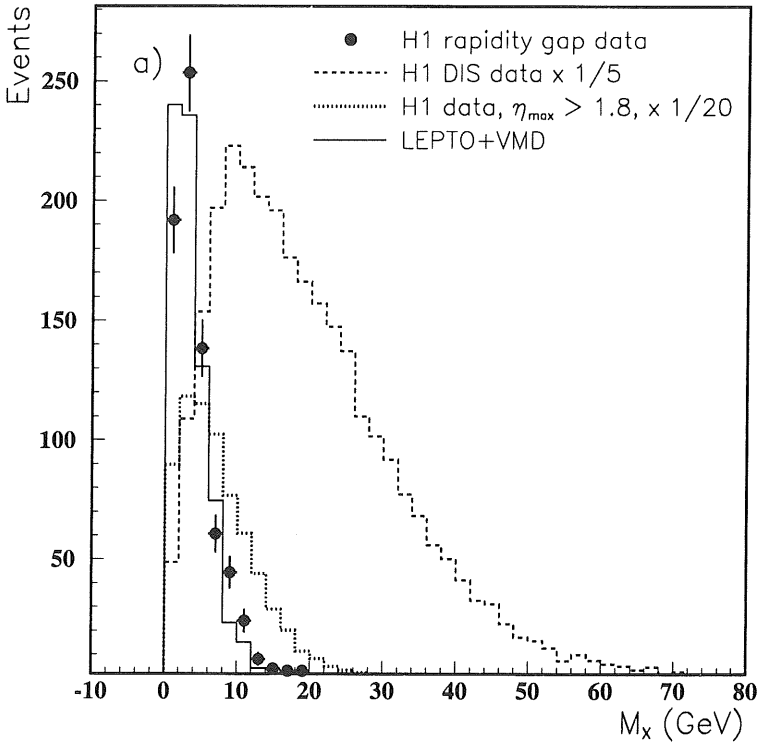

Figure 6.15: Invariant mass spectrum of the measured hadronic final state for rapidity gap events, for DIS events (scaled by a factor $\frac{1}{5}$ for display purposes), and for DIS events with $\eta_{\max} > 1.8$ omitting energy deposits with $\eta > 1.8$ from the calculation of the mass (scaled by a factor of $\frac{1}{20}$ for display purposes): the solid line is the expectation of the VMD-like simulation, with a small contribution from LEPTO.

their respective mass shells. Fig. 6.16 shows the respective Feynman diagrams.

Together with the standard DIS events from LEPTO, the VMD model gives a good description of the measured $\eta_{\max}$ distribution as shown in Fig. 6.17a.

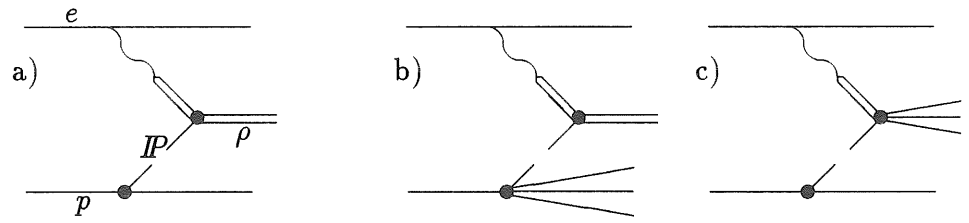

Figure 6.16: Diagrams which illustrate the VDM description of the rapidity gap events: (a) $\rho^0(770)$ production via elastic VDM; (b) VDM $\rho^0(770)$ production with soft dissociation of the proton; (c) VDM interaction followed by soft dissociation of the vector meson. The double dissociation diagram is not shown.

Another possibility to describe the data is within a partonic or QCD based model. Within this model it is assumed that the virtual photon scatters off the partonic content of an colourless object in, or emitted by, the proton. The natural candidate for this is again the Pomeron. The model follows the proposal by Ingelman and Schlein [152] to assume a partonic nature of the Pomeron and to cast the diffractive cross section into a Pomeron flux factor times a Pomeron structure function (see 5.8). The Monte Carlo generators RAPGAP [204] and POMPYT [205] are in this manner based on a partonic substructure of the Pomeron. The parton type of substructure, i.e. quarks or gluons may be chosen. The parton distribution functions $zp(z)$ chosen for a first comparison to the data were in both cases of the form $zp(z) \sim z(1-z)$ with z being either the fraction of the Pomeron momentum carried by the struck quark or by the gluon which splits into a quark-antiquark pair prior to the interaction with the photon. Since the Pomeron is not colour connected to the proton, a rapidity interval between the proton remnant and the hadronic system probed by the virtual photon without colour flow is expected. This would lead to an observable gap in the detector. The prediction of the RAPGAP generator either based on a quark or gluonic Pomeron structure function when combined with the LEPTO one also describe the $\eta_{\max}$ distribution measured in the data. This is shown in Figs. 6.17b and 6.18.

Depending on which model of diffraction is used, the relative contribution of diffractive events in our data changes. For the VMD case, where the Pomeron does not have a sub-structure, we find that about 15% of the total observed DIS sample ($5 < Q^2 < 120\,\mathrm{GeV}^2$, $10^{-4} < x < 10^{-2}$) is of diffractive nature. If the Pomeron is primarily composed of quarks this number is about 13% and in the case of a gluonic Pomeron we find about 10%. These investigations in themselves are not yet proof of the diffractive nature of these events, let alone of the partonic nature of the Pomeron. Also meson exchange processes would lead to events with observable rapidity gaps.

With this investigation, however, a new class of events in DIS is established beyond doubt. The simulations based on diffractive processes mediated by Pomeron exchange can describe the measured characteristics. It is thus at least a valid assumption to assume these events to be diffractive and to investigate the sub-

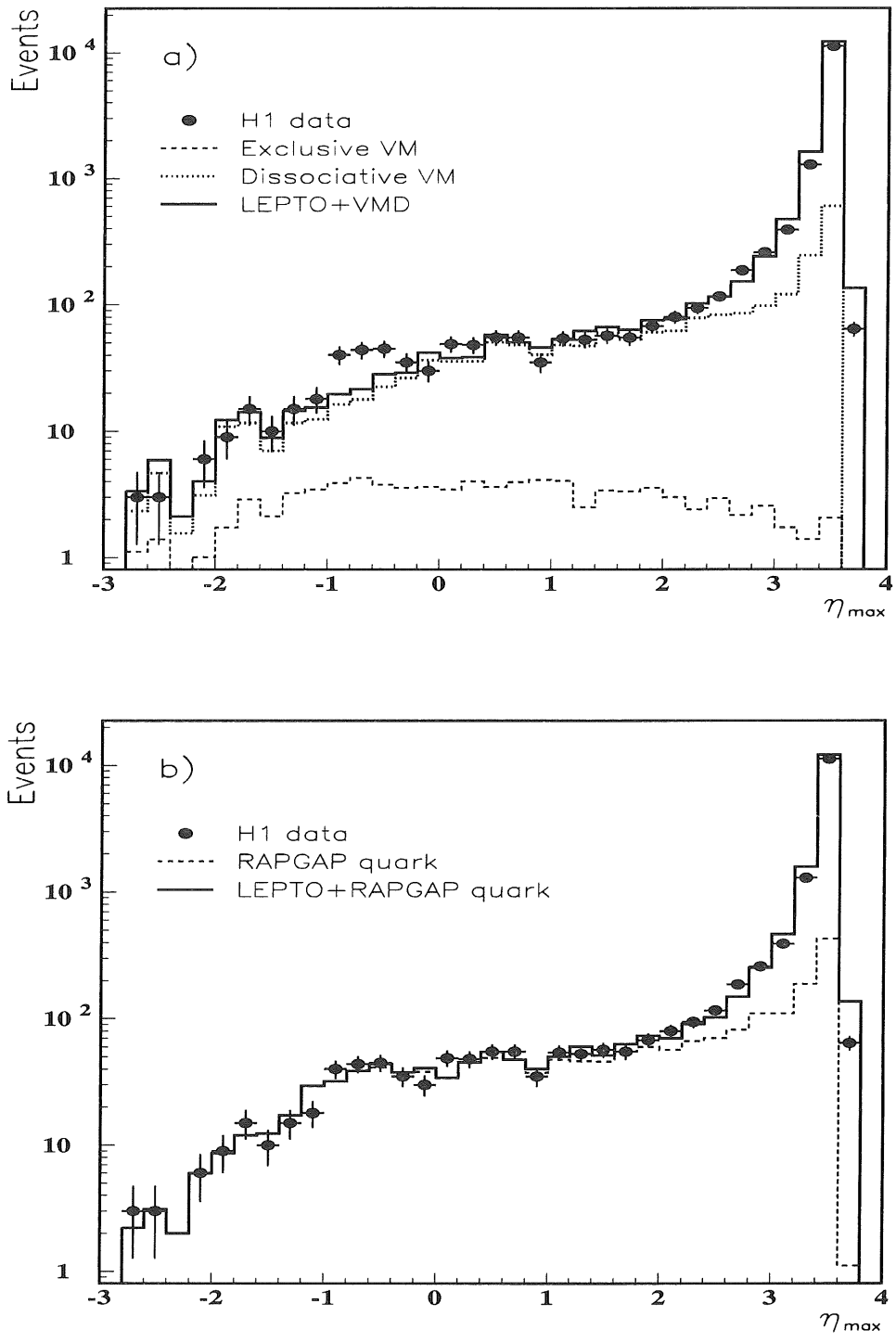

Figure 6.17: (a) Distribution of measured $\eta_{\max}$ for all DIS events together with the VMD expectation; shown are the contributions from exclusive ρ, ω and ϕ production (exclusive VM), from inelastic production (dissociative VM), and from the sum of total VMD and LEPTO.(b) Distribution of measured $\eta_{\max}$ for all DIS events with the VMD expectations from RAPGAP assumong a quark parametrization for the pomeron structure function, and from the sum of LEPTO and RAPGAP. The normalization of VMD and RAPGAP is such that each reproduces the number of observed DIS events with $\eta_{\max} < 1.8$.

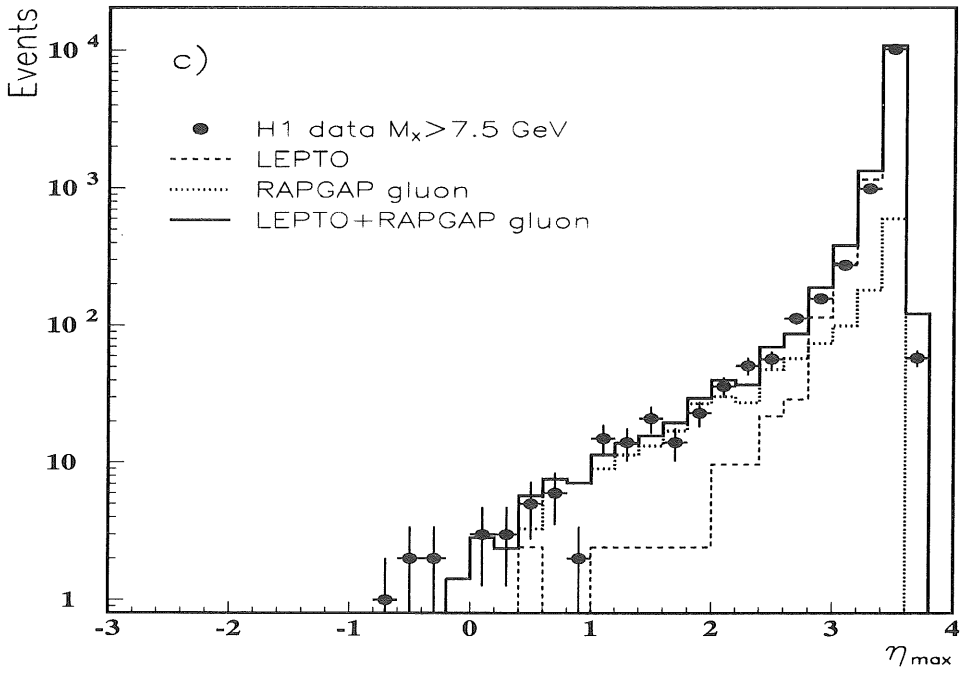

Figure 6.18: Distribution of measured $\eta_{\max}$ for all DIS events with measured invariant mass $M_X > 7.5\,\text{GeV}$ with the expectations from LEPTO, from RAPGAP assuming a hard gluon parametrization for the Pomeron structure function, and from their sum. The normalization of VMD and RAPGAP is such that each reproduces the number of observed DIS events with $\eta_{\max} < 1.8$.

structure of the Pomeron following from this assumption.

6.6.2 The Diffractive Structure Function F_2^D

The reaction to be analysed is thus

$$\gamma^*(q) + p(P) \rightarrow X + p'(P'). \tag{6.17}$$

Since we observe the exchange of a colourless object in DIS, we can in the next natural step investigate its substructure analogous to the investigation of the structure of the proton.

This has been done by the H1 Collaboration [206]. We have quantified the contribution of the rapidity gap events to the inclusive DIS structure function F_2 of the proton discussed in 6.2. In addition to the kinematic variables x and Q^2, the variables

$$x_{\mathbb{P}} = \frac{q \cdot (P - P')}{q \cdot P} \qquad \text{and} \qquad \beta = \frac{-\mathrm{q}^2}{2\mathrm{q} \cdot (\mathrm{P} - \mathrm{P}')} \tag{6.18}$$

are defined. Here q, P and P' are the 4-momenta of the virtual boson, the incident proton, and the final state colourless remnant respectively. The latter

can be either a nucleon or some excited state thereof. The relationship

$$x = \beta x_{\mathbb{P}} \tag{6.19}$$

holds. Neglecting the proton mass and the momentum transfer t in the t-channel we are measuring DIS at

$$x = \frac{Q^2}{Q^2 + W^2} \ll 1$$

followed by diffractive excitation of the virtual photon into the state X of mass M with W the total energy in the boson-proton CMS. The variable $x_{\mathbb{P}}$ can be written as

$$x_{\mathbb{P}} = \frac{(M^2 + Q^2)}{(W^2 + Q^2)} \ll 1$$

and interpreted as the fraction of the proton's momentum carried by the Pomeron, while

$$\beta = \frac{Q^2}{(Q^2 + M^2)}$$

is the Bjorken variable for the deep inelastic scattering on the Pomeron, i.e. the fraction of the Pomeron's momentum carried by the quark interacting with the boson. The final state proton, p', carries the fraction $(1-x_{\mathbb{P}})$ of the beam proton's momentum and is seperated from the hadronic final state X of the photon by the pseudorapidity gap $\Delta\eta \simeq \log\frac{1}{x_{\mathbb{P}}}$.

With the intermediate Pomeron the cross section becomes differential in 4 variables: the 4-momentum transferred at the virtual photon vertex, Q^2, the 4-momentum transferred at the proton vertex, t, the fraction of the proton's momentum carried by the Pomeron, $x_{\mathbb{P}}$, and the fraction of the Pomeron's momentum carried by the interacting parton, $\beta = x/x_{\mathbb{P}}$. The scaling property of this cross section is given by two structure functions as

$$\frac{d^4\sigma_{ep\to ep'X}}{dx dQ^2 dx_{\mathbb{P}} dt} = \frac{4\pi\alpha^2}{xQ^4}\left\{1 - y + \frac{y^2}{2[1 + R^{D(4)}(x, Q^2, x_{\mathbb{P}}, dt)]}\right\} F_2^{D(4)}(x, Q^2, x_{\mathbb{P}}, dt). \tag{6.20}$$

Since t is unmeasured in the current H1 setup, a particular choice of the t-dependence of the fourfold differential cross section $\frac{d^4\sigma(ep\to ep'X)}{dx dQ^2 dx_{\mathbb{P}} dt}$ is made and the threefold differential cross section $\frac{d^3\sigma(ep\to epX)}{dx dQ^2 dx_{\mathbb{P}}}$ is determined. We chose to set $R^{D(4)}$ to 0 for all t and we evaluated

$$\frac{d^3\sigma_{ep\to ep'X}}{dx dQ^2 dx_{\mathbb{P}}} = \frac{4\pi\alpha^2}{xQ^4}\left\{1 - y + \frac{y^2}{2}\right\} F_2^{D(3)}(x, Q^2, x_{\mathbb{P}}). \tag{6.21}$$

The event selection first of all was the standard DIS selection constrained to the kinematical ranges $7.5 < Q^2 < 70\,\mathrm{GeV}^2$ and $0.3 < y < 0.7$. After this, the selection procedure was modified compared to the investigation establishing this new class of events in DIS as discussed above. With the detector response in the forward region well understood by now, the selection could be based on a much

looser cut on $\eta_{\max}$ of $\eta_{\max} < 3.2$ and additional cuts based on detector elements situated in the forward direction, i.e. at large pseudorapidities. These are the PLUG calorimeter covering the pseudorapidity range from $3.54 < \eta < 5.08$ and the forward muon detector (FMD) covering $5.0 < \eta < 6.6$. The cut on the energy deposition in the PLUG was $E_{\mathrm{PLUG}} < 1\,\mathrm{GeV}$ and on the number of charged track segments reconstructed in the FMD $N_{\mathrm{FMD}} \leq 1$.

In order to perform the necessary acceptance and efficiency corrections, Monte Carlo simulations were performed using both the RAPGAP and the VMD model shown to describe the data. Because of the strong correlation between $\eta_{\max}$ and $x_{\mathbb{P}}$ as shown in Fig. 6.19, the evaluation of the Pomeron structure function is confined to small values of $x_{\mathbb{P}}$, i.e. $x_{\mathbb{P}} < 0.05$. The extraction of F_2^D from the

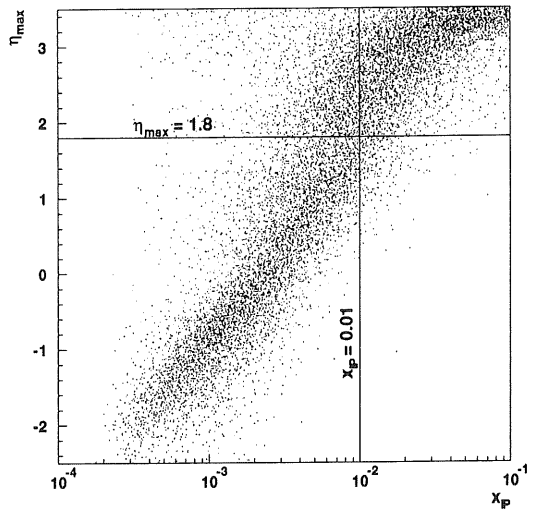

Figure 6.19: Correlation between η_{max} and $x_{\mathbb{P}/p}$ ($x_{\mathbb{P}}$ in the figure) from Monte Carlo studies by the H1 collaboration.

measured cross section was performed by means of Eq. (6.21). The β, Q^2, and x dependence of the measured data was transformed into the desired β, Q^2, and $x_{\mathbb{P}}$ dependence by using Eq. (6.19). The results for $F_2^D(\beta, Q^2, x_{\mathbb{P}})$ are shown in Fig. 6.20.

This result can unambiguously be interpreted by diffractive scattering or diffractive dissociation of the proton. The reason is the following: $F_2^{D(3)}$ was found to decrease monotonically with increasing $x_{\mathbb{P}}$ in the measured range $3 \cdot 10^{-4} < x_{\mathbb{P}} < 0.05$. An excellent fit to the data was obtained for the dependence $x_{\mathbb{P}}^{-n}$ with $n = 1.19 \pm 0.06(\mathrm{stat}) \pm 0.07(\mathrm{syst})$. Such a dependence on $x_{\mathbb{P}}$, independent of β and Q^2, is expected for the scattering off a (colourless) target which carries only a small fraction of the proton's momentum. The diffractive structure function can thus be written as a flux factor ($\propto x_{\mathbb{P}}^{-n}$) describing the flux of the target in the proton, and a term describing the structure of the target and which is only a function of β and Q^2. We will discuss this result in a little more detail in 6.7.

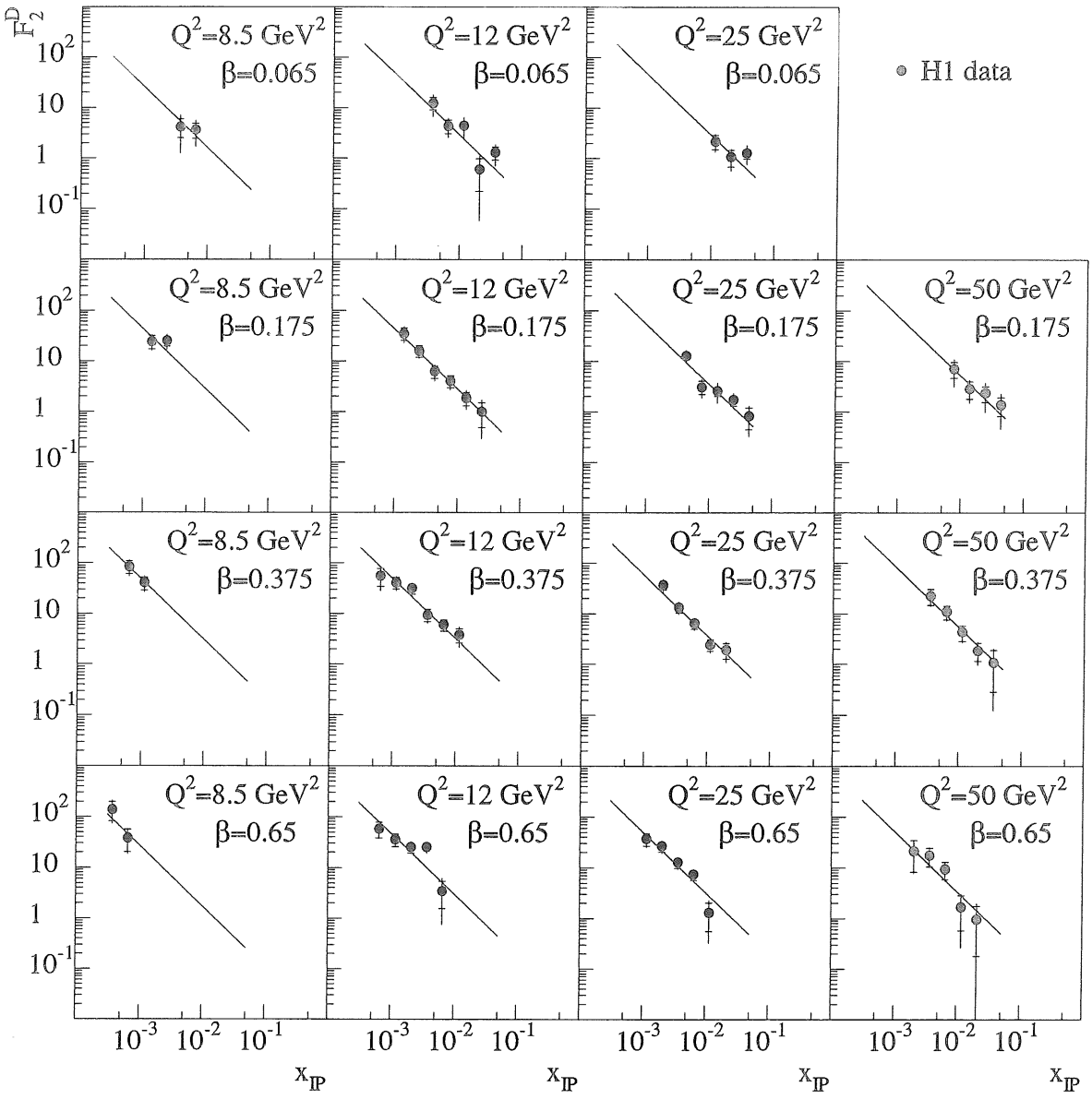

Figure 6.20: The diffractive contribution $F_2^{D(3)}(\beta, Q^2, x_{\mathbb{P}})$ to the proton structure function F_2 as a function of $x_{\mathbb{P}}$ ($x_{\mathbb{P}}$ in the figure) for different β and Q^2; the inner error bar is the statistical error; the full error shows the statistical and systematic error added in quadrature; superimposed is the result of the fit establishing a factorisable dependence of the form $\propto x_{\mathbb{P}}^{-n}$ (see text). Note that an overall systematic error of 8% is not included.

If we assume this scattering process to be "Reggeised", i.e. being mediated by a Reggeon, than the $x_{\mathbb{P}}$ dependence is specified by the leading Regge trajectory $\alpha(t)$ in the asymptotic limit $x_{\mathbb{P}} \to 0, t/s \to 0$. This dependence will be $x_{\mathbb{P}}^{-(2\alpha(t)-1)}$ (see Eq. (6.34)). Although we integrate over t in this analysis, with the assumption of the interaction to be peripheral, i.e. dominated by low t exchanges, we can replace $\alpha(t)$ by the intercept $\alpha(0)$. Inserting the observed $x_{\mathbb{P}}$ dependence, we find

$$\alpha(0) = 1.10 \pm 0.03(\text{stat}) \pm 0.04(\text{syst}). \tag{6.22}$$

This value is well compatible with the leading (effective) trajectory determining the total cross section as disussed in 5.3. Its intercept is $\alpha(0) = 1.085$ and its slope $\alpha' = 0.25\,\text{GeV}^{-2}$. Taking this slope into consideration and assuming a t-dependence known from peripheral interactions in soft pp collisions (e^{bt} with $b > 1$) we can estimate the systematic error on the above ignorance of any t-dependence to be less than 4%. With the leading meson trajectories only showing intercepts of about 0.5 (see 5.3), we can now exclude meson exchange being responsible for the observed rapidity gap events.

This brings us back to the BFKL Pomeron. Is it excluded by these data? The intercept of the BFKL Pomeron was found to be $\alpha_{\text{BFKL}}(0) \lesssim 1.5$. Combining in quadrature our statistical and systematic errors, the intercept cannot exceed 1.25 with 99.7% confidence. A recent calculation within the dipol ansatz for the BFKL Pomeron shows, however, that the ansatz of factorization of the $x_{\mathbb{P}}$ dependence into a term $\propto x_{\mathbb{P}}^{-n}$ may not strictly hold [207]. The "hard" Pomeron can thus not be excluded on the basis of these data.

We also determined the ratio of the diffractive contribution $F_2^D(x, Q^2)$ to the proton structure function $F_2(x, Q^2)$ [176] for $x_{\mathbb{P}} < 0.01$. Comparing the values of $F_2^D(x, Q^2)$ with $F_2(x, Q^2)$ for $x < 10^{-3}$ we find that the diffractive contribution amounts to about 10% of the proton structure function and can therefore not explain the steep increase of F_2 with decreasing x. The Q^2 dependence of $F_2^D(x, Q^2)$ at fixed x is found to be not significantly different from the Q^2 dependence of $F_2(x, Q^2)$ (see 6.7).

The determination of the size of the diffractive contribution relative to the inclusive cross section, however, may serve within Regge theory to determine the size of screening corrections as contained in Eqs. (5.119) or (5.120). This will be discussed in 6.7.

6.6.3 The DIS Structure of the Pomeron

With the factorization property of $F_2^{D(3)}(\beta, Q^2, x_{\mathbb{P}})$ over $3 \cdot 10^{-4} < x_{\mathbb{P}} < 0.05$ for different values of β and Q^2 established in the data, the β and Q^2 dependence of $F_2^{D(3)}$ can be interpreted as the deep inelastic structure of the diffractive exchange or the deep inelastic structure of the Pomeron. Assuming factorization,

the integral

$$\tilde{F}_2^D(\beta, Q^2) = \int_{0.0003}^{0.05} F_2^{D(3)}(\beta, Q^2, x_{\mathbb{P}}) dx_{\mathbb{P}} \tag{6.23}$$

is proportional to the structure function of the Pomeron. The range of integration was chosen to be the full measurement interval of $x_{\mathbb{P}}$. This is shown in Fig. 6.21.

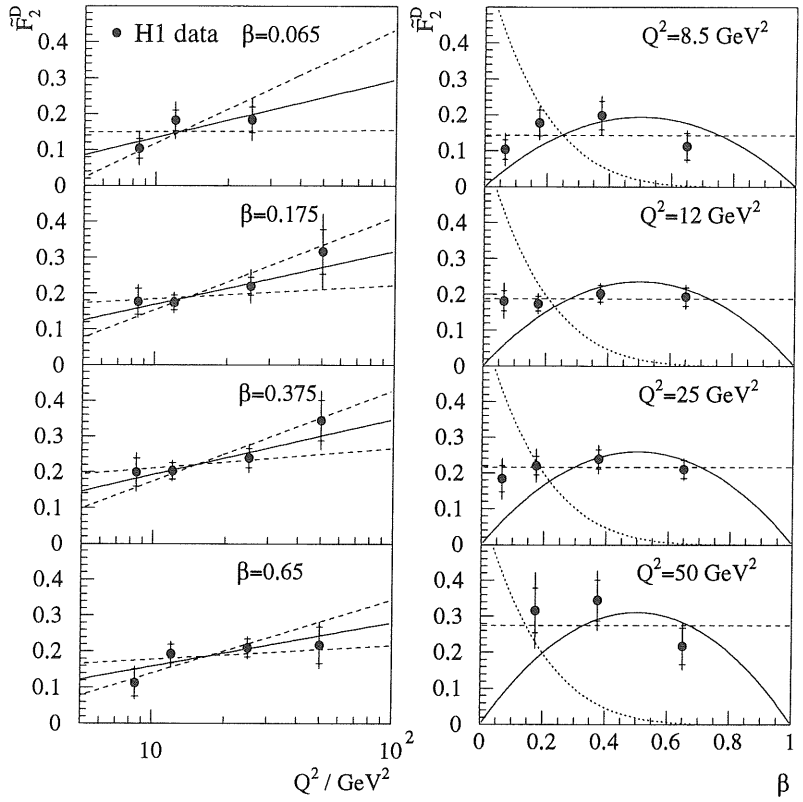

Figure 6.21: Dependence of $\tilde{F}_2^D(\beta, Q^2)$ on Q^2 and β^2; superimposed on the Q^2 dependence are the results of fits at each β which assume leading logarithmic scaling violations; the best fit (continuous curve) and the curves corresponding to change of ± 1 standard deviation (dashed curves) in the slope are shown; superimposed on the β dependence are the simplest $q\bar{q}$ expectation for $\mathbb{P}$ structure: $[\beta(1-\beta)]$ (continuous curve), and a constant dependence (dashed curve), for which the overall normalizations are determined from fits to the data; also displayed is a dependence of the form $[(1-\beta)^5]$ (dotted curves) with arbitrary normalization. Note that an overall normalization uncertainty of 8% is not included.

The form chosen here allows us to present the data without having to assume a normalisation, i.e. the flux of Pomerons. The data can directly be compared to theoretical predictions of the Pomeron structure.

The dependence of $\tilde{F}_2^D(\beta, Q^2)$ on Q^2 is found to be weak. QCD like logarithmic scaling violations though are permitted by the data. The interaction is thus nearly scale invariant and the scattering partners nearly point-like.

The β dependence of $\tilde{F}_2^D(\beta, Q^2)$ is also shown in Fig. 6.21 together with the expectations for a "hard" quark-antiquark like $\beta(1-\beta)$ behaviour of deep-inelastic diffraction. This type of dependence has been suggested by Donnachie and Landshoff [155], by the UA8 data [153], and results from the Nikolaev and Zakharov approach [207]. This behaviour is compatible with the data. A flat distribution, i.e. no dependence of F_2^D on β is also acceptable. A very soft ansatz like $(1-\beta)^5$ is ruled out on its own. The simplest interpretation of these data is thus that the events are due to the "soft" Pomeron having a two-parton "valence-like" substructure which carry most of the Pomeron's momentum. A contribution of a harder BFKL Pomeron cannot be excluded though.

6.7 Discussion of the Diffractive Structure Function

The HERA data on diffractive processes have served to give a boost to Regge theory. For an overview of diffraction in Regge theory see [209]. In this section we will discuss the H1 measurement of the diffractive structure function once within the framework of Regge theory extended by QCD and once within a picture advocated by Buchmüller.

As we will discuss in chapter 7, the real photon can be treated like a hadron up to some additional components. In the case of virtual photon-hadron scattering the smaller size of the virtual photon compared to the real photon introduces a Q^2 dependence. This is where the HERA experiments will contribute important information, since diffractive reactions in photoproduction and in DIS are going to be investigated at the same experimental setup.

6.7.1 Diffraction within Regge Theory

Triple-Pomeron graph

Within Regge theory the triple-Pomeron graph depicted in Fig. 6.22 is responsible for the high-mass single diffractive processes in hadron-hadron and real photon-hadron scattering. High mass in this context denotes masses larger than those of the vector mesons. The cut Pomeron gives rise to the multiparticle final state and the uncut Pomeron is responsible for the observable gap in rapidity.

Besides the triple-Pomeron also Reggeon-Pomeron-Pomeron and Reggeon-Reggeon-Pomeron processes may contribute to the diffractive process. These mainly contribute to the small-mass diffraction and lead to differential cross sections with different dependences on the produced mass. These channels will not be discussed

any further. In hadronic or real photon interactions, the triple-Pomeron regime corresponds to large CMS energies. In DIS, the kinematical region has to be defined by a set of cuts (see below and [208]).

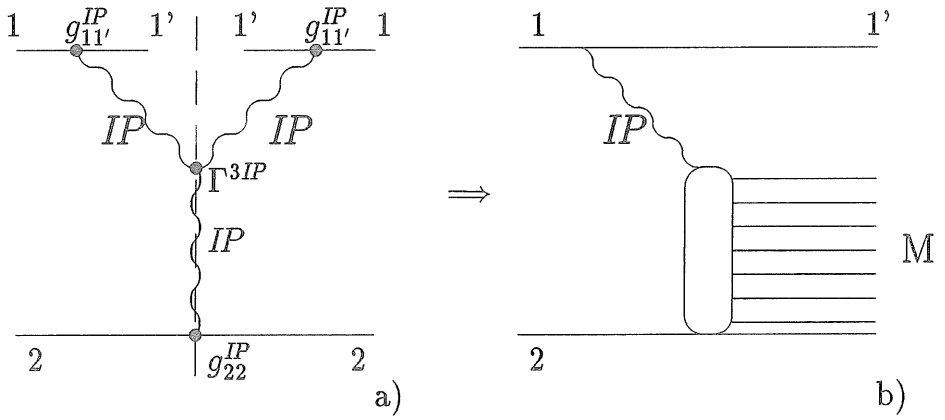

Figure 6.22: The cut triple-Pomeron graph giving rise to high-mass single diffractive final states on the side of the cut Pomeron and to a rapidity gap on the side where the cut is between the two Pomerons.

The Pomerons are defined by propagators $\xi_{\mathbb{P}}(t)(s/s_0)^{\alpha_{\mathbb{P}}(t)}$ with the signature factor

$$\xi_{\mathbb{P}}(t) = -\frac{1 + e^{-i\pi\alpha_{\mathbb{P}}(t)}}{sin(\pi\alpha_{\mathbb{P}}(t))}. \tag{6.24}$$

M is the mass of the diffractively produced system, $\alpha_{\mathbb{P}}(t) = 1 + \Delta + \alpha'_{\mathbb{P}}(0)t$ the Pomeron trajectory, $s_0 = 1\,\mathrm{GeV}^2$, and $g_{11'}^{\mathbb{P}}$, $g_{22}^{\mathbb{P}}$, and $\Gamma^{3\mathbb{P}}$ are the couplings as indicated in Fig. 6.22. In DIS, QCD effects will lead to a Q^2 dependence of the effective couplings. An experimental determination may help to uncover the nature of these effects, i.e. which type of approximation is necessary in which region of phase space, and will thus influence EAS simulations.

The cross section for this process is given in lowest order as

$$\frac{d^2\sigma_{3\mathbb{P}}(s,t)}{dtdM^2} = \frac{1}{16\pi s^2}|g_{11'}^{\mathbb{P}}(t)|^2 g_{22}^{\mathbb{P}}(0)\Gamma^{3\mathbb{P}}(t,0)|\xi_{\mathbb{P}}(t)|^2 \left(\frac{s}{M^2}\right)^{2\alpha_{\mathbb{P}}(t)} \left(\frac{M^2}{s_0}\right)^{\alpha_{\mathbb{P}}(0)}. \tag{6.25}$$

The salient features of this equation are i) the functional dependence dM^2/M^2 for the diffractively produced mass and ii) it allows to extract the triple-Pomeron coupling $\Gamma^{3\mathbb{P}}$ [209]. Based on Tevatron data this has been done by Golec-Biernat and Kwieciński in [211].

Following Kaidalov [209], the total cross section for the interaction of particle b (denoted 2 in Fig. 6.22) with the Pomeron can be introduced and written as

$$\sigma_{\mathrm{tot}}^{p\mathbb{P}}(M^2,t) = g_{22}^{\mathbb{P}}(0)\frac{\Gamma^{3\mathbb{P}}(t,0)}{s_0}\left(\frac{M^2}{s_0}\right)^{\alpha_{\mathbb{P}}(0)-1}. \tag{6.26}$$

The diffractive cross section Eq. (6.25) can in this picture be interpreted as the product of a Pomeron flux factor times this cross section, i.e.

$$\frac{d^2\sigma_{3\mathbb{P}}(s,t)}{dtdM^2} = \frac{1}{16\pi s^2}|g^{\mathbb{P}}_{11'}(t)|^2|\xi_{\mathbb{P}}(t)|^2\frac{s^{2\alpha_{\mathbb{P}}(t)}}{(M^2)^{2\alpha_{\mathbb{P}}(t)-1}}\sigma^{p\mathbb{P}}_{\rm tot}(M^2,t). \tag{6.27}$$

These formulae allow to extract the total Pomeron-particle cross section from the data provided the triple-Pomeron coupling is known. Once the detectors for the final state proton p' now under construction become operational, HERA data will contribute to this measurement.

The triple-Pomeron coupling can be extracted from data in the so-called triple-Pomeron regime in the reaction $a + p \to X + p'$, where a may be a hadron or a real photon(Q^2 =0) via

$$\frac{M^2}{\sigma^{ap}_{\rm tot}} \cdot \frac{d\sigma_D(a \to X)}{dtdM^2}\,|_{t=0} \approx \Gamma^{3\mathbb{P}}. \tag{6.28}$$

For virtual photons, in order to extract this coupling, the kinematical region has to be chosen such that Pomeron exchange is dominating over Reggeon exchange; this is valid for $x_{\mathbb{P}} < 0.05 - 0.1$ and/or the rapidity gap extending over 2.5-3 units. Then in DIS

$$\frac{M^2+Q^2}{\sigma^{\gamma^*p}_{\rm tot}} \cdot \frac{d\sigma_D(\gamma^* \to X)}{dtdM^2}\,|_{t=0} \approx \Gamma^{3\mathbb{P}}. \tag{6.29}$$

The first direct calculation of this quantity based on the dipole approach to the BFKL Pomeron has been performed by Genovese *et al.* [208]. They find satisfactory agreement between calculation ($\Gamma^{3\mathbb{P}} = 0.23\,\mathrm{GeV}^{-2}$) and the measurement of $\Gamma^{3\mathbb{P}} \approx 0.16\,\mathrm{GeV}^{-2}$ [210]. In addition, they predict a rise of $\Gamma^{3\mathbb{P}}(Q^2)$ by a factor of 1.6 between $Q^2 = 0$ and $Q^2 \approx 10\,\mathrm{GeV}^2$. Forthcoming HERA data and supplementary forward detectors will help to test this prediction and thus help to identify which QCD corrections have to be applied to the Regge picture.

Since the couplings introduced in Fig. 6.22 enter into the Monte Carlo programs for EAS, HERA data will provide important input at this point once the forward directions of the detectors are equipped and read out.

Pomeron Structure and Diffraction Dissociation Cross Section

The total cross section, $\sigma^{p\mathbb{P}}_{\rm tot}$, contains both soft and hard processes. The Pomeron structure function, $\tilde{F}_2^D(\beta,Q^2)$, can be converted into the individual Pomeron parton densities, $f^{\rm i}_{\mathbb{P}}(\beta,Q^2)$, provided enough data are assembled. These densities enter into hard diffractive processes, i.e. jet production in rapidity gap events, like the parton densities of ordinary hadrons (see Eq. (5.126)) as

$$\sigma^{p\mathbb{P}}_{\rm hard} = \sum_{i,j,k,l}\frac{1}{1+\delta_{kl}}\int_0^1 d\beta_1\int_0^1 d\beta_2\int_{p_{\rm T,min}} d\hat{t}\frac{d\hat{\sigma}_{\rm QCD,ij\to kl}}{d\hat{t}} f^{\rm i}_p(\beta_1,Q^2) f^{\rm j}_{\mathbb{P}}(\beta_2,Q^2) \tag{6.30}$$

with $p_{T,min}$ the usual QCD regularization cutoff. With the H1 results on the diffractive structure function and the structure of the Pomeron, these processes may be calculated and compared to the data. These measurements will be important to check the consistency of EAS Monte Carlo generators.

Another possibility to determine the parton densities in the Pomeron is to relate the Pomeron structure function to the deuterium structure function using Regge arguments and thus extract the quark densities. This was done in the studies by Capella *et al.* [212] and Engel *et al.* [213] with the additional assumption of a gluon contribution deduced from the HERA data in [213]. The prediction for the Pomeron structure function obtained by Engel *et al.* is shown in Fig. 6.23. The study performed by Capella *et al.*, for comparison, arrives at a somewhat softer Pomeron structure function, with the same qualitative behaviour at low $x = \beta$.

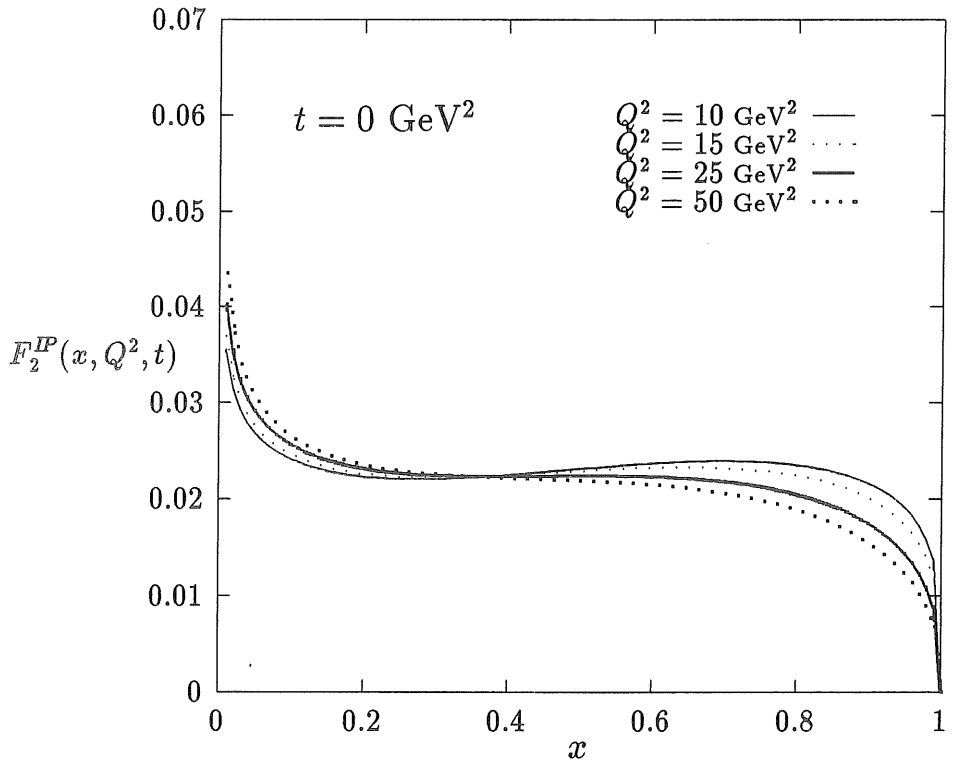

Figure 6.23: The Pomeron structure function $F_2^{I\!P}(x, Q^2, t = 0)$ with $x = \beta$ as calculated by Engel *et al.* [213] within the framework of the Dual Parton Model. The Q^2 evolution is based on leading $\log(1/x)$ approximation.

The qualitative comparison with the H1 data shown above reveals a potential problem at low β values for both predictions and at large x for the prediction of Capella *et al.* [212]. The data statistics is too low, however, to draw strong conclusions. The results of the study of Engel *et al.* [213] concerning hard diffractive processes in photoproduction will be shown in 7.7.

The absolute size of the diffractive cross section is an important measurement for EAS, since it allows to determine the size of shadowing corrections. If we write the structure function as

$$F_2(x,Q^2) = F_2^{\mathrm{GLAP}}(x,Q^2) - \Delta F_2(x,Q^2), \tag{6.31}$$

Levin and Wüsthoff [214] have shown that from the AGK cutting rules it follows that

$$\left|\frac{\Delta F_2(x,Q^2)}{F_2(x,Q^2)}\right| = \frac{\sigma_{\gamma^* p}^{\mathrm{DD}}}{\sigma_{\mathrm{tot}}}. \tag{6.32}$$

The measurement of $\sigma_{\gamma^* p}^{\mathrm{DD}}$ is thus an important experimental observable in order to get a handle on the screening corrections due to parton saturation. As shown in 6.6.2 the size of the diffractive structure function measured by H1 relative to the inclusive one is about 10%.

At the same time, based on Regge theory, the screening corrections to $F_2^p(x,Q^2)$ can be calculated provided the Pomeron structure is known. In [212] this calculation was performed at $Q^2 = 15\,\mathrm{GeV}^2$ and $30\,\mathrm{GeV}^2$ in the x-interval $10^{-4} < x < 10^{-3}$ based on the Pomeron structure function derived in that study, and resulted in 16 - 18% shadowing contribution at $Q^2 = 15\,\mathrm{GeV}^2$ and 12 - 14% at $Q^2 = 30\,\mathrm{GeV}^2$ at $x = 10^{-4}$ in rough agreement with the ratio of F_2^D to F_2.

Taking the measured fraction of F_2^D relative to F_2 as the size of the diffraction dissociation cross section relative to the total cross section, the size, R, of the gluon concentration region contained in Eqs. (5.119) and (5.120) can be determined from the 10% screening corrections observed in the data. R turns out to be of the same size as the proton radius r_{proton} [215] (see also [168]). If we thus interpret F_2^D as the signal of screening due to parton saturation, the saturation sets in distributed over the whole proton and not in much smaller hot-spots.

6.7.2 Regge Theory Ansatz and QCD

Golec-Biernat and Kwieciński [211] have performed a QCD analysis of the diffractive structure function assuming the dominance of the "soft" Pomeron. To describe the diffractive process $\gamma^* + p \to X + p$ the factorizing ansatz for the diffractive structure function

$$\frac{dF_2^D(x_{\mathbb{P}},\beta,Q^2,t)}{dx_{\mathbb{P}}\,dt} = f(x_{\mathbb{P}},t)F_2^D(\beta,Q^2,t) \tag{6.33}$$

with $f(x_{\mathbb{P}},t)$ the "Pomeron flux factor" and $F_2^D(\beta,Q^2,t)$ the Pomeron structure function was found to describe the data. The "Pomeron flux factor" can be written as

$$f(x_{\mathbb{P}},t) = N x_{\mathbb{P}}^{1-2\alpha_{\mathbb{P}}(t)} \frac{B^2(t)}{16\pi} \tag{6.34}$$

with $B(t)(= g_{11'}^{\mathbb{P}}$, see Fig. 6.22) the coupling of the Pomeron to a proton. This coupling is normalized such that the total pp cross section is given by

$$\sigma_{\text{tot}} = B^2(0)\left(\frac{s}{s_0}\right)^{\alpha_{\mathbb{P}}(0)-1} \tag{6.35}$$

and N a normalization factor chosen as $2/\pi$. The coupling $B(t)$ was chosen as

$$B(t) = 4.6\text{mb}^{1/2} e^{1.9\text{GeV}^{-2}t}. \tag{6.36}$$

The parton densities in the Pomeron were chosen at the reference scale $Q_0^2 = 4\,\text{GeV}^2$ and evolved with leading order DGLAP evolution equations with $\Lambda = 0.255\,\text{GeV}$. The functional form for the individual parton densities can be found in [211]. The resulting prediction for the Q^2 and β dependence of the diffractive structure function is shown in Fig. 6.24 together with the H1 data shown in 6.6.

Within the large measurement errors satisfactory agreement is found. Further measurements with higher statistics and the incorporation of NLO QCD predictions for the ratio of the longitudinal to transverse diffractive structure function as also calculated in [211] will yield more insight into the Pomeron structure as assumed in this type of analysis.

6.7.3 The Buchmüller Approach to Diffraction

The behaviour of $F_2^D(x, Q^2)$, i.e. the independence of the ratio of diffractive to inclusive cross section as a function of Q^2, is the signal of the diffractive cross section being a "leading twist" effect just like the inclusive cross section given by F_2. With a leading twist effect commonly regarded as evidence for scattering on point-like scattering this cross section should be calculable within QCD similar to F_2. The problem to overcome, however, is that quarks and gluons carry colour.

A promising ansatz in this direction which is not based on the QCD Pomeron or the phenomenological Pomeron has been proposed and worked out by Buchmüller and co-workers [216, 217, 218]. In this semi-classical model diffractive scattering is due to $q\bar{q}$ pair production in electron-gluon scattering and a non-perturbative mechanism of colour neutralization in which "wee partons" are treated as a classical colour field. To work out the prediction the inclusive production cross section of quark-antiquark pairs proceeding through the photon-gluon fusion process as depicted in Fig. 6.25 has to be calculated.

The inclusive cross section $\frac{d\sigma(ep\to e(q\bar{q}X))}{dx dQ^2 d\xi}$ at small values of x is dominated by the gluon density and will thus be simply proportional to the gluon density in the proton. The variable ξ here replaces the variable $x_{\mathbb{P}}$ used up to now to signify it's different meaning in this model. Essentially the calculation corresponds to calculating the sea quark densities at the scale Q in terms of the gluon density $g(\xi)$ at a scale $m_g = \mathcal{O}(1\,\text{GeV})$. From the inclusive $ep \to e(q\bar{q}X)$ cross section

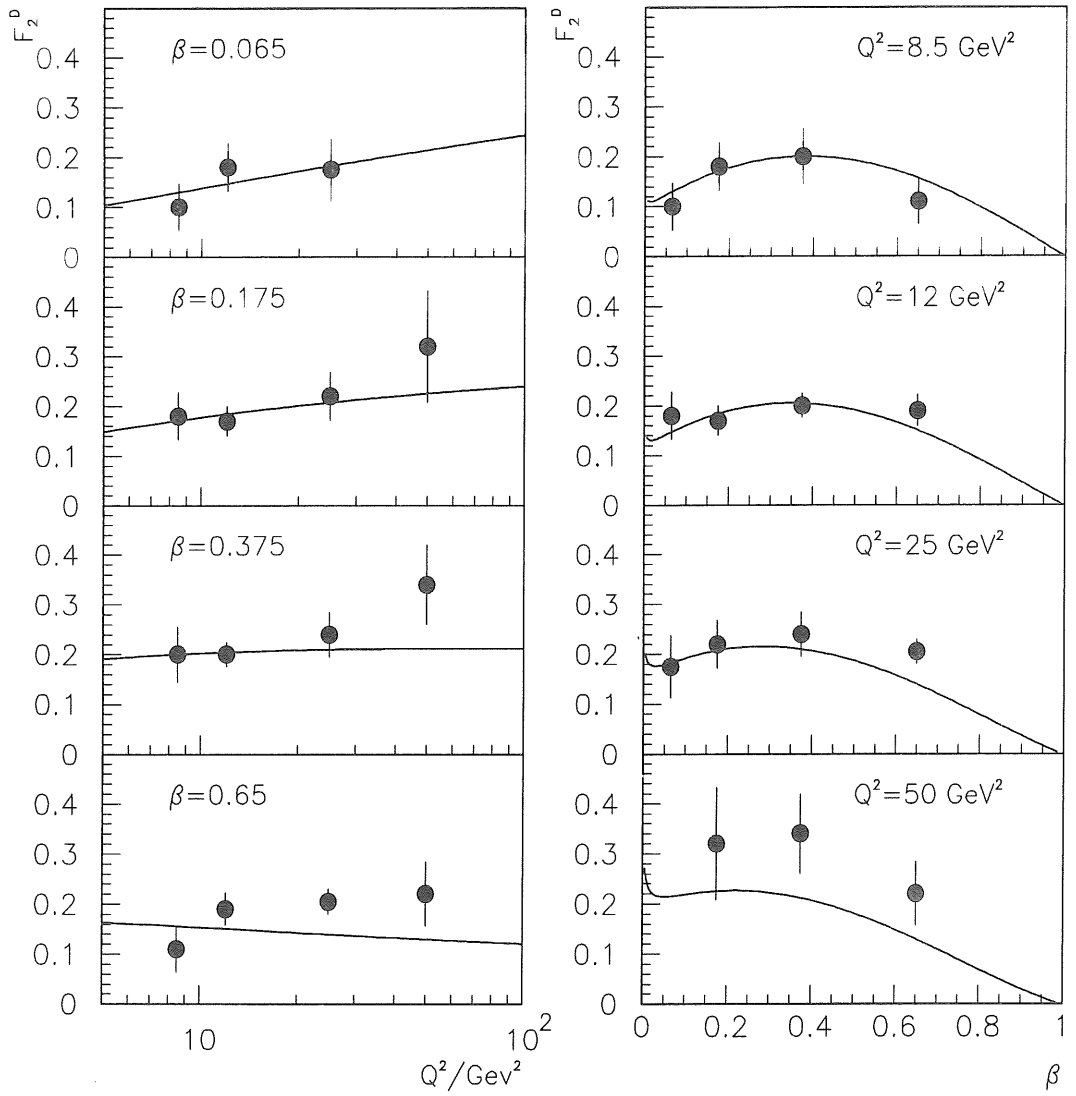

Figure 6.24: Comparison of the theoretical prediction by Golec-Biernat and Kwieciński [169] for the diffractive structure function $\tilde{F}_2^D(\beta, Q^2)$ with the H1 data shown in Fig. 6.20.

the inclusive structure function $F_2(x, Q^2)$ follows as

$$F_2(x, Q^2) = x\frac{\alpha_s}{2\pi}\sum_q e_q^2 \int_x^1 \frac{d\xi}{\xi} g(\xi) B(\beta, Q^2) \tag{6.37}$$

with

$$B(\beta, Q^2) = (\beta^2 + (1-\beta)^2)\ln\frac{Q^2}{m_g^2\beta^2} - 2 + 6\beta(1-\beta). \tag{6.38}$$

The calculation is performed in the "massive gluon" scheme where the virtuality $m_g^2 = -p_g^2 \ll Q^2, M^2$ of the gluon, with $\vec{p}_g = \xi\vec{P}$, is used as regularization cut-off when integrating over ξ. Parametrizing the gluon density by

$$g(\xi) = A_g \xi^{-1-\lambda} \tag{6.39}$$

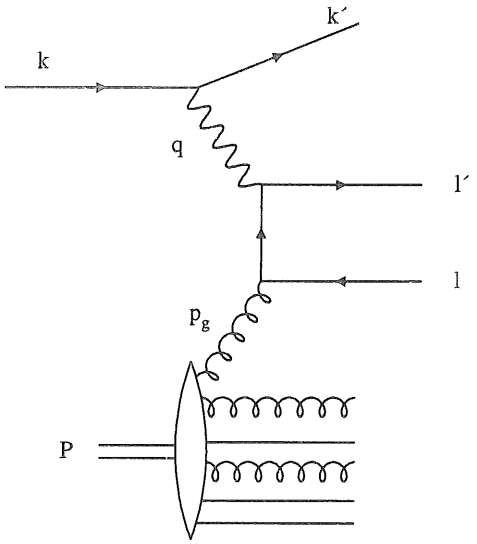

Figure 6.25: Quark-antiquark pair production in electron-gluon scattering [218].

where A_g is a constant, the inclusive structure function $F_2(x, Q^2)$ is obtained for small values of the exponent λ as

$$F_2(x, Q^2) \simeq \frac{\alpha_s}{3\pi} \sum_q e_q^2 x g(x) \left(\frac{2}{3} + \ln \frac{Q^2}{m_g^2} \right). \tag{6.40}$$

Buchmüller and Hebecker find good aggreement with the H1 data on F_2 for $\lambda = 0.23$, $m_g = 1.0\,\mathrm{GeV}$, and $A_g \alpha_s \sum_q e_q^2 = 0.61$.

The diffractive structure function as defined in Eq. (6.21), with $x_{\mathbb{P}} = \xi$, now is derived utilizing the idea that the quark-antiquark pair produced in a colour octet state, with some probability $P_1 = 1 - P_8$, evolves into a colour singlet state within the colour field of "wee partons" in the proton. Here P_8 is the corresponding probability for the evolving partonic system to stay in a colour octet state and which leads to colour and corresponding hadron flow between the proton remnant and the final state fragments. The underlying picture is one of a fast rotating colour spins where then the probabilities are simply given by the statistical weight factors for the possible states of the quark-antiquark pair, which are $P_1 \simeq 8/9, P_8 \simeq 1/9$. Thus

$$\int_x^1 d\xi F_2^D(x, Q^2, \xi) \simeq \frac{1}{9} F_2(x, Q^2) \tag{6.41}$$

and the diffractive structure function is unambiguously predicted.

The form of the diffractive structure function, i.e.

$$F_2^D(x, Q^2, \xi) \simeq \frac{1}{9} \frac{\alpha_s}{2\pi} \sum_q e_q^2 g(\xi) \tilde{F}_2^D(\beta, Q^2) \tag{6.42}$$

with $\tilde{F}_2^D(\beta, Q^2) = \beta B(\beta, Q^2)$ and $B(\beta, Q^2)$ given by Eq. (6.38) is thus also factorizing into a flux factor $g(\xi)$ corresponding in the Ingelman-Schlein ansatz to the "Pomeron flux factor" and the differential distribution for the production of quark-antiquark pairs with the invariant mass $M^2 = (q + p_g)^2$ which can be identified as the "Pomeron structure function". Buchmüller and co-workers achieve a good description of the measured H1 data. The experimental data can be parametrized as

$$F_2^D(x, Q^2, \xi) \propto \ln(Q^2)\xi^{-n} \tag{6.43}$$

with $n = 1.19 \pm 0.06 \pm 0.07$ which is in good agreement with the determination of $\lambda = 0.23$.

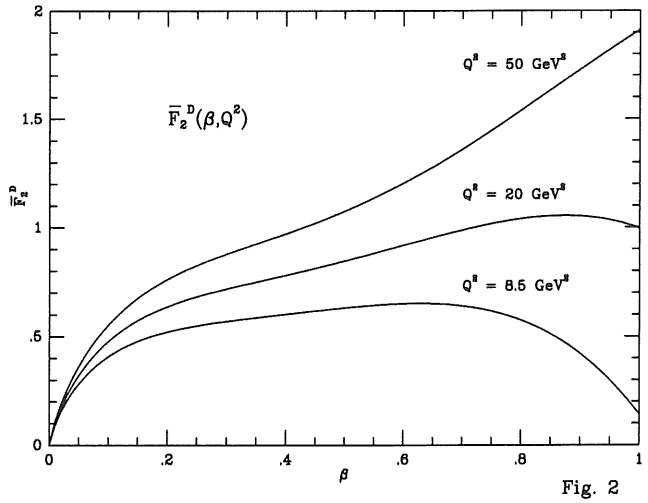

Figure 6.26: The dependence of the diffractive structure function on β and Q^2 as predicted in the model by Buchmüller et al.. Taken from [218].

This model is very appealing, since the Pomeron does not have to be introduced as a partonic object within the proton. The predictions of this model concerning the size of the diffractive contribution, i.e. 1/9 of the inclusive cross section, and the shape of the differential cross section for producing quark-antiquark pairs with the invariant mass $M^2 = Q^2(1-\beta)/\beta$ in the form $\tilde{F}_2^D(\beta, Q^2)$ agree well with most of the data points as can be judged by qualitatively comparing Fig. 6.26 and Fig. 6.21. The authors caution however that still some additional theoretical work is needed on the model.

Chapter 7

Hadronic Photon Interactions

At EAS experiments we are primarily searching for the sources of γ radiation. To distinguish γ and hadron initiated showers we have to know the possible reaction channels of real photons. The channel that we want to utilize is the Bethe-Heitler pair production process $\gamma \rightarrow e^+e^-$ with a cross section of about 500 mb giving rise to a distinctive electromagnetic airshower in the atmosphere.

As known for a long time, the photon not only interacts electromagnetically as a pointlike object, but can also interact strongly like a hadron. In this chapter we will discuss H1 measurements important for EAS experiments. This will first of all be the measurement of the total γp cross section. As will be discussed in 7.1, "soft" photon-proton and proton-proton interactions are expected to be very similar due to the hadron-like nature of the photon in many interactions. This opens up the possibility to perform analogous analyses as discussed in chapter 6 concerning the structure of the Pomeron in diffractive γp events which are again characterized by rapidity gaps observed in the detector. The main results in this direction are expected from the ongoing analyses where the characteristics measured for virtual photon scattering are compared in detail to the characteristics of real photon scattering. These analyses are not completed yet and will not be discussed here. Due to the very similar nature of the individual analyses and results, we will not discuss all of these analyses here and only concentrate on a few aspects of photon proton interactions at HERA and the discussion thereof. A result derived from real photon interactions which shows the potential of these studies with respect to the structure of the Pomeron concerns hard diffractive processes and will be presented in 7.7.

In the case of virtual photon-hadron scattering the smaller size of the virtual photon compared to the real photon introduces a Q^2 dependence. At this point the HERA experiments will contribute important information, since diffractive reactions in photoproduction and in DIS are going to be investigated at the same experimental setup. This we will take up again in the discussion in chapter 9.

7.1 Overview of Photon-Proton Interactions

A picture to describe the hadronic interactions of the photon was developed in the early years of strong interaction experiments and is known as Vector Meson Dominance (VMD) model [219, 220]. In this model, at low four-momentum transfer, prior to the interaction, the photon turns into a vector meson which has the same quantum numbers as the photon, i.e. a $\rho(770), \omega(782), \phi(1020), J/\psi(3097)$. This vector meson then interacts strongly with the target hadrons.

In the framework of QCD these interactions can be regarded as due to the photon's interactions with the QCD vacuum which lead to it fluctuating into pairs of charged leptons or quarks. According to the uncertainty principle, the pair the photon fluctuates into can live for a time

$$\Delta t = \frac{2E_\gamma}{m^2_{\text{pair}}}. \tag{7.1}$$

At high photon energies, if the photon fluctuates into a $q\bar{q}$ pair, this time may be long enough for the quark-antiquark pair to form a complex partonic object due to quark-gluon cascades. This hadron-like object may then interact with the target. If the mass of the quark-antiquark pair is equal to the mass of a vector meson, a hadron is formed. This part of the cross section will be described by the VMD model. In the extended VMD model, the Generalized VMD model, a continuous spectrum of non-bound hadronic states is added to account for measured differential cross sections [220].

Since the photon is a point-like colour neutral boson, in addition to this hadronic channel another strong interaction channel is open. This is the so-called anomalous photon splitting into a $q\bar{q}$ pair prior to the interaction. These very hard partons then can interact with target photons. In case of the anomalous channel, radiation of daughter partons can be treated within perturbative QCD. This contribution to the scattering cross section is characterized by a transverse momentum cutoff $p_{\text{T,min}}$ which regularizes the amount of hard scattering (mini-jet production) resulting from the interaction of the resolved partons in the photon with partons in the target hadron.

Analogous to the proton structure function we can define a phenomenological photon structure function to express the differential cross section for $e\gamma$ scattering as

$$\frac{d\sigma(e\gamma \to eX)}{dxdy} = \frac{2\pi\alpha^2 s}{Q^4}[1-(1-y)^2]F_2^\gamma \tag{7.2}$$

where we have neglected the contribution corresponding to the longitudinal polarization of the virtual photon. The structure function F_2^γ expressed in terms of x and Q^2 describes the x-weighted probability to find a quark within the photon. The photon structure function can be measured in deep inelastic scattering with a photon target. In these experiments a (almost) real photon γ as the target is studied by a virtual photon γ^* probe. This type of experimental setup is found in

e^+e^-experiments in the $\gamma\gamma$ reactions where one photon is almost on-shell while the other is the high virtuality probe. For a review on $\gamma^*\gamma$ scattering see [221].

Fig. 7.1 shows the photon structure function as measured by the PLUTO collaboration [222] at $Q^2 = 5.3\,\mathrm{GeV}^2$. This structure function differs considerably from a typical hadron structure function as it is rising towards large x while a typical hadron structure function shows the opposite behaviour indicated by the dashed line.

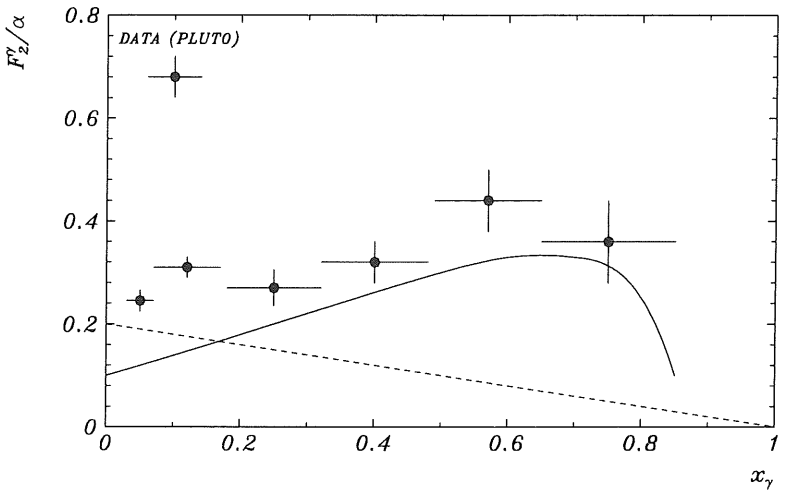

Figure 7.1: The photon structure function as measured by PLUTO [222] at $Q^2 = 5.3\,\mathrm{GeV}^2$.

For γp interactions at HERA, the Feynman graphs giving rise to hard interactions are shown in Fig. 7.2. These interactions consist firstly of the so-called direct processes of QCD-Compton scattering and photon-gluon fusion in which the photon interacts as a pointlike particle. Additionally there are the resolved processes stemming either from the VMD component or from the anomalous photon splitting into a $q\bar{q}$ pair before the partonic interaction. From these four processes only the VMD component dominated by low x contributions occurs in hadron-hadron interactions. This explains the hard photon structure compared to a hadron.

The expectation thus is that the photon structure function at low x is similar to the one of stable hadrons like a ρ meson or a pion, whereas at large x the anomalous and direct contributions play important rôles. In this picture, the photon structure function can be constructed out of the following three pieces:

- a pointlike contribution, $F_2^{\gamma,\mathrm{direct}}$,
- the VMD contribution, $F_2^{\gamma,\mathrm{VMD}} \propto F_2^{\rho^0} \simeq F_2^{\pi^0}$, and
- a contribution calculable within perturbative QCD, $F_2^{\gamma,\mathrm{anomalous}}$.

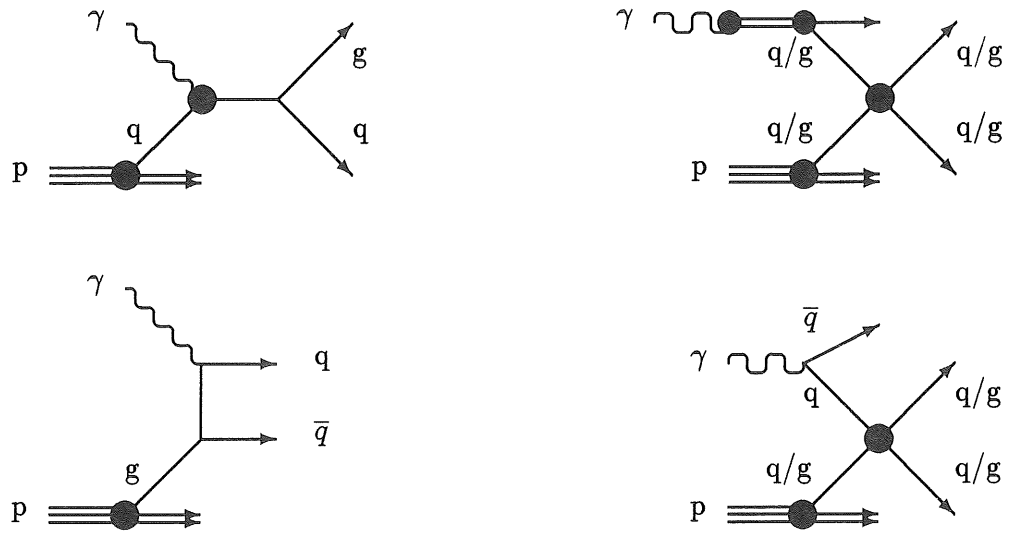

Figure 7.2: Hard γp processes: left part with the direct processes QCD-Compton (top) and photon-gluon fusion (bottom); right part with resolved processes from the hadronic VDM component (top) and anomalous or pointlike component (bottom).

From these contributions, $F_2^{\gamma,\text{direct}}$ is calculable within QED and the anomalous one within QCD. The anomalous contribution is experimentally not distinguishable from the hadron-like contribution, but this picture turns out to be useful when studying the differences between photon and hadron interactions.

In ep collisions, the process of γp interactions where the γ is real is termed photoproduction. With the above picture of the hadron-like photon, we expect to observe in photoproduction reactions measurable at HERA a similar diversity of final states as in hadron-hadron reactions, and in addition a dominance of soft hadronic processes just as observed in hadron-hadron interactions.

Before the startup of HERA calculations were performed in which the total cross section for photon-proton scattering was predicted to rise very sharply at photon energies equivalent to fixed target energies around 10 TeV due a strong enhancement of the QCD hadron-like photon interactions giving rise to mini-jets similar to the one observed in hadron-hadron collisions [159]. See the discussion in 3.3.1.

Turning to the measurements performed at H1, we have to distinguish the various photon components by experimental observables. These turn out to be the transverse momenta of the hadronic final state and the kinematics of observed jets. At HERA, the interactions of quasi-real photons with protons involve transverse momenta from effectively $p_T = 0$ (in the measurement of the total cross section σ_{tot}), small, i.e. $p_T \leq 1$ GeV/c (in the elastic production of ρ^0 vector mesons) through $p_T \geq 10$ GeV/c (resulting in the production of clearly separated jets).

The above discussed model of γp interactions can be summarized in the following

picture. Note, that in this generic model we treat the total cross section for photoproduction as the *incoherent sum* of the three contributions which arise from three different manifestations of the photon in its interactions [223]. See 7.8. Schematically:

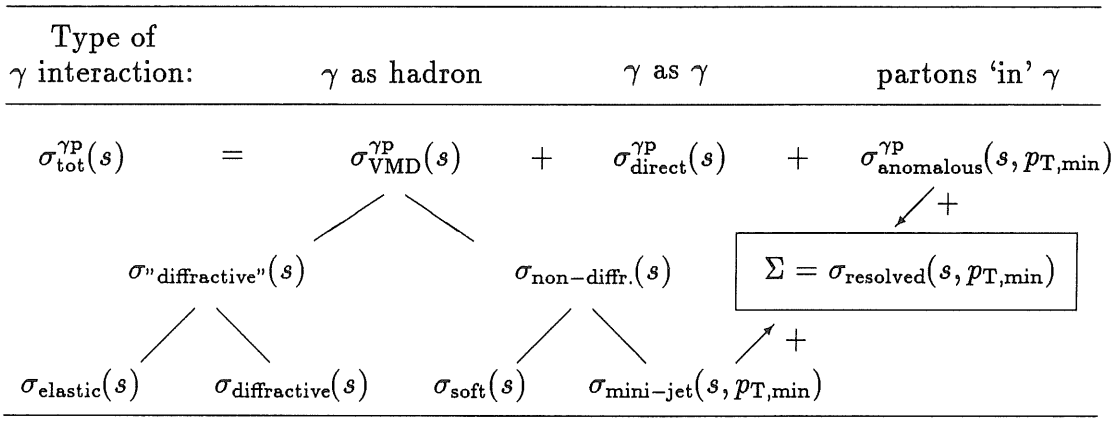

Different aspects of the data are sensitive to different ingredients of this model.

The measurement of the total cross section, $\sigma_{tot}^{\gamma p}$(s), restricts the sum of the components as well as the regularization cutoff $p_{T,min}$ and it is sensitive to the relative ratios of the cross sections. The measurement of vector meson production and of the event rate of rapidity gap events will determine $\sigma_{\text{"diffractive"}}$(s) and the jet cross sections will restrict $\sigma_{resolved}$(s, $p_{T,min}$) and σ_{direct}(s).

The selection of results discussed in the following are based either on H1 data collected in 1992 at 26.7 × 820 GeV *ep* collision energy and corresponding to an integrated luminosity of $\mathcal{L} \simeq 25$ nb^{-1} or on the 1993 data corresponding to an integrated luminosity of $\mathcal{L} \simeq 500$ nb^{-1}.

7.2 Event Selection

For the analyses discussed in the following the employed minimum bias γp trigger defined the accepted kinematic region up to some fiducial cuts. This trigger required a coincidence between signals from the H1 tracking system and the small angle electron tagger. Events recorded with this trigger constitute an almost background-free γp sample. The accepted kinematic regions for the different analyses are summarized in the following table:

Analysis	y-range	Q^2-range [GeV^2]
σ_{tot}	0.2 - 0.8	$3 \cdot 10^{-8}$ - 10^{-2}
Inclusive particle cross sections	0.3 - 0.7	$3 \cdot 10^{-8}$ - 10^{-2}
Inclusive jet cross sections	0.25 - 0.7	$3 \cdot 10^{-8}$ - 10^{-2}
Determination of x_γ	0.2 - 0.7	$3 \cdot 10^{-8}$ - 10^{-2}
Hard Diffraction	0.25 - 0.7	$3 \cdot 10^{-8}$ - 10^{-2}

7.3 Measurement of the Total γp Cross Section

The H1 collaboration has updated its first measurement of the total γp cross section with improved statistics. It is now based on $21.9 \pm 1.5\,\mathrm{nb}^{-1}$ of data collected in the fall of 1992. The 16393 ± 174 events with $E_{e'}$ between 5 and 22 GeV yield

$$\sigma_{\mathrm{tot}}(< \mathrm{W}_{\gamma\mathrm{p}} >= 197\ \mathrm{GeV}) = 156 \pm 2(stat) \pm 18(syst)\ \mu\mathrm{b}$$

which is in agreement with the published value [224] and with the ZEUS measurement [225], but has a somewhat smaller error. The energy dependence of the γp total cross section is shown in Fig. 7.3 with the data point from [224]. Regge motivated parametrizations are in good agreement with the data, while models predicting a strong rise of $\sigma_{\mathrm{tot}}(\gamma\mathrm{p})$ [76, 226] at HERA energies can be ruled out. The agreement of the Regge parametrization and the corresponding fit has already been shown for the low energy data in Fig. 5.4. In contrast to the measurement of F_2 we thus here find that Regge theory has managed to survive the leap in energy. As can be seen from Fig. 7.3 this measurement requires for the predictions based on mini-jet production due the anomalous component that $p_{\mathrm{T,min}}$ is larger than 2 GeV/c. The main contributions to the systematic error are a 6% uncertainty in the luminosity measurement and 10% error in the detector acceptance determination.

In this determination of $\sigma_{\mathrm{tot}}(\gamma\mathrm{p})$ the best Monte Carlo description of measured inclusive distributions was achieved for the contributions of $\sigma_{\text{"diffractive"}}=0.26 \pm 0.06$, $\sigma_{\mathrm{resolved}} + \sigma_{\mathrm{direct}}=0.19 \pm 0.15$ and $\sigma_{\mathrm{soft}}=0.55 \pm 0.15$ relative to σ_{tot}. This is consistent with the expectation of $\sigma_{\text{"diffractive"}}$ contributing about 30% of σ_{tot} For this, various experimental distributions including inclusive charged particle distributions were studied. The employed Monte Carlo generators simulate photoproduction processes according to the above model. They are RAYPHOTON [230] for the soft meson-proton collisions of the VMD contribution and PYTHIA [228] for the direct and resolved interactions in leading order. The structure functions used in the generators were taken from the GRV [132] parametrizations of parton densities for the proton and the photon. Note that the knowledge on the photon structure function before the analyses of HERA photoproduction data was based on $\gamma\gamma$ interactions only.

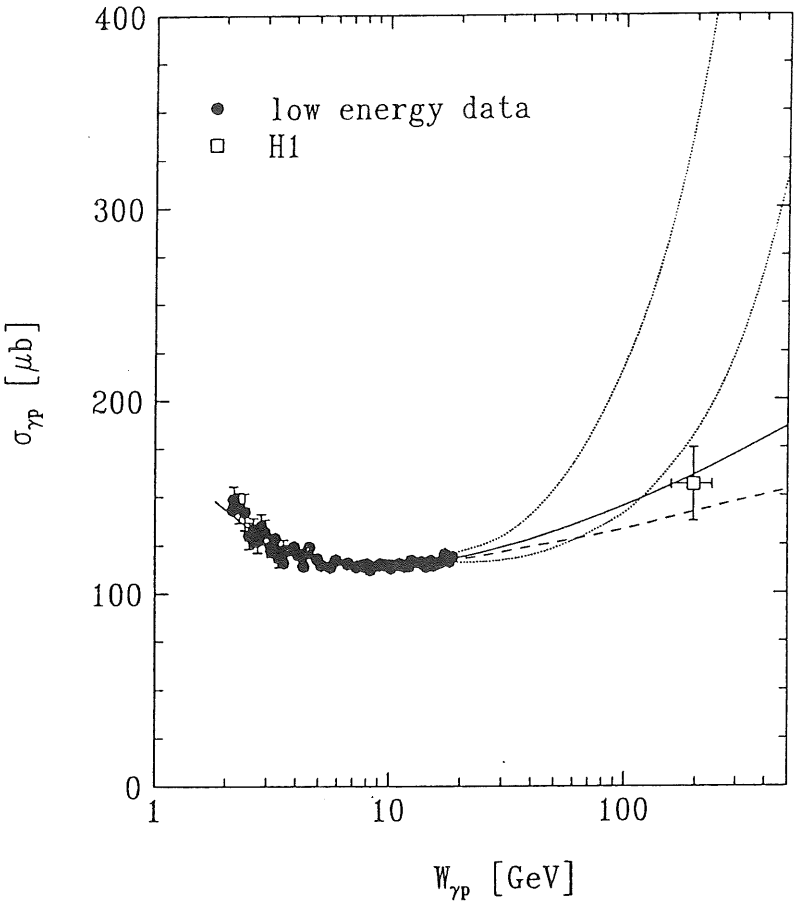

Figure 7.3: The energy dependence of the total γp cross section. The solid curve represents a Regge motivated fit of low energy data [106]. The dashed curve is the prediction of ALLM parametrization [227]. The dotted lines are obtained in the PYTHIA Monte Carlo [228] using the ansatz $\sigma_{\gamma p}(s) = \sigma^{soft} + \sigma^{jet}(s)$ with the Drees-Grassie [229] parametrization of the photon structure function for the lower transverse momentum cutoffs in the calculation of $p_{T,min} = 1.4$ GeV/c (upper line) and $p_{T,min} = 2.0$ GeV/c (lower line).

7.4 Inclusive Charged Particle Cross Sections

The measurement of the inclusive charged particle cross section, which relies only on the central tracking detectors, has been performed by the H1 collaboration in order to study the transition from soft to hard scattering, and to study the description of the data by QCD calculations based on the above model. The details of the analysis can be found in [231].

For the analysis charged tracks in the central region of the detector, i.e. the pseudorapidity interval $|\eta| < 1.5$ having transverse momenta $p_T > 0.3$ GeV/c were selected. The Monte Carlo generators employed to perform the acceptance and efficiency corrections are as described above. The obtained γp event sample could be well described by the sum of the contribution from the VMD, the direct and the resolved contributions. After unfolding we obtained the inclusive ep cross section for charged particles in photoproduction. This cross section is shown in

Fig. 7.4.

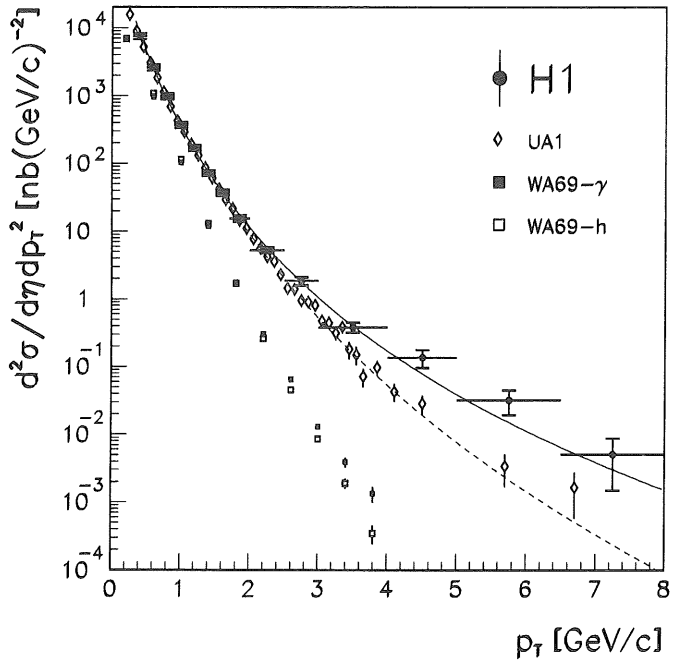

Figure 7.4: Inclusive ep cross section for charged particles in photoproduction (data points) measured in the kinematical region $|\eta| < 1.5$, $Q^2 < 10^{-2}\,\mathrm{GeV}^2$ and $0.3 < y < 0.7$, at an average CMS energy of $\sqrt{s_{\gamma p}} \simeq 200\,\mathrm{GeV}$. The error bars indicate the statistical and systematic errors added in quadrature. An overall uncertainty of 7% from luminosity uncertainties is not included. Also shown are the UA1 measurements (open diamonds) at $\sqrt{s_{p\bar{p}}} \simeq 200\,\mathrm{GeV}$ for $|\eta| < 2.5$, normalized to the H1 data at $p_T = 1.5\,\mathrm{GeV/c}$. The curves indicate power law fits. The rectangles show the shape of the measurements performed by WA69 at $\sqrt{s} \simeq 18\,\mathrm{GeV}$ for γp (filled rectangles) and for *hadron p* (open rectangles) data.

This measurement is compared to the measurement performed in proton-antiproton collisions at the CERN $p\bar{p}$ collider by UA1 [232] at the same CMS energy of about 200 GeV. The UA1 data are normalized to the H1 point at $p_T = 1.5\,\mathrm{GeV/c}$. The p_T-spectra agree well for $p_T \leq 2\,\mathrm{GeV/c}$ showing the similarity between photon-hadron and hadron-hadron collisions in accordance with the VMD expectation. For large transverse momenta the p_T spectrum in γp collisions is found to be much harder than in $p\bar{p}$ collisions. This trend can also be seen in the WA69 data on γp and *hadron p* scattering [233] at CMS energies around 18 GeV as shown in Fig. 7.4.

The harder spectrum in γp interactions can be interpreted as coming from the photon contributions absent in hadron-hadron collisions. This can be seen from Fig. 7.5a where the measured cross section is compared to the leading order QCD calculation contained in the PYTHIA Monte Carlo generator. The full line cor-

responds to taking into account the direct and the resolved contributions. Good agreement with the data is obtained. Also shown is a hadron-like expectation of the VMD model as resulting from taking the pion structure function for the resolved contribution. The difference between the resolved prediction (dashed) and the hadron-like prediction (dotted) indicates the growing importance of the anomalous contribution at large p_T. The difference between the resolved (dashed) and all (full) in addition indicates the growing importance of the direct component with growing p_T.

In Fig. 7.5b the measured cross section is compared to an analytical calculation by Kniehl and Kramer [234]. Excellent agreement in shape and absolute rate is found. The growing importance of the direct component is again indicated in the figure.

7.5 Jet Production in Photon Interactions

The inclusive jet production cross section has been measured as a function of transverse energy and pseudorapidity and compared to leading order QCD calculations. See [235] for details. Constructing the jets was done with a cone algorithm in the pseudorapidity-azimuthal-angle metric based on the transverse energies measured in the calorimeters. Jets with $E_T > 7$ GeV within $R = \sqrt{\Delta\eta^2 + \Delta\phi^2} = 1.0$ and a jet axis inside the central pseudorapidity interval $-1 < \eta < 1.5$ were used in the analysis. The PYTHIA Monte Carlo program was employed for acceptance corrections and comparison with the data. The jet cross section decreases with transverse energy like $E_T^{-5.5}$. As shown in Fig. 7.6 this measurement of the E_T and the η dependences of jet production agree well with the QCD prediction based on the partonic picture of the photon discussed above. It is sensitive to the full parton content (quarks and gluons) of the photon model used in the simulation, i.e. it can in principle be used to constrain the gluon content of the photon. A similar ansatz was used in the analysis of parton distributions in the photon.

7.6 Parton Distributions in the Photon

The kinematic region of the observed 2-jet production involving quasi-real photons is dominated by the resolved photon contributions. The momentum fraction x_γ which a parton from a resolved photon carries into the hard process can be calculated from the transverse energy E_{T_i} and polar angle Θ_i (wrt. the outgoing proton direction) of the final state jets and the energy of the photon E_γ:

$$x_\gamma \approx \frac{E_{T_1} \tan\frac{\Theta_{T_1}}{2} + E_{T_2} \tan\frac{\Theta_{T_2}}{2}}{2E_\gamma} \tag{7.3}$$

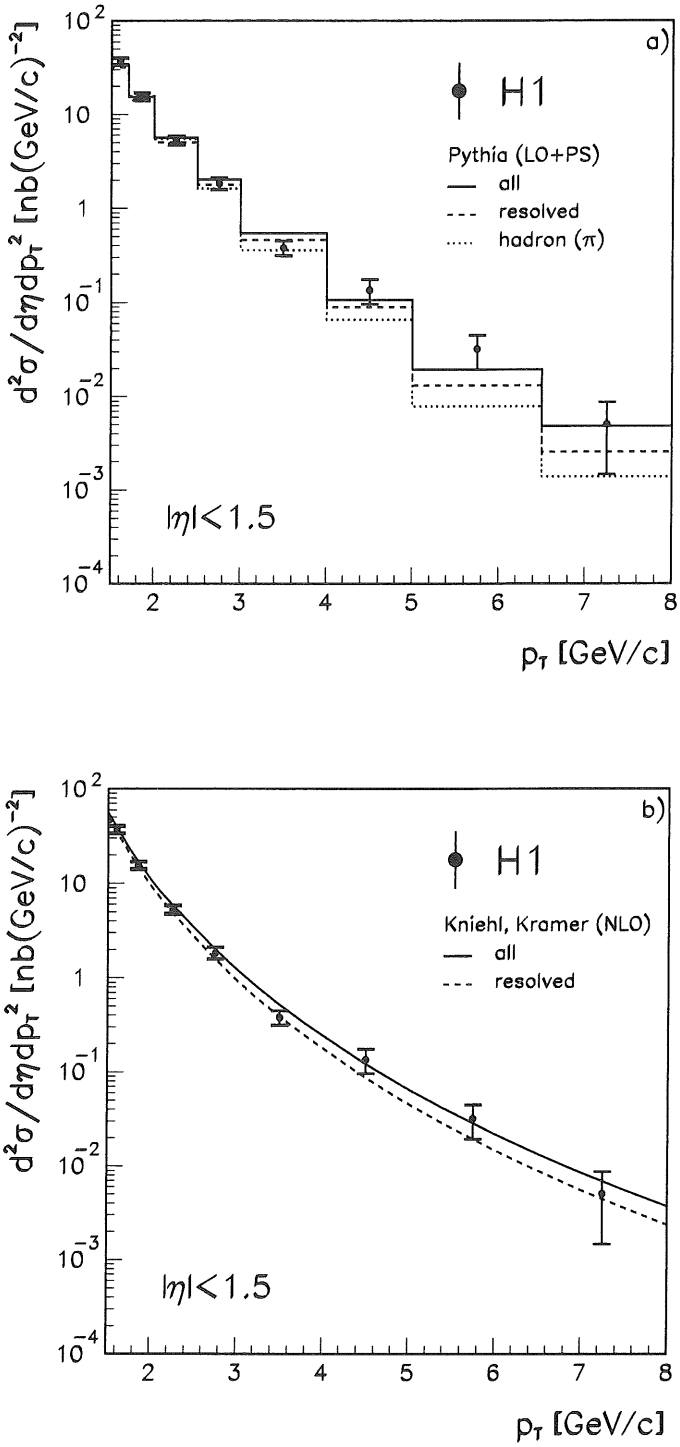

Figure 7.5: a) Inclusive ep cross section for charged particles in photoproduction (data points) as shown in Fig 7.4 compared in the $p_T > 1.5$ GeV/c region with the prediction of a leading order QCD calculation contained in PYTHIA. The histograms indicate the individual contributions to the calculation: resolved (dashed), all=direct+resolved (full), hadron using the pion structure function (dotted). b) The same data compared with an analytical next to leading order calculation [234]. The full line represents the sum of resolved and direct photon contributions.

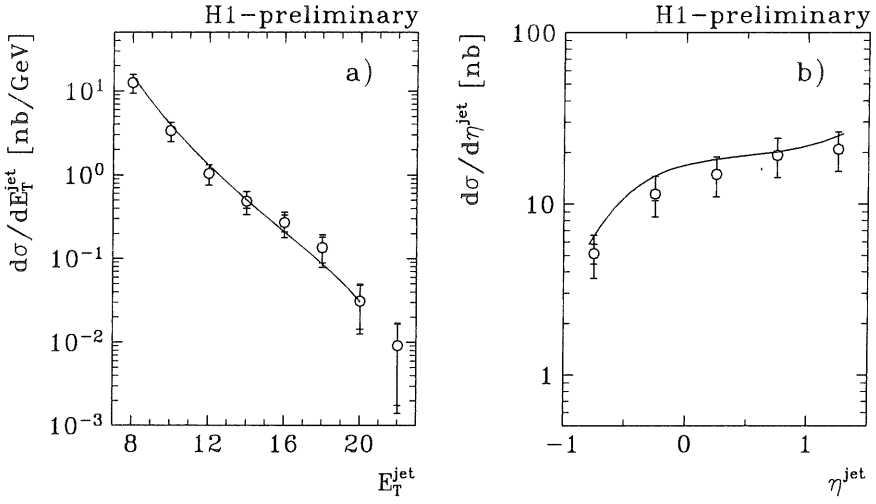

Figure 7.6: Inclusive jet E_T spectrum (a) integrated over the pseudorapidity interval $-1.0 < \eta < 1.5$ and inclusive η spectrum (b) for jets with $E_T > 7$ GeV. The inner error bars represent the statistical errors, the outer error bars the statistical and bin-to-bin systematic errors added in quadrature. The curves show leading-order QCD calculations in the framework of the PYTHIA event generator using the GRV-LO (full line) photon structure functions.

The details of the analysis can be found in [236]. In Fig. 7.7 the distribution of the parton momentum x_γ is shown for the events with two constructed jets. Again a cone algorithm has been used with the defining parameters for jets now being a transverse energy of $E_T \geq 5\,\text{GeV}$ and a rapidity of $|\eta| \leq 2.5$. The distribution is shown with statistical errors only. The full line corresponds to the expected partonic density due to quarks within the photon based on GRV-LO parton densities [132]. The dashed line the expected direct contribution.

Subtracting the quark and direct contributions, the gluon density within the photon may be obtained. The H1 result is shown in Fig. 7.8 together with parametrization from GRV [132], LAC1 and LAC3 [237]. Although the systematic error of this determination of the gluon density is large, the extreme predictions of the LAC parametrizations, which arose due to the lack of constraints from the data, are highly disfavoured.

7.7 Hard Diffraction in Photoproduction

Like in DIS, in photoproduction a large fraction of the events show a large rapidity gap between proton remnant and the hadronic final state observed in the H1 detector. The comparison between data and Monte Carlo yields consistency when adding non-diffractive and diffractive contributions. This is shown in Fig. 7.9 where the measured distribution of the maximum pseudo-rapidity, $\eta_{\max}$, is compared to the PYTHIA Monte Carlo expectation for the non-diffractive and the

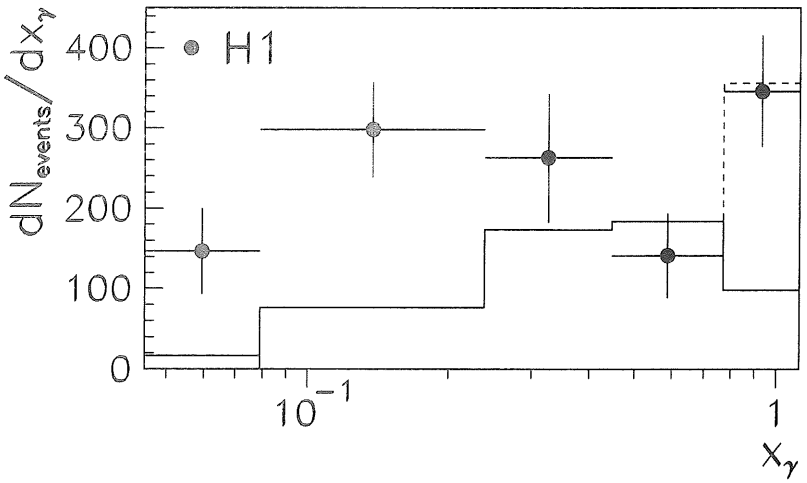

Figure 7.7: The 2-jet distribution of the measured true fractional momentum x_γ of the parton from the photon. Only the statistical errors are shown. The full line represents the predicted contribution of the quark resolved processes, the dashed line shows the size of the direct photon contribution as obtained by the PYTHIA Monte Carlo.

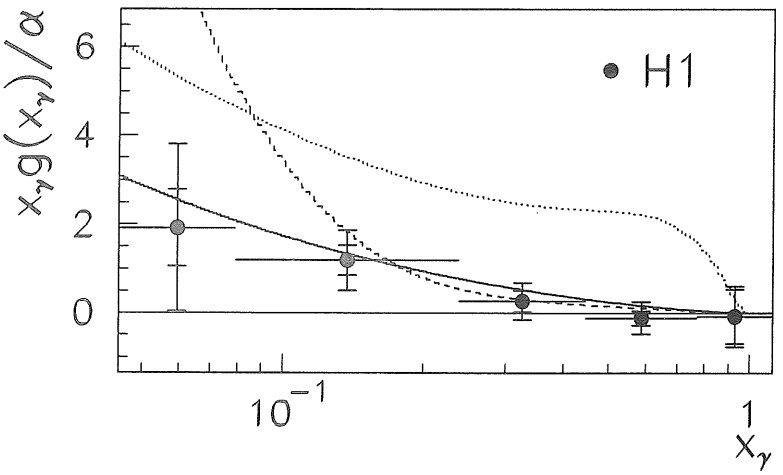

Figure 7.8: The gluon density of the photon divided by the fine structure constant α at the scale of $< p_T >^2 = 75\,\mathrm{GeV}^2$. For comparison the GRV-LO (full line), the LAC1 (dashed), and the LAC3 (dotted) parametrizations are shown.

diffractive contribution. Their sum well describes the measured data. The details of the analysis can be found in [238].

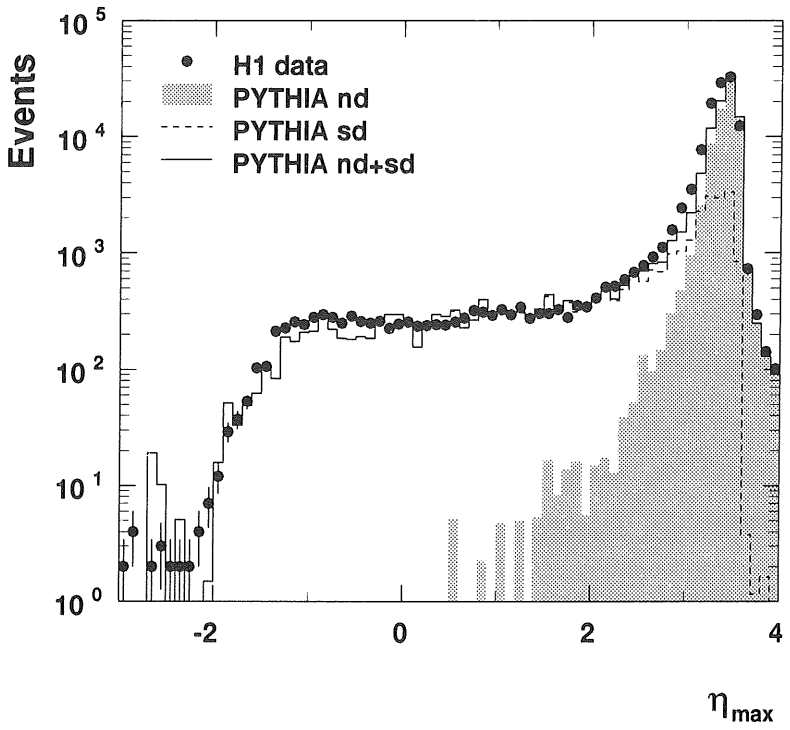

Figure 7.9: The maximum pseudo-rapidity η_{max} distribution measured in photoproduction compared to a diffractive (dashed line) and a non-diffractive (shaded area) Monte Carlo simulation using the PYTHIA generator, and their sum (full line).

That a part of the diffractive events are due to hard partonic interactions becomes evident when the cone algorithm to define jets is sucessfully applied to this fraction of events. The cone jet reconstruction algorithm defines jets as a transverse energy deposition of more than 4 GeV within a cone of radius 1 in the pseudo-rapidity η and azimuthal angle ϕ metric, i.e. $\sqrt{\Delta\eta^2 + \Delta\phi^2} = 1$. It was applied to calorimeter cells in the region $-2 < \eta_{cell} < 2.5$. Fig. 7.10 shows the measured inclusive transverse energy and azimuthal angle jet distributions and the distribution of the azimuthal angle between the jets for events with two reconstructed jets compared to the POMPYT Monte Carlo prediction [205] using a hard (G0) or a soft (G5) parton density parametrization for partons within the Pomeron.

Qualitatively, a hard structure is favoured and the two jets in two-jet events are found to be back-to-back as expected for a hard partonic interaction.

In the study by Engel *et al.* discussed in 6.7 these data are used in a comparison to the two-component Dual Parton Model based on Regge theory. Since the data

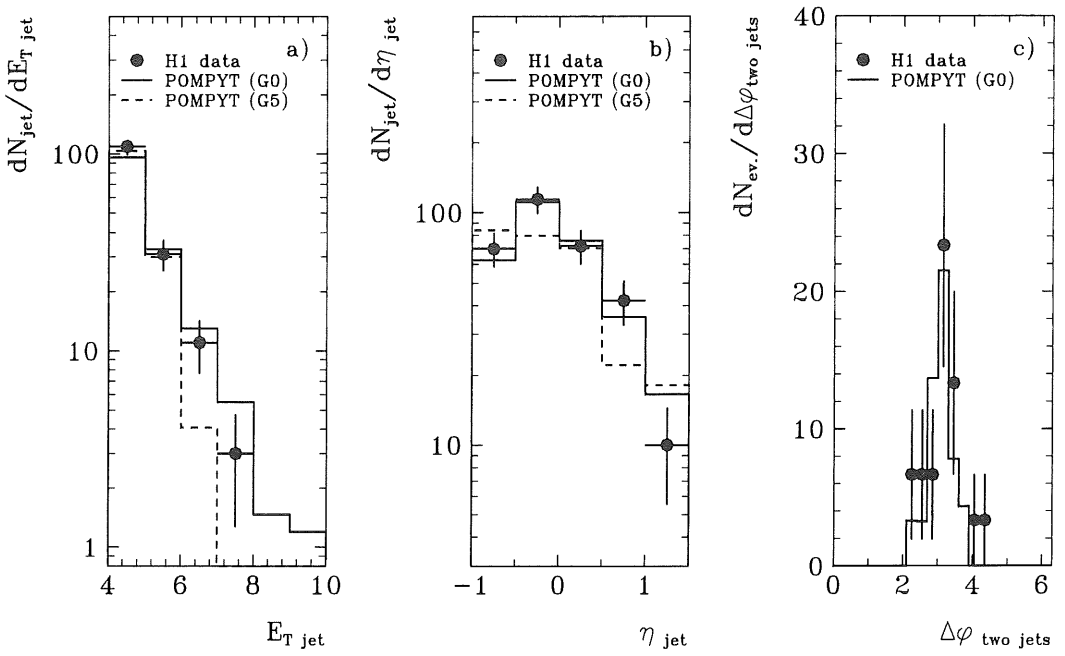

Figure 7.10: The maximum pseudo-rapidity η_{max} distribution measured in photoproduction compared to a diffractive (dashed line) and a non-diffractive (shaded area) Monte Carlo simulation using the PYTHIA generator, and their sum (full line).

have not yet been corrected for acceptance, the comparion is only qualitative. The shape of the jet transverse energy and azimuthal angle distributions are both well described as can be seen in Fig. 7.11 taken from [213].

More data statistics will have the potential of differentiating between models and will pin down the parton distribution in the Pomeron in the factorizing ansatz. Since both DIS and photoproduction events are yielding results on diffraction, the ongoing studies on the similarities of the diffractive interaction of the photon in its two incarnations, real and virtual, are expected to shed more light on the structure of the Pomeron.

7.8 Discussion

The measurement of the total γp cross section can be interpreted in three scenarios:

- Regge theory
- constant soft contribution plus a rising mini-jet fraction unitarized in an eikonalization ansatz
- the theory of expanding protons.

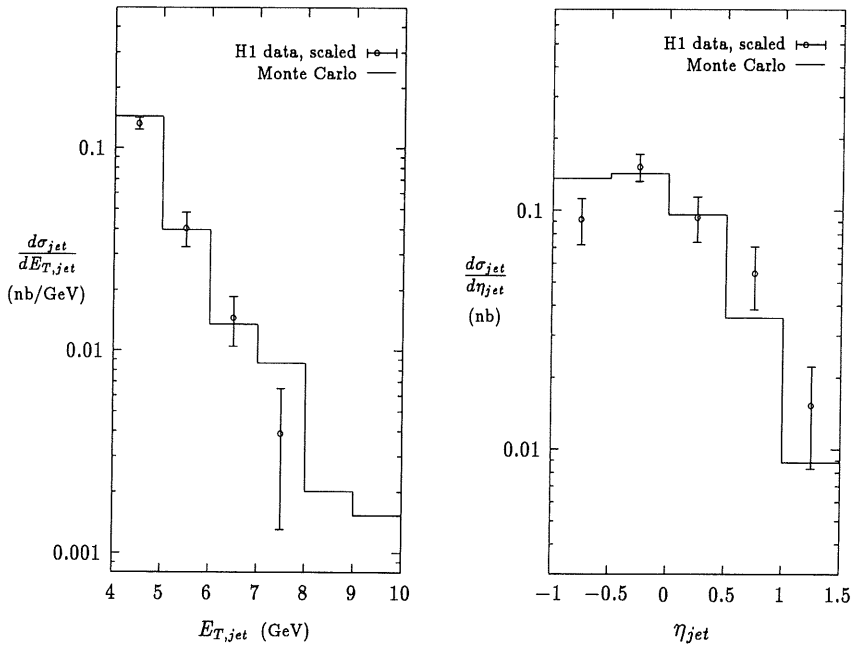

Figure 7.11: Qualitative comparison of the inclusive transverse energy distribution and the inclusive pseudorapidity distribution of jets as measured by H1 with a calculation by Engel *et al.* [213].

7.8.1 Regge Ansatz

As shown in Fig. 7.3, the measurement of the total γp cross section is well described by Regge motivated fits. In this ansatz the total cross section is determined by a Reggeon and a Pomeron exchange term in the form

$$\sigma_{\rm tot}^{\gamma p}(s) = X_{\rm Reggeon}\, s^{-0.4525} + X_{\rm Pomeron}\, s^{0.0808} \quad [\rm mb] \tag{7.4}$$

with $X_{\rm Reggeon} = 0.129, X_{\rm Pomeron} = 0.677$ and s expressed in GeV^2.

Schuler and Sjöstrand [223, 239], after introducing the decomposition of the total γp cross section as

$$\sigma_{\rm tot}^{\gamma \rm p} = \sigma_{\rm VMD}^{\gamma \rm p} + \sigma_{\rm direct}^{\gamma \rm p} + \sigma_{\rm anomalous}^{\gamma \rm p},$$

have calculated and parametrized the total VMD cross section as

$$\sigma_{\rm VMD}^{\gamma p} = 0.115\, s^{-0.4525} + 0.53\, s^{0.0808} \quad [\rm mb]. \tag{7.5}$$

From this we see that almost independent of the CMS energy about 80% of the total cross section is stemming from the VMD like contribution. The remaining 20% are from the direct and the anomalous components.

7.8.2 Soft and Hard Interaction Ansatz

Since part of the total cross section may be treated within QED or QCD, we may ask the question whether we expect the above relationship to hold for all energies, or whether we expect the QCD component to become dominant at very high energies? To study this question, we take up again the discussion of 7.1 where we stated that in addition to the photon being an elementary particle, it can fluctuate into a vector meson, a $q\bar{q}$ or a lepton-antilepton pair. The photon wave function is thus given as

$$|\gamma>= c_{\rm bare}|\gamma_{\rm bare}> + \sum_{\rm V=V=\rho^0,\omega,\phi,J/\psi} c_{\rm V}|V> + \sum_{\rm q=u,d,s,c,b} c_{\rm q}|q\bar{q}> + \sum_{\rm l=e,\mu,\tau} c_{\rm l}|l^+l^-> \tag{7.6}$$

with c_i the respective coupling strengths and $p^2_{T,0}$ a cut-off parameter to separate the low and high virtuality of the $q\bar{q}$ fluctuations.. The couplings are $c^2_V = 4\pi\alpha/f^2_V$ with f^2_V the coupling of the photon to vector mesons V determined from data, $c_l \simeq (\alpha/2\pi)(2/3)\ln(\mu^2/m^2_l)$, $c_q \simeq (\alpha/2\pi)2e^2_q\ln(\mu^2/p^2_{T,0})$, and $c^2_{\rm bare} = Z_3 = 1 - \sum c^2_V - \sum c^2_q - \sum c^2_l$.

In practice, $c^2_{\rm bare}$ will always be close to unity, i.e. the probability for the photon to be in a hadronic state, $P_{\rm had}$, is small. Collins and Ladinsky [240] estimated $P_{\rm had}$ within the VMD model to be about 1/300. The parton distributions f_i in the photon in this ansatz are given as

$$f^\gamma_i = f^{\gamma,\rm dir}_i(x,\mu^2) + f^{\gamma,\rm VMD}_i(x,\mu^2) + f^{\gamma,\rm anom}_i(x,\mu^2,p^2_{T,0}) \tag{7.7}$$

with

$$f^{\gamma,\rm dir}_i(x,\mu^2) = Z_3\delta^\gamma_i\delta(1-x), \tag{7.8}$$

and

$$f^{\gamma,\rm VMD}_i(x,\mu^2) = \sum_{\rm V=\rho^0,\omega,\phi,J/\psi} c^2_V f^V_i(x,\mu^2), \tag{7.9}$$

with μ^2 the mass factorization scale. The anomalous part is calculable in QCD with the boundary condition that it should vanish at the cut-off $\mu^2 = p^2_{T,0}$. In order to get a consistent picture of the photon, Schuler and Sjöstrand [239] determined the parameter $p_{T,0}$ to be $\simeq 0.5\,\mathrm{GeV}^2$. In practice the VMD structure function is approximated by the pion structure function due the unknown distributions of the vector mesons themselves.

By comparing to the photon picture described in 7.1 we find that the relevant parton distribution functions when discussing a potential rise of the total cross section due to enhanced QCD contributions of the $2 \to 2$ parton-parton scattering cross section is only sensitive to the resolved contribution which can be regarded as a phenomenological input distribution analogous to the parton distributions of the proton and whose energy dependence is completely determined by QCD. We thus have to investigate the parton densities

$$f^{\gamma,\rm resolved}_i = f^{\gamma,\rm VMD}_i(x,\mu^2) + f^{\gamma,\rm anom}_i(x,\mu^2;p^2_0) \tag{7.10}$$

entering into the calculation of hard scatterings.

The calculation of the parton-parton cross section giving rise to mini-jet production analogous to hadron-hadron scattering, is diverging for $p_T \to 0$ and has to be regulated by the cut-off $p_{T,min}$ introduced in 7.1. This regularization can be easily understood on quantum mechanical grounds. We expect a breakdown of the perturbative picture of coloured parton-parton scattering at small values of p_T due to the effective coupling vanishing at some cut-off wavelength λ_T^{max}. Gluons with wavelengths larger than this will not anymore resolve individual coulours within the target, i.e. the colour is screened for large wavelengths or small values of the transverse momentum via $\lambda_T \sim 1/p_T$.

When performing the calculations of the parton-parton cross section with values of the cutoff below a few GeV/c, it turns out that the inclusive mini-jet contribution to the total photoproduction cross section is rising much faster with CMS energy than the total cross section. The mini-jet cross section thus found at the HERA CMS energy of 200 GeV is just about equal to the total photoproduction cross section for $p_{T,min} \simeq 2\,\mathrm{GeV/c}$. This is an indication of multiple interactions, i.e. a large muliplicity of mini-jets, which do not change the total cross section by the full amount of the inclusive cross section. This has also been observed in hadron-hadron collisions. Only after unitarisation, i.e. dividing the inclusive cross section by the average number mini-jets per event, the cross section is found to be consistent with the measurement.

Since also soft and semi-hard scatterings may occur simultaneously due to the extended size of target and projectile, unitarisation of the total cross section can be obtained by eikonalization in the impact parameter approach as in hadron-hadron collisions. Following Honjo *et al.* [245], the total inelastic γp cross section can be written as

$$\begin{aligned}\sigma_{\mathrm{inel}}^{\gamma p} = \sigma_{\mathrm{dir}} \; &+ \; 2\lambda \mathcal{P}_\rho \int d^2b(1 - e^{-\mathrm{Re}\chi_{\rho p}}) \\ &+ \; \sum_q 2e_q^2 \frac{\alpha_{\mathrm{em}}}{\pi} \int_{Q_0^2} \frac{dp_{T,0}^2}{p_{T,0}^2} \int d^2b(1 - e^{-\mathrm{Re}\chi_{q\bar{q}p}})\end{aligned} \tag{7.11}$$

where $\lambda = 4/3$ for equal ρp, ωp, and ϕp cross sections, and $\lambda = 10/9$ for complete suppression of the ϕ contribution, $\mathcal{P}_\rho = c_\rho$, Q_0^2 the QCD scale where the input parton distributions in the photon are defined,

$$2\mathrm{Re}\chi_{\rho p} = A_{\rho p}(b)[\sigma_{\mathrm{soft}}(s) + \sigma_{\mathrm{QCD}}^{\rho p}(s)], \tag{7.12}$$

and

$$2\mathrm{Re}\chi_{q\bar{q}p}(b, s, p_{T,0}) = A_{q\bar{q}p}(b, p_{T,0})[\sigma_{\mathrm{soft}}^{q\bar{q}p}(s, p_{T,0}) + \sigma_{\mathrm{QCD}}^{q\bar{q}p}((s, p_{T,0})]. \tag{7.13}$$

For the definitions of the overlap functions $A_{\rho p}(b)$ and $A_{q\bar{q}p}(b, p_{T,0})$ see [245]. The soft cross sections can be parametrized as suggested by Regge theory (see 5.8) with $\sigma_{\mathrm{soft}}^{q\bar{q}p}(s, p_{T,0})$ related to $\sigma_{\mathrm{soft}}(s)$ by a scale factor $(\mu^2/4p_{T,0}^2)$ to ensure continuity at $p_{T,0} = Q_0$. The QCD cross sections $\sigma_{\mathrm{QCD}}^{\rho p}(s)$ and $\sigma_{\mathrm{QCD}}^{q\bar{q}p}(s, p_{T,0})$ can

be calculated according to Eq.(5.126) with the parton densities of the ρ meson, the proton, and $f_i^{q\bar{q}} \approx (Q_0^2/p_{T,0})^2 f_i^{\rho}$, respectively.

Honjo *et al.* [245] fitted the above ansatz to existing pre-HERA data and found a value for the regularization cutoff $p_{T,min}$ of 1.4 GeV. Extrapolating the fit to the HERA CMS energy results in a overshooting of the measured H1 and ZEUS data points. As shown by the HERA measurements of $\sigma_{tot}^{\gamma p}$, in order for the resolved cross section contribution to be consistent with the HERA data alone, this cut-off has to be chosen larger than 2 GeV/c. To describe the measured mini-jet cross sections at hadron-hadron colliders, cutoffs of this order of magnitude also typically have to be used in the QCD calculations. For the parton densities in the photon, Honjo *et al.* besides the pion structure function, also used the Drees-Grassie parametrization [229]. Using these parametrization of parton densities in the photon, the low and high energy data cannot be described with the same ansatz, i.e. $p_{T,min} = 1.4$ GeV/c, with the prediction for the HERA energy grossly overshooting the HERA measurements. Using the pion structure function the discrepancy at high energies is smaller but still the prediction is higher than the measurement.

A similar study concerned with the high energy data was performed by Fletcher *et al.* [246]. The low energy data here were used to fix the parameters of the model consisting of a soft plus mini-jet contribution and using a value for P_{had} of 1/204. The authors find good agreement between the soft plus hard interaction ansatz and the high energy HERA and Tevatron data for the total cross sections in photoproduction and in $p\bar{p}$ scattering for $p_{T,min}$ larger than 2.25 GeV/c using the Drees-Grassie [229] and Duke-Owens [252] parametrizations of the parton densities in the photon.

To conclude, either the ansatz of Honjo *et al.* is wrong, or some of the assumptions or parametrizations entering into the evaluation are not well defined or energy dependent in a different way than assumed. Of the assumptions contained in the model, the pion structure function might not be an adequate substitute for the ρ structure function, the cutoff $p_{T,min}$ might be energy dependent, or the soft contribution might rise as a function of energy. The scenario where $p_{T,min}$ would be energy dependent would be the worst case, since the model would loose its predictive power.

In the eikonal approach the total cross section thus depends on the parton densities in the photon, the cutoff $p_{T,min}$ on the integration in Eq. (5.126), on P_{had}, $A(b)$ and $\sigma_{soft}^{\gamma p}$. The HERA data alone limit p_T^{min} to larger than 2 GeV/c. All of these parameters or parametrizations have to be investigated in more detail in the future in order to arrive at a consistent description of the photon and its interactions at low and high energies.

7.8.3 Expanding Proton Ansatz

The asymptotic high energy behaviour of quantum electrodynamics led Cheng and Wu to the formulation of the impact picture of high energy electrodynamic scattering [241]. Only the most general characteristics of the scattering amplitude determine the asymptotics in this picture. When applied to strong interactions this picture led to a series of predictions for high energy cross sections, both inclusive and exclusive [242], which are due to the expanding black core of hadrons, i.e. $R_h \propto R_0 \ln s$ and a grey fringe where diffractive dissociation occurs. Concerning the total γp cross section the prediction of the expanding proton picture is [243]

$$\sigma_{\rm tot}^{\gamma p} = \text{const.}\alpha[\sigma_{\rm tot}^{\pi^+ p} + \sigma_{\rm tot}^{\pi^- p}], \tag{7.14}$$

where α is the fine structure constant. As shown in [243] the prediction of this model is well compatible with the H1 and ZEUS data on $\sigma_{\rm tot}^{\gamma p}$.

7.8.4 Impact on EAS Applications

Even though the HERA measurement can be described by Regge fits and by adding energy dependent mini-jet contributions to an almost energy independent soft contribution, the effect of eikonalization at this energy is already large in the above ansatz as shown by Honjo *et al.* [245]. In other models using an energy dependent soft contribution the effect of eikonalization is reduced. At higher energies eikonalization will, however, always have a large effect. In [245] the influence of the HERA results on $\sigma_{\rm inel}^{\gamma\, air}$ in this eikonalized model has been studied with the pion structure function chosen for the VMD parton densities in the photon. The authors arrive at a value of $\sigma_{\rm inel}^{\gamma\, air}$ at PeV fixed target energies of about 2-3 mb, i.e. much less than the $\mathcal{O}(100)$ mb needed to explain the muon-rich airshowers observed in the 1980s. The ratio of the Bethe-Heitler cross section to the hadronic cross section for PeV photon energies is thus of the order of 0.5%. Only through large fluctuations in the number of produced mini-jets could photon showers produce multi-muon showers. The observations of the experiments claiming to have observed point sources in muon-rich showers, however, cannot be explained by the hadronic structure of the photon.

The diffractive contribution to the total photoproduction cross section can be investigated in various channels, ranging from exclusive vector meson production, rapidity gap contributions to the total cross section to hard diffractive events. The full potential of this class of events to discriminate between Pomeron models, the expanding proton picture, or to determine or check the consistency of the parton densities in the Pomeron in a factorizing ansatz will be used once more data statistics is available.

The picture that we have painted of the structure of the photon in terms of its different interaction channels and the magnitude of the calculated cross sections

is thus in satisfactory agreement with the HERA data and consistent with the hadron pictures found at hadron-hadron colliders up to the additional hard direct photon channels. The hadronic contribution to the photon structure is rising with energy but not nearly as fast as that it could explain the point source observations in muon-rich events. Multiple interaction models like the eikonalization ansatz work both in pp and γp interactions. In the future, however, details of the model, especially the parton densities in the photon, have to be investigated and determined with better accuracy.

Chapter 8

The Monte Carlo Generator

In this chapter an overview of the CORSIKA Monte Carlo generator [4] employed in the HEGRA EAS experiment is given. On the *ep* generators used by the H1 collaboration there exists a large amount of secondary literature and they will not be discussed in the following. See *e.g.* [247] for an overview. The EAS and *ep* generators are conceptually very different. In EAS simulations the physics processes that set the scale of the reactions are "soft". The application of perturbative QCD is thus not possible. The simulations therefore are based on phenomenological theories. The *ep* simulations on the other hand mostly rest on differential cross sections for hard processes calculated within perturbative QCD. These are then modified by adding parton showers and/or phenomenological fragmentation routines.

8.1 The CORSIKA Generator

The HEGRA collaboration currently makes use of the CORSIKA program [4] in its version 4.068 to simulate the high energy interactions and subsequent air shower development in the atmosphere. We have used the program in the primary energy range between 10^9 eV to 10^{17} eV. Detailed studies in this energy range are still in progress. The electromagnetic part of the EAS is simulated with the well-known EGS4 code [248]. For the simulation of low energy hadron-nucleus collisions ($E < 100$ GeV) and the calculation of hadronic cross sections it uses the GHEISHA [249] package. The simulation of high energy interactions is either performed on the basis of the Dual Parton Model (DPM) [82] as developed by J. N. Capdevielle or on the basis of the VENUS (Very Energetic NUclear Scatttering) model as developed by K. Werner [84].

The user can set a number of parameters to steer the CORSIKA program. Among them are program versions to select special versions, like a mode to also simulate Čerenkov radiation or to switch between the DPM and VENUS for high energy

nucleus-nucleus interactions. Other steering options include the primary particle type, its angle of incidence, the threshold energy per particle type down to which the particles are tracked within the program, and the observation level, which in case of the HEGRA experiment is 2200 m.

The DPM and VENUS both are developed on the basis of the Gribov-Regge theory of hadronic interactions at high energies (see also 5.3) and are identical concerning elastic scattering. For the inelastic channels the models differ due to a different Regge philosophy of the realization of Pomeron exchange in the Dual Topological Unitarisation approach used in the DPM compared to VENUS. For details refer to [82] and [84]. The different ansätze lead to different weights for multi-Pomeron graphs and accordingly to different energy sharing between the Pomerons when more than one Pomeron is exchanged and cut.

The DPM part of the CORSIKA program is not a full installation of the DPM model but it only tries to reproduce relevant kinematical distributions as far as they have been measured or predicted by theory. We will not discuss it any further, but concentrate on VENUS. The VENUS model aims at simulating heavy-ion collisions in detail based on the creation and fragmentation of strings. The fragmentation properties of the strings determine the multiparticle distribution functions for the specific subprocess. A unique feature of the VENUS model is the possibilitiy of forming strings connecting more than one parton within individual nucleons in an interaction.

Both models are phenomenological realizations of a topological expansion of QCD which is equivalent to Gribov-Regge theory. The developments which led to these models can not be discussed in detail here. Below only a overview is given and the aspects in the models pointed out where the HERA results may influence parameters or models.

8.1.1 Topological Expansion of QCD

Besides the strong coupling, g, the QCD Lagrangian contains the number of colours, N_c, and the number of flavours, N_f, as parameters. In high energy hadron-hadron collisions in the limit where N_c is large, and N_f and $g^2 N_c$ are fixed, the parameter $1/N_c$ may be used as the expansion parameter [250, 251].

In this expansion, both the gluon and the quark propagator can be represented by a double-line. For the gluon this line is characterized by two oppositely directed colour lines on its edges, while for a quark, one edge is a colour line and the other a flavour line. For internal quark and gluon lines this leads to closed colour and flavour lines and each can be thought of as forming a polygon-face. For graphs without external lines one thus arrives at closed oriented two-dimensional surfaces.

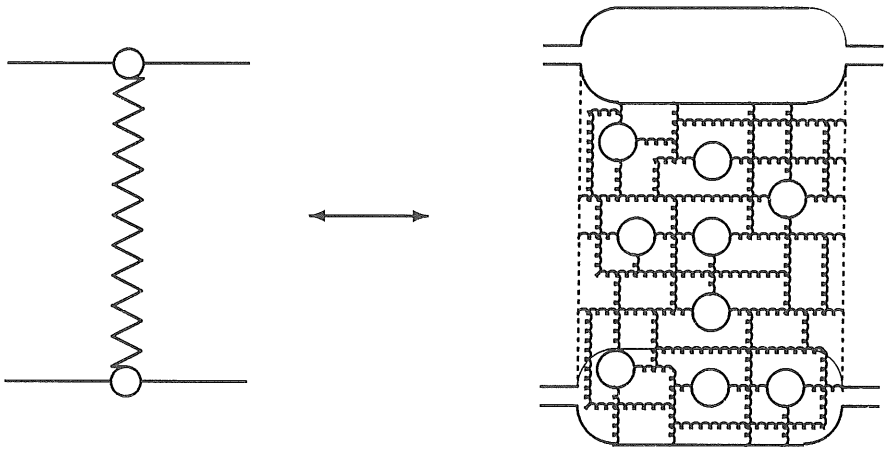

Figure 8.1: Pomeron = Cylinder.

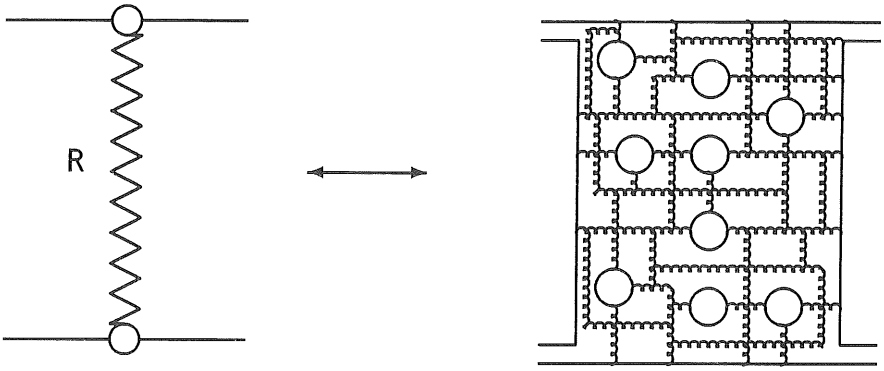

Figure 8.2: Reggeon = Plane.

In this way each Feynman graph is found to represent a two-dimensional surface weighted by an appropriate power of $1/N_c$ and the full Feynman expansion can be expressed as a sum over the surface topologies. External particles are attached to boundaries and are characterized by an external flavour line.

This topological expansion of QCD was found to be also representable by an effective string-like theory with a three-string coupling, g_s, serving as the expansion parameter. Each string propagator can also be represented by a directed double-line with both lines, however, being flavour lines. The leading behaviour of a four-point elastic amplitude is N_c^{-1}. The next order term behaves like N_c^{-2} and has the topology of a cylinder.

The reson why this expansion is important for this discussion is that there is a one-to-one correspondence between terms in the topological expansion of QCD and those in Regge field theory as found by Veneziano [250]. In the Veneziano model, Pomerons can be identified as cylindrical topological diagrams as depicted in Fig. 8.1 and Reggeons which correspond to colour exchange processes as planar ones as shown in Fig. 8.2.

This one-to-one correspondence is known as the dual topological expansion. The

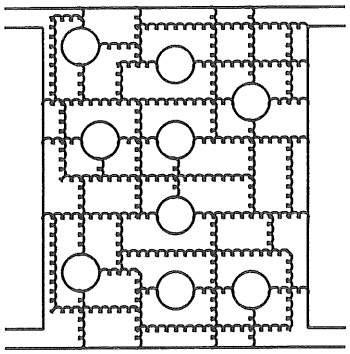

Figure 8.3: Reggeon.

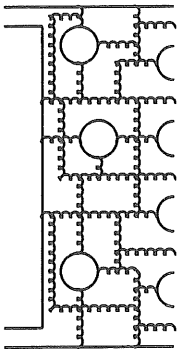

Figure 8.4: Cut plane.

topological expansion of QCD can therefore be used to provide a partonic picture of the Reggeons and Pomerons exchanged in Regge theory. In particular, with Pomeron exchange dominating at high energies, it allows to describe consistently both elastic scattering through the exchange of the leading closed topology, the Pomeron, and multiparticle production through cut Pomerons which give rise to chains of partons stretched between coloured endpoints. Schematically a Reggeon and the partonic configuration resulting from a cut are shown in Figs. 8.3 and 8.4.

Since the graphs in the topological expansion of QCD are not symmetric in relation to the cutting line, interference between all possible cut graphs has to taken into consideration when calculating the multiparticle final state probabilities. In this respect, the topological expansion also leads to the Reggeons and the Pomeron as the sum of a whole class of graphs and which could be viewed as the QCD picture of the trajectories.

8.1.2 The VENUS Model

The details of the VENUS model are described in [84]. Please refer to this work for extensive references on the following discussion.

VENUS is based on the phenomenological Gribov-Regge theory as introduced in 5.3 and assumes *multiple* Pomeron/Reggeon exchange as the dominating process at high energies and thus allows for the exchange and production of multiparticle intermediate or final states. The basic process is elastic scattering given by Pomeron exchange. Inelastic scattering is treated via the optical theorem and the application of the AGK cutting rules [105] which play the rôle of the factorization theorem for soft physics. The elementary inelastic process is thus represented by a "cut Pomeron" which is equivalent to the exchange of colour of between the scattering partners. This exchange of colour is modelled by the formation of two

strings.

VENUS thus uses the AGK cutting rules to establish the expansion of the total cross section in the form

$$\sigma_{\rm tot} = \sum_{0}^{\infty} \sigma_{\rm m},$$

where $\sigma_{\rm m}$ corresponds to the topological cross section of cutting m Pomerons and σ_0 to zero cut Pomerons, i.e. elastic and diffractive scattering. These cross sections are then related in the VENUS model to the formation and fragmentation of colour strings leading to multiparticle distributions in the final state. The important fact for a writer of a Monte Carlo generator is that the individual cross sections $\sigma_{\rm m}$ are all positive and can be used as weights for specific subprocesses in the MC generator.

In VENUS the elastic cross sections can thus be calculated and the total cross section is then derived from the optical theorem. The relation between the cross section contributions is expressed in eikonal form as reviewed in 5.8. The eikonal χ can be identified as the Fourier transform of the Pomeron propagator and $C = 1$ (see Eq. (5.127)). In this way a microscopic model of the eikonal approach is obtained.

Multiple Pomeron exchange is simulated by forming multistrings between the interacting hadrons. Then a procedure termed AMOR based on relativistic classical string dynamics handles the string fragmentation. The AMOR string fragmentation model has been tested against e^+e^-, νp, and μp data on momentum and rapidity distributions of the hadronic final states. Satisfactory agreement was obtained. Another positive feature of the Gribov-Regge theory becomes visible in the comparison of VENUS with measured multiplicity distributions. The possible exchange of multiple Pomerons not only saves the Froissart bound, but it also serves to broaden the multiplicity distributions. In contrast to single Pomeron exchange models, in this way a good description of collider data was obtained.

This expansion finally leads to multiparticle distribution functions which can be evaluated in a Monte Carlo generator to generate full events. The link to QCD is obtained through the Veneziano model. Additional assumptions are contained in VENUS which in part make use of the picture of a Pomeron as a gluon ladder within QCD.

Dependence on Parton Densities

The weights $\sigma_{\rm m}/\sigma_{\rm tot}$ correspond to weights of processes where m number of colour exchanges occurred between the two scattering partners. Colour exchanges are performed through relativistic strings stretched between quark-(anti)quark or quark-diquark systems. A certain set of strings is chosen in the generator according to the parton density distributions in the nucleons $F_i(k)$ of partons with

momentum k. The parton densities are assumed to scale and to factorize, i.e.

$$F_i(k) = f_i(k_{||}/\vec{p}_{||})g(k_\perp^2), \tag{8.1}$$

where the transverse momentum distribution of the partons is either taken as

$$g(k_\perp^2) \sim k_\perp \cdot e^{[-(2/\overline{k}_\perp)k_\perp]} \tag{8.2}$$

in the exponential option or as

$$g(k_\perp^2) \sim k_\perp \cdot e^{[-(\pi/4\overline{k}_\perp^2)k_\perp^2]} \tag{8.3}$$

in the Gaussian option with the free parameter $\overline{k}_\perp$. The scaling property of the $F_i(k)$ is generally assumed if the momenta involved are small.

The parton densities used are of the form

$$f_i^{\text{tot}} = f_i^{\text{sea}} + \frac{n_v}{3} f_i^{\text{val}} \tag{8.4}$$

with n_v counting the number of valence quarks. This number is reduced by 1 after each interaction involving one valence quark. The parametrization chosen for the parton densities is the one of Duke and Owens (DO) [252] modified by a μ dependent term according to

$$f_i^{\text{sea,val}} = A_i x^{a_i}(1-x)^{b_i}(1+\alpha_i x) \cdot \frac{1}{\sqrt{x^2 + 4\mu^2/s}}.$$

The parameter μ determines the onset of elastic scattering. Since elastic reactions are not considered in VENUS, μ has to be chosen small enough so as not to influence the results for the inelastic processes. In the DO parametrization, the parton densities for small x behave as derived in the Regge Model (see 5.3):

$$f_{\text{sea}}(x) \sim \frac{1}{x}, \quad \text{i.e.} \quad x f_{\text{sea}}(x) \sim \text{const.}$$

and

$$f_{\text{val}}(x) \sim \frac{1}{\sqrt{x}}, \quad \text{i.e.} \quad x f_{\text{val}}(x) \sim \sqrt{x}.$$

In the generator this behaviour would lead to the generation of events clustered at small x values, and thus strings with zero mass would mainly be produced. The mass of a $q - \bar{q}$ string is roughly

$$m_{q-\bar{q}} = \sqrt{x_1 x_2 s}$$

and the one of a $q - qq$ string

$$m_{q-qq} = \sqrt{x_1(1-x_2)s}.$$

The decay of very low mass strings will only lead to very few particles in the final state. The leading hadrons will consequently carry the full initial momentum.

This is a characteristics of forward elastic scattering. Since the aim is to generate inelastic reactions, a cutoff on the leading particles momentum is introduced in the program.

To define the endpoints of the strings and to produce the final state particles, the parton distribution functions in the colliding hadrons and fragmentation functions are thus needed and the rapidity distribution of the produced hadrons is given as a convolution of parton distribution functions and fragmentation functions. The effective values of the momentum fractions of the quark and the diquark systems at the endpoints of the hadron chains are typically around 0.05 and 0.95 for the diquarks, respectively.

Although the influence of the HERA data on this region of fractional momenta is small, the program is influenced by the HERA data since the Monte Carlo program will choose the x-values of the chain endpoints from the integral over the parton densities from x=0 to 1. The integral over the new parton densities differs from the old ones on the percent level. The new parametrizations should thus be included.

"Soft" and "Hard" Pomerons

In Monte Carlo generators based on an eikonal ansatz the different contributions to the scattering cross section are easily incorporated. In the Dual Parton Model two types of Pomerons are assumed to contribute to the scattering processes. In VENUS, where the eikonal χ (Eq. (5.127)) corresponds to the Fourier transform of the Pomeron propagator, the eikonal is accordingly being composed of two components

$$\chi = \chi_{\text{soft}} + \chi_{\text{hard}}$$

with χ the full Pomeron propagator. All that is changed when incorporating mini-jet production is that a colour exchange will be treated as a "hard" exchange with a probability p_{hard} and that the string endpoints in these cases will receive larger transverse momenta.

With the HERA results in hand this treatment of the hard scattering contribution does not seem to be appropriate any longer. The VENUS generator will thus undergo substantial changes in order to comply with the knowledge on the transition from soft to hard QCD gained at HERA [191].

8.1.3 Discussion

To summarize, the VENUS EAS Monte Carlo generator is based on the eikonal scattering model. The cross sections are calculated from Regge theory and the AGK cutting rules with multiple supercritical Pomeron exchange. The energy

sharing between the Pomerons in multiple-Pomeron exchange reactions is performed according to the probability for multi-colour exchange. The fragmentation of the colour strings stretched between the hadrons due to cut Pomerons are fragmented using the relativistic string model AMOR.

The behaviour of the endpoints of the generated rapidity distributions is a function of the assumed low x behaviour of the valence and sea structure functions. While the knowledge on valence quarks has not been changed due to the HERA results, the behaviour of the sea quarks was found to be much more singular than predicted by Regge Model based predictions. As these only enter into the Monte Carlo generator in the integral over parton densities, the direct effect at moderate energies ($\sim 10^{15}$ eV) will be small. At larger energies the new parton densities will have considerable influence as discussed by Capedeville [253].

The knowledge gained on the QCD Pomeron and the theoretical advances stimulated by the HERA data will have a major impact on the VENUS generator in supplying a more physical ansatz for both the soft and the hard eikonal through the Q^2 dependence of the effective intercept observed in the data. This will be discussed in the final chapter.

Chapter 9

Discussion

In this chapter the H1 data presented in the last chapters are summarized and some conclusions concerning EAS applications are drawn.

9.1 Summary of Presented H1 Results

The HERA data on F_2 show a strong rise towards low x. The overall slope can be fitted by a $x^{\sim -0.3}$ or an $\ln(Q^2) \cdot x^{-0.19}$ dependence.

This is a much steeper slope than expected in the framework of conventional Regge theory. *Regge theory* predicted a $x^{-0.08}$ slope arising from the "soft" Pomeron determining the growth of the total γp cross section as measured at HERA up to $\sqrt{s} = 200\,\mathrm{GeV}$ and as measured in the total pp cross section up to $\sqrt{s} = 1.8\,\mathrm{TeV}$. And, Regge theory works well in the fixed target region ($Q^2 < 10\,\mathrm{GeV}^2$). It nicely describes the flat x dependence of the recent NMC data on F_2 [137] (see Fig. 6.3) taken at $x \geq 0.008$ and $Q^2 < 10\,\mathrm{GeV}^2$. Regge models based on a bare Pomeron intercept of 1.25 and not taking screening corrections into account also show problems in the comparison to data in the Q^2 range from 4.5 to $8.5\,\mathrm{GeV}^2$.

Predictions based on QCD evolution of the factorization scale in the DGLAP scheme can be made to agree well with the strong rise of F_2. These are either derived from evolving "valence-like" input distributions from a small scale $Q_0^2 = 0.3\,\mathrm{GeV}^2$ up to the measurement region of $Q^2 \geq 4.5\,\mathrm{GeV}^2$ (GRV) [132], or from evolving phenomenological already steep input distributions over a short lever arm of Q^2/Q_0^2. The agreement of the second approach with the data is not very spectacular. It is only noteworthy that DGLAP evolution can describe the inclusive cross section measurement. The agreement of the GRV approach, however, is more fascinating. The GRV parametrizations describe both the fixed target Regge-like, and the HERA perturbative QCD-like data sets with the same

inputs. There thus might be some other more general principle behind the low x behaviour of structure functions. The reason, why in the GRV parametrizations, however, a perturbative evolution chain may start at scales, which, by general prejudice in the community of physicists, are not large enough for perturbative results to apply, has to be further investigated. Either, this agreement is only coincidence, or the reason for this peculiar behaviour of perturbative expansions has to be understood. One possibility is that higher twist corrections to the observable structure functions are very small and the Born perturbative result thus may be used at very small scales.

From the experimental point-of-view at the moment we can only say that the data on F_2 are well compatible with HERA probing the same DGLAP phase space region as the fixed target experiments even though the strong rise of F_2 was a surprise. The success of the GRV prediction was not anticipated by the community for obvious reasons. Parametrizations of parton densities used in predictions for yet unmeasured energy regimes which were commonly based on Regge expectations are changed considerably due to the HERA results.

BFKL dynamics, i.e. dominance of leading $\log(1/x)$ terms in the **perturbative** calculations predicts a growth of the gluon parton density like $x^{-\lambda}$ with $\lambda \lesssim 0.5$ at asymptotically high energies, i.e. after a long QCD evolution. In the current HERA regime corrections and a non-singular background term have to be taken into account. Since higher order corrections and the background term reduce the effective λ, the observed growth of F_2, under the assumption of it being driven by the gluon density, is also well compatible with HERA already probing the QCD phase space of BFKL dynamics. The issue of which domain of the QCD phase space we are probing in the HERA low x domain can thus not be settled by the F_2 measurement.

The gluon density $xg(x, Q^2)$ has been measured down to $x \approx 10^{-3}$ at Q^2 values between 20 and 30 GeV^2. Two different analyses yield well compatible distributions. The distribution are describable by the GRV parametrization as well as by a mixed DGLAP-BFKL ansatz.

The charged current cross section at HERA has been measured by H1. The measurement is in agreement with the theoretical prediction. Converting this cross section into the νN cross section, the H1 measurement corresponds to an equivalent fixed target neutrino energy of 50 TeV. In this view the W propagator effect becomes visible.

The H1 data on the transverse energy flow in DIS events show energy flow shifted from the current region towards the remnant. This could tentatively be interpreted as a signal of the BFKL region of QCD phase space being approached at the lowest values of x accessible at HERA. This is supported at a qualitative level by the data on the production of jets with $k_T^2 \simeq Q^2$. This may however change after the inclusion of fragmentation corrections.

The data on the diffractive structure function F_2^D are well compatible with a Pomeron intercept of 1.08 and thus support the "soft" Pomeron. The Pomeron structure function derived under the assumption of factorization is predominantly hard, favouring "valence-like" constituents in the Pomeron with a considerable soft gluon contribution however allowed by the data. A LO QCD analysis based on a Regge ansatz using the "soft" Pomeron shows satisfactory agreement with the Q^2 and β dependences measured in the H1 data. Qualitatively the data are also consistent with the Buchmüller picture of diffraction. More data and theoretical work are needed for firm conclusions.

The size of the diffraction dissociation cross section in DIS is about 10% of the total cross section. In Regge theory this cross section directly reflects the size of screening correction. If these are due to parton saturation this can be transformed into the size of the gluon concentration region, $R = r_{\text{proton}}$. This is much larger than theoretical estimates based on QCD sum rules [254] which result in $R \simeq 0.3 \cdot r_{\text{proton}}$.

The data on diffractive scattering in photoproduction support a predominantly hard Pomeron structure in the factorizing ansatz. More data and detailed comparisons of real and virtual photon diffractive dissociation will shed light on the Pomeron structure and the validity of the different ansätze.

The size of diffraction dissociation cross section in photoproduction is about 30% of the total cross section. Compared to DIS the screening corrections in this region of phase space are thus much larger than in DIS.

The total γp cross section at $\sqrt{s} \simeq 200\,\text{GeV}$ has been measured to $156 \pm 2 \pm 18$ μb.

A measurement of the gluon density and the distribution of fractional momenta of partons in the photon has been performed. Some extreme parametrizations of the gluon density could be excluded. The GRV-LO parametrization gives a good description of the data.

9.2 Conclusions

The main conclusions from the H1 data is that at HERA we clearly see QCD at work in the low x region. Some of the main questions can however not yet be answered. This is either due to limited statistics, or systematics when incomplete QCD Monte Carlo generators have to be used, or it is due to HERA not yet probing the proton deeply enough.

Important results for EAS applications are that

- the total photoproduction cross section is not growing rapidly and its energy dependence is well described by Regge parametrizations, the expanding proton ansatz, and an eikonalized soft and hard interaction picture if the cutoff regularizing the hard contribution is chosen to be larger than 2 GeV/c. The photon behaves like a hadron but for the additional hard direct and anomalous component which are growing as a function of energy. With the regularization cutoff chosen as 1.4 GeV/c and the pion structure function for the VMD parton densities in the photon, extrapolations of the total photon-air cross section into the unmeasured region of the PeV airshower observations of 2-3 mb fall below the value of $\mathcal{O}(100)$ mb needed to describe the observed muon-rich airshower in terms of photon interactions. The hadronic cross section for photon-air collisions compared to the Bethe-Heitler pair production cross section stays below 1% up to PeV energies. In order to really understand the interactions of the photon at high energies, however, more work on the photon model and the determination of the parton densities in the photon is needed.

- the structure functions at low x can be described by QCD evolutions based on $\ln 1/x$ or $\ln Q^2$ approximations. The resolution of the regions of phase space where the different evolutions apply has thus not yet been achieved. This has important consequences for very high energy EAS installations, since we now know that the hard cross sections are growing more rapidly than anticipated before.

- the structure functions at low x grow more rapidly than predicted by conventional (soft) Regge theory, i.e. assuming only a soft Pomeron with an "effective" intercept of 1.08. Also a different Regge model based on a Pomeron with a "bare" intercept of around 1.25 cannot describe the structure function data for $Q^2 \leq 8.5\,\mathrm{GeV}^2$. There are more than one possible explanation for this observation. Either the soft Pomeron intercept itself is dependent on Q^2 or some admixture of a hard Pomeron is needed. The structure of the hard Pomeron, whether $\ln 1/x$ or $\ln Q^2$, cannot be decided by the data, yet. This observed Q^2 dependence of the effective Pomeron intercept will be discussed in more detail below.

- the size of the diffractive dissociation cross section in DIS at small x is much smaller than in photoproduction. This can be interpreted as different sizes of screening corrections visible in DIS and photoproduction. This fact will be also discussed in more detail below.

- the gluon density in the proton has been measured in the x region important for the hard eikonal in EAS generators. All other parton densities have been determined from fits to available data including the HERA data. This resulted in new parametrizations, *e.g.* MRS H. We also have learned that the parton densities may be taken from the GRV parametrization as well. As discussed in 5.8.4, for the first time we now have a measurement of the energy dependence of the hard eikonal in hand. This has to be incorporated into the EAS Monte Carlo generators.

- in a factorizing ansatz the structure of the Pomeron is predominantly hard with a considerable admixture of soft structure still allowed by the data. This will allow for the production of high p_T final states in cut Pomeron graphs once this is incorporated into the Monte Carlo generators. In an alternative picture of the diffractive structure function data by Buchmüller (see 6.7), this Pomeron structure function is identified with the differential distribution for the production of quark-antiquark pairs and subsequent colour neutralization by interactions with "wee" partons. The hard structure with a soft admixture is obtained as a **prediction** in this model in accordance with the measurement. The development of this model has to be closely followed by the builders of EAS Monte Carlo generators, since its predictive power might be large as it is based on well-known QCD. With the Pomeron as an effective representation of a topological expansion of QCD one might be able to derive important knowledge concerning the extrapolation of the Pomeron nature into higher energy regimes. A connection of this model to high energy asymptotics is given by the energy dependence of single gluon exchange which has been discussed as responsible for the continuing rise of the total hadronic cross sections.

To emphasize the importance of the changing nature of the effective Pomeron as seen in the H1 data, we will discuss its implications in a little more detail. The H1 data taken together may be interpreted as both a Q^2 and energy dependence of the effective Pomeron intercept being visible in the transition from fixed target experiments to HERA.

This can be visualized as follows: at low x the relationship

$$W = \sqrt{Q^2(1/x - 1) + M_p^2} \simeq \sqrt{Q^2/x} \tag{9.1}$$

holds and the total cross section for virtual photon proton scattering is expressable through $F_2(W, Q^2)$ as

$$\sigma_{\gamma^* p}(Q^2, s_{\gamma^* p}) \simeq \frac{4\pi^2\alpha}{Q^2} \cdot F_2^p(W, Q^2) \tag{9.2}$$

If we plot the H1 data on F_2 for $x > 0.001$ against W as shown in Fig. 9.1 we can fit the W dependence up to $W \simeq 130\,\mathrm{GeV}$ by a straight line according to $F_2(W, Q^2) = 0.0058 W/\mathrm{GeV} + 0.42$. For larger W a decrease of the slope seems to develop at low Q^2 indicating the transition to the soft Pomeron. The H1 data for even lower values of Q^2 (down to $4.5\,\mathrm{GeV}^2$) or for $x \leq 10^{-3}$ also appear to deviate from the linear behaviour. The energy dependence of the virtual photon proton cross section $\sigma_{\gamma^* p}(s) \propto s^{0.5}$ with $s_{\gamma^* p} = W_{\gamma p}^2$ is much stronger than the one observed for real photons in the total photoproduction cross section where $\sigma_{\gamma p}(s) \propto s^{0.08}$. We thus observe a hard Pomeron intercept at large Q^2 and large W which seems to decrease when going to lower Q^2 or the largest measured values of W.

In a similar fashion, the ZEUS measurements of $F_2(x, Q^2)$ and the total cross section for photon-hadron scattering have been collected by Levy [255] and plotted

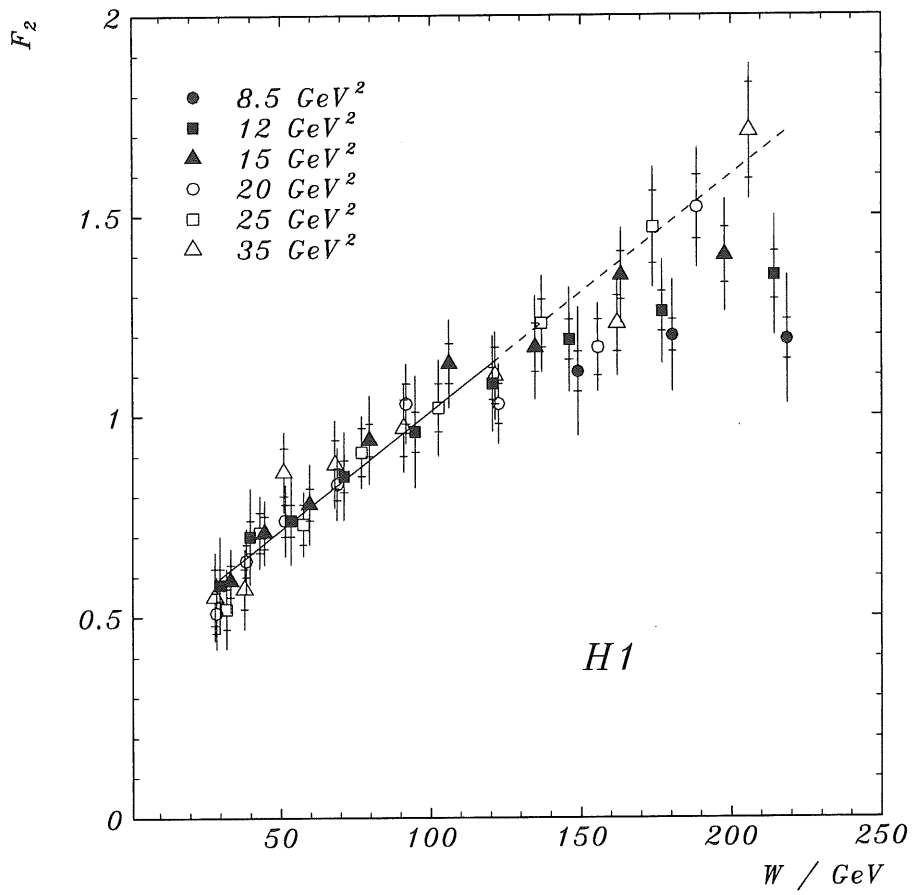

Figure 9.1: Comparison of the low Q^2 structure function data of H1 plotted as functions of the invariant mass W of the $\gamma^* p$ system. The straight line is a fit $F_2(W, Q^2) = 0.0058 W/\mathrm{GeV} + 0.42$ for $x > 0.001$ which extends up to $W \simeq 130\,\mathrm{GeV}$ where F_2 scales for Q^2 range considered. Data for $Q^2 \geq 80\,\mathrm{GeV}^2$ have a similar slope versus W but are below the lower Q^2 data.

against W^2 as shown in Fig. 9.2. The energy dependence at low Q^2 can be interpreted as a threshold effect when $Q^2 > W^2$. One also sees the strong rise of the structure function with energy as soon as W^2 is larger than the fixed target energies, i.e. above $2500\,\mathrm{GeV}^2$, or as soon as Q^2 is larger than about $10\,\mathrm{GeV}^2$, while the total cross section and the low W^2 ($W^2 < 400\,\mathrm{GeV}^2$) and low Q^2 ($Q^2 < 10\,\mathrm{GeV}^2$) structure function data follow a much milder energy trend compatible with the "soft" Pomeron prediction at large energies as contained in the ALLM parametrization [256]. The H1 results depicted in Fig.9.1 are practically identical.

We thus see that in the measured HERA regime ($Q^2 \geq 4.5\,\mathrm{GeV}^2$ and $W^2 \geq 2500\,\mathrm{GeV}^2$) the Pomeron nature is different from the low energy one. Levy fitted a simple ansatz

$$\alpha_{\mathbb{P}}^{\mathrm{eff}} = a(Q^2) \cdot \alpha_{\mathbb{P}_{\mathrm{soft}}} + (1 - a(Q^2))\alpha_{\mathbb{P}_{\mathrm{hard}}} \tag{9.3}$$

for the effective Pomeron intercept to the data with $\alpha_{\mathbb{P}_{\mathrm{soft}}} = 1.08$ and $\alpha_{\mathbb{P}_{\mathrm{hard}}} = 1.5$

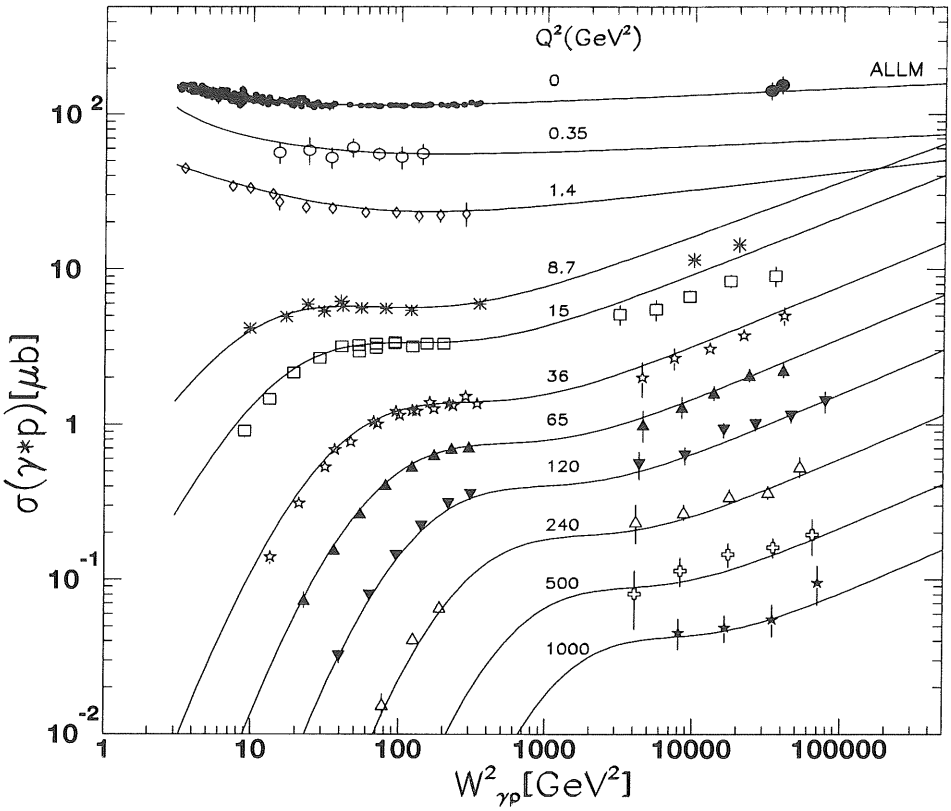

Figure 9.2: Comparison of measurements of the total γp cross section with the ZEUS measurements of the structure function $F_2(W^2, Q^2)$ as a function of W^2 by Levy [255].

and a slope of the hard Pomeron of $0.025\,\mathrm{GeV}^{-2}$, i.e. a factor of 10 less than for the soft Pomeron. He finds a transition of the effective intercept from hard which is about 1.4 to soft between Q^2 of $8.7\,\mathrm{GeV}^2$ and $1\,\mathrm{GeV}^2$.

This transition which is also seen in the H1 data is to be expected as evident in Fig. 9.2, since the cross section for virtual photon proton scattering can not exceed the one for real photon proton scattering. The data could be understood in the following Pomeron pictures:

1. In the Pomeron model by Capella *et al.* [187] the phenomenological "bare" Pomeron has an intercept of about 1.25 and it is the only Pomeron, i.e. the hard Pomeron does not exist in this model. In hadron-hadron collisions (and photon-hadron collisions) the contributions from two or more Pomeron exchanges are large. These lead to screening corrections which reduce the effective intercept to 1.08. Virtual photons on the other hand are point-like objects. For these, screening corrections are supposed to be smaller and the effective intercept thus larger. The Q^2 dependence of the effective intercept

in this model is of the form

$$\Delta(Q^2) = \Delta(0) \cdot \left[1 + \frac{2Q^2}{Q^2 + d}\right] \tag{9.4}$$

with d chosen such that with $\Delta(0) \approx 0.07 - 0.08$ the value $\Delta(Q^2 \to \infty) \approx 0.20 - 0.24$ is obtained. The value of Q^2 where the changeover from soft to more hard takes place might be very small. According to the H1 data at least smaller than $4.5\,\mathrm{GeV}^2$.

2. If the observed differences between photoproduction and DIS are due to a saturation of the parton density, the "hard" Pomeron in **both** cases is responsible for the behaviour of the total cross section and only the greatly different sizes of the screening corrections for small and large virtualities lead to the observed steep x-dependence of the structure functions compared to the slow s-dependence of the total cross section for photoproduction.

   This scenario is equivalent to the one by Capella et al. and also leads to a smooth transition from small to large virtualities. More data at smaller values of Q^2 at low x are needed to shed light on this transition region. In EAS Monte Carlo applications, however, this scenario would differ from the one by Capella et al. due to the hard QCD Pomeron being the basic ingredient instead of a phenomenological one with a softer intercept. This will lead to different sizes of higher order contributions and thus different final state distributions.

3. In the picture where we have two distinct Pomerons, the soft Pomeron acting at scales below Q^2_{min} and the hard one at scales larger than this, the variation of the measured effective intercept can be viewed as the changing relative contribution of the two Pomerons. The transition region, in this case, is somewhat arbitrary. In EAS applications two basic ingredients would be needed and the actual partonic configuration of inelastic final states from cut Pomerons would differ due to discontinuities at the transition points from soft to hard Pomerons.

4. The measurement of structure functions can be viewed in a "mini-jet" picture where the production of mini-jets is a multiple interaction process, i.e. occuring on top of an underlying soft event. The total cross section is in this picture determined by the soft Pomeron. The hard cross section on the other hand, for fixed $Q^2 \approx p_{\mathrm{T}}^2$, is growing as a function of energy due to the growing phase space. The size of the diffractive cross section can be derived in the Buchmüller approach to diffraction and should be about 1/9 of the inclusive cross section, in accordance with the measurement. In EAS applications this scenario would only need the soft Pomeron to determine the energy dependence of the total cross section, while the inelastic final states can be derived from higher order corrections to electron-gluon scattering.

To summarize, experimentally we find at low x (i.e. high energies) a transition from soft to hard scattering (i.e. Pomeron exchange) as a function of Q^2 in a Q^2

dependence of the effective intercept. This Q^2 dependence could be due to different sensitivity of the observables to screening corrections, due to phase space effects in a multiscattering mini-jet picture for the structure functions, or due to the existence of two disjunct Pomerons, a soft and a hard one and what we observe is the superposition of these two with the resulting intercept depending on the observable. Independent of which of the above pictures or if all of them are appropriate, in the data gathered at HERA we clearly see evidence for QCD at work in the low x region.

Since higher order screening corrections or the superposition of the two Pomerons will have some energy dependence, in phenomenological models the relative contributions of the soft and hard processes and the smooth transition from one to the other will have to be incorporated. The scale dependence of the relative importance of soft and hard Pomerons here constitutes the main parameter which has to be obtained from the data. In addition, the development of the model by Buchmüller and co-workers has to be follwed closely. The measurements performed at HERA provide insight into the transition region and thus have an important influence on the improvement of simulation programs for EAS. For growing energies the importance of large $Q^2 \approx p_T^2$ processes grows. The HERA data provide vital information for the extrapolation of the effective Pomeron into the large energy and $Q^2 \neq 0$ regime. This extrapolation will be especially important when developing simulation programs for the planned 10^{20} eV installations. The HERA data analyses do in some respects not yet allow as firm conclusions as necessary for extrapolations over the large voids in energy that have to be bridged towards these simulations. Further measurements at HERA will have to aim for lower Q^2 and if possible higher CMS energies. On the analysis side a more detailed incorporation of known QCD into the Monte Carlo generators is unavoidable in order to bring more clarity into these questions.

9.3 HERA Influence on EAS Related Subjects

To round of the above conclusions we will discuss some examples on the influence of the HERA structure function data on EAS related subjects. These are concerned with the possible onset of the Quark-Gluon Plasma phase in heavy-ion collisions, very high energy neutrino cross sections, and enhanced inelastic cross sections of CR at high energies.

9.3.1 Quark-Gluon Plasma

Alhough the detector acceptances are widely different in EAS experiments and experiments at colliders, the physics reactions governing EAS are similar to the physics the planned proton-proton (LHC) or heavy ion collider (RHIC, LHC in

heavy ion mode) will be sensitive to. Some lessons for EAS application might therefore be learned from studies performed for collider experiments.

Analyses by Eskola *et al.* on multiplicities for LHC nuclear collisions performed with the DO set of parton densities in 1989 [257] and with the MRS D0', D$^-$' and H sets of densities in 1994 [258] show a dramatic increase in the QCD expectation for the charged multiplicity in the central rapidity region, defined by $|y| \leq 0.5$, when going from the DO to the MRS parametrizations. The estimates were performed for central Pb on Pb collisions at $\sqrt{s} = 5500$ AGeV. This is of course not the general collision type in CR interactions in the atmosphere, where the event rate is dominated by the "soft" interactions and the resulting EAS is observed at $y \rightarrow y_{\max}$. But nevertheless, this revision of the LHC expectation serves to clarify a point.

For Pb on Pb collisions at LHC the use of any set of parton densities results in gluon interactions to dominate the cross sections calculable in QCD perturbation theory via

$$\sigma_{\text{jets}} = \sum_{i,j} \int dx_1 \int dx_2 \int dt g_i(x_1, Q^2) g_j(x_2, Q^2) \frac{d\sigma_{i,j}}{dt}.$$

A lower limit on the expected multiplicities can therefore be obtained by only considering gluon contributions. In Fig. 9.3 the gluon densities of DO 1, MRS D-', and MRS H are shown for a QCD scale of $Q = 2$ GeV. This is a value for the scale typically chosen as signifying the validity of QCD perturbation theory.

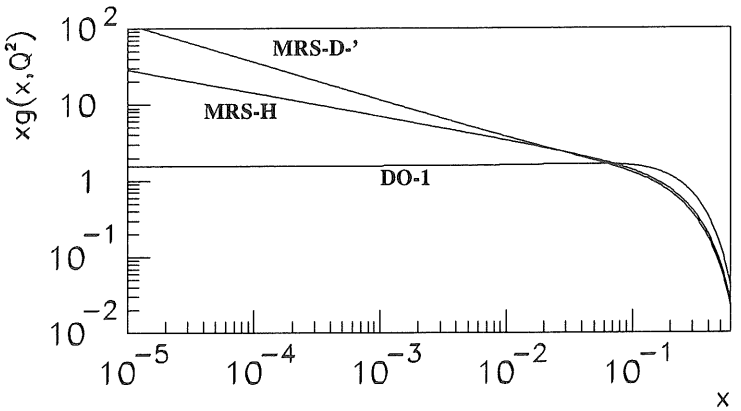

Figure 9.3: The gluon distributions $xg(x, Q^2)$ for the DO-1, MRS-H, and MRS-D$^-$' parametrizations at $Q^2 = 4\,\text{GeV}^2$.

For the determination of the gluon distribution at HERA see 6.4. In the DO set of parton densities the gluon behaves as $xg(x, 4\,\text{GeV}^2) \propto$ const, in the MRS D-' set $xg(x) \propto x^{-0.5}$, and in the latest MRS H set $xg(x) \propto x^{-0.3}$. The resulting lower limits on the charged multiplicities are $dN_{\text{ch}}/dy > 910$ for the DO 1, $dN_{\text{ch}}/dy > 3400$ for the D-', and $dN_{\text{ch}}/dy > 2200$ for the H set.

The anticipated Quark-Gluon Plasma phase is characterized by a thermalized system of dense quarks and gluons. Since the multiplities using the new HERA inspired parton densities are found to be much larger, the average energy per parton will be smaller, the system thus closer to thermal equilibrium. This gives hope for the heavy ion collider experiments to see the onset of this new QCD phase.

It also enhances the chances of EAS experiments to observe events with significantly different topology due to the decay of a thermalized Quark-Gluon Plasma-Ball produced in very high energy CR interactions. The anticipated signal for the HEGRA installation has been discussed in 3.3.6. Assuming that a 500 TeV iron nucleus impinging on atmospheric argon with a CMS energy of around 60 GeV/nucleon yields a sufficient energy density, the number of candidate events collected in HEGRA is about 10 per day. We thus have about 3000 events per year of data taking where the formation of QGP might have occurred. Since the probability for central collisions is small, however, the number of signal events is considerably smaller than this. The signal events have to be found in a data sample consisting of about $5{\cdot}10^8$ events. Given the limited computer power the chance to find these events is thus small but finite.

9.3.2 Very High Neutrino-Air Cross Sections

The detection of the Fly's Eye event with a reconstructed energy of $3.0\pm^{0.36}_{0.54} \cdot 10^{20}$ eV [55] has triggered many theoretical and experimental activities in the Astrophysics community. With the hard GZK-cutoff imposed on the energy of extragalactic hadrons due to interactions with the CMB (see 2.2.1), the possibility of these events stemming from photon or neutrino interactions has been discussed [259] besides the most commonly assumed hadron (proton or heavier) nature of the event. While the measured shower development is found to be inconsistent with a photon hypothesis, neutrino origin of this event is compatible with the observed characteristics. Since the hypothesis test is performed on the longitudinal shower development, however, the influence of the HERA structure function data is particularly strong. This test thus needs to be repeated once the next generation of EAS Monte Carlo generators is available (see 9.3.3).

The event if due to an incident proton implies a flux of [55]

$$\frac{dN_p}{dE} = 7.4 \cdot 10^{-41} (\mathrm{cm}^2\,\mathrm{s}\,\mathrm{sr}\,\mathrm{eV})^{-1} \tag{9.5}$$

which has to be scaled according to the respective cross sections if we assume the incident particle was a neutrino. To calculate the neutrino-air cross section for $E_{\mathrm{max}} = 3 \cdot 10^{20}$ eV, the HERA results on the structure function enter. In Fig. 9.4 we show the total cross section for neutrino scattering on an isoscalar target for incident neutrino energies between 10^6 and 10^{11} GeV calculated with the parton density parametrizations MRS H, MRS D0 [185], GRV HO [132], EHLQ 1 [260],

and DO 1 [252]. The parton densities at x values below the ones probed at HERA do not contribute up to these energies.

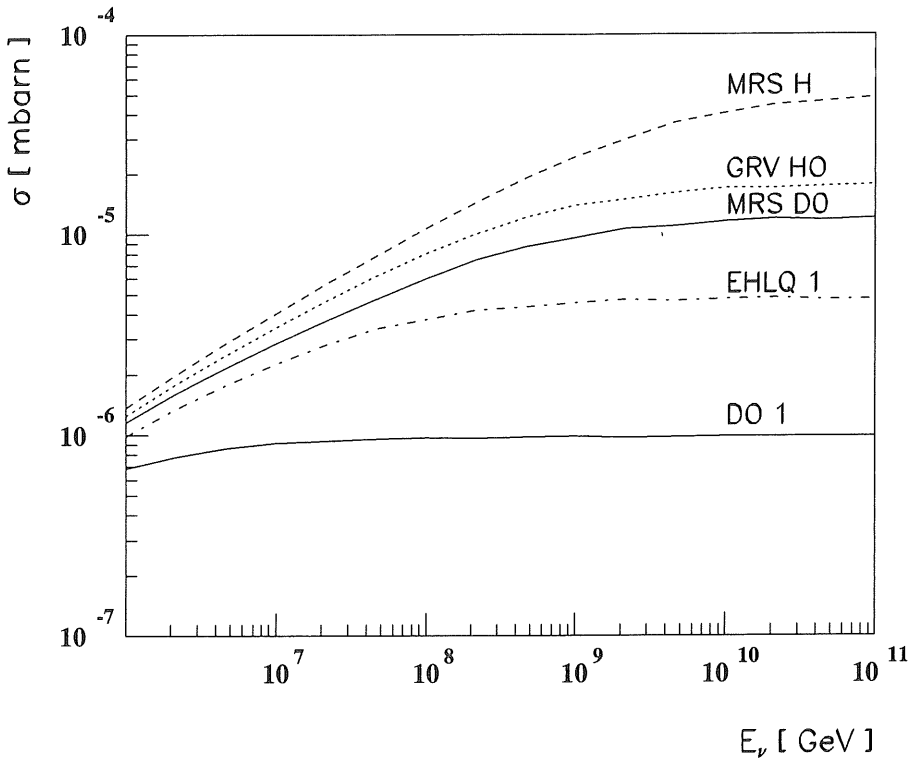

Figure 9.4: High energy neutrino cross section using different parton parametrizations.

The W propagator effect ends the rapid rise of the cross section at around 10^8 GeV. The parametrizations of MRS H and GRV HO give a good description of the H1 data. The remaining uncertainty of the cross section is thus about a factor of 3. The absolute value of the cross section at $10^{11} GeV$ is about a factor of 10 (EHLQ 1) to 50 (DO 1) higher than for the calculations based on pre-HERA data.

Halzen *et al.* [259] have estimated the AGN neutrino luminosity needed to produce the highest energy event and they arrive at values between 10^{45} and 10^{51} erg s^{-1} which are within the range of possible AGN luminosities. Thus also the highest energy event provides some support for the planned experiments aiming to search for very high energy neutrino fluxes or sources. Once these experiments are operating, the influence of the HERA measurements on derived fluxes or flux limits is obvious from Fig. 9.4.

9.3.3 Very High Energy pp Cross Section

Capdevielle [253] has studied the influence of the chosen parton density parametrization on the inelastic pp cross section at very high energies ($s \geq 3.4 \cdot 10^6\,\mathrm{GeV}^2$) using the DTUJET92 Monte Carlo generator [261]. In this investigation the influence of changing from the Duke and Owens (DO 1) parton densities to the newer parton distributions MRS B0 and MRS D- [136] (see also 5.6), which correspond to a high energy asymptotic behaviour corresponding to the critical and the hard Pomeron, respectively, was studied. With the HERA results in hand we know the data to lie between these extremes but closer to the MRS D- prediction. The parton densities enter into the calculation of the semi-hard and hard QCD cross sections and determine the distribution of the string endpoints in rapidity space. As discussed in 5.8, eikonalization tends to reduce the influence of the hard cross section on the total cross section and the impact of eikonalization will grow when going to higher energies.

We have taken the parametrized results of Capdevielle's investigation for the inelastic pp cross section and calculated the inelastic pp cross section as a function of the square of the CMS energy between 2 and 20 TeV^2, corresponding to incoming proton energies between about 1000 and 10,000 TeV on a stationary proton target and corresponding to the range in energy where the "knee" in the CR spectrum has been observed.

Fig. 9.5 shows the cross sections for the three choices of the parton distributions. In Fig. 9.6 we also show the prediction of DTUJET92 for the charged multiplicities produced in these interactions. Compared to the old DO 1 parametrization which also is used in the VENUS 4.10 generator, the new parton distributions result in cross sections lower by about 10% and charged multiplicities larger by 10 to 30%. Please note that this reflects the fact that, although the x region of the parton densities determining these observables is around 10^{-2}, the HERA data influenced the fits to the combined data in regions of x beyond the actual measurement range.

One of the major observables in EAS experiments needed for discriminating incident particle types is the height of the shower maximum X_{max}. Using the MRS D- parton densities instead of DO 1 will lead to an earlier start and faster development of the EAS. This leads to a X_{max} distribution shifted to lower values and thus strongly influences the determination of the chemical composition of CR. Capdevielle has investigated this for incoming energies between 10^{17} and 10^{19} eV and finds differences in the position of X_{max} of up to about 15% when using MRS B0 or MRS D- parton distributions. Since this study involved some approximations and short-cuts, it needs to be repeated with modified EAS generators once they are available.

This example, however, highlights the influence of the HERA measurements on EAS experiments. The next generation of EAS Monte Carlo generators will

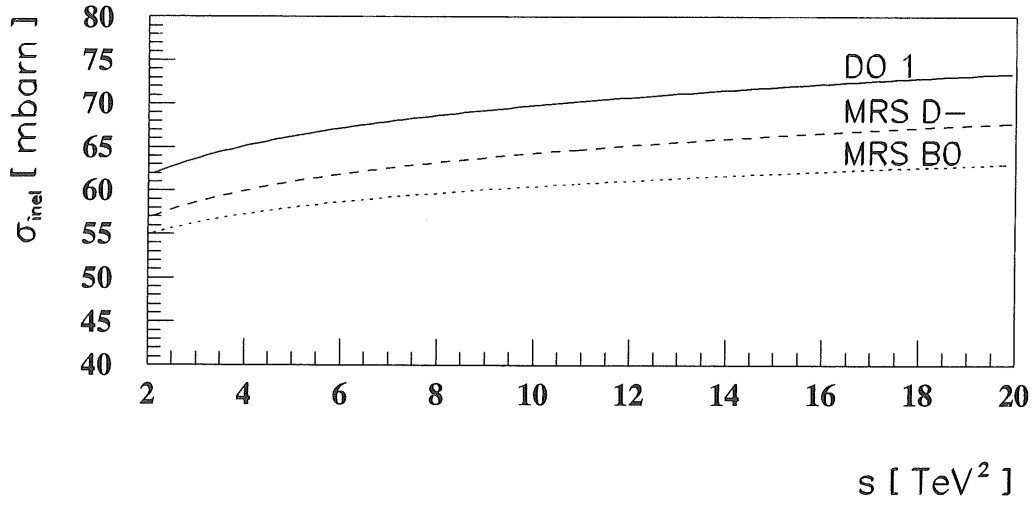

Figure 9.5: The inelastic pp cross section for CMS energies squared between 2 and 20 TeV^2 as determined with the DTUJET92 Monte Carlo generator using the parton distributions of the MRS B0, MRS D-, and DO 1 parametrizations. Formulae taken from [4] and [253].

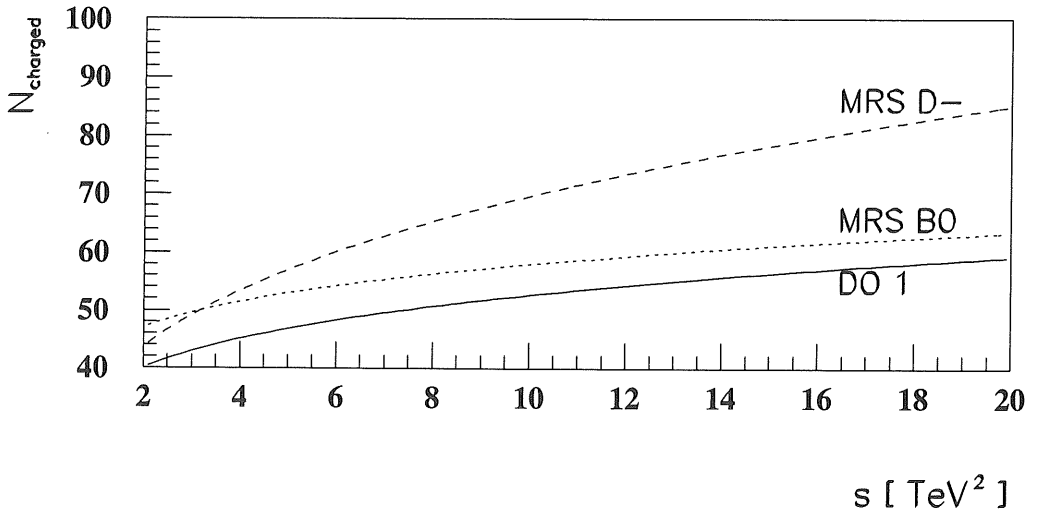

Figure 9.6: The charged multiplicity resulting from inelastic pp scattering for CMS energies squared between 2 and 20 TeV^2 as determined with the DTUJET92 Monte Carlo generator using the parton distributions of the MRS B0, MRS D-, and DO 1 parametrizations. Formulae taken from [4] and [253].

be greatly modified due to the HERA results pertaining to the proton and the Pomeron. Especially the planned ultrahigh energy experiments have to await these modified generators before the extraction of meaningful parameters is possible.

9.4 Outlook

The study of low x physics, both theoretically and experimentally, is providing some fundamental insights into the workings of QCD when approaching the non-perturbative limit. The data indicate how the transition region can be treated in phenomenological models. Since this region also constitutes the Regge limit of QCD, we are gathering important information for the extrapolation from the accelerator regime to the much higher energies available in CR interactions. The hope is that knowledge on collective phenomena in QCD can be gathered at low x and that the understanding of the Pomeron as a compound object can be improved.

The first round of HERA data yielded important results on the deep structure of the proton, the nature of the Pomeron, and the interactions of high energy photons. For some of the results, *e.g* diffraction in DIS and photoproduction and the determination of the structure of the photon and the energy dependence of it's interaction channels, sizable statistical and systematic errors leave too much room for interpretations. In the next round of data analyses the aim is to differentiate between competing models. For this it is necessary to utilize the full potential of the HERA machine.

The advances in QCD are thus found to directly influence our understanding of the measurements of high energy processes made available to us by just looking out into the universe. We must conclude that in order to perform astronomical and astrophysical measurements in the full observation window spanning now more than 28 decades in energy, we need to stay in close contact with the other fields of physics.

Acknowlegements

The author wishes to thank all the people who contributed to this report.
In particular my thanks go to H. Meyer for providing the environment and stimulating support throughout the years of our cooperation.
The use of infra-structures provided by the H1 and HEGRA collaborations is acknowledged. My thanks goes to all collaborators without whom non of the reported results would have been obtained. Especially I wish to thank the H1 collaborators from UC Davis for the opportunity to spend a fruitful year at their institute.

I am grateful to D. Heck, S. Ostapachenko, A. Rostovtsev, H. Spiesberger and T. Thouw for helpful discussions, to K. Werner for providing the LaTeX files of the pictures in chapter 8, and to M. Kuhlen, W. Rhode, P. Schnürer and A. v. Struve for commenting on the manuscript.
Finally I want to thank Christine and all my family for their constant emotional support.

Bibliography

[1] S. Kayakawa, *Cosmic Ray Physics*, Wiley-Interscience, New York, 1969.

[2] M. S. Longair, *High Energy Astrophysics*, Cambrige, Cambridge University Press, 1981.

[3] V. S. Berezinskĭi et.al., *Astrophysics of Cosmic Rays*, North-Holland, Amsterdam, 1990.

[4] J. N. Capdevielle et al., *The Karlsruhe Extensive Air Shower Simulation Code CORSIKA*, **KFK report 4998 (1992)**, Kernforschungszentrum Karlsruhe.

[5] M. T. Ressel and M. S. Turner, *Comm. Astrophys.* **14** (1990) 323.

[6] A. Karle et al., *Design and Performance of the Angle Integrating Čerenkov Array AIROBICC*, *Astropart. Phys.*, in press.

[7] W. Galbraith and J. V. Jelley, *Nature* **171** (1953) 350.

[8] P. P. Kronberg, *Rep. Prog. Phys.* **325** (1994) 382.

[9] G. B. Khristiansen and G. V. Kulikov, *JETP* **35** (1958) 635.

[10] M. Nagano et al., *Proc. 22nd Int. Cosmic Ray Conf.*, Dublin, 1991, vol. **2** 89.

[11] B. Wiebel, *Chemical Composition in High Energy Cosmic Rays*, University of Wuppertal preprint, WUB 94-08, 1994.

[12] P. L. Biermann, H. Meyer, B. Wiebel-Sooth, *Cosmic Ray Electron Spectra: Prediction and Data*, to appear in *Proc. 24th Int. Cosmic Ray Conf.*, Rome, 1995.

[13] M. Teshima et al., *Nucl. Instr. Meth.* **A427** (1986) 399.

[14] G. B. Christiansen, *Proc. 19th Int. Cosmic Ray Conf.*, La Jolla, 1985, vol. **9** 487.

[15] A. Vilenkin, *Phys. Rep.* **121** (1985) 263.

[16] P. Bhattacharjee, C. T. Hill and D. N. Schramm, *Phys. Rev. Lett.* **69** (1990) 365.

[17] V. L. Ginzburg and S. I. Syrovatiskiĭ, *The Origin of Cosmic Rays*, Pergamon Press, Oxford, 1964.

[18] G. J. Cesarsky, in *High Energy Astrophysics*, edited by F. K. Lamb, Benjamin/Cummings, Menlo Park, CA, 1985, p. 245; J. Ormes and P. Freier, *Astrophys. J.* **222** (1978) 471.

[19] W. Baade and F. Zwicky, *Proc. Nat. Acad. Science*, vol. **11** 259.

[20] M. Garcia-Munoz, G. M. Mason and J. A. Simpson, *Astrophys. J.* **217** (1977) 859.

[21] H. Alfvén, *Phys. Rev. 2nd ser.* **vol 55** (1939) 425.

[22] G. Cocconi, *Nuovo Cim., 10th ser.* **vol 3** (1956) 1433.

[23] P. O. Lagage and C. J. Cesarsky, *Astron. & Astrophys.* **118** (1983) 223.

[24] P. L. Biermann, Preprint Max-Planck-Institut für Radiastronomie, Bonn, MPIFR-616, 1994; contributed to *Trends in Astroparticle Physics*, Stockholm, Sweden, 1994.

[25] H. J. Völk and P. L. Biermann, *Ap. J. Lett.* **333** (1988) L65.

[26] M. Samorski and W. Stamm, *Ap. J. Lett.* **268** (1983) L17.

[27] J. Lloyd-Evans et al., *Nature* **305** (1983) 784.

[28] A. K. Harding and T. K. Gaisser, *Ap. J.* **358** (1989) 561.

[29] T. K. Gaisser, A. K. Harding and T. Stanev, *Ap. J.* **345** (1989) 423.

[30] V. S. Berezinskiĭ, *Proc. Neutrino 77*, Nauka, Moscow, 1977, **1** 177;
R. Silberberg and M. M. Shapiro, *Proc. 16th Int. Cosmic Ray Conf.*, Kyoto, 1979, vol. **10** 357;
V. S. Berezinskiĭ and V. L. Ginzburg, *Mon. Not. Royal Astr. Soc.* **194** (1981) 3.

[31] R. J. Protheroe and D. Kazanas, *Ap. J.* **265** (1983) 620.

[32] D. Kazanas and D. Ellison, *Ap. J.* **304** (1986) 178.

[33] J. H. Krolik et al., *Ap. J.* **371** (1991) 541.

[34] R. F. Mushotzsky, C. Done and K. A. Pounds, *Ann. Rev. Astron. Astrophys.* **31** (1993) 717.

[35] M. C. Begelman, B. Rudak and M. Sikora, *Ap. J.* **362** (1990) 38.

[36] F. W. Stecker, C. Done, M. H. Salomon and P. Sommers, *Phys. Rev. Lett.* **66** (1991) 2697; *ibid.* **69** (1992) 2738;
F. W. Stecker, O. C. de Jaeger, M. H. Salomon, *Ap. J.* **39** (1992) L49.

[37] T. K. Gaisser, F. Halzen and T. Stanev, *Phys. Rep.* **258** (1995) 173.

[38] C. Done and A. C. Fabian, *Mon. Not. R. Astr. Soc.* **240** (1989) 81.

[39] *Proc. Workshop on High Energy Neutrino Astrophysics*, Hawaii, 1992.

[40] P. Biermann and P. L. Strittmatter, *Ap. J.* **322** (1987) 643.

[41] J. P. Rachen, T. Stanev and P. L. Biermann, *Astron. Astrophys.* **273** (1993) 377.

[42] C. D. Dermer, R. Schlickeiser and A. Mastichiadis, *Astron. Astrophys.* **256** (1992) L27.

[43] A. A. Zdiarski and J. H. Krolik, *Ap. J.* **409** (1993) L33.

[44] M. Sikora, M. C. Begelman and M. J. Rees, *Ap. J.* **421** (1994) 153.

[45] C. E. Fichtel et al., *Astrophys. J. Suppl.* **94** (1994) 551.

[46] Whipple Collaboration, M. Punch et al., *Proc. 22d Int. Cosmic Ray Conf.*, Dublin, 1991, vol. 1 464; *Nature* **160** (1992) 477;
Whipple Collaboration, G. Mohanty et al., *Proc. 23rd Int. Cosmic Ray Conf.*, Calgary, 1993, vol. 1 440.

[47] HEGRA Collaboration, D. Petry et al., *A Search for high energy γ-radiation from Mkn 421 using the imaging Cherenkov telescopes of the HEGRA collaboration*, to appear in *Proc. 24th Int. Cosmic Ray Conf.*, Rome, 1995.

[48] Whipple Collaboration, A. D. Kerrick et al., *Ap. J.* **438** (1995) L59.

[49] T. Takahashi et al., *IAU Circ.*, No. 6167, 1995.

[50] T. Takahashi et al., *IAU Circ.*, No. 5993, 1994.

[51] M. Kamionkowski, *Phys. Rev.* **D44** (1991) 3021.

[52] K. Greisen, *Phys. Rev. Lett.* **16** (1966) 748.

[53] N. N. Efimov et al., *Catalogue of the Highest Energy Cosmic Rays*, Ed. WDC-C2 for Cosmic Rays, (1988) No. 3, p. 1.

[54] N. N. Efimov et al., *Astrophysical Aspects of the most energetic Cosmic Rays*, Ed. M. Nagano, F. Takahara, World Scientific, Singapore, 1992, p. 20-33.

[55] D. J. Bird et al., *Phys. Rev. Lett.* **71** (1993) 3401.

[56] N. Hayashida et al., *Phys. Rev. Lett.* (in press) (check)

[57] G. T. Zatsepin and V. A. Kuzmin, *JETP Lett.* 4 (1966) 78.

[58] *Proc. Snowmass 94, Particle and Nuclear Astrophysics and Cosmology in the Next Millenium*, Snowmass, Colorado, 1994.

[59] C. Fabjan, *Experimental Techniques in High Energy Physics*, Ed. T. Ferbel, Addison-Wesley, (1987), p. 257.

[60] K. Kamata and J. Nishimura, *Prog. Theoretical Phys. Suppl.* **6** (1958), 93.

[61] MILAGRO Collaboration, J. A. Goodman et al., *Proc. High Energy Gamma-Ray Astronomy*, Ann Arbor, Michigan, 1990, Ed. J. Matthews.

[62] HEGRA Collaboration, S. Westerhoff et al., *Neural Networks for γ/Hadron-Separation with the HEGRA Geiger Towers*, to appear in *Proc. 24th Int. Cosmic Ray Conf.*, Rome, 1995.

[63] HEGRA Collaboration, A. Karle et al., *Phys. Lett.* **B 347** (1995) 161.

[64] P. Sokolsky, *Introduction to Ultrahigh Energy Cosmic Ray Physics*, Addison-Wesley, 1989.

[65] HEGRA Collaboration, A. Lindner et al., *Composition and Energy Measurement wih a New Method Applied to the HEGRA Data in the Energy Range of the Knee*, to appear in *Proc. 24th Int. Cosmic Ray Conf.*, Rome, 1995.

[66] F. Arqueros et al., Preprint MPI-PhE/95-10, 1995.

[67] R. M. Baltrusaitis et al., *Nucl. Instr. Meth.* **A240** (1985) 410.

[68] R. M. Tennent, *Proc. Phys. Soc.* **92** (1967) 622;
D. M. Edge et al., *J. Phys. A: Math. Nucl. Gen.* **6** (1973) 1612.

[69] Whipple Collaboration, M. F. Cawley et al., *Exper. Astron.* **1** (1990) 173.

[70] R. Mirzoyan et al., Max-Planck-Institut für Physik preprint, MPI-PhE/94-24.

[71] J. R. Patterson and T. Kifune, *Australian and New Zealand Physicist* **29** (1992) 58.

[72] Themistocle Collaboration, P. Ballion et al., *Astropart. Phys.* **1** (1993) 341.

[73] T. K. Gaisser, *Cosmic Rays and Particle Physics*, Cambridge, Cambridge University Press, 1990.

[74] Acharya et al., *Nature* **347** (1990) 3614.

[75] B. L. Dingus et al., *Phys. Rev.* **D 48** (1988) 1906.

[76] M. Drees and F. Halzen, *Phys. Rev. Lett.* **61** (1988) 275.

[77] G. Schuler, *Proc. Workshop on Physics at HERA*, DESY, Hamburg, 1991, vol. 1 461.

[78] V. Matheis, Thesis, University of Heidelberg, 1994, unpublished.

[79] N. Gehrels et al., *Astron. Astrophys. Suppl. Ser.* **97** (1993) 5.

[80] G. J. Fishman et al., *Proc. Gamma Ray Observatory Science Workshop*, Washington:NASA, 1989.

[81] T. K. Gaisser et al., to appear in *Proc. Snowmass 94, Particle and Nuclear Astrophysics and Cosmology in the Next Millenium*, Snowmass, Colorado, 1994; Bartol Preprint BA-94-70.

[82] A. Capella, H. Sukhtame, C. I. Tan and J. Tran Than Van, *Dual Parton Model in hadronic multiparticle production*, Ed. P. Carruthers, World Scientific, Singapore (1988), p. 428.

[83] A. Kaidalov, *Nucl. Phys.* **A 525** (1991) 39c.

[84] K. Werner, *Phys. Rep.* **232** (1993) 87.

[85] V. N. Gribov, *Sov. Phys. JETP* **26** (1968) 414.

[86] *Conceptual Design of the Relativistic Heavy Ion Collider RHIC*, Brookhaven Natinal Laboratory Report BNL-52195 (May 1989).

[87] *Proc. of the Large Hadron Collider Workshop*, Aachen, 1990.

[88] R. Plaga and A. Karle, *Proc. 23rd Int. Cosmic Ray Conf.*, Calgary, 1993, vol. 4 295.

[89] A. A. Anselm, *Phys. Lett.* **B217** (1989) 169;
A. A. Anselm and M. Ryskin, *Phys. Lett.* **B266** (1991) 482;
A. A. Anselm and M. Bander, Preprint UCI TR 93-32, 1993;
J. D. Bjorken, *Int. J. Mod. Phys.* **A7** (1992) 4819;
J. D. Bjorken, *Acta Phys. Pol.* **B23** (1992) 561.

[90] C. M. G. Lattes, T. Fujimoto and S. Hasegawa, *Phys. Rep.* **65** (1980) 151.

[91] F. Brasse, The H1 detector at HERA, *Proc. of the 26th Int. Conf. on High Energy Physics*, Dallas, 1992;
H1 Collaboration, I. Abt et al., The H1 detector at HERA, DESY preprint DESY 93-103 (1993).

[92] V. Haustein, Thesis, University of Hamburg, 1995, to appear.

[93] R.W. McAllister and R. Hofstadter, *Phys. Rev.* **102** 1956 851.

[94] G. Zweig, CERN Report **TH 401, 412** 1964; M. Gell-Mann, *Phys. Lett.* **8** (1964) 214. R. Feynman, *Phys. Rev. Lett.* **23** (1969) 1415.

[95] SLAC-MIT Coll., *Proc. 14th Int. Conf. High Energy Physics*, Vienna, 1968;
E.D. Bloom et al., *Phys. Rev. Lett.* **23** (1969) 930;
M. Breidenbach et al., *Phys. Rev. Lett.* **23** (1969) 935;
J.I. Friedman and H.W. Kendall, *Ann. Rev. Nucl. Science* **22** (1972) 203.

[96] J. Bjorken, *Phys. Rev.* **179** (1969) 1547.

[97] R. Feynman, *Phys. Rev. Lett.* **23** (1969) 1415.

[98] H. Fritsch, M. Gell-Mann and H. Leutwyler, *Phys. Lett.* **B47** (1973) 365;
D.J. Gross and F. Wilczeck, *Phys. Rev.* **D8** (1973) 3633;
S. Weinberg, *Phys. Rev. Lett.* **31** (1973) 494.

[99] CTEQ Collaboration, R. Brock et al., Fermilab-Pub-93-094.

[100] R. G. Roberts, *The Structure Of The Proton*, Cambridge, Cambridge University Press, 1990.

[101] M. Froissart, *Proc. of the La Jolla Conf.* (unpublished)

[102] T. Regge, *Nuovo Cim.* **14** (1959) 951.

[103] P. D. B. Collins, *An introduction to Regge theory and high energy physics*, Cambridge, Cambridge University Press, 1977.

[104] WA91 Collaboration, S. Abatzis et al., *Phys. Lett.* **B324** (1994) 509.

[105] V. A. Abramovskii, V. N. Gribov, O. V. Kancheli, *Sov. J. Phys.* **18** (1974) 308.

[106] A. Donnachie and P. V. Landshoff, *Phys. Lett.* **B296** (1992) 277.

[107] G. Miller et al., SLAC-MIT Coll., *Phys. Rev.* **D5** (1972) 528.

[108] J. C. Collins, D. E. Soper and G. Sterman in: *Perturbative QCD*, edited by A. H. Mueller, World Scientific, Singapore (1989).

[109] N. Magnussen et al., *Proc. Workshop on Physics at HERA*, DESY, Hamburg, 1991, vol. **3** 1167.

[110] G. t'Hooft, *Nucl. Phys.* **35** (1971) 167;
G. t'Hooft and M. Veltman, *Nucl. Phys.* **B44** (1972) 189.

[111] E. C. G. Stueckelberg and A. Petermann, *Helv. Phys. Acta* **26** (1953) 499.

[112] M. Gell-Mann and F. E. Low, *Phys. Rev.* **95** (1954) 1300.

[113] C. Callan, *Phys. Rev.* **D2** (1970) 1541;
K. Symanzik, *Com. Math. Phys.* **18** (1970) 227.

[114] M. R. Pennington, *Rep. Prog. Phys.* **46** (1983) 393.

[115] D. J. Gross and F. Wilczek, *Phys. Rev. Lett.* **30**, No. 26 (1973) 1343;
H. D. Politzer, *Phys. Rev. Lett.* **30**, No. 26, 1346 (1973).

[116] W. Caswell, *Phys. Rev. Lett.* **33** (1974) 244;
D, R. T. Jones, *Nucl. Phys.* **B75** (1974) 531.

[117] O. V. Tarasov, A. A. Vladimirov and A. Y. Zharkov, *Phys. Lett.* **B93** (1980) 429.

[118] F. Bloch and A. Nordsieck, *Phys. Rev.* **52** (1937) 54.

[119] T. Kinoshita, *J. Math. Phys.* **3** (1962) 768;
T. D. Lee and M. Nauenberg, *Nucl. Phys.* **B120** (1977) 77.

[120] R. K. Ellis et al., *Nucl. Phys.* **B152** (1979) 285.

[121] A. H. Mueller, *Phys. Rev.* **D18** (1978) 3705.

[122] D. Amati et al., *Nucl. Phys.* **B140** (1978) 54.

[123] A. Efremov and A. Radyushkin, *Theor. Math. Phys.* 44 (1981) 664.

[124] J. C. Collins et al., *Phys. Lett.* **109B** 388; *Nucl. Phys.* **B223** (1983) 381; *Phys. Lett.* **134B** (1984) 263.

[125] G. Altarelli, *Phys. Rep.* **81** No. 1 (1982)

[126] J. Kogut and L. Susskind, *Phys. Rep.* **C8** (1973) 76.

[127] V. N. Gribov and L. N. Lipatov, *Sov. Journ. Nucl. Phys.* **15** (1972) 438 and 675;
G. Altarelli and G. Parisi, *Nucl. Phys.* **B126** (1977) 298.
Yu. L. Dokshitzer, *Sov. Phys. JETP* **46** (1977) 641.

[128] K. Wilson, *Phys. Rev.* **179** (1969) 1499.

[129] E. Reya, *Phys. Rep.* **69** No. 3 (1981).

[130] EMC Collaboration, J. J. Aubert et al., *Nucl. Phys.* **B272** (1986) 158.

[131] A. D. Martin, R. G. Roberts, W. J. Stirling, *Phys. Rev.* **D47** (1993) 867.

[132] M. Glück, E. Reya and A. Vogt, *Z. Phys.* **C48** (1990) 471; *ibid.* **C53** (1992) 127; *Phys. Lett.* **B306** (1993) 391.

[133] CTEQ Collaboration, J. Botts et al., *Phys. Lett.* **B304** (1993) 159;

[134] W. L. van Neerven, *Proc. of the XXI Int. Meeting on Fundamental Physics*, Miraflores de la Sierra, Madrid, 1993.

[135] R. T. Herrod and S. Wada, *Phys. Lett.* **96B** (1980) 195;
R. T. Herrod, S. Wada and B. R. Webber, *Z. Phys.* **C9** (1981) 351.

[136] A. D. Martin, R. G. Roberts, W. J. Stirling, *Phys. Lett.* B306 (1993) 145.

[137] NMC Collaboration, P. Amaudruz et al., *Phys. Lett.* **259B** (1992) 159; Preprint CERN-PPE/94-32.

[138] BCDMS Collaboration, A. Baldit et al., *Phys. Lett.* **B223** (1989) 485.

[139] CCFR Collaboration, A. Bazarko et al., Columbia University preprint NEVIS-1492 (1993); Published in Moriond 1993: Hadronic:43-46 (QCD161:R4:1993:V.2).

[140] WA70 Collaboration, M. Bonesini et al., *Z. Phys.* **C38** (1988) 371.

[141] E. A. Kuraev, L. N. Lipatov and V. Fadin, *Zh. Eksp. Teor. Fiz.* **72** (1977) 373; *Sov. Phys. JETP* **45** (1977) 199.

[142] T. Jaroszewicz, *Acta. Phys. Polon.* **B11** (1980) 965.

[143] L. N. Lipatov, in *Perturbative QCD*, edited by A. H. Mueller, World Scientific, Singapore, 1989.

[144] A. D. Martin, *Proc. Int. Workshop on DIS and related subjects*, Eilat, Israel, Feb. 1994.

[145] Ya. Ya. Balitskij and L. N. Lipatov, *Yad. Fiz.* **28** (1978) 1597 [*Sov. J. Nucl. Phys.* **28** (1978) 822].

[146] J. Bronzan and R. L. Sugar, *Phys. Rev.* **D17** (1978) 585.

[147] M. Ciafaloni, *Nucl. Phys.* **296** (1988) 49;
S. Catani, F. Forani and G. Marchesini, *Phys. Lett.* **B234** (1990) 339; *Nucl. Phys.* **B336** (1990) 18.

[148] G. Marchesini, *Proc. Workshop QCD at 200 TeV*, Erice, Italy, 1990, edited by L. Cifarelli and Yu. L. Dokshitzer, Plenum Press, New York, 1992.

[149] L. V. Gribov, E. M. Levin and M. G. Ryskin, *Phys. Rep.* **100** (1983) 1.

[150] J. Bartels and M. G. Ryskin, *Z. Phys.* **C60** (1993) 751.

[151] K. Golec-Biernat, M. W. Krasny and S. Riess, *Phys. Lett.* **B337** (1994) 367. (1994).

[152] G. Ingelman and P. Schlein, *Phys. Lett.* B152 (1985) 256.

[153] UA8 Collaboration, R. Bonino et al., *Phys. Lett.* **B211** (1988) 239; UA8 Collaboration, A. Brandt at al., *Phys. Lett.* **B297** (1992) 417.

[154] A. Donnachie and P. V. Landshoff, *Nucl. Phys.* **B244** (1984) 322.

[155] A. Donnachie and P. V. Landshoff, *Phys. Lett.* **B191** (1987) 309; *Nucl. Phys.* B303 (1988) 634.

[156] P. V. Landshoff, J. C. Polkinghorne and R. D. Short, *Nucl. Phys.* **B28** (1971) 225.

[157] A. H. Mueller, *Journ. of Phys.* **G19** (1993) 1463.

[158] N. N. Nikolaev, B. G. Zakharov and V. R. Zoller, *Pis'ma Zh. Eks. Teor. Fis.* 59 (1994) 8; *Phys. Lett.* **B328** (1994) 486.

[159] UA1 Collaboration, C. Albajar et al., *Nucl. Phys.* **B309** (1988) 405.

[160] T. Hara et al., *Phys. Rev. Lett.* **50** (1983) 2058.

[161] T. K. Gaisser, U. P. Sukhatme and G. P. Yodth, *Phys. Rev.* **D 36** (1987) 1350.

[162] M. Honda et al., *Phys. Rev. Lett.* **70** (1993) 525.

[163] V. Barger et al., *Nucl. Phys.* **B88** (1975) 237.

[164] N. N. Nikolaev, *Proc. 3rd BLOIS Workshop on Elastic and Diffractive Scattering*, Evanston, 1989.

[165] R. M. Baltrusaitis et al., *Phys. Rev. Lett.* **52** (1984) 1380.

[166] R. J. Glauber, in *Lectures in Theoretical Physics*, Interscience, New York, 1959, vol. 1.

[167] J. D. Bjorken, *Proc. Int. Workshop on DIS*, Eilat, Israel, 1994.

[168] A. J. Askew, J. Kwieciński, A. D. Martin and P. J. Sutton, *Phys. Rev.* **D47** (1993), 3775.

[169] K. Golec-Biernat, J. Kwieciński, A. D. Martin and P. J. Sutton, *Phys. Lett.* **B335** (1994) 220.

[170] A. H. Mueller, *Nucl. Phys. B (Proc. Suppl.)* **18C** (1990) 125; *J. Phys.* **G17** (1991) 1443.

[171] A. H. Mueller and H. Navelet, *Nucl. Phys.* **B282** (1987) 727.

[172] G. Ingelman and R. Rückl, *Phys. Lett.* **201** (1988) 369.

[173] Particle Data Group, *Phys. Rev.* **D45** (1992).

[174] F. Jaquet and A. Blondel, *Proc. Study of an ep Facility in Europe*, ed. U. Amaldi, 1979, p. 391.

[175] S. Bentvelsen, J. Engelen and P. Kooijman, *Proc. Workshop on Physics at HERA*, DESY, Hamburg, 1991, vol. 1 23.

[176] H1 Collaboration, T. Ahmed et al., *Nucl. Phys.* **B439** (1995) 471.

[177] U. Bassler and G. Bernardi, DESY preprint DESY 94-231 (1994), submitted to *Nucl. Instr. and Meth.*.

[178] H1 Collaboration, I. Abt et al., *Nucl. Phys.* **B407** (1993) 515.

[179] ZEUS Collaboration, M. Derrick et al., *Phys. Lett.* B316 (1993) 412.

[180] ZEUS Collaboration, M. Derrick et al., *Z. Phys.* **C65** (1995) 379.

[181] E665 Collaboration, A. V. Kotwal et al., *Proc. QCD in High Energy interactions, XXXth Recontre de Moriond*, FERMILAB-Conf-95/046-Expt., 1995.

[182] L. Whitlow et al., *Phys. Lett.* **B282** (1992) 475.

[183] BCDMS Collaboration, A. C. Benvenuti et al., *Phys. Lett.* **B223** (1989) 485.

[184] CTEQ Collaboration, J. Botts et al., preprint MSUHEP 93/18 (unpublished).

[185] A. D. Martin, R. G. Roberts, W. J. Stirling, *Phys. Rev.* **D50** (1994) 6734.

[186] M. Glück, E. Reya and A. Vogt, DESY preprint DESY 94-206 (1994).

[187] A. Capella et al., *Phys. Lett.* **B337** (1994) 358.

[188] A. Donnachie and P. V. Landshoff, *Z. Phys.* **C61** (1994) 139.

[189] K. Golec-Biernat, M. W. Krasny and S. Riess, *Phys. Lett.* **B337** (1994) 367.

[190] W. Zhu, D. Xue, Kang-Min Chai and Zai-Xin Xu, *Phys. Lett.* **B317** (1993) 200.

[191] S. Ostapachenko, private communication.

[192] J. Kwiecinski, A. D. Martin, P. J. Sutton, *Phys. Rev.* **D46** (1992) 921.

[193] H1 Collaboration, S. Aid et al., *Phys. Lett.* **B354** (1995) 494.

[194] K. Prytz, *Phys. Lett.* **B311** (1993) 286; Rutherford-Appleton Laboratory preprint, RAL-94-036.

[195] H1 Collaboration, I. Abt et al., *Phys. Lett.* **B321** (1994) 161.

[196] J. E. Huth et al., Fermilab-Conf-90/249-E (1990).

[197] H1 Collaboration, S. Aid et al., DESY preprint DESY 95-086 (1995).

[198] H1 Collaboration, T. Ahmed et al., *Phys. Lett.* **B324** (1994) 241.

[199] D. Haidt and H. Pietschmann, Landolt-Börnstein New Series I/10, Springer (1988).

[200] NMC Collaboration, D. Allasia et al., *Phys. Lett.* **B258** (1991) 493.

[201] ZEUS Collaboration, *Phys. Lett.* **B345** (1995) 576.

[202] ZEUS Collaboration, M. Derrick et al., *Phys. Lett.* **B315** (1993) 481.

[203] H1 Collaboration, T. Ahmed et al., *Nucl. Phys.* **B429** (1994) 477.

[204] H. Jung, DESY preprint DESY 93-182 (1993), to appear in Comput. Phys. Commun..

[205] P. Bruni and G. Ingelman, in *Proc. of the Europhysics Conference*, Marseilles, France, July 1993, eds J. Carr and M. Perrottet, p. 595 and unpublished program manual.

[206] H1 Collaboration, T. Ahmed at al., *Phys. Lett.* **B348** (1995) 681.

[207] M. Genovese, N. N. Nikolaev, B. Zakharov, Inst. für Kernphysik, KFA, Jülich preprint KFA-IKP(Th)-1994-37, 1994.

[208] M. Genovese, N. N. Nikolaev, B. Zakharov, Inst. für Kernphysik, KFA, Jülich preprint KFA-IKP(Th)-1994-36, 1994.

[209] A. B. Kaidalov, *Phys. Rep.* **50** (1979) 157.

[210] T. J. Chapin et al., *Phys. Rev.* **D31** (1985) 17.

[211] K. Golec-Biernat and J. Kwieciński, *Phys. Lett.* **B353** (1995) 329. 1670/PH, 1995.

[212] A. Capella, A. Kaidalov, C. Merino and J. Tran Thanh Van, *Phys. Lett.* **B343** (1995) 403.

[213] R. Engel, J. Ranft and S. Roesler, University of Siegen preprint, SI 95-16, 1995.

[214] E. Levin and M. Wüsthoff, FERMILAB-PUB-92/334-T, Nov. 1992.

[215] E. Levin, *Proc. Int. Workshop on DIS and related subjects*, Eilat, Israel, Feb. 1994.

[216] W. Buchmüller, *Phys. Lett.* **B335** (1994) 479.

[217] W. Buchmüller, *Phys. Lett.* **B353** (1995) 335.

[218] W. Buchmüller and A. Hebecker, *Phys. Lett.* **B355** (1995) 573.

[219] J. J. Sakurai, *Ann. Phys.* (N. Y.) **11** (1960) 1;
M. Gell-Mann and F. Zachariasen, *Phys. Rev.* **124** (1961) 953.

[220] T. H. Bauer et. al., *Rev. Mod. Phys.* **50** (1978) 261.

[221] Ch. Berger and W. Wagner, *Phys. Rep.* **146** (1987).

[222] PLUTO collaboration, Ch. Berger et al., *Phys. Lett.* **B142** (1984) 111.

[223] G. A. Schuler and T. Sjöstrand, *Phys. Lett.* **B300** (1993) 169.

[224] H1 Collaboration, T. Ahmed et al., *Phys. Lett.* **B299** (1993) 374.

[225] ZEUS Collaboration, M. Derrick et al., *Phys. Lett.* **B293** (1992) 465.

[226] R. Gandhi and J. Sarcevic, *Phys. Rev.* **D44** (1991) 410.

[227] H. Abramowicz et al., *Phys. Lett.* **B269** (1991) 465.

[228] H.-U. Bengtsson and T. Sjöstrand, *Comp. Phys. Comm.* **46** (1987) 43;
T. Sjöstrand, *Proc. Workshop on Physics at HERA*, DESY, Hamburg, 1991, vol. **3** 1405.

[229] M. Drees and K. Grassie, *Z. Phys.* **C28** (1985) 451.

[230] N. H. Brook, A. DeRoeck and A. T. Doyle, RAYPHOTON 2.0, *Proc. Workshop on Physics at HERA*, DESY, Hamburg, 1991, vol. **3** 1453.

[231] H1 Collaboration, I. Abt et al., *Phys. Lett.* **B328** (1994) 176.

[232] UA1 Collaboration, C. Albajar et al., *Nucl. Phys.* **B335** (1990) 261.

[233] OMEGA Photon Collaboration, R. J. Apsimon et al., *Z. Phys.* **C43** (1989) 63.

[234] B. A. Kniehl and G. Kramer, *Z. Phys.* **C62** (1994) 53.

[235] H1 Collaboration, I. Abt et al., *Phys. Lett.* **B314** (1993) 436;

[236] H1 Collaboration, T. Ahmed et al., *Nucl. Phys.* **B445** (1995) 195.

[237] H. Abramowicz, K. Charchula and A. Levy, *Phys. Lett.* **B269** (1991) 458.

[238] H1 Collaboration, T. Ahmed et al., *Nucl. Phys.* **B435** (1995) 3.

[239] G. A. Schuler and T. Sjöstrand, *Proc. Workshop on Two-Photon Physics from DAΦNE to LEP200 and Beyond*, Paris, 1994; CERN preprint, CERN-TH.7193/94, 1994.

[240] J. C. Collins and G. A. Landinsky, *Phys. Rev.* **D43** (1991) 2847.

[241] H. Cheng and T. T. Wu, *Proc. 1971 Int. Symp. on electron and proton interactions at high energies*, Cornell University, Ithaca, N.Y, 1972.

[242] H. Cheng and T. T. Wu, *Phys. Lett.* **B44** (1973) 97.

[243] C. Bourrely, J. Soffer and T. T. Wu, *Phys. Lett.* **B339** (1994) 322.

[244] J. C. Collins and G. A. Ladinsky, *Phys. Rev.* **D43** (1991) 2847.

[245] K. Honjo et al., *Phys. Rev.* **D47** (1993) 4815; *Phys. Rev.* **D48** (1993) 1048.

[246] R. S. Fletcher, T. K. Gaisser and F. Halzen, *Phys. Lett.* **B298** (1993) 442.

[247] *Proc. Workshop on Physics at HERA*, DESY, Hamburg, 1991, vol. **3**.

[248] W. R. Nelson et al., *The EGS4 Code SYSTEM*, SLAC Report 265 (1985).

[249] H. Fesefeldt, *The Simulation of Hadron Showers*, RWTH Aachen preprint PITHA 85/02.

[250] G. Veneziano, *Nucl. Phys.* **B117** (1976) 519.

[251] G. t'Hooft, *Nucl. Phys.* B72 (1974) 461.

[252] D. W. Duke and J. F Owens, *Phys. Rev.* **D30** (1984) 49.

[253] J. N. Capdevielle, *Nucl. Phys. B (Proc. Suppl.)*, **39A** (1995) 154.

[254] V. Braun, M. Gornicki, L. Mankievicz and A. Shafer, *Phys. Lett.* **B302** (1993) 291.

[255] A. Levy, DESY preprint DESY 95-003 (1995).

[256] H. Abramowicz et al., *Phys. Lett.* **B269** (1991) 465.

[257] K. J. Eskola, K. Kajantie and J. Lindfors, *Nucl. Phys.* **B323** (1989) 37.

[258] K. J. Eskola, K. Kajantie and P. V. Ruuskanen, *Phys. Lett.* **B332** (1994) 191.

[259] F. Halzen et al., *Proc. 6th International Symposium on Neutrino Telescopes*, Venice, 1994.

[260] E. Eichten, I. Hinchliffe, K. Lane and C. Quigg, *Rev. Mod. Phys.* **56** (1984) 579.

[261] A. Aurenche et al., *Phys. Rev.* **D45** (1992) 92.

List of Figures

List of Tables